

MAGNETIC FIELD EFFECTS ON MOLECULAR EMISSIVITY IN SOLUTIONS

Tomoyasu Mani

A DISSERTATION

in

Biochemistry and Molecular Biophysics

Presented to the Faculties of the University of Pennsylvania

in

Partial Fulfillment of the Requirements for the

Degree of Doctor of Philosophy

2013

Supervisor of Dissertation

\_\_\_\_\_

Sergei A. Vinogradov

Associate Professor, Biochemistry and Biophysics

Graduate Group Chairperson

\_\_\_\_\_

Kathryn M. Ferguson

Associate Professor, Physiology

Dissertation Committee

S. Walter Englander, Chair, Jacob Gershon-Cohen Professor, Biochemistry and Biophysics

P. Leslie Dutton, Eldridge Reeves Johnson Professor, Biochemistry and Biophysics

Yale E. Goldman, Professor, Physiology

Joseph E. Subotnik, Assistant Professor, Chemistry

A. Joshua Wand, Benjamin Rush Professor, Biochemistry and Biophysics

Eric Borguet, Professor, Chemistry, Temple University

MAGNETIC FIELD EFFECTS ON MOLECULAR EMISSIVITY IN SOLUTIONS

COPYRIGHT

2013

Tomoyasu Mani

This work is licensed under the  
Creative Commons Attribution-  
NonCommercial-ShareAlike 3.0  
License

To view a copy of this license, visit

<http://creativecommons.org/licenses/by-nc-sa/2.0/>

*To my family.*

## ACKNOWLEDGMENT

I would like to acknowledge everyone who contributed to this work. Foremost, I would like to thank my advisor Sergei A. Vinogradov who provided guidance, support, and stimulus and intellectual environment throughout my graduate career. I appreciate the support from Arjun G. Yodh. I would like to thank Robin M. Hochstrasser for helpful discussions and insight throughout the work. I would also like to thank Tatiana V. Esipova and Louise E. Sinks for helpful discussions and assistance they have provided. Tom Troxler of Regional Laser and Biomedical Technology Laboratories at Penn helped me perform nanosecond transient absorption spectroscopy and fluorescence lifetime measurements. For other instrumental supports, Eiko Nakamura-Ogiso kindly supported me to use EPR, and Suzanne Wehrli helped me perform NMR. I would like to thank Nikolai Tkachenko of Tampere University of Technology, who kindly allowed me to perform femtosecond transient absorption spectroscopy and other experiments in his lab at Tampere for the works presented in Chapter 5 and 6. Many thanks to Dariusz M. Niedzwiedzki of Washington University in St. Louis for femtosecond transient absorption spectra presented in Chapter 4, and to Mana Tanabe and Seigo Yamauchi of Tohoku University who performed time-resolved EPR in the work presented in Chapter 6. I was very fortunate to have interacted with two late scientists: Robin M. Hochstrasser as a former chair of my dissertation committee and Seigo Yamauchi as a collaborator. I would also like to thank Research Foundation for Opto-Science and Technology (Hamamatsu, Japan) for the generous support. Finally, I want to thank my wife Chikako who has supported me in many ways.

## ABSTRACT

### MAGNETIC FIELD EFFECTS ON MOLECULAR EMISSIVITY IN SOLUTIONS

Tomoyasu Mani

Sergei A. Vinogradov

Control over dynamics of excited states of molecules is fundamental to utilization of these states in all areas of technologies, including optical microscopy and tomography. We explored the possibility of magnetically controlling molecular emissivity by influencing spin dynamics in radical pairs (RPs) and triplet-triplet pair. We envisioned that by including RPs into a pathway leading to the formation (or decay) of an emissive triplet state, magnetic influence on phosphorescence could be realized *via* modulation of the RP's spin dynamics. RPs can initially be produced in their singlet or triplet spin state. These two cases were explored in the studies of electron and energy dynamics in series of donor-acceptor systems, comprising phosphorescent platinum (II) porphyrins (PtP) and rhodamine B (RhB<sup>+</sup>) derivatives.

In one series, the phosphorescent triplet state of PtP is generated by way of photo-excitation of RhB<sup>+</sup>, followed by photoinduced electron transfer with formation of a singlet-born RP, RP intersystem crossing, and subsequent recombination of the triplet RP. Similarly, singlet-born RPs were included into a pathway leading to PtP triplet state in a triad system comprising PtP, anthracene, and boron dipyrromethene.

Using another series, we have demonstrated that visible room-temperature phosphorescence can be modulated by weak magnetic fields (<1T). In this case, the RP is initially born in its triplet state upon direct excitation of PtP, followed by electron transfer originating in the PtP triplet state. External magnetic field modulates spin dynamics in the RP, affecting contribution of the singlet charge recombination channel and thereby influencing the phosphorescence.

Spin dynamics of triplet-triplet pair is also susceptible to magnetic field. Triplet-triplet pair can undergo triplet-triplet annihilation (TTA) process leading to photon upconversion, which is

typically observed as *p*-type delayed fluorescence. We have demonstrated TTA-sensitized delayed fluorescence and delayed phosphorescence, mediated by near-infrared absorbing metalloporphyrins as sensitizers in solution at room temperature, can be magnetically modulated.

These studies present unusual and interesting examples of magnetic field effects on molecular emission and set the stage for rational design of optical imaging probes with magnetically controlled emissivity.

## TABLE OF CONTENTS

<b>ACKNOWLEDGMENT</b> .....	<b>IV</b>
<b>ABSTRACT</b> .....	<b>V</b>
<b>TABLE OF CONTENTS</b> .....	<b>VII</b>
<b>LIST OF TABLES</b> .....	<b>XI</b>
<b>LIST OF ILLUSTRATIONS</b> .....	<b>XII</b>
<b>CHAPTER 1 INTRODUCTION</b> .....	<b>1</b>
1.1 Triplet state.....	1
1.2 Unified view of magnetic field effects.....	6
1.3 Electron transfer.....	9
1.4 Magnetic field effects on emissivity in solutions.....	12
1.5 Outline.....	13
<b>CHAPTER 2 ENVISIONED APPLICATIONS</b> .....	<b>15</b>
2.1 Optical tomography.....	15
2.2 Optical microscopy.....	17

2.3 Photodynamic therapy .....	18
<b>CHAPTER 3 INTRODUCTION TO MAGNETIC FIELD EFFECTS ON SPIN DYNAMICS IN RADICAL PAIRS.....</b>	<b>19</b>
3.1 Spin selectivity .....	19
3.2 Radical pair mechanism .....	20
3.3 Relaxation mechanism .....	24
3.4 Photophysical pathways leading to triplet state .....	24
3.5 Magnetic field effects on triplet emissivity through RPs.....	26
<b>CHAPTER 4 GENERATION OF EMISSIVE TRIPLET STATE VIA PHOTOINDUCED ELECTRON TRANSFER AND RADICAL PAIR INTERSYSTEM CROSSING.....</b>	<b>28</b>
4.1 Summary.....	28
4.2 Introduction .....	29
4.3 Experimental methods .....	32
4.4 Results and discussion.....	40
4.5 Conclusions.....	59
4.6 Appendix.....	59

<b>CHAPTER 5 EMISSIVE TRIPLET STATE AND RADICAL PAIR SPIN DYNAMICS IN THE TRIAD CONTAINING PT(II) PORPHYRIN .....</b>	<b>73</b>
5.1 Introduction .....	73
5.2 Experimental methods .....	75
5.3 Results and discussion .....	81
5.4 Conclusions.....	102
5.5 Appendix.....	102
<b>CHAPTER 6 MODULATION OF VISIBLE ROOM TEMPERATURE PHOSPHORESCENCE BY WEAK MAGNETIC FIELDS .....</b>	<b>118</b>
6.1 Summary.....	118
6.2 Introduction .....	119
6.3 Experimental methods .....	119
6.4 Results and discussion.....	125
6.5 Conclusions.....	132
6.6 Appendix.....	133
<b>CHAPTER 7 INTRODUCTION TO THE MAGNETIC FIELD EFFECTS ON TRIPLET-TRIPLET EXCITON PAIR .....</b>	<b>142</b>
7.1 Johnson-Merrifield theory.....	142

7.2 Atkins-Evans theory .....	146
7.3 Summary .....	148
<b>CHAPTER 8 MAGNETIC FIELD EFFECTS ON TRIPLET-TRIPLET ANNIHILATION IN SOLUTIONS: MODULATION OF VISIBLE/NIR LUMINESCENCE .....</b>	<b>149</b>
8.1 Summary .....	149
8.2 Introduction .....	150
8.3 Experimental methods .....	153
8.4 Results and discussions .....	153
8.5 Conclusions .....	161
8.6 Appendix .....	161
<b>CHAPTER 9 CONCLUDING REMARKS .....</b>	<b>163</b>
<b>APPENDIX .....</b>	<b>166</b>
A.1 Matlab (MathWorks, MA) code for Förster-type energy transfer .....	166
<b>BIBLIOGRAPHY .....</b>	<b>169</b>

## LIST OF TABLES

### Chapter 4

<b>Table 4.1.</b>	Selected photophysical properties of the PtP-Ph <sub>n</sub> -pRhB <sup>+</sup> dyads <b>1-3</b> (n=1-3) and of their components	45
<b>Table 4.2.</b>	Rate constants associated with the pathways displayed in Fig. 4.6	55
<b>Table 4.A1.</b>	Rate constants for compounds <b>1-3</b> – summary (s <sup>-1</sup> )	72

### Chapter 5

<b>Table 5.1.</b>	Quantum yields ( $\Phi \times 10^{-2}$ ) of emission at room temperature	86
<b>Table 5.2.</b>	Rate constants (s <sup>-1</sup> ) associated with the pathway displayed in Fig. 5.6 and Fig. 5.A10	101
<b>Table 5.A1.</b>	Quantum yields ( $\Phi \times 10^{-2}$ ) of emission at room temperature	103

### Chapter 6

<b>Table 6.A1.</b>	Redox potentials (vs SCE)	138
<b>Table 6.A2.</b>	Time constants of rise and decay phases of TREPR signals (in $\mu$ s)	138
<b>Table 6.A3.</b>	Photophysical rate constants and emission quantum yields	138

### Chapter 8

<b>Table 8.1.</b>	MFE on delayed emission in systems containing MTBP's as donors and perylene as acceptor	160
-------------------	---	-----

## LIST OF ILLUSTRATIONS

### Chapter 1

- Figure 1.1.** General energy diagram of molecules that contain even numbers of electrons and do not exhibit orbital degeneracy 2
- Figure 1.2.** Vector representation of singlet and triplet spin states 6
- Figure 1.3.** Potential energy surfaces (U) for electron transfer processes between An initial state and the final state in harmonic approximation 11

### Chapter 2

- Figure 2.1.** Schematic illustration of tomographic imaging experiment utilizing optical and magnetic fields 16

### Chapter 3

- Figure 3.1.** A schematic diagram for chemical reactions that occur through radical pairs 20
- Figure 3.2.** Energy diagram of electronic spin states of a radical pair in magnetic field (B) 23
- Figure 3.3.** Reaction scheme of generation of emissive triplet states *via* RPs 25
- Figure 3.4.** Energy diagram of radical pairs in the absence (OFF) and the presence (ON) of external magnetic field 26

### Chapter 4

- Figure 4.1.** Energy diagram of bichromophoric antenna (A) – core (C) systems 31
- Scheme 4.1.** Synthesis of dyads 1-3 35
- Chart 4.1.** Studied dyads 1-3 41
- Figure 4.2.** Optical spectra of PtP, pRhB<sup>+</sup> and dyad 1 in benzonitrile 44

<b>Figure 4.3.</b> Early time evolution of dyad <b>1</b> upon photo excitation at 580 nm	47
<b>Figure 4.4.</b> Time evolution of dyad <b>1</b> probed by nanosecond transient absorption spectroscopy	51
<b>Figure 4.5.</b> Emission spectra of <b>1</b> at 60 $\mu$ s after excitation pulse ( $\lambda_{\text{max}}=580$ nm).	53
<b>Figure 4.6.</b> Pathways occurring in PtP-RhB dyads	55
<b>Figure 4.A4.</b> Evolution of species B	61
<b>Figure 4.A1.</b> Absorption spectra of dyads <b>1-3</b> and their components, pRhB <sup>+</sup> and PtP, in benzonitrile	62
<b>Figure 4.A2.</b> Emission spectra of dyads <b>1-3</b> and of the individual chromophores, obtained by linear decomposition	63
<b>Figure 4.A3.</b> Early time evolution of dyad <b>2</b> upon photo excitation at 580 nm	64
<b>Figure 4.A5.</b> FSTA spectra of <b>1</b> (A) and <b>2</b> (B) in the NIR range (765-910 nm)	65
<b>Figure 4.A6.</b> Additional FSTA spectra	66
<b>Figure 4.A7.</b> Structural considerations for dyads <b>1</b> and <b>2</b>	67
<b>Figure 4.A8.</b> Phosphorescence decays and their time constants for <b>1</b> (A), <b>2</b> (B), and <b>3</b> (C)	68
<b>Figure 4.A9.</b> Nanosecond transient absorption (NSTA spectra of <b>2</b> (A) and <b>3</b> (C) in the visible range upon excitation at 532 nm (10 ns pulse)	69
<b>Figure 4.A10.</b> Emission spectra of <b>1</b> (A), PtP-Ph <sub>1</sub> (B) and pRhB <sup>+</sup> (C) at 77K, $\lambda_{\text{ex}}=580$ nm.	70
 <b>Chapter 5</b>	
<b>Figure 5.1.</b> Two photophysical pathways leading to emissive triplet states	74
<b>Scheme 5.1.</b> Synthesis of PtP-An-BD	78
<b>Chart 5.1.</b> Studied triad PtP-An-BD	83
<b>Figure 5.2.</b> Absorption and emission spectra of PtP, An-BD, and the triad PtP-An-BD	84

<b>Figure 5.3.</b> Excitation spectra of PtP-An-BD	87
<b>Figure 5.4.</b> Early time evolution of An-BD and PtP-An-BD upon photo excitation at 490 nm	91
<b>Figure 5.5.</b> Time evolution of PtP-An-BD upon photo excitation at 415 nm	99
<b>Figure 5.6.</b> Pathways occurring in PtP-An-BD triad upon excitation of BD	100
<b>Figure 5.A1.</b> Emission spectra of An-BD	107
<b>Figure 5.A2.</b> Steady-state spectra of An-BD and PtP-An-BD in toluene	108
<b>Figure 5.A3.</b> Time evolution of PtP-An-BD and An-BD at selected wavelengths	109
<b>Figure 5.A4.</b> FSTA spectra of An-BD at selected time points	110
<b>Figure 5.A5.</b> Time evolution of An-BD in toluene	111
<b>Figure 5.A6.</b> NSTA spectra of An-BD at 50 ns time point ( $\lambda_{\text{ex}} = 532$ nm) in toluene	112
<b>Figure 5.A7.</b> NSTA spectra of PtP-An-BD	113
<b>Figure 5.A8.</b> Phosphorescence decay curves of PtP and PtP-An-BD	114
<b>Figure 5.A9.</b> Emission spectra of An-BD in toluene at 77K ( $\lambda_{\text{ex}} = 505$ nm)	115
<b>Figure 5.A10.</b> Pathways occurring in PtP-An-BD triad upon excitation of BD unit	116
<b>Figure 5.A11.</b> Computed molecular structure of PtP-An-BD	117
 <b>Chapter 6</b>	
<b>Scheme 6.1.</b> Synthesis of PtP-Ph <sub>n</sub> -RosB	121
<b>Figure 6.1.</b> Energy diagram and structures of dyads PtP-Ph <sub>n</sub> -RosB <sup>+</sup> ( <b>1-2</b> , n=1-2)	125
<b>Figure 6.2.</b> Magnetic field effects on phosphorescence emission from <b>1</b> and <b>2</b>	127
<b>Figure 6.3.</b> Spectral features of <b>1</b> probed by FSTA and TREPR	128
<b>Figure 6.4.</b> Energy diagram and a proposed mechanism of MFE on phosphorescence	130
<b>Figure 6.A1.</b> Diagram of the setup for phosphorescence MARY spectroscopy	133
<b>Figure 6.A2.</b> Some spectral features of <b>1</b> and <b>2</b>	134
<b>Figure 6.A3.</b> Time evolution of <b>2</b> upon photo excitation at 405 nm	135

<b>Figure 6.A4.</b> TREPR signal evolution for <b>1</b>	136
<b>Figure 6.A5.</b> TREPR signal evolution for <b>2</b>	137
<b>Chapter 8</b>	
<b>Figure 8.1.</b> Energy diagram associated with sensitized triplet-triplet annihilation	151
<b>Figure 8.2.</b> Structures and steady-state electronic properties of the molecules used in this work	154
<b>Figure 8.3.</b> Some spectral features of PdTBP and PtTBP in the presence and absence of perylene	155
<b>Figure 8.4.</b> Magnetic field effects on luminescence in PdTBP/perylene system	157
<b>Figure 8.5.</b> Ratio of rate constants ( $k_{TTA}$ ) as a function of magnetic field	159

## CHAPTER 1 Introduction

Optical imaging is a powerful technique in biomedical research. Emissive small molecules and proteins enable investigation of diverse biological processes in qualitative and quantitative ways. In order to fully exploit the potential of luminescent molecules in optical imaging, these molecules must be rationally designed based on understanding of their photophysical, electrochemical, and structural properties. While a variety of small molecules and genetically engineered proteins are already available for biological imaging applications, search for new probes is still at the forefront of the imaging field. In particular, it is of great interest to gain control over molecular emissivity using external forces or fields other than optical field in order to be able to modulate the emissivity and thereby create new imaging modalities with potentially higher sensitivity, selectivity and resolution.

In this work, we explored the possibility of controlling and/or modulating emissive excited electronic states of molecules by external magnetic field. Typically, chemical and photophysical processes are not magnetically sensitive; however, reactions which involve magnetically susceptible intermediate states, such as radical pairs or triplet-triplet exciton pairs, potentially can exhibit magnetic sensitivity. Here we investigate the possibility of constructing optical probes whose emission is made responsive to external magnetic fields. From here and throughout the text we term such probes as *magneto-optical* probes. We begin with a brief discussion of magnetically responsive electronic states, which underpin molecular designs presented in this dissertation.

### **1.1 Triplet state**

#### **1.1.1 Physical description of photo-excited states**

Photon absorption by a molecule triggers various photophysical processes, one of which can be emission of a photon (Fig. 1.1). The energy diagram in Fig. 1.1 is called Jablonski diagram (due to Alexander Jablonski),<sup>1</sup> where electronic energy levels are drawn as heavy horizontal lines and lighter horizontal lines represent vibrational states. Only a few of many modes of vibration are shown in Fig 1.1. The box beside an electronic energy level represents the molecular orbital (MO) electronic configuration that describes the respective level. Spin-components of only two of the highest energy electrons of the molecule are shown. The lowest sub-box represents the highest occupied molecular orbital (HOMO) of the ground singlet state ( $S_0$ ), the middle sub-box represents the lowest unoccupied molecular orbital (LUMO). Here we consider molecules with even numbers of electrons, and only two electrons are explicitly shown in Fig. 1.1. All other electrons are considered to be paired, so that their total spin angular momentum is zero. This kind of representation is routinely used in the literature.<sup>2</sup>

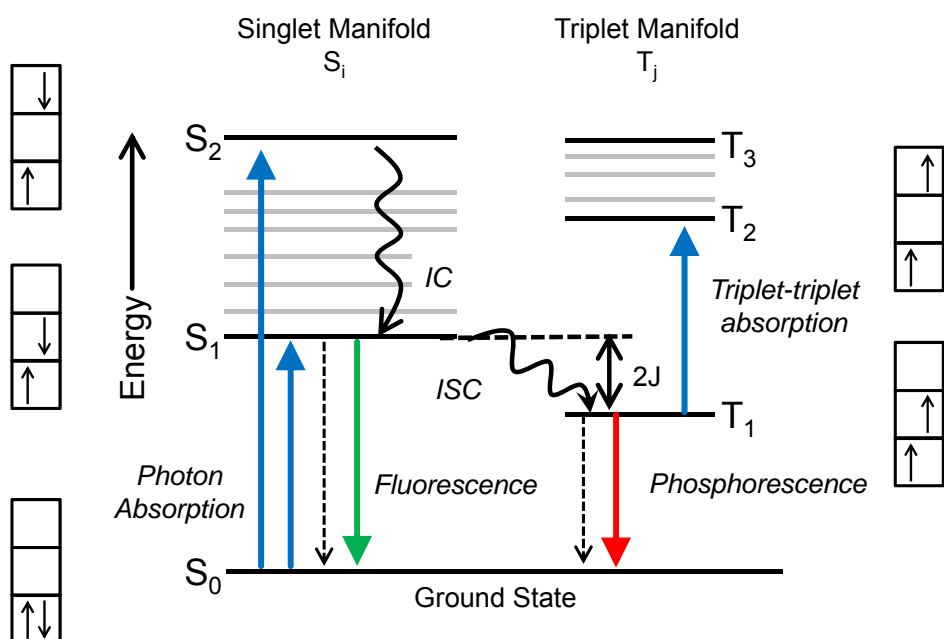


**Figure 1.1.** General energy diagram of molecules that contain even number of electrons and do not exhibit orbital degeneracy.

The levels on the left constitute the manifold of singlet states ( $S_i$ ), while those on the right constitute the manifold of triplet states ( $T_j$ ). The energy within each manifold increases with increasing subscript number of a state (i.e.  $E(S_2) > E(S_1)$ ). The lowest energy triplet state is usually a  $T_1$  state. There may be a difference between the energies of the singlet and triplet states corresponding to the same electronic configuration (i.e. the same orbital occupancy). This energy gap  $\Delta E_{ST}$  is the result of electron exchange interaction ( $2J$ ). Typically, in a molecule, the energy of the triplet state is lower than that of the singlet state for the same electronic configuration.<sup>3</sup>

Photon absorption  $S_i \leftarrow S_0$  ( $i \neq 0$ ) leads to population of a singlet electronic excited state of a molecule. Higher excited states in molecules usually decay non-radiatively to the lowest excited state possessing the same spin multiplicity (i.e.  $S_1$  for the singlet manifold and  $T_1$  for the triplet manifold) - the phenomenon known as Vavilov-Kasha rule.<sup>4</sup> Such non-radiative decay is called internal conversion (IC), and it typically occurs with rate constants in the range of  $>10^{12} \text{ s}^{-1}$ . From the lowest singlet excited state ( $S_1$ ), molecules can emit photons (fluorescence - a radiative pathway between electronic states of the same spin multiplicity), non-radiatively decay to the ground state or undergo intersystem crossing (ISC) to produce an electronic state within the triplet manifold. The process  $S_1 \rightarrow T_1$  is the main pathway that produces  $T_1$  triplet state under ordinary illumination. Absorption  $T_1 \leftarrow S_0$  is typically characterized by very small extinction coefficients, in the range  $<10 \text{ M}^{-1} \text{ cm}^{-1}$ , because of being a spin-forbidden transition. It is worth noting that transition  $S_1 \rightarrow T_1$  may occur *via*: 1) direct ISC from  $S_1$  to an upper vibrational level of  $T_1$ , or 2) ISC from  $S_1$  to an upper electronic  $T_n$  state, followed by rapid  $T_n \rightarrow T_1$  internal conversion.

$T_1$  state can relax back to the ground state by emitting a photon (phosphorescence - a radiative pathway between two electronic states of the different spin multiplicity), or by non-radiatively by  $T_1 \rightarrow S_0$  ISC. Since the transition between  $T_1$  and  $S_0$  states is spin-forbidden, both the radiative and non-radiative rates are orders of magnitude slower than for spin-allowed transitions, e.g.  $S_1 \rightarrow S_0$ . If  $T_1$  state is sufficiently populated, absorption processes associated with the excitations  $T_2 \leftarrow T_1$ ,  $T_3 \leftarrow T_1$ , ...,  $T_j \leftarrow T_1$ , can be observed. These processes constitute triplet-

triplet absorption, first example of which was observed in a solution of fluorescein in boric acid.<sup>5</sup> The technique named flash photolysis or Nanosecond Transient Absorption Spectroscopy (NSTA), pioneered by Porter and Windsor, makes it possible to observe triplet-triplet absorption on nano/microsecond time scale and thus track the dynamics of non-emissive triplet excited states.<sup>6</sup> In the case of emissive triplet excited states, dynamics can be monitored by time-resolved phosphorescence measurements.

The photophysical processes described above are the main radiative and non-radiative transitions occurring in a molecule upon absorption of a photon. Rate constants of these processes vary greatly, but for a typical fluorescent dye molecule, such as Rhodamine 6G, the combined rate of  $S_1 \rightarrow S_0$  radiative and non-radiative pathways ( $10^9$ - $10^{11} \text{ s}^{-1}$ ) is much higher than the rate of  $S_1 \rightarrow T_1$  ISC ( $\sim 10^6$ - $10^8 \text{ s}^{-1}$ ). However, ISC may occur at a significantly higher rate ( $\sim 10^{11}$ - $10^{12} \text{ s}^{-1}$ ) if a molecule is characterized by a strong spin-orbit coupling interaction. These are usually present in molecules with heavy atoms. In some rare cases the rate of ISC may greatly exceed the rates of all competing relaxation processes, leading to the formation of triplet states with high quantum yields. Furthermore, in some cases, radiative transition from the triplet state (phosphorescence) is also greatly enhanced and occurs with high quantum yield even at room temperature.

### 1.1.2 Representation of triplet state

Vector representation of the spin states of an electron pair is customarily employed to visualize spin motion (Fig. 1.2).<sup>3</sup> Such representation is especially useful when we consider interactions of spins with magnetic field. In this representation, we consider individual electron spins precessing around the axis of quantization (e.g. external magnetic field  $B$ ) and pointing either upward ( $\alpha$ -spin) or downward ( $\beta$ -spin). In a pair, the spins can either be aligned parallel to each other (in the vector mode at an angle to each other, but in the same general direction) so that the total spin  $S=1$ , or antiparallel,  $S=0$ . The quantum mechanical angular momentum has the

length  $\sqrt{S(S+1)}\hbar$ , and in the case of triplet state it has three projections on the axis in the direction of the magnetic field, to which the spin motion is coupled. These projections are given by  $M_S\hbar$ , where  $M_S=1,0,-1$ . In the zero-field, the electron spins are coupled to the field created by the orbital motion of electrons, and the energy difference between the three triplet sub-levels is very small. However, in the presence of external magnetic field, the triplet sub-levels split due to the Zeeman effect, since the two spin states ( $T_+$ ,  $T_-$ ) have equal but opposite magnetic moments, while the third ( $T_0$ ) has no magnetic moment in the direction of the applied field. The corresponding spin eigenfunctions are shown in Fig. 1.2. One has to be careful not to over-interpret graphical representation of S and  $T_0$  in this simplified vector diagram.<sup>7</sup> The picture as drawn suggests that there is some phase relation between the spin motions of different electrons in states S and  $T_0$ . However, the phase relation distinguishing S and  $T_0$  is actually between the spin function products  $\alpha_1\beta_2$  and  $\beta_1\alpha_2$ , and not between the individual spins. While there are other extended models, proposed by Atkins<sup>8</sup> and by Syage,<sup>9</sup> and by Monhick and Adrian,<sup>10</sup> the vector model presented in Fig. 1.2 is most convenient for visualization and it is widely used.

When two interacting electrons belong to the same molecular system, the singlet and triplet states corresponding to their spin motion are called “local” (Fig. 1.1). In this case, the electron-exchange interaction  $2J$  and the corresponding energy gap  $\Delta E_{ST}$  is large. When two electrons reside on two different molecules composing a weakly coupled system, e.g. a radical pair (RP), their spin motion may still be correlated, but  $2J$  is much smaller, as it decays exponentially with the distance between the interacting spins. In the absence of magnetic field, the three sublevels of a local triplet state are split due to spin dipole-dipole interaction (Zero-field splitting – ZFS). While ZFS does not play a role in molecular phosphorescence in solutions at ambient temperatures, it becomes important in molecular crystals possessing triplet-triplet exciton pairs. This will be treated in more detail in Chapter 7.

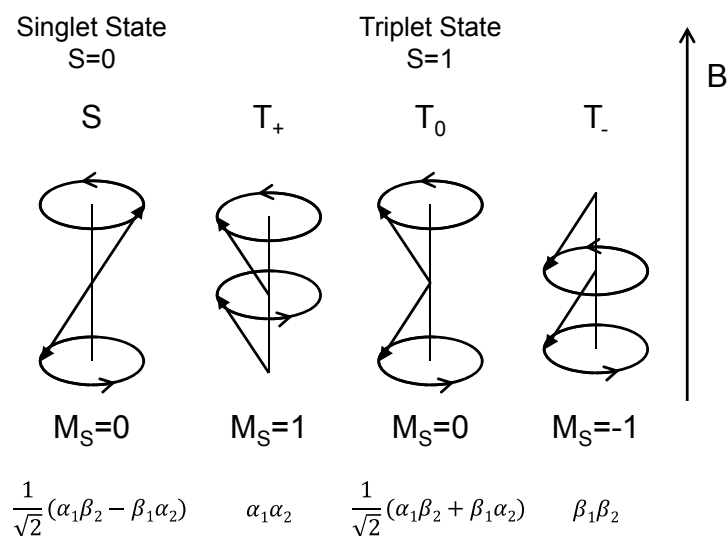


**Figure 1.2.** Vector representation of singlet and triplet states.

## 1.2 Unified view of magnetic field effects

From the energetic viewpoint, weak magnetic fields ( $\leq 1$  Tesla) are not able to impose any appreciable effects on chemical or photochemical reactions because their effects are much smaller than both thermal energy and typical activation energy. Indeed, the Zeeman splitting for a single electron at  $B=1$  T is as small as  $\sim 1 \text{ cm}^{-1}$  (or  $0.00012 \text{ eV}$ ) and for nuclear spins at  $B=1$  T it is  $\sim 10^{-3} \text{ cm}^{-1}$ . Their energies are  $10^2$ - $10^5$  times smaller than the thermal energy ( $k_B T$ ) at room temperature ( $T=295 \text{ K}$ ), i.e.  $\sim 200 \text{ cm}^{-1}$ , and  $10^3$ - $10^6$  times smaller than the activation energies of typical chemical reactions, i.e.  $\sim 3000 \text{ cm}^{-1}$ .<sup>11</sup> These numbers clearly show that ordinary magnetic fields should not normally affect chemical reactions.

At the same time it has been known for a long time that certain chemical reactions do in fact respond to external magnetic fields. These reactions involve magnetically sensitive intermediate species in their reaction paths. Research of magnetic field effects (MFE) on chemical reactions has given rise to variety of information on the kinetics and dynamics of these species and their reactions. Such investigations are collectively called "spin chemistry". The

unified view of MFE has been developed by Steiner and Ulrich, and here we will follow their description.<sup>7</sup> The key requirement for magnetic sensitivity of a reaction is “diabaticity,” i.e. a rather discontinuous change of the electronic wave function near the barrier separating the initial and the final states. The rate constant of a decay of a quantum state is expressed by the Fermi Golden rule:<sup>12</sup>

$$k_{i,f} = \frac{2\pi}{\hbar} \sum_m P_m \sum_n \left| \langle i,m | H' | f,n \rangle \right|^2 \delta(\epsilon_{i,m} - \epsilon_{f,n}) \quad (\text{Eq. 1.1})$$

where  $i$  and  $f$  are the initial and final electronic states, combined with vibrational manifolds  $\{m\}$  and  $\{n\}$ , respectively;  $p_m$  are the population probabilities, which are usually expressed by thermal equilibrium values. The states  $|i,m\rangle$  and  $|f,n\rangle$  are experimentally observable quasi-stationary states of a suitable Hamiltonian  $H_0$ . These states become non-stationary through the perturbation  $H'$ , whereby the rate of the decay of the initial state is proportional to the square of the corresponding matrix element, and the  $\delta$ -function selects for those final states that are allowed by conservation of energy (Eq. 1.1). Within the context of our discussion, states  $|i,m\rangle$  and  $|f,n\rangle$  would be electronic states of different spin character.

The MFE on the decay kinetics originate through a magnetic contribution  $H_B$  to the Hamiltonian  $H$ :

$$H = H_0 + H' \quad (\text{Eq. 1.2})$$

$H_B$  may be included either in  $H_0$ , defining the quasi-stationary states or in perturbation  $H'$ , inducing their decay. When  $H_B$  contribute to  $H'$ , the magnetic field directly induces coupling between the initial and final manifolds, causing irreversible decay. This is the so-called *direct mechanism*, as defined by Atkins and Stannard.<sup>13</sup> Examples of the direct mechanism include the case of magnetic quenching of iodine fluorescence and glyoxal.<sup>14</sup> These phenomena are typically restricted to small molecules in gas phase and we do not discuss further in this work.

A more important case is when the magnetic interaction  $H_B$  is a part of  $H_0$ , which itself may be decomposed as:

$$H_0 = H_{st} + H_{rel} \quad (\text{Eq. 1.3})$$

where  $H_{st}$  is a time-independent part and  $H_{rel}$  is a stochastically modulated contribution. This case of magnetic modulation is called the indirect mechanism. The stationary part  $H_{st}$  consists of the electronic orbital and vibrational components, electronic and nuclear spin component, spin-orbit coupling, and magnetic field dependent Zeeman Hamiltonian, which depends on either stationary or time-dependent field  $B$ . The effect of  $H_{rel}$  accounts for time-dependent coupling within the manifolds, and is typically manifested as a cause of relaxation within the manifolds. The essence of the indirect mechanism is that: 1) the magnetic field causes transformation of the eigenstates corresponding to zero-field into a new basis in the presence of magnetic field; and 2) the coupling to the final states varies significantly for different initial states, thus affecting the kinetics of the decay.

The electronic spin manifold may be realized as a triplet state of a single molecule or as the spin manifold of a paramagnetic reaction pair, such as of two doublets (radical pairs), two triplets, or a triplet-doublet pair. In a single molecular system (Fig. 1.1), the magnetically sensitive species is a local triplet state. However, the spin dynamics of a local triplet state is practically magnetically insensitive in solutions at room temperature because of rapid thermal exchange between the three spin substates.<sup>2</sup> Therefore, the focus of our study is on RPs and triplet-triplet exciton pairs, both of which are formed as a result of interactions between two molecules. Formation of a triplet state in a typical photochemical process is already discussed in the preceding section. In the next section, we will discuss formation of RPs through an electron transfer process.

## 1.3 Electron transfer

### 1.3.1 Nonadiabatic electron transfer

Electron transfer (ET) is one of the fundamental chemical processes that may lead to the formation and/or decay of radical intermediates. ET process can be defined as a spontaneous transition from an initial state of a bimolecular system to a final state of this system such that the charge densities on the individual molecules are significantly different between the initial and final states. An ET process initiated by photon absorption is termed Photoinduced Electron Transfer (PET). It is often sufficient to consider ET as a result of the transition of a single electron from an initial MO of the electron donor to the final MO of the electron acceptor. When the electronic couplings ( $V$ ) between donor and acceptor is weak (electronic transmission factor is  $\ll 1$ ) this reaction type is called nonadiabatic ET. When the couplings are strong (electronic transmission factor is close to unity), the reaction is called adiabatic. In a nonadiabatic process, the region where the potential surfaces of initial and final states cross is approached by the system multiple times before a transition occurs *via* electron tunneling. For the systems to be discussed in this work, it is assumed that the ET reactions are nonadiabatic.

We focus on electron transfer processes over long distances (long-range ET), as this type of ET leads to the formation of radical intermediates sensitive to weak external magnetic field. Long-range ET is a nonadiabatic process because electronic coupling between the donor and acceptor is typically weak. We consider that the Golden Rule as an approximate connection between the transition rate and the transition probability.

Summing over the vibrational energy levels in the initial state, weighted by the Boltzmann factors, we define a thermal rate constant as:

$$k_{ET} = \frac{2\pi}{\hbar} V_{ET}^2 FCWD \quad (\text{Eq. 1.4})$$

where the matrix  $V_{ET}$  refers to the electronic coupling between the initial and final states and thus depends on the overlap of the electronic wavefunctions of the electron donor and acceptor; FCWD is the Franck-Condon weighted density of states, which gives the thermally averaged vibronic overlap between the potentials of the initial and final states. Semi-classical Marcus-Jortner approximation, the expression for nonadiabatic ET rate constant in the high temperature limit, is expanded as:<sup>15-16</sup>

$$k_{ET} = \frac{2\pi}{\hbar} V_{ET}^2 (4\pi\lambda k_B T)^{-1/2} \exp(-S) \sum_{n=0}^{\infty} \frac{S^n}{n!} \exp\left[-\frac{(\Delta G + \lambda_S + n\hbar\omega)^2}{4\lambda_S k_B T}\right] \quad (\text{Eq. 1.5})$$

where  $\lambda_S$  is the solvent reorganization energy;  $\hbar\omega$  is the vibrational quantum;  $S=\lambda_i/\hbar\omega$  is the dimensionless Huang-Rhys factor for internal reorganization energy  $\lambda_i$ ;  $\Delta G$  is the free energy difference between the initial and final states;  $k_B$  is the Boltzmann constant and  $T$  is the absolute temperature; the summation is over the quantum levels  $n$ . In the limit of  $S=0$ , the Eq. 1.5 reduces to:<sup>17</sup>

$$k_{ET} = \frac{2\pi}{\hbar} V_{ET}^2 (4\pi\lambda k_B T)^{-1/2} \exp\left[-\frac{(\Delta G + \lambda)^2}{4\lambda k_B T}\right] \quad (\text{Eq. 1.6})$$

In this expression,  $\lambda$  is the total reorganization energy which is the sum of  $\lambda_S$  and  $\lambda_i$ . The Eq. 1.6 is called the classical Marcus equation for nonadiabatic ET. A schematic illustration of ET is given in Figure 1.3. The equation predicts that as  $|\Delta G|$  increases, so does the ET rate. This region ( $|\Delta G| < \lambda$ ) is defined as the normal region. The ET rate increases until the maximum rate is achieved at  $\lambda = -\Delta G$ , where the reaction has no activation barrier. Further increases in  $|\Delta G|$  will decrease the reaction rate and this region ( $|\Delta G| > \lambda$ ) is defined as the inverted region.<sup>18</sup> The existence of the inverted region was experimentally validated by Closs and Miller.<sup>19-20</sup>

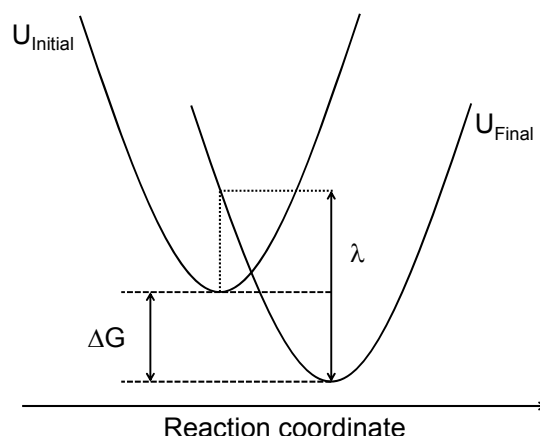


**Figure 1.3.** Potential energy surfaces ( $U$ ) for an electron transfer process between an initial state  $U_{\text{initial}}$  and the final state  $U_{\text{final}}$  in harmonic approximation.  $\Delta G$  is the Gibbs free energy difference and  $\lambda$  is the total reorganization energy.

### 1.3.2 Mechanism of electron transfer

In many cases, electron transfer involves bridging molecular elements (of fragments) between the donor and the acceptor. Bridge-mediated ET processes may take place *via* two different mechanisms: the strongly distance-dependent *tunneling* mechanism and the weakly distance-dependent *incoherent hopping* mechanism. The first case is generally considered to be that of superexchange, i.e. the transfer of electrons or holes from the donor to the acceptor through an energetically isolated bridge.<sup>21-22</sup> The bridge molecules act only as a "coupling medium". The incoherent hopping mechanism involves real intermediate states that couple to internal nuclear motions of the bridge molecules and the surrounding medium. The electron (or hole) jumps from one bridge element to another bridge element, as these bridge elements are energetically accessible.<sup>23-24</sup>

The ET rate constant  $k$  as a function of donor-acceptor distance,  $r_{DA}$ , is expressed as:

$$k = k_0 \exp(-\beta r_{DA}) \quad (\text{Eq. 1.7})$$

where,  $\beta$  is the distance sensitivity parameter. This relationship has been used to determine the “robustness” of donor-bridge-acceptor systems as conducting media: the smaller  $\beta$  value, the longer the distance over which electron or hole can be transferred without penalty.  $\beta$  is used to characterize all types of transport, including incoherent hopping, although by definition  $\beta$  this is only applicable to exponentially decaying processes. In the case of incoherent hopping, the distance dependence, however, becomes close to the inverse of the distance ( $1/r_{DA}$ ). Parameter  $\beta$  should be considered intrinsic not to the bridge, but rather to the entire system (i.e. donor + bridge + acceptor).<sup>25</sup>  $\beta$  values reported for various molecular systems vary even when the identical bridge molecules are used. This highlights the fact that most fundamental aspects of electron or hole transport, including distance dependence, are exquisitely sensitive to its environment.<sup>25-26</sup> One must take that into account when incorporating ET processes into photophysical pathways to produce RPs.

#### 1.4 Magnetic field effects on emissivity in solutions

From the unified description of MFE as discussed above, we can conjecture that when final states  $|f,n\rangle$  are emissive, MFE on molecular emissivity may be observed. In fact, there are two main types of MFE on emission of molecules in solutions.<sup>7, 11</sup> The first involves emission from exciplex states existing in equilibrium with RPs formed upon PET.<sup>27-28</sup> External magnetic field modulates spin interconversion within a RP (we will discuss this in more detail in Chapter 3), affecting the charge recombination channel coupled to the formation of emissive exciplexes. In some cases fluorescence from the parent local singlet state may also be modulated.<sup>28-29</sup> The second kind is the MFE on triplet-triplet annihilation (TTA) and subsequent  $p$ -type delayed fluorescence.<sup>30-31</sup> (This type will be discussed in Chapters 7 and 8.) While MFEs are known for decades, the molecular systems exhibiting MFEs on emission are largely limited to UV excitable molecular systems. Those are not very useful for imaging applications. In order to uncover the full potential of MFE for imaging and biological imaging in particular, it is necessary to develop

magnetically sensitive molecular systems with strong visible-NIR absorption/emission and possibly expand emission types that are sensitive to MFE.

### 1.5 Outline

In this work, we explore the possibility of affecting molecular emissivity in solutions at ambient temperatures by weak external magnetic fields (up to 1 Tesla) and investigate mechanisms of these MFE. We examine: 1) whether we can incorporate magnetically sensitive intermediate species (radical pairs and triplet-triplet pairs) into the photophysical pathways leading to emissive states in a biomedically relevant context (i.e. molecular emissivity in solutions and room temperature and visible-NIR absorption/emission); and 2) whether we can achieve magnetic modulation of emission. In radical pair based systems, we focus on emissive triplet states as an emission type. We show that molecular emissivity can be indeed magnetically modulated by influencing spin dynamics in radical pairs as well as in triplet-triplet exciton pairs, demonstrating that in principle magnetic control over molecular emissivity is feasible, although so far observed MFE are weak for practical applications, and further improvements of molecular designs are necessary.

In Chapter 2, potential applications of magnetically controlled optical probes in biomedical fields are described.

Chapter 3 is the introduction to the concept of MFE on radical pairs. We describe how weak magnetic fields can affect chemical reactions by influencing the spin dynamics of radical pairs. The works in Chapter 4-6 will be based on this concept.

In Chapter 4, we present model molecular system, comprising Pt(II) porphyrin (PtP) and Rhodamine B (RhB<sup>+</sup>) derivatives. In this PtP-RhB<sup>+</sup> system, an emissive triplet state of PtP is produced in an unusual way through a radical pair pathway.

In Chapter 5, a study of another molecular system sheds light on the relationship between emissive triplet states and radical pairs. The molecular system consists of PtP, anthracene (An), and boron dipyrromethene (BD). In this triad PtP-An-BD, an emissive triplet state of PtP is produced in a pathway involving a radical pair, but different from that in PtP-RhB<sup>+</sup>. Here, we observe solvent dependence of triplet emissivity, which stems from the existence of radical pairs in the photophysical pathway.

In Chapter 6, we show experimentally that visible room-temperature phosphorescence can be modulated by magnetic fields by influencing spin dynamics in radical pairs. The molecular system consists of PtP and Rosamine B (RosB) - another Rhodamine B derivative.

Chapter 7 introduces the concept of MFEs on triplet-triplet annihilation. We discuss Johnson-Merrifield theory and Atkins-Evans theory. The latter theory is applied to the molecular system presented in Chapter 8.

In Chapter 8, magnetic modulation of molecular emissivity in solution through sensitized triplet-triplet annihilation is discussed. Using Pt(II)/Pd(II)  $\pi$ -extended porphyrins and perylene we demonstrate MFE on delayed fluorescence from perylene upon excitation of NIR absorbing porphyrins. A new type of MFE, i.e. MFE on “delayed phosphorescence,” has also been revealed.

In Chapter 9, some concluding remarks are made.

## CHAPTER 2 Envisioned Applications

In this chapter, we introduce some potential applications of *magneto-optical* probes that we began developing in this work. We envision that development of such probes will generate new technology including imaging methods that combine high sensitivity of optical detection with high spatial resolution achievable in magnetic resonance imaging (MRI).

### 2.1 Optical tomography

Diffuse optical tomography (DOT)<sup>32-34</sup> and fluorescence-enhanced molecular tomography (FMT)<sup>35,36</sup> have been successful in generating useful physiological information through visualization of distributions of optical probes and/or endogenous chromophores in tissue *in vivo* in 3D. Unfortunately, a fundamental limit to the resolution of all diffuse optical methods is imposed by scattering.<sup>37,38</sup> Even the most advanced optical tomographic systems typically result in images with ca 1 cm spatial resolution at depths of 5-6 cm into the tissue. To overcome this limitation, coupling of diffuse optical methods with other imaging modalities (e.g. as in photoacoustic tomography<sup>39,40</sup>) is being actively explored. Along these lines, we would like to explore synergy between optical tomography and magnetic resonance imaging. Our idea is to impose control over the formation of emissive states of optical probes by magnetic field gradients. In one such dual-modality imaging scheme high degree of informational content and sensitivity of detection – the key advantages of optical methods – will be preserved, while the resolution of imaging detection will be greatly enhanced, ideally approaching that of MRI.

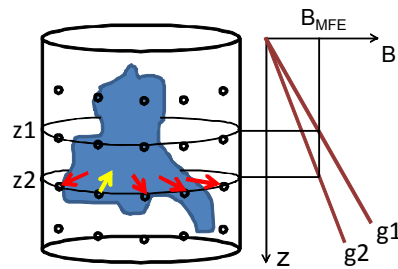


**Figure 2.1.** Schematic illustration of tomographic imaging experiment utilizing optical and magnetic fields. Z- direction of magnetic field gradient;  $B_{MFE}$  – magnetic field strength required to switch on emission of optical probes;  $z1$  and  $z2$  – image planes in which the emission is switched on by applying gradients  $g1$  and  $g2$ . Black circles on the object boundary indicate sites for light sources and detectors. Yellow arrow – active source. Red arrows – detectors receiving the majority of the photons when gradient  $g2$  is applied.

Provided magnetically-controlled optical probes (*magneto-optical* probes) are available, the following tomographic imaging scheme can be envisioned (Fig. 2.1). The probes may be attached to antibodies specific to selected biological targets – the strategy similar to that employed in other types of contrast-enhanced imaging, e.g. in fluorescence molecular tomography (FMT). The imaging setup will be similar to that used in FMT, e.g. multiple point source-detector pairs on the object boundary. However, the object will be positioned inside a magnetic field scanner, similar to that used in MRI. In the absence of the magnetic field, the emission of the probe will be fully quenched, and no signal will be observed upon irradiating the object at the excitation wavelengths required to induce luminescence. However, if a magnetic field of certain strength is applied ( $B_{MFE}$ ), the emission will be switched on. The key feature will be that the emission will be generated only if the field strength will correspond to a certain resonance condition imposed by probe's electronic properties. By creating a field gradient throughout the object, the emission will be initiated only in a defined imaging plane, as opposed to the entire volume simultaneously. By varying the field gradient ( $g1$  and  $g2$  in Fig. 2.1), different imaging planes ( $z1$  and  $z2$ ) within the object will be interrogated selectively one by one. Thus, the resulting composite image will have the resolution, at least in the direction of the magnetic field gradient, defined by this magnetic field gradient, as in MRI; whereas the sensitivity and

informational content will remain as in optical detection schemes. It is possible to imagine that after applying gradients in Z-direction, sequences of gradients can be applied also in X and Y directions, ensuring uniformly high resolution throughout the entire volume.

It has already been demonstrated that essentially the same technology as FMT can be effectively applied for imaging triplet probes,<sup>41,42</sup> and for imaging distributions of molecular oxygen.<sup>41,43</sup> In this latter case, triplet probes based on metalloporphyrins<sup>44</sup> were chosen such that their phosphorescence quantum yields and lifetime are particularly sensitive to oxygen. However, emitters with shorter triplet lifetimes (e.g. 1  $\mu$ s or less), such as Ru<sup>2+</sup>(bpy) and similar complexes<sup>45,46</sup> or cyclometallated complexes of Pt and Ir<sup>47-50</sup> possess very low intrinsic sensitivity to oxygen and retain their high emissivity at physiological oxygen concentrations. These probes can be linked to biological targets much in the same way as fluorescent reporters and used for visualization of distributions of analytes of interest. We can, therefore, utilize triplet emitters as well as singlet emitters for this type of application as long as magnetic modulation can be achieved.

## 2.2 Optical microscopy

The advent of super-resolution microscopy methods during the past two decades allowed us to go beyond the diffraction limit.<sup>51,52</sup> These technologies typically rely on the ability to switch on and off emissive states of molecules. Switching might occur due to stochastic processes, such as in PALM<sup>53</sup> or STORM<sup>54</sup> methods, or due to external radiation, such as in STED microscopy.<sup>55,56</sup> Overall, it is the control over the excited state dynamics that enables imaging beyond the diffraction limit. Magnetic switching of emission may be a very useful addition to the toolkit of these methods,<sup>57-58</sup> especially if the magnetic field required to affect molecular emissivity is weak and will not cause unwanted photodamage to the biological objects.

### **2.3 Photodynamic therapy**

The same rationale applies to therapeutic utilization of triplet states, such as in photodynamic therapy (PDT). PDT is a medical modality that utilizes combination of light and photosensitizer drugs, presumably targeted to diseased tissue, to generate singlet oxygen that produces active intermediates, subsequently destroying diseased tissues and cells. Because targeting of drugs is never ideal, one of the main challenges in PDT is to confine singlet oxygen generation to a volume occupied only by diseased tissues, minimizing unwanted side effects. Excitation is scattered, especially at depth, and currently clinical use of PDT is limited only to superficially localized tissues, e.g. melanomas. Utilization of MFE to control formation of triplet states of photosensitizers,<sup>59</sup> which give rise to singlet oxygen, should allow targeted therapy at higher depths, since singlet oxygen generation will be confined only to those areas where the magnetic field strengths will be appropriate for triplet generation.

All the above mentioned technologies are rooted in molecules whose emission of light or formation of chemically active excited states can be modulated by magnetic fields. In this work, we explore the possibility of developing such kinds of molecules.

## CHAPTER 3 Introduction to Magnetic Field Effects on Spin Dynamics in Radical Pairs

One of magnetically sensitive states of species are radical pair (RPs) states; a pair of transient radicals created simultaneously, such that the motions of two electronic spins, one per each radical, are correlated. RPs have the unique property that their chemical fate is dependent on weak magnetic interactions ( $\ll k_B T$ ). The RP spin remains far enough from equilibrium for long enough, so that the thermal energy  $k_B T$  becomes irrelevant. The so called radical pair mechanism is at the heart of magnetic field effects on many chemical reactions.<sup>7</sup> Radical pair mechanism may also play a key role in biological compass magnetoreception in birds and other animals.<sup>60</sup> Nevertheless, there exist some other mechanisms by which external magnetic field can affect chemical reactions, including effects on triplet-triplet or triplet-doublet pairs or in some cases on individual triplets. In this chapter, we will outline the theory behind the magnetic field effects (MFE) on RPs. We will deal with one other mechanism of MFE, namely MFE on triplet-triplet exciton pairs, in the Chapters 7 and 8.

### 3.1 Spin selectivity

One of important concepts in dealing with radical pair mechanism is spin selectivity. The concept is illustrated in Figure 3.1. Spin multiplicity is preserved during transitions leading to formation or decay of RPs. RPs are born in their singlet states from singlet precursors typically *via* electron or hole transfer process. Singlet RPs recombine into singlet products. On the other hand, RPs can be born in their triplet states when the reaction formation occurs from triplet precursors. Triplet RPs recombine into triplet products. There are, however, some exceptions for this rule; i.e. singlet RPs sometimes recombine directly into triplet products. One such case is discussed in Chapter 5.

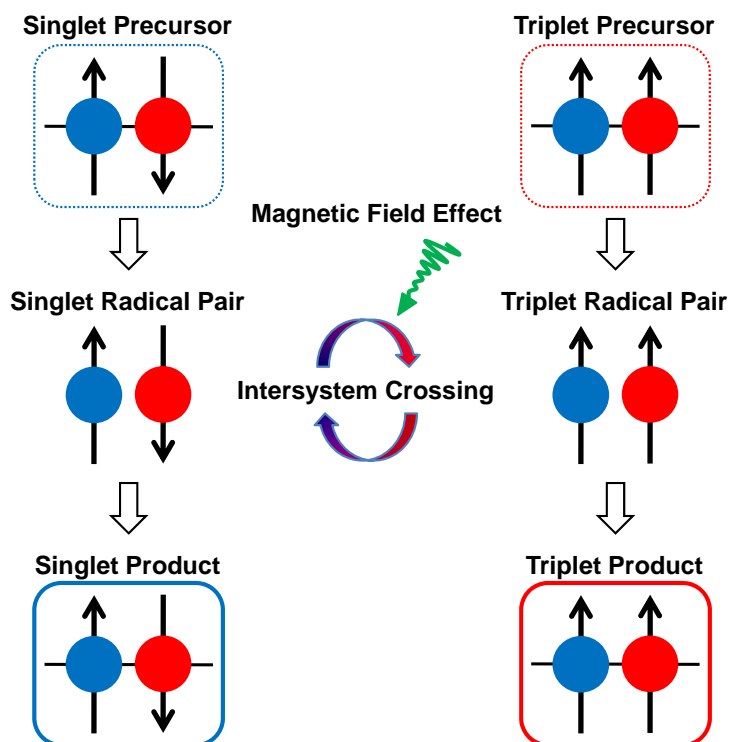


**Figure 3.1.** A schematic diagram for chemical reactions that occur through radical pairs. Blue and red circles represent individual electrons, and the arrows are their spins.

### 3.2 Radical pair mechanism

Consider a magnetic system with spin Hamiltonian,  $H_{S-T}$ , whose eigenstates are vibrationally and orbitally degenerate.  $H_{S-T}$  for a RP, where S and T denote singlet and triplet spin states, comprises exchange interaction and magnetic terms.

$$H_{S-T} = H_{ex} + H_{mag} \quad (\text{Eq. 3.1})$$

where

$$H_{ex} = -2JS_1 \cdot S_2 \quad (\text{Eq. 3.2})$$

$$H_{mag} = \beta B_0 (g_1 S_1 + g_2 S_2) + \sum_i a_{1i} S_1 I_i + \sum_k a_{2k} S_2 I_k \quad (\text{Eq. 3.3})$$

where  $\beta$  is the Bohr magneton,  $B_0$  is applied magnetic field,  $g_1$  and  $g_2$  are electronic g factors for each radical (radicals 1 and 2),  $S_1$  and  $S_2$  are electron spin operators for the two radicals,  $a_{1i}$  and  $a_{2k}$  are the isotropic hyperfine coupling constants with nuclear spins ( $I_i$  and  $I_k$ ) in radicals 1 and 2, respectively. Eq. 3.2 denotes the exchange interaction between the spins  $S_1$  and  $S_2$ . In the absence of magnetic field, the magnitude of the exchange interaction  $2J$  corresponds to the singlet-triplet splitting  $E_{S-T}$  in RPs. Eq. 3.3 contains the contribution from g factors in the first term and from the hyperfine coupling in the second and third terms. Anisotropic exchange interactions and anisotropic hyperfine couplings as well as the magnetic dipole-dipole interaction can be neglected for the case of solutions at ambient temperatures.

The pure spin states (singlet or triplet) of radical pairs are not the eigenfunctions of the spin Hamiltonian  $H_{S-T}$ . Therefore, if the system was born in one such state, it will undergo the process called “spin evolution”. Interconversion or mixing of singlet and triplet states of a RP is also called RP intersystem crossing (RP-ISC) (Fig. 3.1). This interconversion and subsequently the fate of a RP can be influenced by both internal molecular and external magnetic fields.

Because g-factors of typical organic radicals are very close, the main driving force of spin evolution in RPs is in many cases hyperfine coupling interaction, i.e. the interaction between electron and nuclear spins. Consider that a RP is born in its singlet spin state after electron transfer between singlet precursors. Electron spins on individual radicals can now precess independently around the resultant of the external magnetic field and their respective local fields, created by spins of the nearby magnetic nuclei, e.g. Schulten and Wolynes<sup>61-62</sup> have introduced semi-classical description of such spin motion. The precession frequency (Larmor frequency) for an individual electron spin is given by:

$$\omega_0 = g\mu_B B / \hbar \quad (\text{Eq. 3.4})$$

The active magnetic field  $B$  consists as a vector sum of an external magnetic field  $B_0$  and an effective magnetic field  $B_{hfc}$ , consisting of the sum of the hyperfine couplings of the various nuclear spins in the corresponding radical:

$$B = B_0 + B_{hfc} \quad (\text{Eq. 3.5})$$

It is important to note that isotropic hyperfine coupling constants, i.e. interaction of electron and nuclear spin, are independent of external magnetic field. In this simplified description, we ignore the fact that the total spin angular momentum of electrons and nuclei must be conserved and that in the absence of magnetic field a change in electron spin must be compensated by a change in nuclear spin. The precession frequencies of the two electron spins in a RP may differ, and the relative orientation of the two spins of electrons changes in time. In the case of a singlet born RP, ISC due to hyperfine interactions re-aligns spins such that the system becomes a triplet at certain point. Therefore, radical pairs oscillate between S and T states at a frequency determined by hyperfine interactions.

In typical organic molecules, where hyperfine coupling is dominated by  $^1\text{H}$  and  $^{14}\text{N}$  nuclei, HFC coupling constants are in the range of  $10\ \mu\text{T}$ - $10\ \text{mT}$ ,<sup>11, 62</sup> corresponding to frequencies of 300 kHz and 300 MHz. Thus, the time scale for interconversion between S and T states is 1 ns-1  $\mu\text{s}$ . This means that substantial S-T conversion may be encountered when RPs exist on a longer or at least comparable timescale.

When hyperfine and exchange interactions are isotropic and dipolar coupling is weak, the singlet and the three zero-field triplet sublevels of the radical pair are degenerate. The transition from the singlet state to each of the three triplet states is energetically possible. If spin-spin exchange interaction within the RP is non-zero, the triplet manifold is not degenerate, with separation between singlet and triplet  $T_0$  sub-level being  $2J$ , as shown in Figure 3.2. Application of external magnetic field results in Zeeman splitting of the triplet sublevels. In the high field limit, the resulting spin states are closer to pure spin states, i.e. eigenstates of the operator of spin angular momentum:  $T_0$  and  $T_{\pm}$  states. In such high field limit, population of the triplet state of a RP occurs exclusively *via* S- $T_0$  mixing, while the  $T_-$  and  $T_+$  states remain unpopulated. When the Zeeman energy from the applied external magnetic field equals that of the S-T splitting, either the low energy state  $T_-$  or high energy state  $T_+$ , the  $S \leftrightarrow T_-$  or  $S \leftrightarrow T_+$  level crossing transitions will occur, which at still higher magnetic fields will be suppressed again. This gives a type of a certain resonance effect in the field dependence with a maximum at magnetic field of  $B_0 = B_{2J} = 2J/g\mu_B$ .

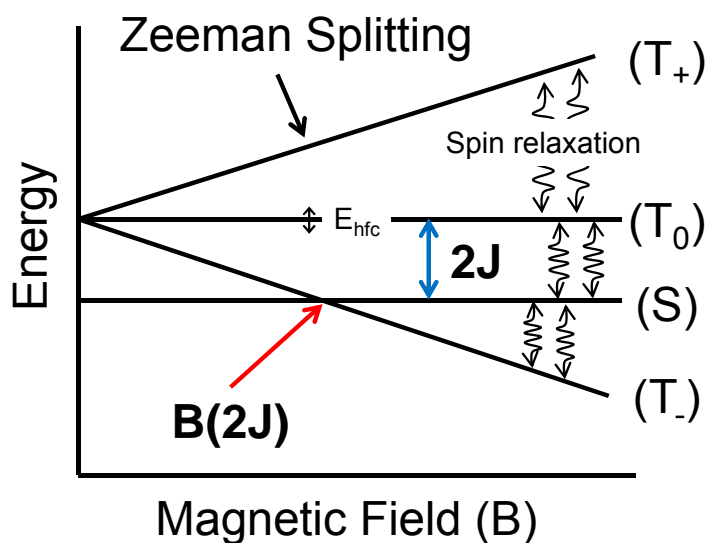


**Figure 3.2.** Energy diagram of electronic spin states of a radical pair in a magnetic field ( $B$ ).  $E_{\text{hfc}}$  is an arbitrary average bandwidth due to hyperfine coupling, and  $J$  is the exchange integral. The sign of  $J$  here is negative. Wavy lines depict spin relaxation.

It should be noted that precession frequency differences and singlet-triplet interconversion may arise not only from hyperfine coupling, but also from different  $g$  factors ( $\Delta g$  mechanism). A  $\Delta g$ -dependent mixing of the  $S$  and  $T_0$  RP states, leading to coherent  $S \leftrightarrow T_0$  transitions will occur at the frequency of:

$$\omega_{\Delta g} = \Delta g \mu_B B_0 / \hbar \quad (\text{Eq. 3.6})$$

Note,  $\Delta g$ -mediated transition occurs only between  $S$  and  $T_0$  states. The  $\Delta g$  contribution is often neglected in typical organic radicals in the magnetic field up to 1T or so. This is because the difference in  $g$  factors in typical organic molecules is  $10^{-3}$ - $10^{-4}$ , which corresponds to  $\omega_{\Delta g} \sim 10^4$ - $10^5$   $\text{s}^{-1}$  (or at 10-100  $\mu\text{s}$ ) at 10 mT and  $\sim 10^7$ - $10^8$   $\text{s}^{-1}$  (or at  $\sim 10$ -100 ns) even at 1 T. Therefore, the transition induced by  $\Delta g$  mechanism is much less significant than those by hyperfine coupling (see above) at low magnetic field and will only become comparable even at high field of 1 T. However, it is apparent that this mechanism can contribute significantly to the transition at higher

field when the exchange interaction is negligible. In addition, if the difference in g factors is large, this mechanism is very efficient and may become dominant.<sup>63</sup>

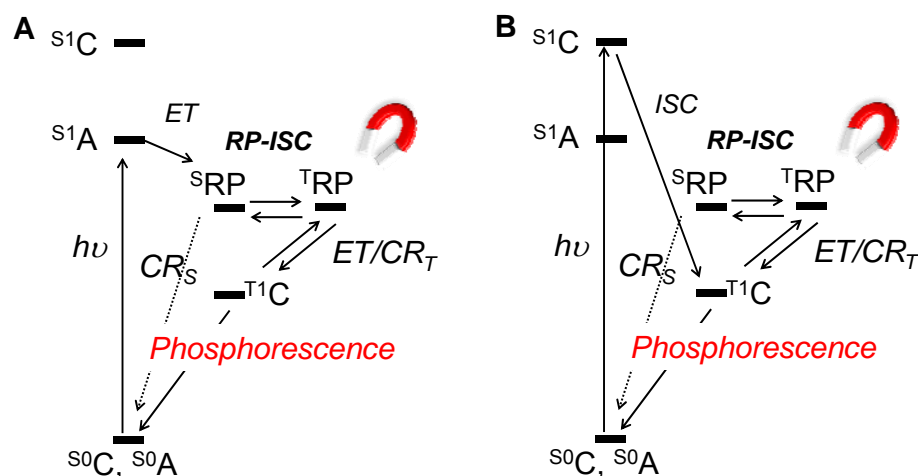
### 3.3 Relaxation mechanism

Within the picture of coherent spin motion, S-T transitions (such as  $S \leftrightarrow T_{\pm}$  in Fig. 3.2) are suppressed at high magnetic fields as these transitions require some source of magnetic energy conservation by coupling with lattice. Such coupling is generally inefficient because there are few states found in the lattice with correct magnetic energy to allow for coupling.<sup>3</sup> However, the stochastically modulated contribution of relaxation can cause incoherent transitions among the spin sub-levels (wavy lines in Fig. 3.2). Their rates are dependent on the strength of magnetic field and on the Zeeman splitting of the sublevels. Singlet-triplet transitions induced by relaxation are generally much slower ( $\mu\text{s}$  time scale) and typically decrease in rate with an increase in the external magnetic field<sup>64</sup> in contrast to those induced by hyperfine coupling. They may influence the overall kinetics of chemical reactions if the lifetime of spin-correlated RPs is long enough for such relaxations to be operative. Relaxation processes act either to cause random spin flip (spin-lattice relaxation – a physical process characterized by exponential behavior with a characteristic time is  $T_1$ ) or to change the relative phase of the components of the spins (spin-spin relaxation – a physical exponential process with a characteristic time  $T_2$ ). The former is responsible for the S and  $T_0$  to  $T_{\pm}$  interconversions and the latter is for  $S \leftrightarrow T_0$  interconversions.

### 3.4 Photophysical pathways leading to triplet state

Based on the framework described in the previous sections, we now discuss how magnetic field effects can affect triplet states through RPs.

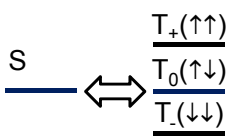
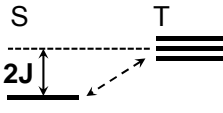
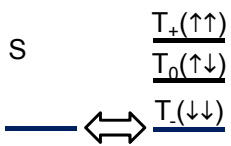
RPs can be born in their singlet or triplet spin states (Fig. 3.3).



**Figure 3.3.** Reaction scheme of generation of emissive triplet states *via* RPs: (A) Pathway of singlet-born RP, and (B) Pathway of triplet-born RP. **C** is the core molecule whose triplet state is emissive and **A** is the antennae molecule capturing excitation energy in (A) and an auxiliary molecule who serves redox partner of the molecule **C** in (B). ET indicates electron transfer and  $CR_S$  and  $CR_T$  indicate singlet and triplet charge recombination, respectively.

MFE on the local triplet product yield can be positive (increase in yield) and negative (decrease in yield) with application of the external magnetic field. A diagram exemplifying the two cases is shown in Fig. 3.4. In the top row, all three triplet sublevels are close in energy, and  $2J$  is close to zero. In the absence of the external field (OFF or  $B=0$ ), the three triplet sublevels are in the resonance with the singlet state and participate in S-T interconversion. Application of the external magnetic field (ON) splits the triplet sublevels due to the Zeeman effect, and sublevels  $T_-$  and  $T_+$  move out of the resonance. As a result, only the  $T_0$  sublevel remains in exchange with the singlet state, and the rate of the ISC decreases compared to that in the absence of magnetic field. In this situation, when RP is born as a singlet, the triplet character within the RP decreases in the presence of magnetic field, and accordingly the yield of the local triplet state upon  $CR_T$  decreases. When RP is born as a triplet, the triplet character within the RP increases, and the yield of the local triplet state increases. The bottom row in Fig. 3.4 is the case in which  $2J$  is non-zero ( $2J > 0$  in Fig 3.4), and no ISC occurs due to HFC in the absence of magnetic field. Interconversion due

to spin relaxation, as described in the section 3.3 still occurs, but it is not as efficient. In the presence of the field, the Zeeman splitting moves the T. sublevel into the resonance with the singlet state, and the rate of ISC increases. In contrast to the case of  $J=0$ , the yield of local triplet increases when RP is born as a singlet and decreases when RP is born as a triplet.

<b>Magnetic Field</b>		<b>Triplet Product Yield</b>	
<b>OFF</b>	<b>ON</b>	<b>Singlet-born</b>	<b>Triplet-born</b>
$J = 0$ 		<b>Decrease</b>	<b>Increase</b>
$J \neq 0$ 		<b>Increase</b>	<b>Decrease</b>

**Figure 3.4.** Energy diagram of radical pairs in the absence (OFF) and the presence (ON) of external magnetic field.  $2J$  is the singlet-triplet splitting within the radical pair in the absence of the external magnetic field. The singlet-triplet ( $S \leftrightarrow T$ ) transitions are indicated by arrows.

### 3.5 Magnetic field effects on triplet emissivity through RPs

The reports on MFE on phosphorescence are scarce and they have only been observed at low temperature. In 1975, the report by Leung and El-Sayed<sup>65</sup> showed that the rate and intensity of the pyrimidine phosphorescence in benzene at 1.6 K decreased when a static magnetic field of 1 Tesla was applied. There are many other examples where external magnetic fields directly affect the triplet sublevels of the molecules by Zeeman splitting and subsequently affect the lifetime and decay of phosphorescence while they are limited to low temperature where tumbling of molecules is severely limited. Another source of magnetic field effects is triplet-triplet

annihilation (Chapter 7 and 8). There are only a few reports of MFE on phosphorescence at cryogenic temperature through triplet-triplet annihilation.<sup>66-67</sup>

The most relevant works were performed by Boxer et al. on the photosynthetic reaction center.<sup>68-69</sup> The triplet state of the primary electron donor,  $^1\mathbf{C}$  in Fig. 3.3, in photosynthetic reaction center is formed exclusively by charge recombination of the initially formed RP.  $^1\mathbf{C}$  state decays back to the ground state by ISC at low temperature. Boxer et al. discovered<sup>70</sup> that at higher temperatures  $^1\mathbf{C}$  state can also decay by thermally activated re-formation of the RP, from which it was originally recombined, followed by RP-ISC and singlet charge recombination. This pathway is magnetic field dependent, and the lifetime and yield of  $^1\mathbf{C}$  can be magnetically sensitive. They showed that the yield of phosphorescence from  $^1\mathbf{C}$  are indeed dependent upon magnetic field at low temperature (liquid nitrogen temperature)<sup>69</sup> while the quantum yields of phosphorescence from  $^1\mathbf{C}$  at room temperature is too low to observe field dependencies. To the best of our knowledge, no reports were made regarding the magnetic modulation of room-temperature phosphorescence by influencing radical pair spin dynamics. However, we have reasoned that it is possible to observe MFE on room-temperature phosphorescence through RP mechanism if we can construct a molecular system in which phosphorescent triplet state is populated by either the reaction scheme A or B (Fig. 3.3). We explored such possibilities in the subsequent Chapters 4-6. In specific, the reaction scheme A in Fig. 3.3 will be the focus of Chapter 4 and 5 while the reaction scheme B will be further discussed in Chapter 6.

## CHAPTER 4 Generation of Emissive Triplet State *via* Photoinduced Electron Transfer and Radical Pair Intersystem Crossing

This work has been published: \* Generation of Phosphorescent Triplet States via Photoinduced Electron Transfer: Energy and Electron Transfer Dynamics in Pt Porphyrin–Rhodamine B Dyads. Mani, T.; Niedzwiedzki, D. M.; Vinogradov, S. A. *J. Phys. Chem. A* **2012**, *116*, 3598-3610.

### 4.1 Summary

Control over generation and dynamics of excited electronic states is fundamental to their utilization in all areas of technology. We present the first example of multichromophoric systems in which emissive triplet states are generated *via* a pathway involving photoinduced electron transfer (ET), as opposed to local intrachromophoric processes. In model dyads, PtP-Ph<sub>n</sub>-pRhB<sup>+</sup> (**1-3**, n=1-3), comprising platinum(II) *meso*-tetraarylporphyrin (PtP) and rhodamine B piperazine derivative (pRhB<sup>+</sup>), linked by oligo-*p*-phenylene bridges (Ph<sub>n</sub>), upon selective excitation of pRhB<sup>+</sup> at a frequency below that of the lowest allowed transition of PtP, room-temperature T<sub>1</sub>→S<sub>0</sub> phosphorescence of PtP was observed. The pathway leading to the emissive PtP triplet state includes excitation of pRhB<sup>+</sup>, ET with formation of the singlet radical pair, intersystem crossing within that pair and subsequent radical recombination. Due to the close proximity of the triplet energy levels of PtP and pRhB<sup>+</sup>, reversible triplet-triplet (TT) energy transfer between these states was observed in dyads **1** and **2**. As a result, the phosphorescence of PtP was extended in time by the long decay of the pRhB<sup>+</sup> triplet. Observation of ET and TT in the same series of

---

\* Adapted with permission. Copyright © 2012, American Chemical Society

molecules enabled direct comparison of the distance attenuation factors  $\beta$  between these two closely related processes.

## 4.2 Introduction

Control over emissivity and dynamics of excited states of molecules is central to practical utilization of these states in all areas of technology and medicine. We are particularly interested in triplet electronic spin states, whose applications encompass medical photodynamic therapy,<sup>71-72</sup> energy up-conversion by triplet-triplet annihilation,<sup>73-74</sup> organic light emitting devices (OLED)<sup>75-76</sup> and biological imaging of oxygen.<sup>77-78</sup> In imaging applications, such as oxygen imaging by phosphorescence lifetime,<sup>79</sup> the ability to impose control over spatial localization of triplet states of probe molecules, e.g. by way of applying external optical or magnetic fields, may lead to new ways to integrate diffuse phosphorescence lifetime imaging<sup>41, 80</sup> with other imaging modalities, thereby enhancing informational content and improving spatial imaging resolution. Similarly, in photodynamic therapy, controlling formation of dark triplet states for generation of singlet oxygen would be invaluable for confining the photodynamic action selectively to the diseased tissue, while reducing undesirable collateral damage. In view of these applications, molecules with intricate energy and electron transfer pathways, providing opportunities for controlling rates and yields of formation of triplet states, are of considerable interest.

Recently we described molecular systems, in which emissive triplet states of Pt(II) porphyrins were populated *via* a route including Förster-type energy transfer from appended multiphoton absorbing antenna chromophores.<sup>81-83</sup> These molecules appeared very useful as probes in two-photon phosphorescence lifetime microscopy (2PLM) of oxygen.<sup>83-85</sup> One studied system comprised Pt(II) tetrabenzoporphyrin (PtTBP) – Rhodamine B (RhB<sup>+</sup>) dyad.<sup>82</sup> Upon excitation of RhB<sup>+</sup>, fast energy transfer from the RhB<sup>+</sup> singlet state (<sup>S1</sup>RhB<sup>+</sup>) onto PtTBP and subsequent intersystem crossing (ISC) yielded local PtTBP triplet (<sup>T1</sup>PtTBP), which was de-

populated *via* efficient  ${}^1\text{PtTBP} \rightarrow \text{RhB}^+$  electron transfer (ET), followed by non-radiative recovery of the ground state species. (Note that rhodamine B is a cation, and therefore its one-electron reduction leads to the neutral radical).

Analyzing energy and electron flow in *antenna* (A) – triplet *core* (C) dyads we reasoned that if a radical pair state (RP) would have its energy higher than the emissive local triplet state of the core emitter ( ${}^C\text{T}_1$ ), and the corresponding singlet state of the core ( ${}^C\text{S}_1$ ) would lie above the initially excited singlet state of the antenna ( ${}^A\text{S}_1$ ), one likely evolution pathway for the system would be: 1) the ET between the antenna and the core, 2) formation of the singlet radical pair ( $\text{RP}_\text{S}$ ), 3) intersystem crossing (RP-ISC) with formation of the triplet  $\text{RP}_\text{T}$ , and 3) subsequent decay of  $\text{RP}_\text{T}$  into  ${}^C\text{T}_1$  and  ${}^A\text{S}_0$  (Fig. 4.1). Alternatively, singlet radical pair  $\text{RP}_\text{S}$  would recombine directly with regeneration of the ground state species. One attractive feature of such scheme would be the possibility to tune the rate of the RP-ISC, e.g. by affecting the spin dynamics in the RP *via* modulation of hyperfine interactions,<sup>7</sup> and thereby to impose magnetic control over the formation of the triplet states. On the other hand, the ability to generate an emissive triplet state *via* ET, as opposed to having to deal with ET to prevent unwanted phosphorescence quenching – a problem we encountered in construction of two-photon oxygen probes,<sup>82</sup> - would greatly extend the choice of antenna chromophores suitable for construction of these useful sensors.<sup>86</sup>

Schemes similar to the one shown in Fig. 4.1 are common for ET systems exhibiting magnetic field effects on the spin dynamics in radical pairs.<sup>7, 11, 87-89</sup> Such systems are currently deemed central for biological magneto-sensory mechanisms<sup>60, 62, 90-93</sup> as well as form the basis for several spectroscopic techniques, including Chemically Induced Dynamic Nuclear polarization (or CIDNP)<sup>94-95</sup> and a set of methods collectively known as Optically Detected Magnetic Resonance (ODMR).<sup>96-98</sup> The latter play an important role in studies of natural photosynthetic systems<sup>99-102</sup> and related artificial mimics, which are important for light harvesting, molecular electronics and spintronics applications.<sup>89-90</sup> Not surprisingly, very large number of models with energy layouts resembling that in Fig. 4.1 has been published to date.<sup>11, 89, 103</sup> Systems most related to our

studies utilize emissive  $^3\text{MLCT}$  states of  $\text{Ru}^{2+}(\text{bpy})_3$  or similar complexes usually as *initial* states in ET reactions.<sup>45, 104</sup> There are also reports where phosphorescent metalloporphyrins participate in triplet-triplet energy transfer as acceptors.<sup>105-106</sup> However, to the best of our knowledge, molecules in which phosphorescent triplet states are the *final* states in cascades involving ET and RP-ISC have never been disclosed.

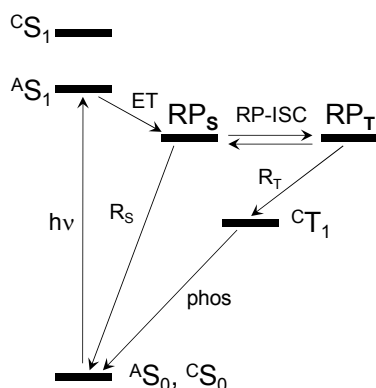


**Figure 4.1.** Energy diagram of bichromophoric antenna (A) – core (C) systems, in which the local triplet state of the core ( $^{\text{C}}\text{T}_1$ ) is populated *via* excitation of the antenna, electron transfer (ET) with formation of the singlet radical pair ( $\text{RPs}$ ), intersystem crossing (RP-ISC) and radical recombination ( $\text{R}_\text{T}$ ) from the resulting triplet radical pair ( $\text{RPT}$ ). Alternatively,  $\text{RPs}$  undergoes charge recombination  $\text{R}_\text{s}$ , yielding the ground state species.

In this study we report dyads, in which the roles of the antenna and the triplet core are played by  $\text{RhB}^+$  and a Pt(II) tetraarylporphyrin (PtP), respectively, whereby the pathway depicted in Fig.4.1 allows observation of the PtP phosphorescence without directly exciting PtP. To investigate our model systems we performed optical spectroscopic studies on the microsecond, nanosecond and femtosecond time scales in order to characterize the transient intermediates. One intriguing feature of the reported molecules is existence of a thermal equilibrium between the triplet states of the dyad components ( $^{\text{T}}\text{RhB}$  and  $^{\text{T}}\text{PtP}$ ), which is manifested by delayed phosphorescence of PtP, presumably mediated by the triplet-triplet (TT) energy transfer. Although observation of dark triplet states *via* coupled emissive triplet states has been previously reported,

<sup>107-110</sup> in our case the presence of both ET and TT in the same series of bichromophoric molecules makes it possible to directly compare distance attenuation factors  $\beta$  between these two closely related processes.

### 4.3 Experimental methods

**4.3.1 General information.** All solvents and reagents were obtained from standard commercial sources and used as received. Selecto silica gel (Fisher Scientific, particle size 32-63 micron) was used for column chromatography. <sup>1</sup>H NMR spectra were recorded on a Varian Unity 400 MHz spectrometer. Mass-spectra were obtained on a MALDI-TOF MS Microflex LRF instrument (Bruker Daltonics), using  $\alpha$ -cyano-4-hydroxycinnamic acid as a matrix. All the photophysical and electrochemical measurements were performed in anhydrous benzonitrile at 22°C, unless otherwise noted.

**4.3.2 Optical measurements.** UV-vis absorption spectra were recorded on a Perkin-Elmer Lambda 35 UV-Vis spectrophotometer. Steady-state and time-resolved phosphorescence measurements were performed on a FS900 spectrofluorometer (Edinburgh Instruments, UK), equipped with R2658P PMT (Hamamatsu). Time-resolved phosphorescence measurements were performed using either the FS900 instrument with a xenon flash lamp as the excitation source or an in-house constructed time-domain phosphorometer. FS900 allows measurements of emission decays with time constants  $>20 \mu\text{s}$  due to its rather long IRF. The custom-built instrument is based on a multichannel data acquisition board (NI-6251 USB, National Instruments), operating at software-selectable digitization frequencies of up to 1.25 MHz. The excitation sources in the instrument are white LEDs (1W Lumiled, Phillips,  $<10 \text{ ns}$  rise time), and the detector is an avalanche photodiode (Hamamatsu). Both the LEDs and the detector were equipped with appropriate optical filters (narrow-band for excitation and long-pass for emission). The light was coupled to the instrument using plastic fibers (3 mm in diameter). The IRF of the phosphorometer has FWHM of  $\sim 3 \mu\text{s}$ , permitting highly accurate measurements of phosphorescence decays with

time constants ranging from  $>3 \mu\text{s}$  to up to 100 ms. The software for the instrument is written in C/C++ (Qt, Nokia). Time-resolved fluorescence measurements were performed by the time-correlated single photon counting method (TCSPC). The TCSPC system consisted of a picosecond diode laser (PicoQuant LDH-C-400,  $\lambda_{\text{max}}=408 \text{ nm}$ , FWHM $\sim 100 \text{ ps}$ , 40 MHz rep. rate), multichannel-plate PMT (Hamamatsu R2809U) and a TCSPC board (Becker & Hickl, SPC-730). Quartz fluorometric cells (1 cm optical path length) were used in all optical experiments. The samples were deoxygenated by Ar bubbling or by applying four pump-freeze-thaw cycles. Quantum yields were measured against fluorescence of Rhodamine 6G in EtOH ( $\Phi_{\text{fl}}=0.94$ ),<sup>111</sup> using rigorously deoxygenated solutions. Time-resolved emission spectra, obtained using the FS900 instrument, were linearly decomposed into sums of their principle components, i.e. fluorescence of  $\text{RhB}^+$  and phosphorescence of PtP, in order to obtain the quantum yields of these emission types individually. Global fitting was performed using OriginPro 8.5 (OriginLab, MA) and MATLAB R2009a (MathWorks, MA). Decay fitting, spectral deconvolution and maximum entropy analysis were performed using custom written software.<sup>112</sup>

**4.3.3 Nanosecond transient absorption spectroscopy (NSTA).** The NS-TA setup consisted of a frequency-doubled Nd:YAG laser as pump (Quanta-Ray DCR-2A,  $\lambda_{\text{max}}=532 \text{ nm}$ , pulse width 10 ns, 10 Hz rep. rate,  $\sim 15 \text{ mW}$ ), a flash lamp (Hamamatsu, pulse width  $\sim 2 \mu\text{s}$ ) as a white-light probe source and a monochromator (SPEX) with a diode-array detector (Princeton Instruments, DIDA-512). Light at 532 nm excites both PtP and  $\text{RhB}^+$ ; however, the absorption at this wavelength is strongly dominated by  $\text{RhB}^+$  ( $>90\%$ ). Therefore, for the purposes of our analysis it was reasonable to assume that the contributions of pathway(s) resulting from direct excitation of PtP were insignificant. The optical densities of the samples were adjusted to be 0.3-0.5 OD at the excitation wavelength.

**4.3.4 Femtosecond transient absorption spectroscopy (FSTA).** Femtosecond time-resolved pump-probe absorption experiments were carried out using a Helios spectrometer (Ultrafast Systems, LCC), coupled to a femtosecond laser system (Spectra-Physics). The system consisted

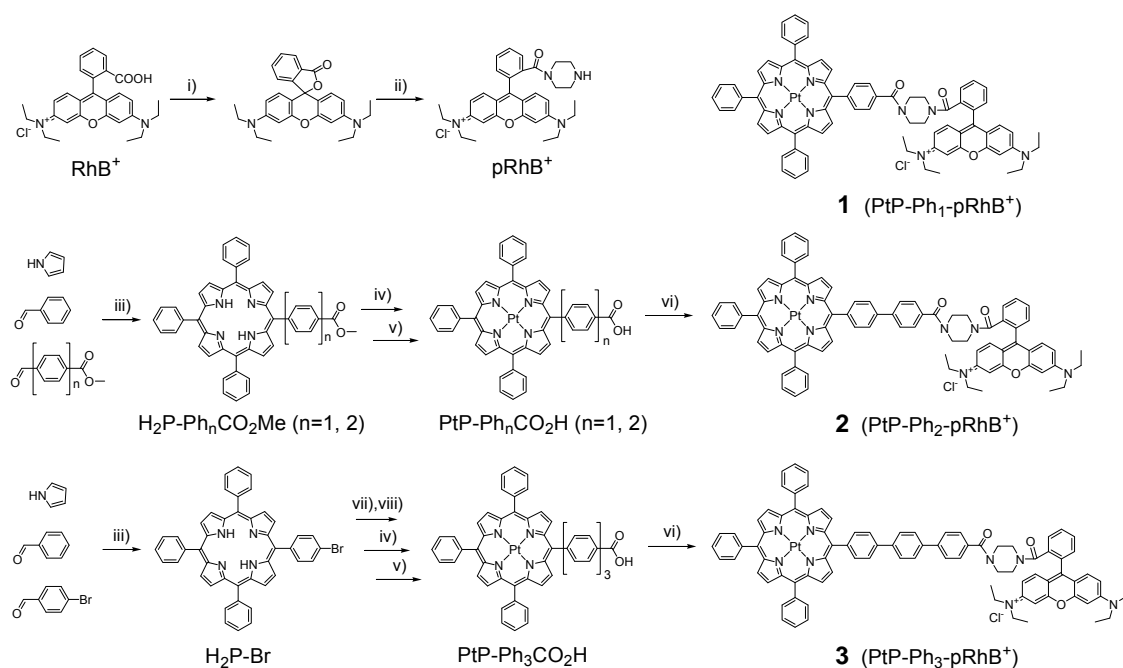
of a Solstice one-box regenerative amplifier, a Mai-Tai Ti:sapphire oscillator as the seeding source and an Empower diode-pumped solid-state pulsed green laser as the pump. The pulse had FWHM  $\sim 90$  fs at 800 nm with energy of  $\sim 3.5$  mJ/pulse at 1 kHz repetition rate. The output of the amplifier was divided by a beam splitter. The first beam (ca 90% of the total power) was used as the input for a Topas-C optical parametric amplifier, equipped with a Berek extension (Light Conversion Ltd., Lithuania). The second beam (10% power) was used to generate probe pulses in the Helios spectrometer. The white light continuum pulse in the visible (VIS) region was generated by a 3 mm sapphire plate. The near infra-red (NIR) probe pulse was generated using a proprietary crystalloid plate. A complementary metal–oxide–semiconductor (CMOS) linear array sensor with 1024 pixels was used for detection in the VIS range, while a 256 pixel InGaAs linear diode array was used in the NIR range. To provide isotropic excitation of the sample and to avoid pump-probe polarization effects, the pump beam was depolarized. Individual  $\Delta A$  (OD) measurements were acquired at a frequency of 500 Hz and averaged over 2 s periods. The energy of the pump beam was set between 2 and 4  $\mu\text{J/pulse}$  over a spot size of 1 mm in diameter, which corresponds to the energy density of  $1 \times 10^{15}$ – $1.5 \times 10^{15}$  photons/cm<sup>2</sup> per pulse, depending on the excitation wavelength (405–580 nm). The optical densities were adjusted to be 0.8 OD at 560 nm and 0.5 OD at 510 nm (1 cm optical path length) for excitation for RhB<sup>+</sup> and PtP, respectively. During the measurements, the samples were continuously stirred by a magnetic stirrer.

**4.3.5 Electrochemical methods.** Cyclic voltammetry experiments were performed in an anaerobic glove box using a potentiostat workstation (BAS 100B, Bioanalytical Systems, Inc.) and anhydrous benzonitrile as a solvent. Tetrabutylammomium hexafluoro-phosphate (TBAP) was used as the supporting electrolyte (100 mM). Pt electrode (1.6 mm diameter) was used as the working electrode, an Ag wire as the quasi-reference electrode and a Pt wire as the counter electrode. Ferrocene (Fc) was used as the internal standard; all values are reported relative to Fc<sup>+</sup>/Fc couple (scan rate 0.1 V/s). The three electrodes were fitted into a Claisen Adapter (Kontes Glass Company, Vineland, NJ) with working and reference electrodes positioned as close as

possible to minimize the ohmic resistance. At each scan rate, at least five scans were performed to ensure stability of the system.

**4.3.6 Synthesis.** The complete synthesis is outlined in Scheme 4.1. All free-base porphyrins were synthesized by the Lindsey method.<sup>113</sup> Platinum was inserted upon refluxing the porphyrins with PtCl<sub>2</sub> in anhydrous benzotritrile. Rhodamine B piperazine amide (pRhB<sup>+</sup>) was synthesized from RhB<sup>+</sup> following the reported procedure.<sup>114</sup> PtP's and pRhB<sup>+</sup> were coupled to each other using the HBTU-mediated peptide coupling method. The overall yields of compounds 1-3, starting from the assembly of initial porphyrins, were 4.8%, 5.4% and 0.5%, respectively.

**Scheme 4.1.** Synthesis of dyads 1-3.



i) NaOH/EtOAc; ii) AlMe<sub>3</sub>/piperazine; iii) a) BF<sub>3</sub>·Et<sub>2</sub>O/CH<sub>2</sub>Cl<sub>2</sub>; b) DDQ; iv) PtCl<sub>2</sub>/PhCN; v) KOH/THF; vi) HBTU/DIPEA/DMF; vii) B<sub>2</sub>pin<sub>2</sub>/PdCl<sub>2</sub>(dppf)/DMF; viii) 4-bromo-4'-methoxycarbonyl-biphenyl/Pd(PPh<sub>3</sub>)<sub>4</sub>/KOAc/DMF.

**5-(4-methoxycarbonylphenyl)-10,15,20-triphenylporphyrin (H<sub>2</sub>P-Ph<sub>1</sub>CO<sub>2</sub>Me).** A mixture of pyrrole (1.6 g, 24 mmol), benzaldehyde (1.9 g, 18 mmol) and methyl 4-formylbenzoate (1.0 g, 6.1 mmol) in CH<sub>2</sub>Cl<sub>2</sub> (600 mL) was stirred under Ar for 30 min. BF<sub>3</sub>·Et<sub>2</sub>O (0.61 g, 4.87 mmol) was added in one portion, the mixture was shaded from the ambient light and left under stirring at r.t. for additional 2 hrs. 2,3-Dichloro-5,6-dicyano-1,4-benzoquinone (DDQ) (1.38 g, 6.1 mmol) was added, and the mixture was left overnight under stirring. The resulting solution was washed with Na<sub>2</sub>SO<sub>3</sub> aq (10 %), NaCO<sub>3</sub> aq (10 %), HCl aq (10%), NaOH aq (10 %) and then with distilled water. The organic phase was collected, dried over Na<sub>2</sub>SO<sub>4</sub>, and the solvent was evaporated to dryness. The residual material was purified by column chromatography on silica gel using CH<sub>2</sub>Cl<sub>2</sub>/hexane mixture (2:3 by volume) as the mobile phase. The second band was collected, the solvent was evaporated and the remaining solid was dried in vacuum to afford the title compound as a purple solid (230 mg, 5.6 %). The spectroscopic data matched those previously reported.<sup>115</sup>

**Pt(II) 5-(4-methoxycarbonylphenyl)-10,15,20-triphenylporphyrin (PtP-Ph<sub>1</sub>CO<sub>2</sub>Me).** Free-base porphyrin H<sub>2</sub>P-Ph<sub>1</sub>CO<sub>2</sub>Me (60 mg, 0.09 mmol) was dissolved in benzonitrile (10 mL), PtCl<sub>2</sub> (47 mg, 0.18 mmol) was added in one portion, and the mixture was set to reflux under Ar. The reaction was stopped when the absorption band near 420 nm (CH<sub>2</sub>Cl<sub>2</sub>), characteristic of the porphyrin dication, disappeared. Complete conversion into the Pt complex required 6-8 hrs. The solvent was evaporated in vacuum, and the residue was purified by column chromatography on silica gel, using CH<sub>2</sub>Cl<sub>2</sub> as the mobile phase, to afford the product as an orange powder (76 mg, 99 %). Spectroscopic data matched those previously reported.<sup>115</sup>

**Pt(II) 5-(4-carboxyphenyl)-10,15,20-triphenylporphyrin (PtP-Ph<sub>1</sub>CO<sub>2</sub>H).** PtP-Ph<sub>1</sub>CO<sub>2</sub>Me (75 mg, 0.086 mmol) was dissolved in the mixture of THF (50 mL) and EtOH (1 mL). A pellet of KOH was added to the solution, and the mixture was stirred at r.t. for 8 hrs. The solvents were removed under vacuum, and the remaining solids were dissolved in water (ca 20 ml). The solution was filtered, neutralized by HCl, the precipitate was collected by centrifugation, washed with water and dried in vacuum. The title compound was obtained as an orange solid (74 mg, 99 %).

%).  $^1\text{H}$  NMR (DMSO,  $\delta$ ): 8.71 (br s, 8H, pyrrole- $\beta$ H), 8.31 (m, 2H, ArH), 8.23 (d,  $J = 8$  Hz, 2H, ArH), 8.14 (m, 6H,  $\alpha$ -PhH), 7.78 (m, 9H,  $m,p$ -PhH); UV-Vis ( $\text{CH}_2\text{Cl}_2$ )  $\lambda_{\text{max}}$ : 403, 511, 542 nm; MALDI-TOF ( $m/z$ ): calcd for  $\text{C}_{45}\text{H}_{28}\text{N}_4\text{O}_2$ : 851.19; found; 851.633.

**5-(4-methoxycarbonylbiphenyl)-10,15,20-triphenylporphyrin ( $\text{H}_2\text{P-Ph}_2\text{CO}_2\text{Me}$ ).**  $\text{H}_2\text{P-Ph}_2\text{CO}_2\text{Me}$  was synthesized in a similar fashion as  $\text{H}_2\text{P-Ph}_1\text{CO}_2\text{Me}$ , using pyrrole (0.28 g, 4.2 mmol), benzaldehyde (0.33 g, 3.1 mmol) and methyl 4-formyl-4'-methoxycarbonyl-biphenyl (0.25 g, 1.0 mmol) as starting materials. The title compound was obtained as a purple solid (60 mg, 7.7 %).  $^1\text{H}$  NMR ( $\text{CDCl}_3$ ,  $\delta$ ): 8.92 (d,  $J = 4$  Hz, 2H, pyrrole- $\beta$ H), 8.87 (m, 6H, pyrrole- $\beta$ H), 8.61 (m, 2H, ArH), 8.33 (d,  $J = 8$  Hz, 2H, ArH), 8.28 (d,  $J = 8$  Hz, 2H, ArH), 8.24 (m, 4H, ArH), 8.07-7.99 (m, 6H,  $\alpha$ -PhH), 7.82-7.74 (m, 9H,  $m,p$ -PhH), 4.03 (s, 3H,  $-\text{COOCH}_3$ ), -2.74 (s, 2H,  $-\text{NH}$ ); UV-Vis ( $\text{CH}_2\text{Cl}_2$ )  $\lambda_{\text{max}}$ : 420, 516, 551, 591, 648 nm; MALDI-TOF ( $m/z$ ): calcd for  $\text{C}_{52}\text{H}_{36}\text{N}_4\text{O}_2$ : 748.28; found; 749.469 [ $\text{M}+\text{H}^+$ ].

**Pt(II) 5-(4-methoxycarbonylbiphenyl)-10,15,20-triphenylporphyrin ( $\text{PtP-Ph}_2\text{CO}_2\text{Me}$ ).** The title compound was synthesized from  $\text{H}_2\text{P-Ph}_2\text{CO}_2\text{Me}$  (20 mg, 0.027 mmol) in a similar fashion as  $\text{PtP-Ph}_1\text{CO}_2\text{Me}$  (see above) The target compound was obtained as an orange powder (20 mg, 80 %). UV-Vis ( $\text{CH}_2\text{Cl}_2$ )  $\lambda_{\text{max}}$ : 404, 511, 544. MALDI-TOF ( $m/z$ ): calcd for  $\text{C}_{52}\text{H}_{34}\text{N}_4\text{O}_2$ : 941.93; found; 942.34 [ $\text{M}+\text{H}^+$ ].

**Pt(II) 5-(4-carboxybiphenyl)-10,15,20-triphenylporphyrin ( $\text{PtP-Ph}_2\text{CO}_2\text{H}$ ).**  $\text{PtP-Ph}_2\text{CO}_2\text{H}$  was synthesized in a similar fashion as  $\text{PtP-Ph}_1\text{CO}_2\text{H}$  (see above) starting from  $\text{PtP-Ph}_2\text{CO}_2\text{Me}$  (20 mg, 0.021 mmol). The title compound was obtained as orange solid (19 mg, 96 %).  $^1\text{H}$  NMR (THF,  $\delta$ ): 10.84, (s, 1H, COOH), 8.83 (d,  $J = 4$  Hz, 2H, pyrrole- $\beta$ H), 8.75 (d,  $J = 4$  Hz, 2H, pyrrole- $\beta$ H), 8.74 (br s, 4H, pyrrole- $\beta$ H), 8.28 (d,  $J = 8$  Hz, 2H, ArH), 8.24 (d,  $J = 8$  Hz, 2H, ArH), 8.17 (m, 6H,  $\alpha$ -PhH), 8.16 (d,  $J = 8$  Hz, 2H) 8.08 (d,  $J = 8$  Hz, 2H), 7.77 (m, 9H,  $m,p$ -PhH). UV-Vis ( $\text{CH}_2\text{Cl}_2$ )  $\lambda_{\text{max}}$ : 403, 513, 544 nm. MALDI-TOF ( $m/z$ ): calcd for  $\text{C}_{51}\text{H}_{32}\text{N}_4\text{O}_2$ : 927.22; found; 928.45 [ $\text{M}+\text{H}^+$ ].

**5-(4-bromophenyl)-10,15,20-triphenylporphyrin (H<sub>2</sub>P-Br).** H<sub>2</sub>P-Br was synthesized as previously reported<sup>116</sup> and isolated as a purple solid (460 mg, 3.1 %). MALDI-TOF (m/z): calcd for C<sub>44</sub>H<sub>29</sub>BrN<sub>4</sub>: 694.16; found; 695.15 [M+H<sup>+</sup>].

**5-(4-methoxycarbonyl-*p*-triphenyl)-10,15,20-triphenylporphyrin (H<sub>2</sub>P-Ph<sub>3</sub>CO<sub>2</sub>Me).** 1) H<sub>2</sub>P-Br (40 mg, 0.057 mmol), bis(pinacolato)diboron (37 mg, 0.144 mmol) and KOAc (0.23 g, 0.58 mmol) were dissolved in DMF (1 ml). PdCl<sub>2</sub>(dppf)<sub>2</sub> (9 mg, 0.012 mmol, 20 %), used as a catalyst in this Miyaura coupling reaction, was dissolved separately in DMF (1 ml). The solution of the catalyst was added to the mixture of the reactants, and it was stirred vigorously at 80°C for 12 hrs. The mixture was cooled down, CH<sub>2</sub>Cl<sub>2</sub> (10 mL) was added and the resulting solution was washed with water (3×10 mL) in a separatory funnel. The organic phase was collected, dried over Na<sub>2</sub>SO<sub>4</sub>, and the solvent was evaporated to dryness. The remaining solid was purified by column chromatography on silica gel (CH<sub>2</sub>Cl<sub>2</sub>/hexane=1:1) to afford the target porphyrin-pinacolatoboron as a purple solid after removing the solvent and drying the product in vacuum (20 mg, 47 %). MALDI-TOF (m/z): calcd for C<sub>50</sub>H<sub>41</sub>BN<sub>4</sub>O<sub>2</sub>: 740.70; found; 741.32 [M+H<sup>+</sup>]. The spectroscopic data matched those previously reported.<sup>117</sup>

2) Porphyrin-pinacolatoboron, obtain at the previous step (20 mg, 0.027 mmol), 4-bromo-4'-methoxycarbonyl-biphenyl (12 mg, 0.041 mmol) and Cs<sub>2</sub>CO<sub>3</sub> (22 mg, 0.067 mmol) were dissolved in DMF (3 ml). Pd(PPh<sub>3</sub>)<sub>4</sub> (3 mg, 0.003 mmol, 10 %) used as a catalyst, was dissolved separately in DMF (1 mL). The catalyst solution was added to the mixture of the reactants, and it was stirred vigorously at 80 °C for 12 hrs. The reaction mixture was cooled down, CH<sub>2</sub>Cl<sub>2</sub> (10 mL) was added, and the resulting solution was washed with water (3×10 mL). The organic phase was collected, dried over Na<sub>2</sub>SO<sub>4</sub> and the solvent was evaporated to dryness. The remaining solid was purified by column chromatography on silica gel using CH<sub>2</sub>Cl<sub>2</sub> as the mobile phase. The title compound was isolated as a purple solid (12 mg, 55 %). <sup>1</sup>H NMR (CDCl<sub>3</sub>, δ): 8.95 (d, J = 4 Hz, 2H, pyrrole-βH), 8.88 (m, 6H, pyrrole-βH), 8.33 (d, J = 8 Hz, 2H), 8.24 (m, 6H, *o*-PhH), 8.20 (d, J = 8 Hz, 2H, ArH), 7.88 (d, J = 8 Hz, 2H, ArH), 7.82 (d, J = 8 Hz, 2H, ArH), 7.79 (m, 9H, *m,p*-PhH), 7.49 (m, 4H,

ArH), 4.0 (s, 3H, -COOCH<sub>3</sub>), -2.73 (s, 2H, -2NH). UV-Vis (CH<sub>2</sub>Cl<sub>2</sub>)  $\lambda_{\text{max}}$ : 421, 516, 550, 595, 649 nm. MALDI-TOF (m/z): calcd for C<sub>58</sub>H<sub>40</sub>N<sub>4</sub>O<sub>2</sub>: 824.96; found; 825.33 [M+H<sup>+</sup>].

**Pt(II) 5-(4-carboxy-*p*-triphenyl)-10,15,20-triphenylporphyrin (PtP-Ph<sub>3</sub>CO<sub>2</sub>H).** H<sub>2</sub>P-Ph<sub>3</sub>CO<sub>2</sub>H (12 mg, 0.14 mmol) was dissolved in benzonitrile (60 mL), PtCl<sub>2</sub> (22 mg, 0.060 mmol) was added, and the mixture was set to reflux under Ar. The reaction was stopped when the absorption band of the porphyrin dication disappeared. Complete conversion to the Pt complex required ca 12 hrs. The solvent was evaporated in vacuum, and the residue was purified by column chromatography (silica gel, CH<sub>2</sub>Cl<sub>2</sub>) to afford the Pt complex as an orange powder. The obtained Pt complex was dissolved in THF (10 mL). MeOH (0.5 mL) and a pellet of KOH were added, and the mixture was left under stirring at r.t. for 12 hrs. The solvents were removed under vacuum, and the water was added. The solution was filtered and neutralized by addition of HCl. The precipitate was collected by centrifugation, washed with water and dried in vacuum. The title compound was obtained as orange solid (2.0 mg, 14 %). UV-Vis (CH<sub>2</sub>Cl<sub>2</sub>)  $\lambda_{\text{max}}$ : 403, 512, 542 nm. MALDI-TOF (m/z): calcd for C<sub>57</sub>H<sub>36</sub>N<sub>4</sub>O<sub>2</sub>Pt: 1004.00; found; 1004.80 [M+H<sup>+</sup>].

**PtP-Ph<sub>1</sub>-pRhB<sup>+</sup> (1).** PtP-Ph<sub>1</sub>CO<sub>2</sub>H was dissolved in DMF (20 mL) and stirred under Ar for 5 min. Diisopropylethylamine (DIPEA; 36 mg, 0.28 mmol) and *o*-benzotriazole-*N,N,N',N'*-tetramethyluronium-hexafluoro-phosphate (HBTU; 11 mg, 0.029 mmol) were added to the mixture in one portion, and it was stirred under Ar for another 5 min. pRhB<sup>+</sup> (15 mg, 0.029 mmol) was added, and the mixture was left under stirring and Ar for 24 hrs. The solvent was removed under vacuum, and the residue was purified by column chromatography (silica gel, THF). The second band was collected, the solvent was evaporated, and the product was dried in vacuum. The title compound was isolated as a purple solid (25 mg, 81 %). <sup>1</sup>H NMR (DMSO,  $\delta$ ): 8.77 (d, J = 4 Hz, 2H), 8.71 (m, 6H), 8.22 (m, 2H), 8.14 (m, 6H), 8.07 (d, J = 8 Hz, 2H), 8.04 (br s, 1H), 8.00 (d, J = 8 Hz, 2H), 7.91 (br s, 1H), 7.89 (br s, 1H), 7.78 (m, 9H), 7.55 (d, J = 8 Hz, 2H), 7.11 (m, 2H), 6.94 (d, J = 2 Hz, 2H), 3.64 (q, J = 8 Hz, 8H), 2.85 (br s, 4H), 2.69 (br s, 4H), 1.32-1.28 (m, 12H); UV-

Vis (PhCN)  $\lambda_{\max}$  (log  $\epsilon$ ): 405 (5.2  $\pm$  0.1), 513 (4.4  $\pm$  0.1), 566 (4.80  $\pm$  0.1) nm; MALDI-TOF (m/z): calcd for C<sub>77</sub>H<sub>65</sub>N<sub>8</sub>O<sub>3</sub>Pt<sup>+</sup>: 1344.48; found; 1344.55.

**PtP-Ph<sub>2</sub>-pRhB<sup>+</sup> (2).** The title compound was synthesized in a similar fashion as 1 (see above) from PtP-Ph<sub>2</sub>CO<sub>2</sub>H (20 mg, 0.021 mmol) and pRhB<sup>+</sup> (14 mg, 0.027 mmol) as starting materials. 2 was isolated as a purple solid (28 mg, 92 %). <sup>1</sup>H NMR (DMSO,  $\delta$ ): 8.82 (d, J = 4 Hz, 2H), 8.75 (d, J = 4 Hz, 2H), 8.72 (br s, 4H), 8.30 (m, 4H), 8.23 (d, J = 8 Hz, 2H), 8.14 (m, 6H), 7.81 (m, 9H), 7.71 (d, J = 8 Hz, 2H), 7.42 (br s, 1H), 7.40 (br s, 1H), 7.20 (d, J = 4 Hz, 2H), 7.17 (d, J = 4 Hz, 2H), 7.05 (br s, 1H), 6.78 (m, 2H), 3.64 (q, J = 8 Hz, 8H), 3.46 (m, 4H), 3.20 (m, 4H), 1.32-1.28 (m, 12H); UV-Vis (PhCN)  $\lambda_{\max}$  (log  $\epsilon$ ): 405 (5.2  $\pm$  0.1), 514 (4.4  $\pm$  0.1), 566 (4.8  $\pm$  0.1) nm; MALDI-TOF (m/z): calcd for C<sub>83</sub>H<sub>69</sub>N<sub>8</sub>O<sub>3</sub>Pt<sup>+</sup>: 1421.52; found; 1421.61.

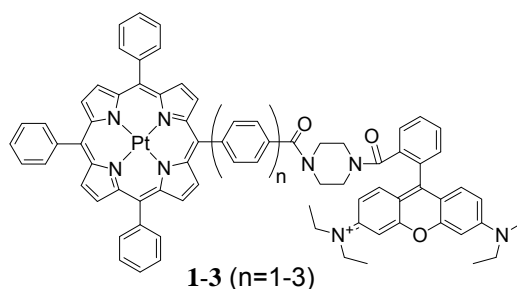
**PtP-Ph<sub>3</sub>-pRhB<sup>+</sup> (3).** The title compound was synthesized in a similar fashion 1 by using PtP-Ph<sub>3</sub>CO<sub>2</sub>H (2 mg, 0.002 mmol) and pRhB<sup>+</sup> (1.2 mg, 0.003 mmol) as starting materials. 3 was isolated as a purple solid (2 mg, 65 %). <sup>1</sup>H NMR (DMSO,  $\delta$ ): 8.81 (d, J = 4 Hz, 2H), 8.71 (m, 6H), 8.26 (d, J = 4 Hz, 2H), 8.14 (m, 6H), 8.11 (d, J = 8 Hz, 2H), 7.92 (d, J = 8 Hz, 2H), 7.86 (d, J = 8 Hz, 2H), 7.80 (m, 9H), 7.73 (br s, 3H), 7.49 (m, 4H), 7.10 (m, 2H), 6.94 (m, 2H), 6.83 (br s, 2H), 3.63 (m, 8H), 3.56 (t, J = 4 Hz, 4H), 3.20 (m, 4H), 1.23-1.18 (m, 12H); UV-Vis (PhCN)  $\lambda_{\max}$  (log  $\epsilon$ ): 405 (5.2  $\pm$  0.1), 515 (4.5  $\pm$  0.1), 567 (5.0  $\pm$  0.1) nm; MALDI-TOF (m/z): calcd for C<sub>89</sub>H<sub>73</sub>N<sub>8</sub>O<sub>3</sub>Pt<sup>+</sup>: 1497.66; found; 1498.32.

## 4.4 Results and discussion

**4.4.1 Choice of chromophores.** The chromophores suitable for the proposed above scheme must satisfy several energetic requirements (Fig. 4.1). First of all, the initially populated excited singlet state of the antenna (<sup>A</sup>S<sub>1</sub>) must have its energy higher than the energy of the triplet state of the core (<sup>C</sup>T<sub>1</sub>). At the same time, <sup>A</sup>S<sub>1</sub> must lie below the singlet state of the core (<sup>C</sup>S<sub>1</sub>) in order to prevent population of <sup>C</sup>S<sub>1</sub> either directly or via <sup>A</sup>S<sub>1</sub> → <sup>C</sup>S<sub>1</sub> energy transfer(s), competing with ET.

Secondly, the energy of the radical pair state RP, created as a result of the ET, must be higher than that of  $^{\text{C}}\text{T}_1$  to allow downhill radical recombination  $\text{R}_{\text{T}}$ . These two requirements set the limits for the entire energy cascade, which has to fit within the singlet-triplet gap ( $2J$ ) of the phosphorescent core.

**Chart 4.1.** Studied dyads **1-3**.



Based on our previous spectroscopic and electrochemical investigations of Pt porphyrins,<sup>86</sup> we conjectured that a suitable dyad could be constructed from Rhodamine B ( $\text{RhB}^+$ ) and a PtP (Pt(II) tetraarylporphyrin) with appropriately tuned oxidation potential. From the synthetic point of view, tetraarylporphyrins with various substitution patterns can be conveniently generated using well-established synthetic protocols.<sup>113, 118</sup> A piperazine amide derivative of  $\text{RhB}^+$ ,  $\text{pRhB}^+$ , directly suitable for amide coupling reactions, is accessible *via* a simple and reliable method.<sup>114</sup>

In Pt porphyrins strong spin-orbit coupling is responsible for high rates of both  $\text{S}_1 \rightarrow \text{T}_1$  intersystem crossing and subsequent radiative  $\text{T}_1 \rightarrow \text{S}_0$  decay,<sup>119</sup> thereby causing bright phosphorescence.<sup>120</sup> Peripheral substituents in the *meso*-aryl rings practically do not affect spectroscopic features of PtP's, while significantly altering their electrochemical potentials.<sup>86</sup> This feature gives the desired flexibility of tuning the level of the RP state without affecting the rest of the chromophoric system.

The lowest energy  $Q_{00}$  state of a representative PtP, Pt tetraphenylporphyrin (PtTPP) ( $\lambda_{\max} \sim 541$  nm, 2.29 eV), is located above the  $pRhB^+$  transition ( $\lambda_{\max} \sim 567$  nm, 2.19 eV). In fact, the  $pRhB^+$  absorption band extends beyond 600 nm, so it is possible to excite  $pRhB^+$  selectively without directly populating the  $Q_{00}$  state ( $^S1PtP$ ) using wavelengths in the range of  $\sim 560$ -600 nm. The energy of the PtP triplet state, based on its phosphorescence maximum ( $\lambda_{\max} = 670$  nm, 1.85 eV for PtTPP), is below that of  $^S1pRhB^+$  state. The entire 2J gap of PtP is ca 0.44 eV. In PtP- $pRhB^+$  pairs,  $^S1pRhB^+$  ( $\lambda_{ex} = 585$  nm, 2.12 eV) is expected to play the role of the electron acceptor, although the exact energy of the RP state depends on the substituents in the porphyrin macrocycle. For PtTPP and  $pRhB^+$ , whose ground state oxidation and reduction potentials in DMF are +1.16V vs SCE (PtTPP $^+$ /PtTPP) and -0.85V vs SCE ( $pRhB^+$ / $pRhB$ ), respectively,<sup>86, 121</sup> the ET driving force  $\Delta G = -0.11$  eV is expected in accordance with the Rehm-Weller equation.<sup>122</sup> Thus, the energy of the radical pair (ca 2.0 eV) is expected to be ca 0.15 eV higher than the energy of  $^T1PtP$ .

Based on these considerations, we chose to study bichromophoric assemblies comprising PtTPP derivative (from here and throughout the text we refer to Pt porphyrin components of the studied dyads simply as PtP), and  $pRhB^+$  connected by oligo-*p*-phenylene linkers (Chart 1,  $Ph_n$ ,  $n=1-3$ : compounds **1-3**) and an amide bond. Oligo-*p*-phenylenes have been extensively used as bridges in ET models,<sup>123</sup> as they can be conveniently constructed using Suzuki-Miyaura chemistry.<sup>124</sup> By varying the number of the phenylene fragments in the bridge, distance dependencies of ET and TT processes can be elucidated.

**4.4.2 Steady-state spectroscopy.** The steady-state absorption and phosphorescence spectra of **1** are shown in Fig. 4.2A (see Fig. 4.A1-A2 for the spectra of **2** and **3**).

The absorption spectra of compounds **1-3** are nearly superpositions of the spectra of the individual chromophores, indicating negligible electronic interactions between PtP and  $pRhB^+$  in their ground and excited electronic states. The emission of spectra of **1** (Fig. 4.2B-D,  $\lambda_{ex} = 425, 510, 580$  nm), as well as of **2** and **3** (Fig. 4.A2), change with excitation wavelength. Assuming that

the overall emission is a linear combination of the pRhB<sup>+</sup> fluorescence and PtP phosphorescence, we could decompose the spectra into the sums of their components and estimate the corresponding quantum yields (Table 4.1) (see the Appendix to this chapter for details of decomposition and analysis). The fluorescence quantum yield of pRhB<sup>+</sup> alone in PhCN was found to be 0.44 ( $\lambda_{\text{ex}}=510$  nm), which is slightly lower than reported for the anionic form of RhB<sup>+</sup> in EtOH (0.65),<sup>111</sup> but higher than that for pRhB<sup>+</sup> in EtOH (0.24).<sup>114</sup> The quantum yields of pRhB<sup>+</sup> fluorescence in the dyads were found to be 0.19, 0.26, and 0.38 for **1-3**, respectively ( $\lambda_{\text{ex}}=510$  nm, ~40% of absorption is due to pRhB<sup>+</sup>), indicating the presence of additional quenching pathways for the pRhB<sup>+</sup> singlet state.

The key feature of the dyads **1-3** is that the phosphorescence of PtP could be observed upon excitation of pRhB<sup>+</sup> at the frequency below that of the lowest allowed transition of PtP, i.e.  $\lambda_{\text{ex}}=580$  nm. It was manifested by the long-lived decay of phosphorescence upon excitation at 580 nm (Fig. 4.2E), the identity of which was confirmed by the time resolved spectral data (Fig. 4.2F). The quantum yield of the phosphorescence observed *via* this pathway was not high ( $\Phi_{\text{phos}}\sim 0.001$ ), but the emission was clearly observable, whereas for the reference porphyrins PtP-Ph<sub>n</sub>CO<sub>2</sub>H (Scheme 4.1; abbreviated in Table 4.1 and further in the text as PtP<sub>n</sub>) as well as for PtTPP no signal could be detected at all upon excitation in the range of 550-600 nm. Additional arguments speaking against direct excitation of PtP in the dyads include virtually zero molar extinction at 580 nm for all our models, very low excitation intensities employed and, as we show below, the presence of a rise phase in the dynamics of the PtP triplet state with the time constant 100-1000 times lower than that of the direct S<sub>1</sub>→T<sub>1</sub> ISC within PtP. Therefore, a different pathway exists in the dyads, which originates in the antenna singlet state <sup>S</sup><sub>1</sub>pRhB<sup>+</sup> and populates the emissive triplet states of the core PtP's.

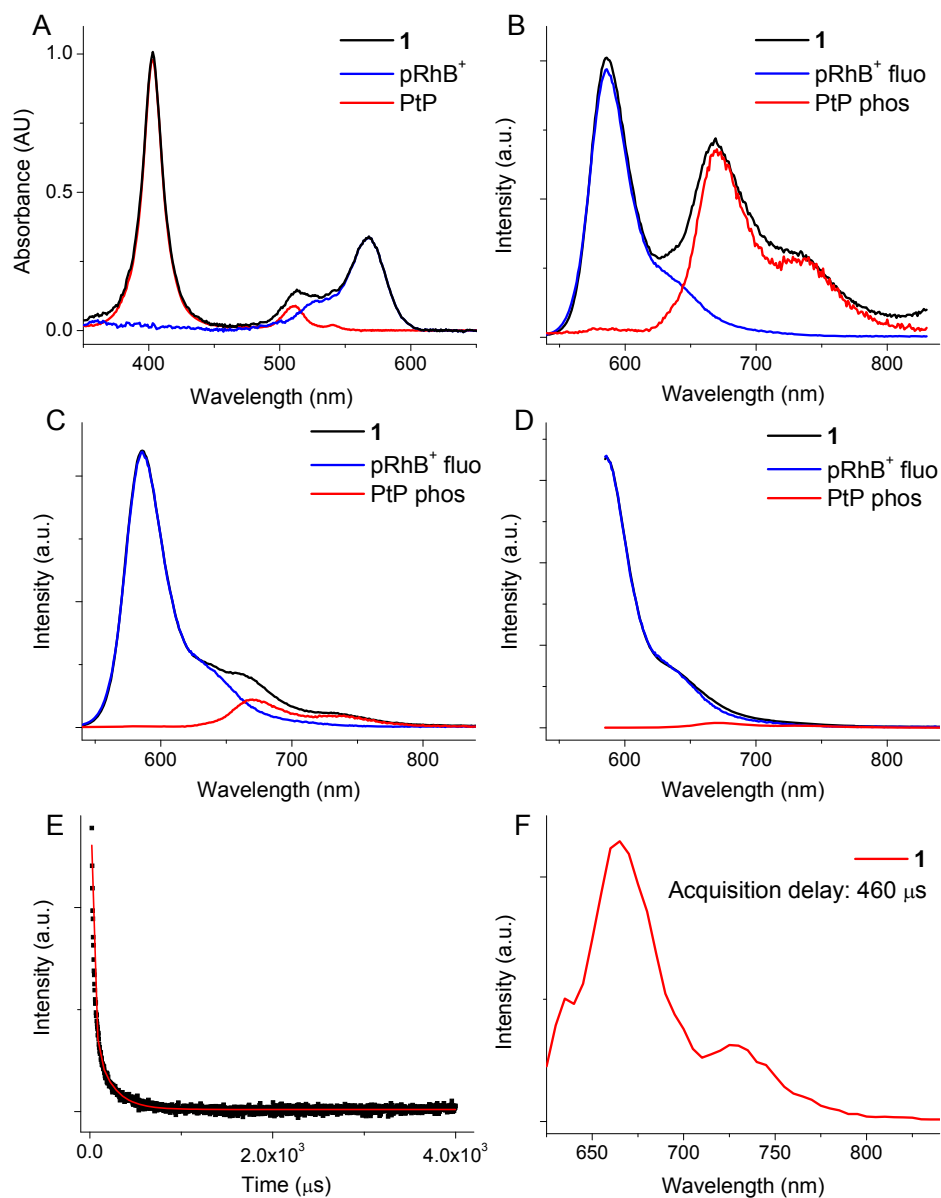


**Figure 4.2.** Various spectra of PtP, pRhB<sup>+</sup> and dyad **1** in benzonitrile. (A) Normalized absorption spectra of PtP, pRhB<sup>+</sup> and dyad **1** in benzonitrile. Emission spectra of **1** acquired using different excitation wavelengths ( $\lambda_{ex}$ ): 425 nm (B), 510 nm (C), and 580 nm (D). The spectra of the components were obtained by linear decomposition. Phosphorescence decay (E) and phosphorescence spectrum registered with delay of 460  $\mu$ s (F) upon pulsed excitation at 580 nm.

**Table 4.1.** Selected photophysical properties of the PtP-Ph<sub>n</sub>-pRhB<sup>+</sup> dyads **1-3** (n=1-3) and of their components.<sup>a</sup> Porphyrins PtP-Ph<sub>n</sub>CO<sub>2</sub>H (Scheme 4.1) are abbreviated in the Table as PtP<sub>n</sub>, for n=1-3.

	$\lambda_{\text{abs}}$ (nm)	$\lambda_{\text{em}}$ (nm) (em. type) <sup>b</sup>	$\Phi_{\text{fl}}^{\text{c}}$ $\lambda_{\text{ex}}$ (510 nm)	$\tau_{\text{fl}}$ (ns) <sup>d</sup>	$\Phi_{\text{ph}}^{\text{c,e}}$ $\lambda_{\text{ex}}$ (425 nm)	$\Phi_{\text{ph}}^{\text{c,f}}$ $\lambda_{\text{ex}}$ (580 nm)	$\tau_{\text{ph}}$ ( $\mu\text{s}$ ) <sup>g</sup>
<b>1</b>	408, 517, 567	585 (f), 670 (p), 730 (p)	0.17 ± 0.04	1.0	0.020 ± 0.02	0.005 ± 0.001	3, <sup>h</sup> 200
<b>2</b>	408, 517, 567	585 (f), 670 (p), 730 (p)	0.24 ± 0.03	1.7	0.031 ± 0.05	0.010 ± 0.002	10, <sup>h</sup> 170
<b>3</b>	407, 516, 567	585 (f), 670 (p), 730 (p)	0.38 ± 0.03	2.2	0.040 ± 0.06	0.010 ± 0.001	30
pRhB <sup>+</sup>	567	585 (f)	0.45 ± 0.03	2.8	--	--	--
PtTPP	407, 514, 542	670 (p), 735 (p)	--	--	0.13 ± 0.01 <sup>j</sup>	--	53 ± 1
PtP <sub>1</sub>	406, 512, 543	670 (p), 735 (p)	--	--	0.08 ± 0.01 <sup>j</sup>	--	43 ± 1
PtP <sub>2</sub>	407, 512, 544	670 (p), 735 (p)	--	--	0.07 ± 0.01 <sup>j</sup>	--	35 ± 1
PtP <sub>3</sub>	406, 512, 541	670 (p), 735 (p)	--	--	0.05 ± 0.01 <sup>j</sup>	--	34 ± 1

<sup>a</sup> All measurements were performed in deoxygenated anhydrous benzonitrile. <sup>b</sup> f – fluorescence, p – phosphorescence. <sup>c</sup> Emission quantum yields were determined relative to the fluorescence of Rhodamine 6G in EtOH ( $\Phi_{\text{fl}}=0.95$ ).<sup>111</sup> <sup>d</sup>  $\lambda_{\text{ex}}=405$  nm. <sup>e</sup> Corresponds to the phosphorescence emitted as a result of direct excitation of PtP (Soret band), followed by intrachromophoric ISC. <sup>f</sup> Phosphorescence emitted as a result of the pathway involving ET and RP-ISC. <sup>g</sup>  $\lambda_{\text{ex}}=510$  nm. <sup>h</sup> Distributions of lifetimes (see text for details). <sup>i</sup>  $\lambda_{\text{ex}} = 510$  nm.

Phosphorescence quantum yields of the dyads were measured upon excitation near the Q band maximum ( $\lambda_{\text{ex}}=510$  nm, ~60% of absorption is due to PtP) and found to be lower than those of the corresponding reference porphyrins PtP<sub>n</sub> and of PtTPP. Notably, in the series of the reference compounds (PtP<sub>n</sub>) the phosphorescence quantum yields decrease with an increase in the length of the oligo-phenylene linker. But in addition, quenching of the PtP triplet states in the dyads appears to be enhanced by the presence of the pRhB<sup>+</sup> fragment. This effect could be a combined result of several phenomena. However, one can probably rule out direct quenching of the porphyrin singlet Soret (S<sub>2</sub>) or Q (S<sub>1</sub>) states by either energy or electron transfer onto pRhB<sup>+</sup>, since both S<sub>2</sub>→S<sub>1</sub> internal conversion and S<sub>1</sub>→T<sub>1</sub> ISC in Pt porphyrins occur on the femtosecond time scale.<sup>125-126</sup> Competing with such fast processes would be improbable. More

likely is that the PtP triplet state already after being formed is partially quenched by the TT energy transfer onto pRhB<sup>+</sup> ( $\Delta G \sim -0.05$  eV – see below), or by the ET onto pRhB<sup>+</sup>, even though the latter process is expected to be endergonic. The evidence for the former pathway was indeed obtained by nanosecond pump-probe and time-resolved phosphorescence measurements (see below).

**4.4.3 Electron transfer.** The most plausible pathway leading to the formation of the triplet state <sup>T1</sup>PtP upon population of <sup>S1</sup>RhB<sup>+</sup> involves ET. Energy transfer processes are much less likely. Indeed, spin-allowed singlet-singlet energy transfer from <sup>S1</sup>RhB<sup>+</sup> to populate <sup>S1</sup>PtP is up-hill ( $\Delta E_{00}(\text{<sup>S1</sup>pRhB}^+) = 2.12$  eV and  $\Delta E_{00}(\text{<sup>S1</sup>PtP}) = 2.3$  eV), while the direct singlet-triplet energy transfer <sup>S1</sup>RhB<sup>+</sup> → <sup>T1</sup>PtP is spin-forbidden. Another potential pathway could involve <sup>S1</sup>RhB<sup>+</sup> → <sup>T1</sup>RhB<sup>+</sup> intersystem crossing within pRhB<sup>+</sup> itself, followed by the population of the <sup>T1</sup>PtP state *via* triplet-triplet (TT) energy transfer. This pathway could be operational in view of the existence of the reversible TT transfer between PtP and pRhB<sup>+</sup> (see below). However, transient absorption measurements ruled out this possibility (see below), showing that the <sup>T1</sup>PtP state precedes the <sup>T1</sup>RhB<sup>+</sup> state and not *vice versa*.

On the other hand, the radical pair state, [PtP<sup>•+</sup>-Ph<sub>n</sub>-pRhB<sup>•0</sup>], is located down-hill from the initially populated state <sup>S1</sup>pRhB<sup>+</sup>. The Gibbs free energy of the ET ( $\Delta G_{ET}$ ) was estimated to be -0.12 eV using the Rehm-Weller formula:  $\Delta G_{ET} = E_{ox}(D) - E_{red}(A) - \Delta E_{00} + \Delta w$ ,<sup>122</sup> where  $E_{ox}(D)$  and  $E_{red}(A)$  are the oxidation and reduction potentials of the donor and acceptor, respectively,  $\Delta E_{00}$  is the excitation energy of the initially populated state and  $\Delta w$  is the electrostatic work term, which in our case is zero, since the ET leads to simple shifting of the charge. The oxidation and reduction potentials of the dyads, measured in benzonitrile solutions, were found to be close for all the compounds **1-3**:  $E_{ox} = +0.53 \pm 0.01$  V and  $E_{red} = -1.46 \pm 0.03$  V; and similar values were obtained for the individual chromophores,  $E_{ox}$  for PtP<sup>+</sup>/PtP and  $E_{red}$  for pRhB<sup>+</sup>/pRhB. Based on these measurements, the energy of the RP state (~2.0 eV), was estimated to be between the energies of <sup>S1</sup>pRhB<sup>+</sup> ( $\Delta E = 2.12$  eV) and <sup>T1</sup>PtP ( $\Delta E = 1.85$  eV).

Assuming that the ET in the dyads is the only deactivation pathway for  $^1\text{pRhB}^+$  in addition to its natural radiative and non-radiative decays, the ET rate constants ( $k_{\text{ET}}$ ) could be calculated directly from the fluorescence lifetime data ( $\tau_{\text{fl}}$ , Table 4.1):  $k_{\text{ET}}=k_{\text{fl}}-k_{\text{fl}}^0$ , where  $k_{\text{fl}}$  and  $k_{\text{fl}}^0$  are the rate constants ( $1/\tau_{\text{fl}}$ ) of the fluorescence of  $\text{pRhB}^+$  in dyads and of free  $\text{pRhB}^+$ , respectively. (Here we assume that the native radiative ( $k_r$ ) and non-radiative ( $k_{\text{nr}}$ ) decay rate constants ( $k_{\text{fl}}^0=k_r+k_{\text{nr}}$ ) do not change upon inclusion of  $\text{pRhB}^+$  into dyads). The  $k_{\text{ET}}$  values were found to be  $6.4 \times 10^8 \text{ s}^{-1}$  for **1**,  $2.3 \times 10^8 \text{ s}^{-1}$  for **2** and  $9.7 \times 10^7 \text{ s}^{-1}$  for **3**. The rate constant of the fluorescence decay of free  $\text{pRhB}^+$  is  $3.4 \times 10^8 \text{ s}^{-1}$ . The rate of the ET is higher than the rate of the  $\text{pRhB}^+$  fluorescence in dyad **1** and lower than that in dyads **2** and **3**.

**4.4.4 Evolution of the radical pair state.** Transient electronic absorption spectroscopy allows detection of non-emissive short-lived intermediates in photoinduced ET reactions. We performed femtosecond transient absorption (FSTA) measurements on dyads **1** and **2** in order to capture the spectroscopic signatures and record time evolution of the RP state. In the case of compound **3**, due to the low rate of the ET and consequently a small amount of the RP species formed, observation of the transient spectra was hampered by noise. However, other spectroscopic data (see below) strongly suggest that the dyad **3** undergoes the same pathway as **1** and **2**.

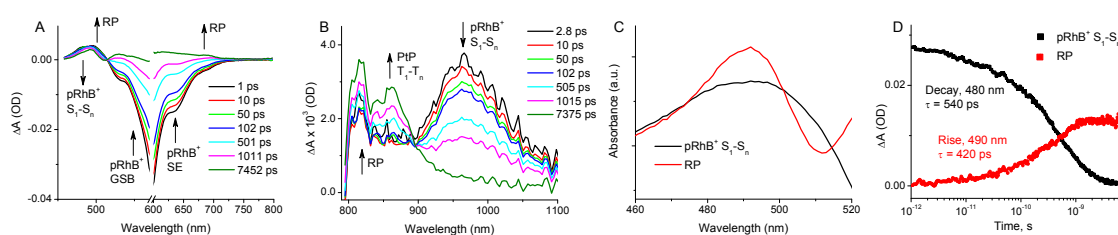


**Figure 4.3.** Early time evolution of dyad **1** upon photo excitation at 580 nm. (A) FSTA spectra of **1** in the visible range at selected times after excitation by a femtosecond laser pulse: FWHM 90 fs,  $\lambda_{\text{max}}=580 \text{ nm}$ . (B) FSTA spectra of **1** in the near infrared (NIR) range. (C) Decay-associated spectra obtained by global fitting of the transients shown in A. (D) Evolution of the spectra shown in C at selected wavelengths (480 and 490 nm) and the corresponding time constants obtained by single-exponential fitting. GSB – ground state bleaching. SE – stimulated emission.

The FSTA spectra of compound **1** upon pulsed excitation at  $\lambda_{\text{max}}=580$  nm (FWHM 90 fs) are shown in Fig. 4.3A,B (see Fig. 4.A3 for the corresponding spectra of **2**). Global fitting of the transients produced two overlapping but distinct spectral features in the region of 400-520 nm (Fig. 4.3C; the related decays are shown in Fig. 4.3D). Based on the comparison with other transients in the spectra and with the literature data, the broad feature decaying with time constant of 540 ps was assigned to the  $S_1 \rightarrow S_n$  absorption of  $\text{pRhB}^+$ . This kinetic is similar to the one of the  $\text{pRhB}^+$  stimulated emission (e.g. at 600 nm), 490 ps, although accuracy in determination of the latter time constant suffered from the proximity of the laser spectrum. In the near infrared (NIR) region, excited state absorption of  $\text{pRhB}^+$  is manifested by a broad peak with the maximum near 960 nm, decaying at the matching rate. Notably, the decay times for  $^{\text{S}1}\text{pRhB}^+$  in the dyads and  $\text{pRhB}^+$  alone obtained by FSTA were shorter than determined by the TCSPC fluorescence lifetime measurements (Table 4.A1). We think that the discrepancy is due to the difference in sampling by the two methods, combined with not perfectly single-exponential nature of the  $\text{pRhB}^+$  decay. Decay binning in our TCSPC system starts at 600 ps and continues up to 50 ns, therefore weighting towards the long-lived components of the decay. In the FSTA system, the first spectrum is acquired at  $\sim 1$  ps, and the entire window is 8 ns, amplifying the contribution of the short-lived components.

Interpretation of transient spectra of dyads **1-3** was complicated by strongly overlapping absorption bands of multiple participating species, i.e. ground and excited singlet, triplet and radical states of the chromophores. Nevertheless, the peaks at 490 nm and 810 nm could be confidently assigned to the RP state based on the global analysis and spectroelectrochemical data (see below). Remarkably, both peaks rise with the time constant of 420-430 ps ( $\sim 2.35 \times 10^9 \text{ s}^{-1}$ ), which is faster than the decay of the parent state  $^{\text{S}1}\text{pRhB}^+$  ( $k_{\text{fl}}(\mathbf{1})=10^9 \text{ s}^{-1}$ ). This seemingly paradoxical result, however, can be expected for a two-component system A/B, where both A and B decay with their own rates constants  $k_{\text{A}}$  and  $k_{\text{B}}$ , and B forms directly from A:  $\text{A} \rightarrow \text{B}$ . In such a system, if  $k_{\text{B}} > k_{\text{A}}$ , then observing the evolution of B one would see it rise with the rate  $k_{\text{B}}$ , which is actually the rate of its decay, and decay at the rate  $k_{\text{A}}$ , which is the decay rate of its precursor

(see the Appendix to this chapter for kinetic equations). Applied to our case, the rate of the formation of RP from  $^S1\text{RhB}^+$  is apparently lower than the rate of the subsequent decay, so that the time constant of the rise (420-430 ps) actually corresponds to the decay of the RP. The fact that we did not observe the decay of the absorption at 490 nm with the time constant corresponding to the decay of  $^S1\text{RhB}^+$  (Fig. 4.3D) suggests that the long-lived species formed from the RP has its own absorption at the same wavelength and approximately the same molar extinction coefficient. This species is the PtP local triplet state (see below).

Spectroelectrochemical data support our assignment of the RP spectra. Although the absorption spectrum of  $\text{pRhB}^{0*}$  is not known, the spectrum of the neutral radical of RhB ( $\text{RhB}^{0*}$ ) has been reported to have an absorption band near 430 nm.<sup>127</sup> The neutral radical of rhodamine B ethyl ester, known as rhodamine 3B, also has been reported,<sup>128</sup> and it also absorbs around 430-450 nm. PtTPP cation radical ( $\text{PtTPP}^{+*}$ ) exhibits a broad absorption band around 600 nm,<sup>121</sup> and in addition has broad absorption centered around 400 nm. In addition to the absorption in the visible range, we also observed a transient peak near 810 nm, partially overlapping with  $T_1 \rightarrow T_n$  absorption of PtP (broad feature near 860 nm) (see Fig. 4.A5 and 4.A6 for details). The peak at 810 nm rises with the time constant of 430 ps, close to that of the peak near 490 nm, and tentatively it has been assigned to the RP as well. Additional evidence for the formation of the RP is provided by the negative peak near 510 nm in the decay-associated spectra (Fig. 4.4C), which is likely to be due to the ground state bleaching of the porphyrin Q-band.

Both nanosecond transient absorption (NSTA) and emission measurements (see below) confirm that upon population of  $^S1\text{RhB}^+$ , the dyads eventually evolve with formation of the local triplet state on PtP. It is, therefore, necessary to consider all plausible evolution pathways of the RP, leading to that state (see Fig. 4.6 for pathway identification). These pathways include: (a) RP-ISC ( $^S[\text{PtP}^{+*}\text{-Ph}_n\text{-pRhB}^{0*}] \rightarrow ^T[\text{PtP}^{+*}\text{-Ph}_n\text{-pRhB}^{0*}]$ ), followed by the radical recombination to yield  $^T1\text{PtP-Ph}_n\text{-pRhB}^+$ ; (b) RP-ISC, followed by the recombination with formation of the triplet state of  $\text{pRhB}^+$ ,  $\text{PtP-Ph}_n\text{-}^T1\text{pRhB}^+$ , and subsequent TT energy transfer  $\text{PtP-Ph}_n\text{-}^T1\text{pRhB}^+ \rightarrow ^T1\text{PtP-Ph}_n\text{-}$

pRhB<sup>+</sup>; and (c) the direct transition  $S_1[\text{PtP}^{+\bullet}\text{-Ph}_n\text{-pRhB}^{0\bullet}] \rightarrow T^1\text{PtP-Ph}_n\text{-pRhB}^+$ . Both pathways (a) and (b) proceed *via* RP-ISC, and, according to our data, pathway (a) appears to be dominant (see below). The rate of the spin-forbidden pathway (c), known as spin-orbit-induced intersystem crossing (SO-ISC),<sup>100</sup> is highly dependent on the mutual orientation of the participating molecular orbitals of the ET partners.<sup>129-130</sup> Molecular dynamics simulations (see Fig. 4.A7) revealed that our dyads exhibit substantial degree of conformational freedom, which is due to rotations around the amide bonds. Conformational flexibility results in a broad distribution of angles between the orbitals of PtP and pRhB<sup>+</sup>, so that the fraction of time spent by the chromophores in the conformation required for the SO-ISC to occur is probably very small. Therefore, pathway (c) is unlikely to contribute significantly to the evolution of the RP. The other two pathways, (a) and (b), are the key to the formation the local triplet states  $T^1\text{PtP}$  and  $T^1\text{RhB}$ .

**4.4.5 Local triplet states and triplet-triplet (TT) energy transfer.** To investigate the dynamics of the local triplet states in the dyads we performed NSTA and time-resolved phosphorescence measurements. Upon excitation into the red edge of the pRhB<sup>+</sup> band (580 nm), **1** and **2** exhibit multiexponential phosphorescence decays in deoxygenated benzonitrile solutions. Almost identical decays were observed when dyads **1** and **2** were excited directly at the PtP Q-band maxima (510 nm). The decays were analyzed by the maximum entropy method (MEM),<sup>112, 131</sup> which, in the case of **1**, as an example, revealed a distribution of lifetimes with peaks near  $\tau_{\text{max}} \sim 5$   $\mu\text{s}$  and  $\tau_{\text{max}} \sim 250$   $\mu\text{s}$ . The peak near 5  $\mu\text{s}$  was broad and extended towards longer lifetimes, exhibiting decays with lifetimes reaching as high as 70-80  $\mu\text{s}$ . Notably, the precursor porphyrins (PtP<sub>n</sub>) and PtTPP under the same conditions reveal narrow unimodal lifetime distributions, corresponding to regular single-exponential kinetics. The decay of **3** was also analyzed by conventional single-exponential analysis (Fig. 4.A8), as this model was sufficient for its phosphorescence kinetics (see below).

Representative NSTA spectra ( $\lambda_{\text{ex}}=532$  nm) for compound **1** are shown in Fig. 4.4 with the earliest time point of 50 ns (see Fig. 4.A9 for the corresponding spectra of **2** and **3**).

Unfortunately, the time period between the last point of the FSTA measurements (7 ns) and the beginning of acquisition of the NSTA data (50 ns) could not be accessed spectroscopically.

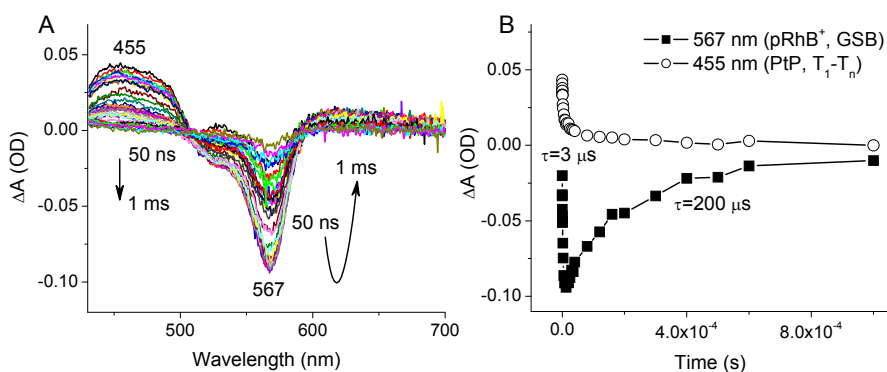


**Figure 4.4.** Time evolution of dyad **1** probed by nanosecond transient absorption spectroscopy. (A) Nanosecond transient absorption spectra of dyad **1** ( $\lambda_{\text{ex}}=532$  nm, pulse FWHM 10 ns). (B) Changes in the absorbance at 567 nm – ground state bleaching (GSB) of pRhB<sup>+</sup>, and 455 nm – T<sub>1</sub>→T<sub>n</sub> absorption of PtP.

The two main features in the NSTA spectra are the T<sub>1</sub>→T<sub>n</sub> absorption of PtP (positive peak near 455 nm)<sup>119</sup> and the ground state bleaching (GSB) of pRhB<sup>+</sup> (negative peak with  $\lambda_{\text{max}}=567$  nm). Importantly, the latter shows a fast decay ( $\tau_d \sim 5 \mu\text{s}$ ), corresponding to the depletion of the pRhB<sup>+</sup> ground state, followed by a slow rise ( $\tau_r=200\text{-}250 \mu\text{s}$ ), i.e. ground state recovery (Fig. 4B). This long rise was attributed to the T<sub>1</sub>→S<sub>0</sub> ISC of pRhB<sup>+</sup>. Indeed, long-lived triplet decay of the parent Rhodamine molecule has been observed previously, also by way of NSTA, in a pyrene-Rh dyad.<sup>132</sup>

In synchrony with fast decaying initial phase of pRhB<sup>+</sup> GSB (Fig. 4.4B, 567 nm trace), PtP triplet-triplet absorption (455 nm trace) is also displaying a fast decaying component. The lifetime distribution of the phosphorescence lifetimes consistently contains significant fraction of decay components near 3-4  $\mu\text{s}$ . These data led us to postulate the existence of the TT energy transfer between <sup>T</sup><sub>1</sub>PtP and <sup>T</sup><sub>1</sub>pRhB<sup>+</sup> states. The directionality of the TT, i.e. from <sup>T</sup><sub>1</sub>PtP to <sup>T</sup><sub>1</sub>pRhB<sup>+</sup>, suggests that after the initial electron transfer the RP state undergoes RP-ISC and recombines to yield the local triplet state <sup>T</sup><sub>1</sub>PtP-Ph<sub>n</sub>-pRhB<sup>+</sup>, rather than PtP-Ph<sub>n</sub>-<sup>T</sup><sub>1</sub>pRhB<sup>+</sup>. Notably,

these data also confirm of our central hypothesis, i.e. that the population of the  $^1\text{PtP}$  occurs *via* the RP route, as opposed to direct  $^1\text{pRhB} \rightarrow ^1\text{pRhB}^+$  ISC within the pRhB moiety, followed by TT transfer from  $\text{pRhB}^+$  to PtP. If the latter was true, the initial phase in the  $^1\text{PtP}$  dynamics would be a rise and not decay.

Remarkably, the GSB recovery phase of  $\text{pRhB}^+$  in **1** and **2** is paralleled by the long-lived components in the PtP phosphorescence (Table 4.1). These lifetimes are much longer than the native decay of the  $\text{PtP}_n$  triplet state ( $\tau \sim 30\text{-}40 \mu\text{s}$ ), suggesting that it is the slow  $^1\text{pRhB}^+$  decay that is reflected in the emission of PtP by way of "delayed phosphorescence". Thus, after being populated the  $^1\text{pRhB}^+$  state either decays to the ground state or undergoes back TT transfer with regeneration of emissive state  $^1\text{PtP}$ . Apparently, equilibrium is established between these two states, forming a pool of triplet excitons. The existence of the equilibrium is supported by the fact that the energy of  $^1\text{RhB}^+$  (1.80-1.84 eV)<sup>133-135</sup> is almost equal to that of  $^1\text{PtP}$  (1.85 eV), and the energetics of  $^1\text{pRhB}^+ \rightarrow ^1\text{PtP}$  process is not completely unfavorable. Furthermore, phosphorescence measurements at 77K (Fig. 4.A11) reveal that the decay of the  $^1\text{PtP}$  state in e.g. dyad **1** becomes nearly perfectly single-exponential, having the lifetime ( $\sim 90 \mu\text{s}$ ) slightly lower than that of PtP alone ( $\sim 120 \mu\text{s}$ ). Hence, at low temperature forward TT transfer becomes slow and only slightly shortens the native PtP decay, while the backward TT transfer virtually stops. In contrast, at high temperature the long-lived non-emissive  $\text{pRhB}^+$  triplet state is able to act as an "energy reservoir",<sup>136</sup> lengthening the overall lifetime of the phosphorescence, although some energy is inevitably lost *via* the non-radiative  $^1\text{pRhB}^+$  decay. Similar cases of triplet lifetime lengthening *via* reversible energy transfer have been noted previously.<sup>110, 137</sup> Our results highlight the possibility of using multiple isoenergetic triplet states to elongate the lifetime of a triplet exciton, tuning in it in accordance with demands of applications.

One interesting feature of the phosphorescence in dyad **1** is the presence of an extra peak with  $\lambda_{\text{max}} = 720 \text{ nm}$  (associated decay time constant  $72 \mu\text{s}$ ) that could be clearly observed in the time-resolved phosphorescence spectra of **1** (Fig. 4.5). Because of its relatively small overall

intensity, this peak could not be seen in the steady-state emission spectra, and its unique time signature blended into the lifetime distribution underlying the phosphorescence decay. Compounds **2** and **3** did not show this spectral feature at all. The emission of **1** at 720 nm was quenched by molecular oxygen, as was the PtP phosphorescence, and remained present in solvents of different polarity, such as THF ( $\epsilon=7.5$ ), benzonitrile ( $\epsilon=25.0$ ) and DMA ( $\epsilon=37.8$ ). Based on the combination of these characteristics this spectral band was attributed to the intramolecular triplet exciplex between PtP and pRhB<sup>+</sup>.

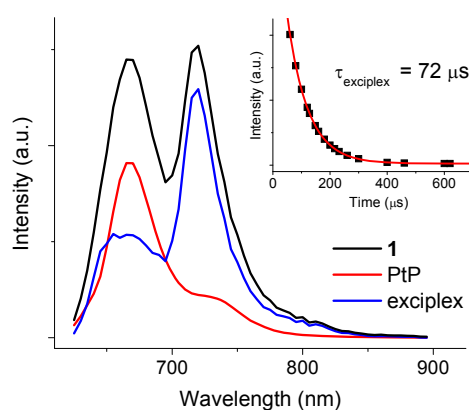


**Figure 4.5.** Emission spectra of **1** at 60  $\mu\text{s}$  after excitation pulse ( $\lambda_{\text{max}}=580$  nm). Inset: decay of the emission line at 720 nm.

Our assignment was based on exclusion of other potential emitters, such as triplet state of pRhB<sup>+</sup> monomer or ground state dimer, or pRhB<sup>+</sup>-pRhB<sup>+</sup> triplet excimer. The monomer of RhB<sup>+</sup> emits phosphorescence at 690 nm and its phosphorescence is detectable only at low temperature (e.g. 77 K in EtOH/H<sub>2</sub>O or EtOH/MeOH),<sup>135, 138</sup> The RhB<sup>+</sup> dimer does have an emission peak at 720 nm, but its observation also requires low temperature. Furthermore, the dimer has significantly different absorption spectra,<sup>135</sup> while in our system the absorption of pRhB<sup>+</sup> clearly matched that of the RhB<sup>+</sup> monomer. On the other hand, intermolecular pRhB<sup>+</sup>-pRhB<sup>+</sup> triplet excimer, which would have the same emission features as the triplet formed upon excitation of the ground state dimer, could be excluded because sample dilutions had no effect at the emission at 720 nm. The remaining candidate was intramolecular exciplex PtP-pRhB<sup>+</sup>, which

presumably could form directly from the triplet RP. In dyads **2** and **3** similar exciplexes could not form due to considerably longer interchromophoric distances. Based on the steady state and emission spectra, the contribution of the exciplex to the overall energy pathway was minimal.

**4.4.6 Energy and electron transfer dynamics.** The complete diagram describing the energy and electron transfer pathways in the studied dyads is shown in Fig. 4.6. The corresponding rate constants are summarized in Table 4.2. The dominant pathway occurring in the dyads upon selective excitation of pRhB<sup>+</sup> is the following: PtP-Ph<sub>n</sub>-<sup>S1</sup>pRhB<sup>+</sup> → <sup>S</sup>[PtP<sup>\*\*</sup>-Ph<sub>n</sub>-pRhB<sup>0\*</sup>] (<sup>S</sup>RP) → <sup>T</sup>[PtP<sup>\*\*</sup>-Ph<sub>n</sub>-pRhB<sup>0\*</sup>] (<sup>T</sup>RP) → <sup>T1</sup>PtP-Ph<sub>n</sub>-pRhB<sup>+</sup> → PtP-Ph<sub>n</sub>-pRhB<sup>+</sup> (ground state). TT energy transfer from <sup>T1</sup>PtP to <sup>T1</sup>RhB plays an important role in elongating the lifetime of the resulting phosphorescence emission, although the intersystem crossing to the ground state of pRhB<sup>+</sup> ( $k_{isc}^{pRhB^+}$ ) provides an extra escape passage for the excitation energy. The main competing pathway to the phosphorescence in the dyads is the singlet radical recombination. Its rate ( $k_{RS}$ ) was not assessed directly, but it is presumed to be comparable to the rate of the triplet recombination times the rate of RP-ISC ( $k_{RP-ISC} \times k_{RT}$ ), since the phosphorescence quantum yields in the dyads are lower than that of the parent porphyrins. Further work on optimization of such emissive triplet systems will need to focus on minimization of this alternative pathway.

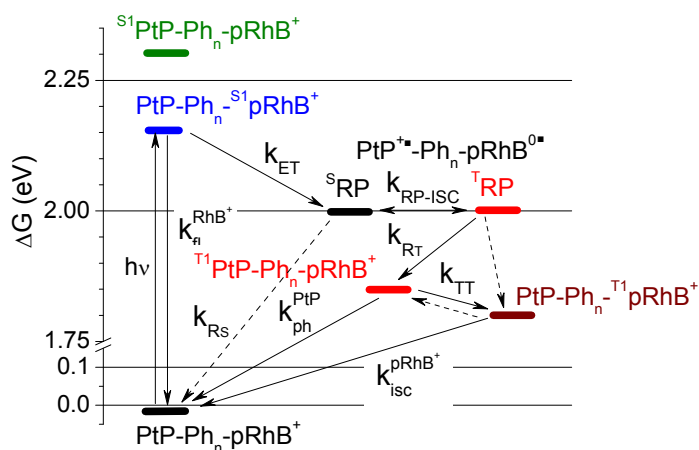


**Figure 4.6.** Pathways occurring in PtP-RhB dyads. The arrows indicate processes whose rate constants were deduced from the spectroscopic measurements. Dashed lines indicate routes for which the rate constants were not experimentally obtained.  $k_{RS}$  and  $k_{RT}$  refer to the recombination of the singlet and triplet radical pairs, respectively.  $k_{TT}$  – rate constant for the forward TT energy transfer.

**Table 4.2.** Rate constants associated with the pathways displayed in Fig. 4.6.<sup>a</sup>

	$k_{fl}$ $\times 10^8 \text{ s}^{-1}$	$k_{ET}$ $\times 10^8 \text{ s}^{-1}$	$k_{RT}$ $\times 10^9 \text{ s}^{-1}$	$k_{TT}^b$ $\times 10^5 \text{ s}^{-1}$	$k_{ph}^{PtP^c}$ $\times 10^5 \text{ s}^{-1}$	$k_{isc}^{pRhB^+}$ $\times 10^3 \text{ s}^{-1}$
1	10.0	6.7	2.4	3.4	3.3, 0.05	5.0
2	5.9	2.3	1.2	1.1	1.0, 0.06	6.7
3	4.5	0.97	-	0.33	0.33	~5.0

<sup>a</sup> All rate constants correspond to the measurements performed in deoxygenated benzonitrile solutions at room temperature. <sup>b</sup> Obtained from NSTA data. <sup>c</sup> Peak maxima in the lifetime distributions.

**4.4.7 Distance attenuation factors.** The dyads prepared in this study are unique in that they feature both ET and TT energy transfer processes. This property is interesting in view of the relationship between the corresponding distance attenuation factors,  $\beta^{ET}$  and  $\beta^{TT}$ , which has been debated in the literature. Closs et al. have originally suggested that the attenuation factor for TT

energy transfer ( $\beta^{\text{TT}}$ ), either *via* direct "through-space" exchange or through saturated bridges, should be two times higher than that for ET. Their TT vs ET studies were based on systems with similar, but not identical donor (D) and acceptor (A) chromophores.<sup>139-140</sup> The theoretical interpretation relied on a simple fact that the Dexter-type TT exchange can be viewed as a concerted transition of one electron and one hole, moving in the same direction. The electron travels from the donor LUMO to the acceptor LUMO, while the hole travels from donor HOMO to the acceptor HOMO. The two transitions are represented by their own electronic coupling matrix elements  $V_{\text{ET}}$  and  $V_{\text{HT}}$ , for ET and hole transfer (HT), respectively, which are considered to exhibit very close distance attenuation factors ( $\beta^{\text{ET}} \approx \beta^{\text{HT}}$ ). Therefore, the coupling matrix element for the TT transfer ( $V_{\text{TT}}$ ) is approximated by the product of the two:  $V_{\text{TT}} \approx |V_{\text{ET}}| |V_{\text{HT}}| = C \times \exp(-2\beta^{\text{ET}} R_{\text{DA}})$ , where  $C$  is a system specific constant, and  $R_{\text{DA}}$  is the donor-acceptor distance. It follows then that:  $\beta^{\text{TT}}/\beta^{\text{ET}}=2$ .

However, later Welter et al. analyzed the data for various D-B-A systems with *p*-phenylene bridges and pointed out that  $\beta^{\text{TT}}$  values for bridge-mediated TT energy transfer reactions are not so different from the corresponding  $\beta^{\text{ET}}$  values.<sup>141</sup> Still, the data analyzed were obtained using systems featuring not identical chromophore pairs. In this regard, our dyads exhibit ET and TT processes separated in time, but occurring in exactly the same molecules, thus providing opportunity for the direct comparison between  $\beta^{\text{ET}}$  and  $\beta^{\text{TT}}$ .

The distance dependencies of the ET and TT transfer rate constants for dyads **1-3** are shown in Fig. 4.7A. Their absolute values are different by  $\sim 3$  orders of magnitude, presumably owing to the difference between the corresponding driving forces, i.e.  $\Delta G_{\text{ET}} = -0.12$  eV and  $\Delta G_{\text{TT}} < -0.05$  eV.

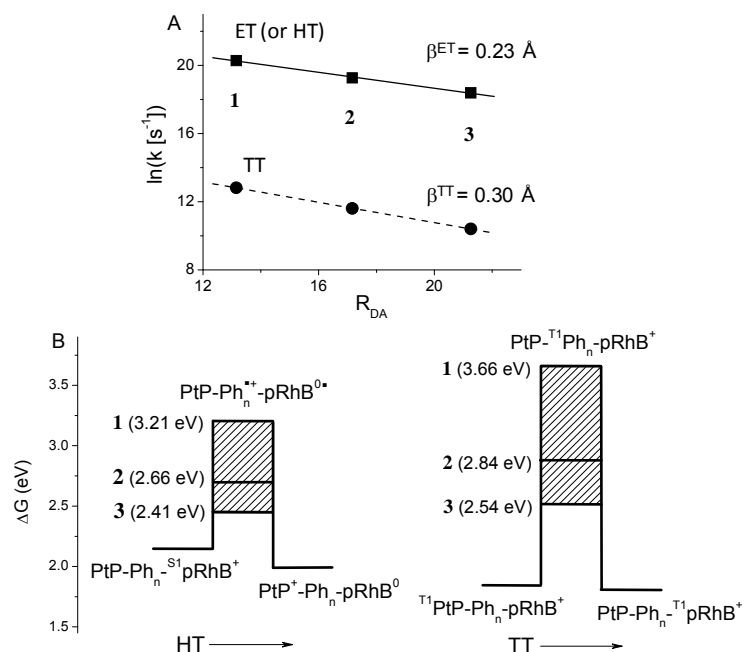


**Figure 4.7.** (A) Distance dependencies of the rate constants for the primary ET, or HT, (■,  $k_{ET}$ ,  $PtP \rightarrow pRhB^+$ ) and TT energy transfer (●,  $k_{TT}$ ,  $PtP \rightarrow pRhB^+$ ). (B) Energy diagrams for HT (hole transfer) and TT energy transfer in the dyads, showing relative heights of the tunneling barriers.

In nonadiabatic high temperature regime, the ET rate constant has exponential dependence on the donor-acceptor distance, i.e.  $k_{ET} \sim \exp(-\beta^{ET} R_{DA})$ .<sup>75,76</sup> Considering that the average distances  $R_{DA}$  in our dyads (i.e. interchromophoric edge-to-edge distances) are 13.2 Å and 17.2 Å and 21.2 Å for 1-3, respectively, the attenuation factor  $\beta^{ET}$  for the initial forward electron transfer ( $k_{ET}$  in Fig. 4.6) was determined to be  $0.23 \text{ \AA}^{-1}$ . Notably,  $\beta^{ET}$  values for superexchange-dominated ET reactions across oligo-*p*-phenylene bridges usually fall into the range of  $0.4\text{-}0.8 \text{ \AA}^{-1}$ , depending on the dihedral angle between the adjacent aromatic rings.<sup>142-143</sup> At the same time, the distance attenuation parameter  $\beta^{TT}$  for the dyads was found to be  $0.30 \text{ \AA}^{-1}$ , which is well within the ranges of values typically observed for TT energy transfer across conjugated bridges.<sup>141, 144-146</sup> Thus, the experimental  $\beta^{ET}$  and  $\beta^{TT}$  in our systems are rather close to each other,  $\beta^{TT}/\beta^{ET} = 1.3$ , i.e. significantly less 2.

From the mechanistic viewpoint, both ET and TT energy transfer in the dyads are likely to be mediated by through-bond couplings and occur *via* the superexchange mechanism, as opposed to incoherent hopping.<sup>12</sup> Indeed, for either electron, hole or triplet migration, the gaps between the initial states ( $\text{PtP-Ph}_n\text{-}^{\text{S}1}\text{pRhB}^+$  for ET and HT;  $^{\text{T}1}\text{PtP-Ph}_n\text{-pRhB}^+$  for TT) and the hypothetical intermediate states involving the bridge ( $\text{PtP}^{+\bullet}\text{-Ph}_n\text{-pRhB}^+$  for ET,  $\text{PtP-Ph}_n\text{-pRhB}^{0\bullet}$  for HT and  $\text{PtP-}^{\text{T}1}\text{Ph}_n\text{-pRhB}$ ) are positive and quite high (Fig. 4.7B), which is a condition required by the superexchange mechanism. It is the height of the tunneling barrier that determines the exponential distance attenuation factors in both ET and TT energy transfer process.<sup>25, 147</sup> Estimations of the levels in Fig. 4.7B were based on our own electrochemical measurements and relevant literature data for oligophenylenes.<sup>85,86</sup> It was more appropriate in our case to consider HT (i.e. positive charge transfer from  $\text{pRhB}^+$  to PtP) rather than ET, since the gap between the initial state and the hypothetically oxidized bridge ( $\text{Ph}_n\text{-}^{+\bullet}$ ) was lower than for the corresponding reduced bridge ( $\text{Ph}_n\text{-}^{\bullet}$ ) (see the Appendix to this chapter for details).

Growing evidence suggests that for through-bond superexchange processes distance attenuation factors are not characteristics exclusively of the bridge, but rather depend on a combination of factors, including donor and acceptor and tunneling gap.<sup>123, 148-149</sup> All three are almost always different for ET (or HT) and TT energy transfer processes. For example in our systems (Fig. 4.7B), the actual donor and acceptor states are  $\text{PtP-Ph}_n\text{-}^{\text{S}1}\text{pRhB}^+$  for HT and  $^{\text{T}1}\text{PtP-Ph}_n\text{-pRhB}^+$  for TT, even though the individual chromophores and bridges are the same. Similarly, the bridge states are  $\text{Ph}_n\text{-}^{+\bullet}$  for HT and  $^{\text{T}1}\text{Ph}_n$  for TT. Thus, valid comparison between distance attenuation factors should probably involve systems with energetically comparable initial, final and bridge states, rather than systems based on identical chromophores. In this regard, the ratio  $\beta^{\text{TT}}/\beta^{\text{ET}}=1.3$  obtained for our dyads proves that ambiguity stemming from the use of different chromophores does not fully account for deviations from the theoretically predicted  $\beta^{\text{TT}}/\beta^{\text{ET}}=2$  ratio.

## 4.5 Conclusions

We have demonstrated that in bichromophoric systems, consisting of phosphorescent triplet cores and auxiliary antenna dyes, emissive triplet states can be generated *via* electron transfer/radical recombination pathway, rather than directly as a result of the core-centered processes. The described PtP-pRhB<sup>+</sup> systems can serve as a prototype for future development of molecules, in which emission from triplet states is potentially susceptible to the control over the dynamics of intermediate radical pair states. Further optimization will need to focus on maximizing the efficiency of the ET/RP-ICS pathway relative to the direct charge recombination. As an extra benefit, the studied PtP-Ph<sub>n</sub>-pRhB<sup>+</sup> dyads featured both ET and TT energy transfer processes in the same molecular systems, which allowed direct comparison between the corresponding distance attenuation factors  $\beta^{\text{ET}}$  and  $\beta^{\text{TT}}$ . Their ratio ( $\beta^{\text{TT}}/\beta^{\text{ET}}=1.3$ ) was found to be much lower than theoretically predicted. Due to the flexibility in tuning the porphyrin redox potentials without altering its spectroscopic properties, PtP-based systems may be instrumental in further studies of the relationship between ET and TT energy transfer processes.

## 4.6 Appendix

### 4.6.1 Quantum yield calculations

Assuming that the complete spectrum is a superposition of the spectra of two contributing chromophores, A and B, linear decomposition can be used to isolate the corresponding individual spectra. The composite spectrum  $F(\lambda)$  is represented as:

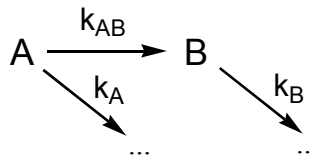
$$F(\lambda) = \alpha F_A(\lambda) + \beta F_B(\lambda) \quad (\text{Eq. 4.A1}),$$

where  $\alpha$  and  $\beta$  are linear coefficients, and  $F_A(\lambda)$  and  $F_B(\lambda)$  are the individual spectra of A and B, respectively. Decomposition was performed by using regularized, positively constrained least-squares method. Both absorption and emission spectra were analyzed for dyads **1-3**. It was assumed that at a selected wavelength, the fraction of photons absorbed by each chromophore

comprising the dyad is proportional to the corresponding absorbance, as determined by the spectral decomposition. Similarly, the emission generated by each chromophore was individually obtained from the decomposition of the composite emission spectra. Integration of the emission component, normalization by the corresponding absorbance and referencing to the normalized fluorescence of Rhodamine 6G, used as the actinometer, gave the quantum yield of the corresponding emission.

#### 4.6.2 Kinetic scheme modeling kinetics of the RP state

Kinetic scheme illustrating the interplay between the rise and decay of species B, produced from species A with rate constant  $k_{AB}$ , is shown in Fig. 4.A4. Both species, A and B, decay at their own rates  $k_A$  and  $k_B$ , respectively. Therefore, the overall rate of the decay of A is given by:  $k=k_A+k_{AB}$ .



The evolution of species B is given by:

$$B(t) = \frac{C}{k_B - k} (e^{-kt} - e^{-k_B t}) \quad (\text{Eq. 4.A2}).$$

According to the above equation, species B will always rise at the rate which is the faster of the two, whether it is  $k_B$  or  $k$ . Thus, if the rate of the decay of B is faster than the rate of the decay of A ( $k_B > k$ ), the kinetics will show the rise with the time constant of the actual decay.

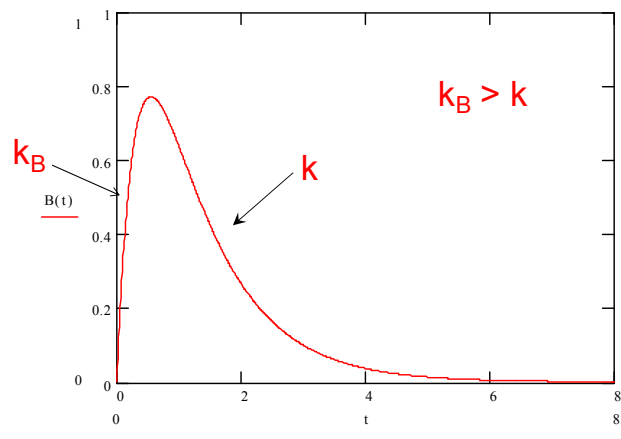


**Figure 4.A4.** Evolution of species B, as in the scheme above.

### 4.6.3 Additional Figures

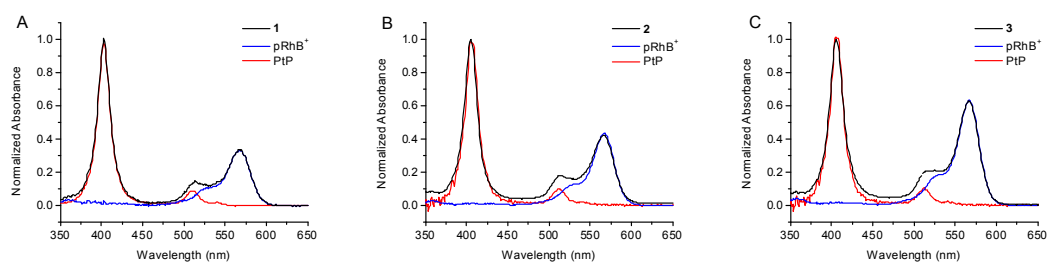


**Figure 4.A1.** Absorption spectra of dyads 1-3 and their components, pRhB<sup>+</sup> and PtP, in benzonitrile.

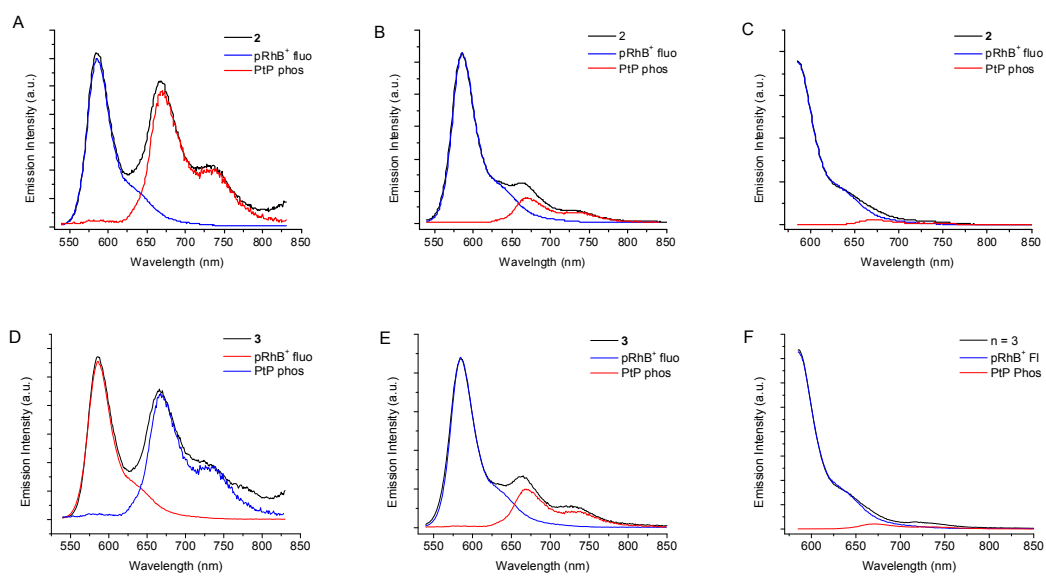


**Figure 4.A2.** Emission spectra of dyads 1-3 and of the individual chromophores, obtained by linear decomposition.  $\lambda_{ex}$ = 425 nm (A, D), 510 nm (B, E), and 580 nm (C, F).

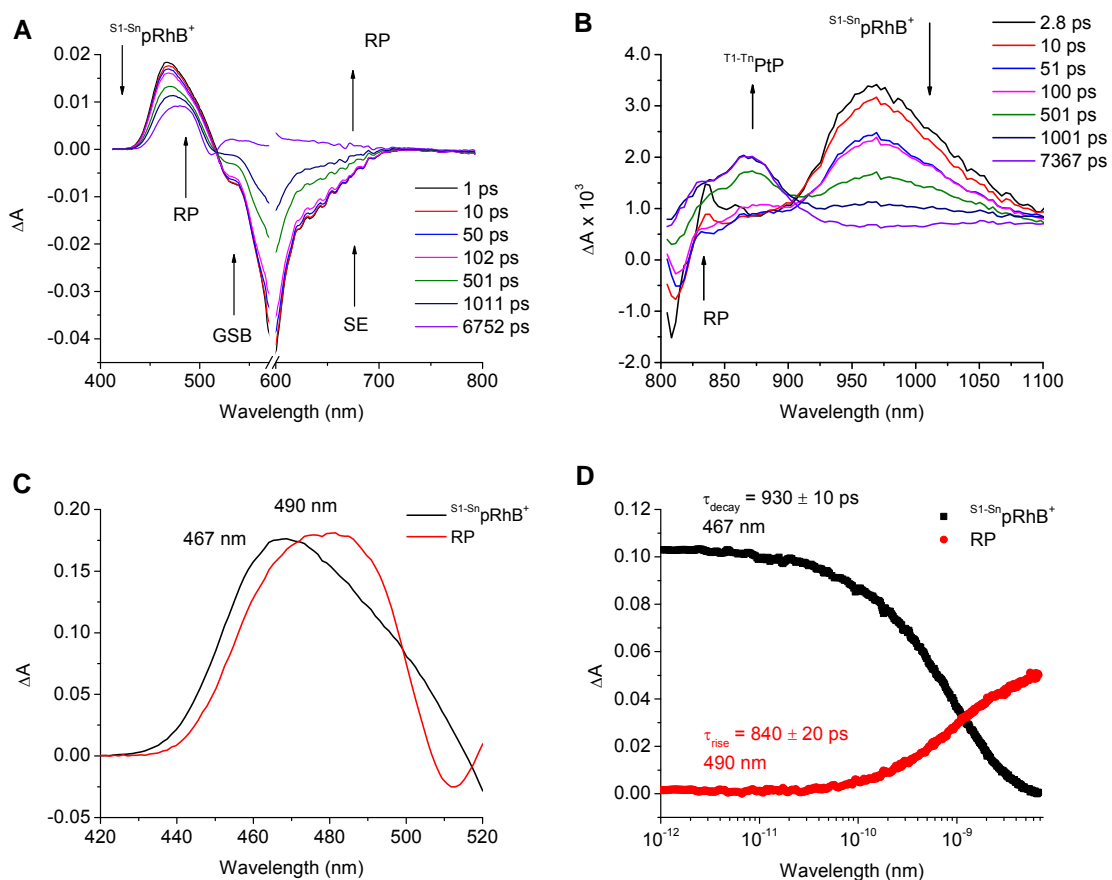


**Figure 4.A3.** Early time evolution of dyad **2** upon photo excitation at 580 nm. (A) Femtosecond transient absorption (FSTA) spectra of dyad **2** in the visible range at the indicated times after the excitation pulse (580 nm, FWHM 90 fs). (B) FSTA spectra of **2** in the NIR range. (C) Decay-associated spectra of **2**. (D) Time evolution of the peaks in the spectra shown in (C): 480 nm 490 nm.

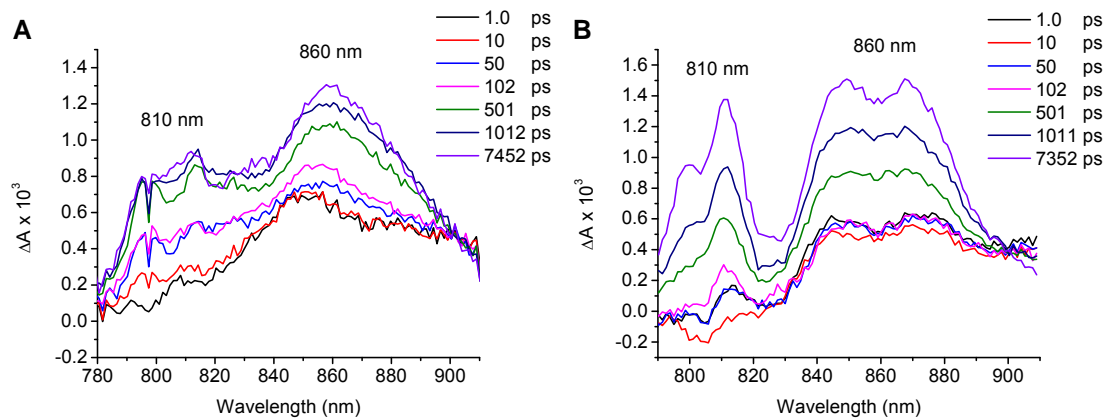


**Figure 4.A5.** FSTA spectra of **1** (A) and **2** (B) in the NIR range (765-910 nm).

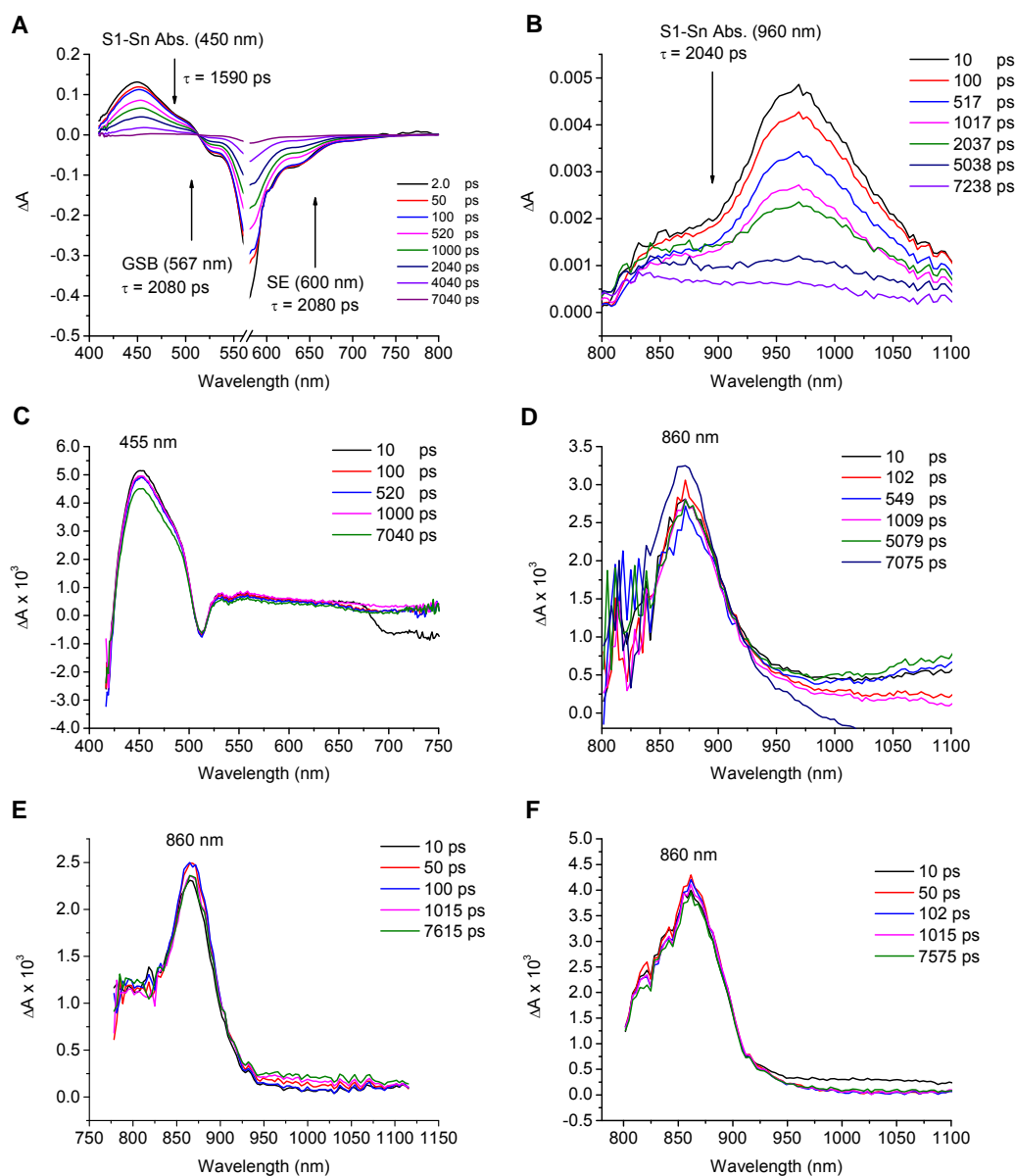


**Figure 4.A6.** Additional FSTA spectra. (A) FSTA spectra of pRhB<sup>+</sup> in the visible range ( $\lambda_{\text{ex}} = 567 \text{ nm}$ ). (B) FSTA spectra of pRhB<sup>+</sup> for in the NIR range ( $\lambda_{\text{ex}}=580 \text{ nm}$ ). (C) FSTA spectra of PtP<sub>2</sub> in the visible range ( $\lambda_{\text{ex}}=405 \text{ nm}$ ). (D) FSTA spectra of PtP<sub>2</sub> in the NIR range ( $\lambda_{\text{ex}}=515 \text{ nm}$ ). (E) FSTA spectra of **1** in the NIR range ( $\lambda_{\text{ex}}=405 \text{ nm}$ ). (F) FSTA spectra of **1** in the NIR range ( $\lambda_{\text{ex}}=405 \text{ nm}$ ).

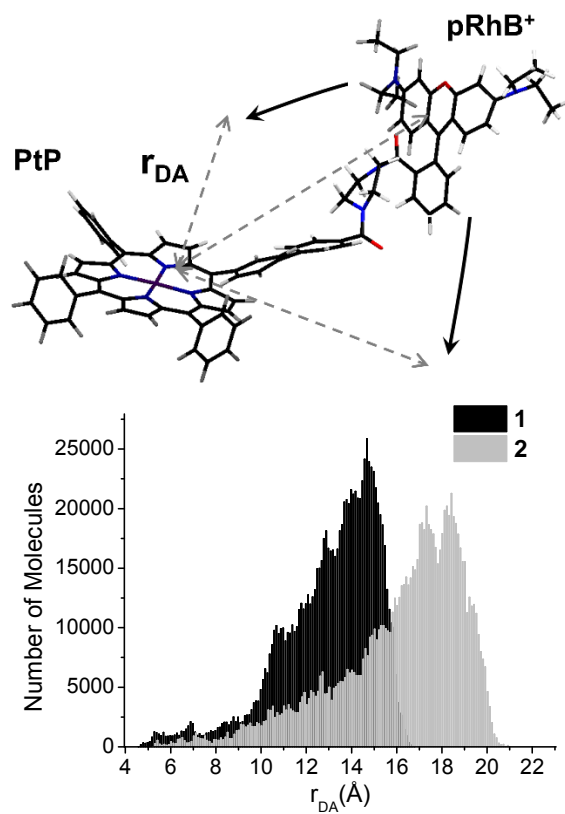


**Figure 4.A7.** Structural considerations of dyads **1** and **2**. (A) Optimized equilibrium structure of **2** (MM+ force field). (B) Distribution of  $r_{DA}$  distances for the compounds **1** and **2**, obtained by molecular dynamics simulation (MM+). Broad distributions reveal conformational flexibility of the molecules.

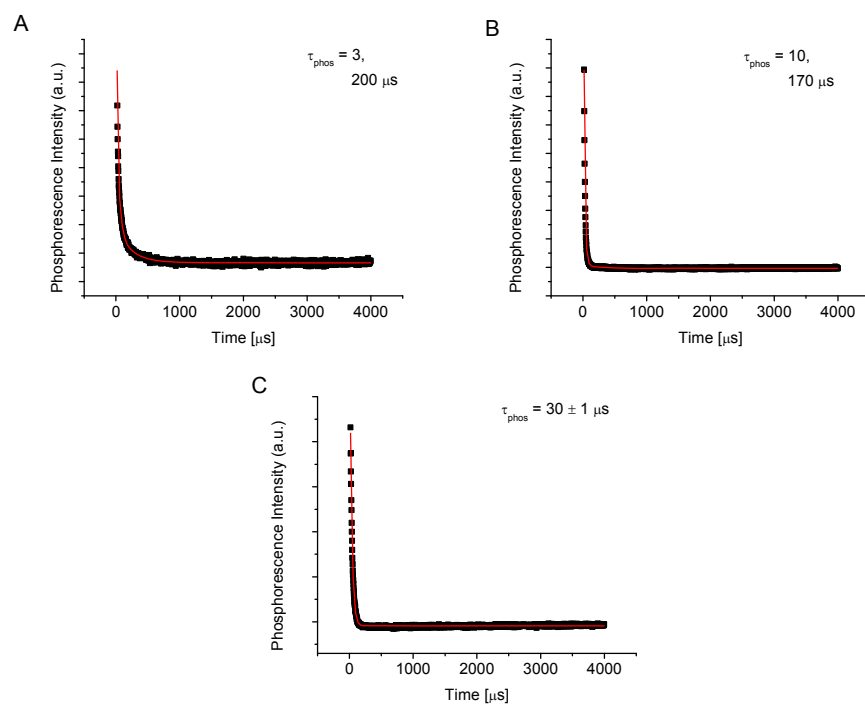


**Figure 4.A8.** Phosphorescence decays and their time constants for **1** (A), **2** (B), and **3** (C).

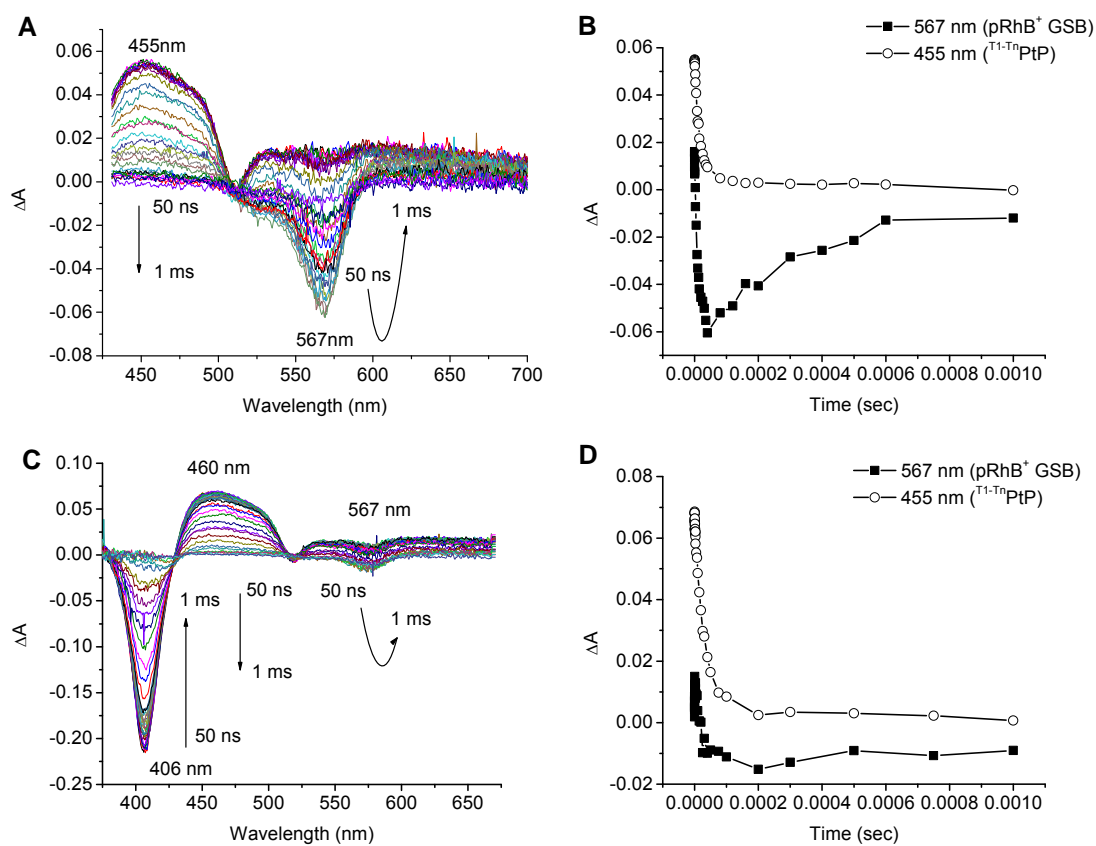


**Figure 4.A9.** Nanosecond transient absorption (NSTA) spectra of **2** (A) and **3** (C) in the visible range upon excitation at 532 nm (10 ns pulse). Time range: 50 ns to 1 ms. Changes in absorbance at 567 nm – ground state bleaching (GSB) and the GSB recovery of pRhB<sup>+</sup>; and at 455 nm – T<sub>1</sub>-T<sub>n</sub> absorption of PtP, for **2** (B) and **3** (D).

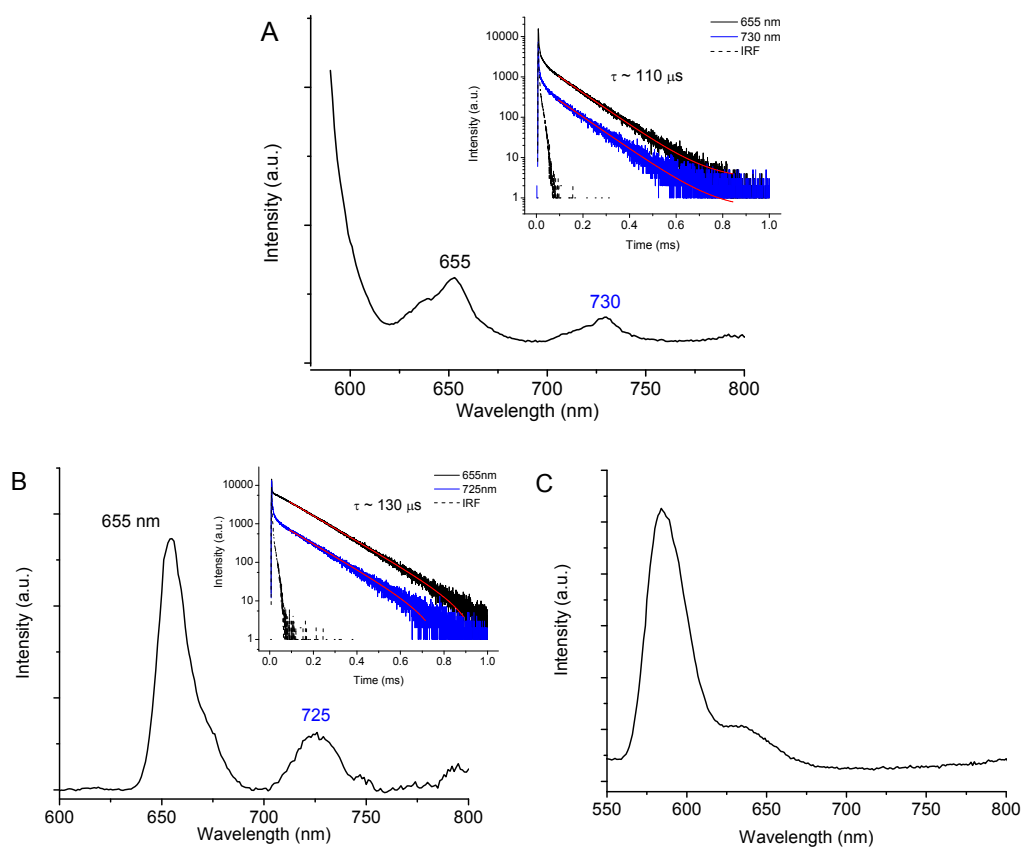


**Figure 4.A10.** Emission spectra of **1** (A), PtP-Ph<sub>1</sub> (B) and pRhB<sup>+</sup> (C) at 77K,  $\lambda_{ex}$ =580 nm. The insets show the corresponding decays. The red lines represent single-exponential fits.

#### 4.6.4 Electrochemical and spectroscopic data used for the calculation of the barriers in Fig. 4.7

Oligo-*p*-phenylenes are oxidized at 2.36, 1.81, and 1.56 V (vs SCE in dichloromethane) and reduced at -3.39, -2.72, and -2.44 V (vs SCE in dimethylamine) for **1-3** respectively. All the values are taken from the literature.<sup>150</sup> Given the redox potentials of PtP and pRhB<sup>+</sup>, oxidized intermediates PtP-Ph<sub>n</sub><sup>+</sup>-pRhB<sup>0</sup> are energetically closer to both the initial and the final states than reduced intermediates PtP<sup>+</sup>-Ph<sub>n</sub><sup>-</sup>-pRhB<sup>+</sup> states. Therefore, instead of electron transfer (ET) we consider hole transfer (HT), whereby PtP-Ph<sub>n</sub><sup>+</sup>-pRhB<sup>0</sup> sets the tunneling barrier.

In the case of TT energy transfer, the energy of the bridge state, <sup>T</sup>Ph<sub>n</sub>, is not known. However, the energy of the triplet states of phenyl, biphenyl, and *p*-terphenyl are known.<sup>151-152</sup> These values served us as estimates.

#### 4.6.5 Additional Table

**Table 4.A1.** Rate constants for compounds **1-3** – summary ( $s^{-1}$ ). The rates measured by FSTA are systematically higher than those from the fluorescence lifetime measurements.

	Fluorescence of pRhB <sup>+</sup>	Decay of <sup>S<sup>1</sup></sup> pRhB <sup>+</sup> decay			Recovery of <sup>S<sup>0</sup></sup> pRhB <sup>+</sup>	Rise of PtP <sup>••</sup>	Rise of PtP <sup>••</sup>	
Peak $\lambda_{max}$	580 nm	S <sub>1</sub> -S <sub>n</sub> abs 460 – 470 nm	SE 600 nm	S <sub>1</sub> -S <sub>n</sub> abs. 966 nm	GSBR 570 nm	abs. 810 nm	T <sub>1</sub> -T <sub>n</sub> abs. 455 nm	T <sub>1</sub> -T <sub>n</sub> abs. 865 nm
pRhB <sup>+</sup>	0.36	0.63	0.48	0.49	0.48	--	--	--
<b>1</b>	1.00	1.85	1.92	2.06	1.96	2.38	2.38	2.32
<b>2</b>	0.59	1.08	0.95	1.23	1.14	1.05	1.20	1.05
<b>3</b>	0.45	--	--	--	--	--	--	--

*Acknowledgements: Dr. Darius M. Niedzwiedzki of Washington University (data collection of femtosecond transient absorption spectroscopy), Dr. Thomas Troxler (technical assistance for nanosecond transient absorption spectroscopy and fluorescence lifetime measurements), and Dr. Robin M Hochstrasser and Dr. Dewey Holten (discussion).*

## CHAPTER 5 Emissive Triplet State and Radical Pair Spin Dynamics in The Triad Containing Pt(II) Porphyrin

In this chapter, we discuss the triad system where emissive triplet state of Pt(II) porphyrin is populated by a photoinduced electron transfer, followed by presumably spin-orbit induced intersystem crossing. We show that such a photophysical pathway can be dependent upon solvent polarity, which stems from the existence of radical pairs in the pathway.

### 5.1 Introduction

Understanding of the mechanism governing molecular emissivity and dynamics of excited states of molecules are crucial for their practical applications in technology and medicine. Triplet electronic spin states find their applications in various fields including energy up-conversion by triplet-triplet annihilation,<sup>73-74</sup> organic light emitting devices (OLED),<sup>75-76</sup> medical photodynamic therapy (PDT),<sup>71-72</sup> and biological imaging of molecular oxygen.<sup>77-78</sup> We are exploring the possibilities of producing emissive triplet states in an unusual way, which may present new possibilities in imaging application and other technologies.

In phosphorescent molecules such as Pt and Pd porphyrins, strong spin-orbit coupling is responsible for high rates of both  $S_1 \rightarrow T_1$  intersystem crossing (ISC) and subsequent radiative  $T_1 \rightarrow S_0$  decay,<sup>119</sup> thereby causing bright phosphorescence.<sup>120</sup> Typically, the phosphorescent state in these molecules is produced *via* intramolecular ISC, preceded by photoexcitation of the respective molecules to  $S_1$  and/or  $S_2$  excited states (Fig. 5.1A). Photoexcitation may be captured by an antenna chromophore and its excitation energy is then transferred onto the singlet excited states of the phosphorescent molecules *via* Förster-type energy transfer, followed by the rapid  $S_1 \rightarrow T_1$  ISC.<sup>81-83</sup> These molecules proved to be very useful as probes in two-photon phosphorescence lifetime microscopy (2PLM) of oxygen.<sup>83-85</sup> In these types of *antenna* (A) –

phosphorescent *core* (C) system, the final step to populate emissive triplet state is still ordinary intramolecular ISC within the phosphorescent core.

As discussed in Chapter 4, we have demonstrated<sup>153</sup> that emissive triplet states can be generated by the photophysical pathway involving singlet ET and radical pair (RP) spin dynamics as opposed to the ordinary intramolecular pathway. The photophysical pathway is summarized in Fig. 5.1B. The system comprises Pt porphyrin (PtP) and the derivative of Rhodamine B (RhB<sup>+</sup>) in which selective excitation of RhB<sup>+</sup> induces photoinduced electron transfer, leading to the formation of singlet RP (<sup>S</sup>RP), followed by the radical pair intersystem crossing (RP-ISC) and triplet radical recombination (CR<sub>T</sub>) to produce the emissive local triplet state of the core (<sup>T</sup>1C). While a very large number of molecular models with energy layouts resembling that in Fig. 5.1 has been published before,<sup>11, 45, 89, 103-106</sup> our model system consisting of PtP-RhB<sup>+</sup> was the first case where room-temperature emissive triplet state is produced in such a photophysical pathway.

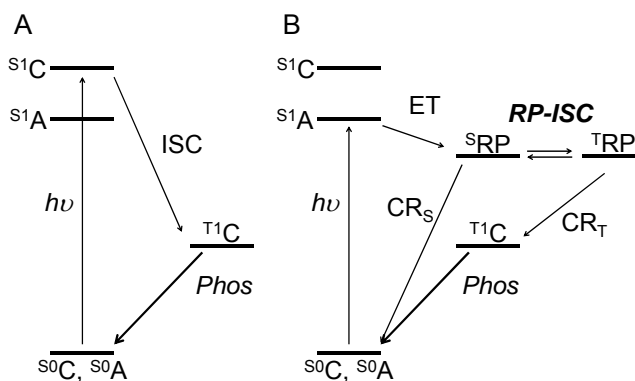


**Figure 5.1.** Two photophysical pathways leading to emissive triplet states. (A) Energy diagram of antenna (A) – core (C) systems, in which the local triplet state of the core (<sup>T</sup>1C) is populated *via* excitation of the core. (B) Energy diagram of A-C systems, in which <sup>T</sup>1C is populated *via* excitation of the antenna, electron transfer (ET) with formation of the singlet radical pair (<sup>S</sup>RP), intersystem crossing (RP-ISC) and radical recombination (CR<sub>T</sub>) from the resulting triplet radical pair (<sup>T</sup>1RP). Alternatively, RP<sub>S</sub> undergoes charge recombination CR<sub>S</sub>, yielding the ground state species.

The work presented in this chapter is concerned with the triad, in which PtP serves as an emissive triplet core and boron dipyrromethene (BODIPY or BD) serves as an antenna chromophore. We investigate the electron and energy dynamics in this system, particularly focusing on the dynamics of RP and triplet states. We demonstrate the quantum yield of phosphorescence from PtP can be solvent dependent. We show that such solvent dependence stems from the properties of incorporated RPs in the photophysical pathway.

## 5.2 Experimental methods

**5.2.1 General information.** All the experiments were performed in the University of Pennsylvania except for nanosecond transient absorption spectroscopy (NSTA) and femtosecond transient absorption spectroscopy (FSTA) measurements, which were performed in Tampere University of Technology. All solvents and reagents were obtained from standard commercial sources and used as received. Selecto silica gel (Fisher Scientific, particle size 32-63 micron) was used for column chromatography.  $^1\text{H}$  NMR spectra were recorded on a Varian Unity 400 MHz spectrometer. Mass-spectra were obtained on a MALDI-TOF MS Microflex LRF instrument (Bruker Daltonics), using  $\alpha$ -cyano-4-hydroxycinnamic acid as a matrix. All the photophysical and electrochemical measurements were performed at 22°C, unless otherwise noted.

**5.2.2 Optical measurements.** UV-vis absorption spectra were recorded on a Perkin-Elmer Lambda 35 UV-Vis spectrophotometer. Steady-state and time-resolved phosphorescence measurements were performed on a FS900 spectrofluorometer (Edinburgh Instruments, UK), equipped with R2658P PMT (Hamamatsu). Quartz fluorometric cells (1 cm optical path length) were used in all optical experiments. The samples were deoxygenated by Ar bubbling or by applying four pump-freeze-thaw cycles. Quantum yields were measured against fluorescence of Rhodamine 6G in EtOH ( $\Phi_{\text{f}}=0.94$ ),<sup>154</sup> using rigorously deoxygenated solutions. Time-resolved emission spectra, obtained using the FS900 instrument, were linearly decomposed into sums of their principle components, i.e. fluorescence of BD and phosphorescence of PtP, in order to

obtain the quantum yields of these emission types individually. Time-resolved phosphorescence measurements were performed using either the FS900 instrument with a xenon flash lamp as the excitation source or an in-house constructed time-domain phosphorometer (see the Chapter 4 for details).

Time-resolved fluorescence measurements were performed by the time-correlated single photon counting method (TCSPC). The TCSPC system consisted of PicoHarp 300 controller, PDL 800-B driver. The samples were excited with a picosecond diode laser (PicoQuant LDH-P-C-485, FWHM~110 ps,  $\lambda_{\text{max}}$ =482 nm, 40 MHz rep. rate), multichannel-plate PMT (Hamamatsu R2809U).

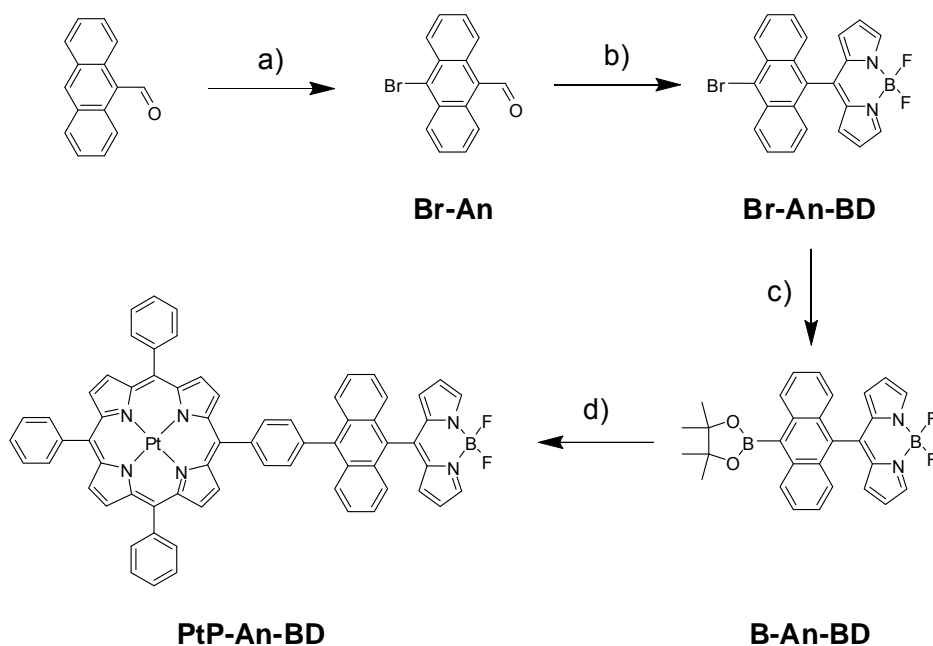
Global fitting was performed using OriginPro 8.5 (OriginLab, MA), MATLAB R2009a (MathWorks, MA), and the freely available software package, Decfit. Decay fitting, spectral deconvolution and analysis of phosphorescence decays were performed using custom written software.<sup>112</sup>

**5.2.3 Nanosecond transient absorption spectroscopy.** The flash-photolysis method was used to study time-resolved absorption in microsecond time-scale. The experiments were carried out with a modified Luzchem laser flash system (mLFP111 prototype from Luzchem Co.) using the second harmonic of Nd:YAG laser, providing 10 ns pulses at 532 nm for excitation. Excitation power density was roughly  $6 \text{ mJ cm}^{-2}$ . A continuous Xe-lamp (Oriel Simplicity Arc Source) was used to provide monitoring light and the signal was recorded with a digitizing oscilloscope (Tektronix, TDS3032B, 300 MHz). The system was controlled with a computer. The sample solutions were deoxygenated by nitrogen bubbling for 15 min prior to the measurements and a nitrogen flow was maintained on the surface of the solution during the measurements.

**5.2.4 Femtosecond transient absorption spectroscopy.** Femtosecond time-resolved transient absorption spectra were collected using a pump-probe technique. The femtosecond pulses of the Ti:sapphire generator were amplified by using a multipass amplifier (GDP-Avesta, Moscow,

Russia) pumped by a second harmonic of the Nd:YAG Q-switched laser (model LF114, Solar TII, Minsk, Belorussia). All measurements were carried out at room temperature. The amplified pulses were used to generate a second harmonic for sample excitation (pump beam) and a white continuum for time-resolved spectrum detection (probe beam). An average of 100 pulses at 10 Hz repetition rate was used to improve the signal-to-noise ratio. The excitation energy was adjusted to the level when sample degradation can be neglected in the end of the measurements. The transient spectra were recorded by a charge coupled device (CCD) detector coupled with a monochromator (Newton DU920N and Shamrock from Andor Technology Ltd., respectively) in the visible and near-infrared ranges. The typical response time of the instrument was 150 fs (fwhm). Initially, the global multiexponential fitting procedure was applied to process the data, but due to highly overlapped spectra of multiple components make it a difficult task to obtain meaningful decay associated curves in many cases. To obtain the kinetic parameters, we fitted the decay curves at the wavelengths where we can assume that the species dominantly contributes to the signal.

**Scheme 5.1.** Synthesis of PtP-An-BD.



a)  $\text{Br}_2/\text{DCM}/\text{heat}$ ; b) i) Pyrrole/DCM/TFA; ii) DDQ/DCM; iii)  $\text{BF}_3 \cdot \text{Et}_2\text{O}/\text{DCM}$ ; c)  $\text{B}_2\text{pin}_2/\text{PdCl}_2(\text{dppf})_2/\text{DMF}$  (Miyaura Boration); d) PtP-Br/ $\text{Pd}_2(\text{dba})_3/\text{tBu}_3\text{P} \cdot \text{HBF}_4/\text{Cs}_2\text{CO}_3/\text{THF}/\text{H}_2\text{O}$  (Suzuki-Miyaura Coupling).

**5.2.5 Synthesis.** The synthetic scheme is summarized in Scheme 5.1. The compound Br-An was synthesized in the same manner as described previously.<sup>155</sup> Brominated An-BD (Br-An-BD) was synthesized by an acid-catalyzed condensation of pyrrole and the corresponding bromo aldehyde, followed by boron complexation with  $\text{BF}_3 \cdot \text{Et}_2\text{O}$ . Miyaura boration was then performed to obtain the boronated An-BD (B-An-BD). B-An-BD was coupled with PtP-Br, which was synthesized as previously described,<sup>153</sup> via Suzuki-Miyaura coupling to produce the compound PtP-An-BD. It turned out that elevated temperature (typically employed for Pd catalyzed Suzuki-Miyaura couplings) caused quick degradation of An-BD. Therefore, Suzuki-Miyaura coupling was performed under the mild condition (room temperature)<sup>156</sup> to avoid the decomposition of An-BD.

**An-BD.** Pyrrole (67 mL, 970 mmol) and 9-anthraldehyde (2.0 g, 9.70 mmol) were added to single-neck round-bottom flask containing a magnetic stir bar. The solution was degassed with a steam

of Argon for 10 min.  $\text{InCl}_3$  (0.21 g, 0.97 mmol) was added and the mixture was stirred at room temperature for 2 hrs. Solid NaOH (1.0 g, 24 mmol) was added to the mixture and stirred for 45 min. The resulting mixture was filtered through a pad of Celite. The filtrate was evaporated in vacuo. The residue was washed with hexanes (10 mL x3). After removal of excess solvents in vacuo, the remaining solid was purified by column chromatography on silica gel (Hexane/DCM/EtOAc=7:2:1) to afford the crude product. Recrystallized from EtOH/ $\text{H}_2\text{O}$  afforded the corresponding dipyrromethane as a solid (480 mg, 1.49 mmol) in 15% yield.  $^1\text{H NMR}$  ( $\text{CDCl}_3$ ,  $\delta$ ): 8.57 (1H, s), 8.06 (2H, d,  $3J = 8.5$  Hz), 7.90 (2H, d,  $3J = 8.8$  Hz), 7.7 (2H, t,  $3J = 1.4$  Hz), 7.46 (2H, ddd,  $3J = 8.3$  and  $6.8$  Hz,  $4J = 1.0$  Hz), 7.37 (2H, ddd,  $3J = 8.3$  and  $6.8$  Hz,  $4J = 1.0$  Hz), 6.24 (2H, dd,  $3J = 4.1$  and  $1.4$  Hz), 6.04 (2H, dd,  $3J = 4.3$  and  $1.0$  Hz); MALDI-TOF ( $m/z$ ): calcd for  $\text{C}_{23}\text{H}_{18}\text{N}_2$ : 322.15; found; 322.09.

The dipyrromethane (400 mg, 1.24 mmol) was dissolved in  $\text{CH}_2\text{Cl}_2$  (45 mL). DDQ (280 mg, 1.24 mmol) was added and the mixture was stirred at room temperature for 30 min. After TLC analysis (Silica, petroleum ether: EtOAc=4:1) confirmed the complete conversion to dipyrins, the mixture was degassed with a stream of Argon for 10 min. DIPEA (1.9 mL, 11 mmol) was added and stirred for another 10 min.  $\text{BF}_3 \cdot \text{Et}_2\text{O}$  was then added dropwise to the mixture. The resulting mixture was stirred for 1 hr. The mixture was then extracted with  $\text{Na}_2\text{SO}_3$ ,  $\text{Na}_2\text{CO}_3$ , and brine. The organic layer was dried with  $\text{Na}_2\text{SO}_4$ . After removal of solvents in vacuo, the remaining solid was purified by column chromatography on silica gel (petroleum ether/EtOAc=4:1) to afford the title compound as a red/green solid (255 mg, 0.69 mmol) in 56% yield (from the dipyrromethane). UV-Vis ( $\text{CH}_2\text{Cl}_2$ )  $\lambda_{\text{max}}$  ( $\log \epsilon$ ): 506 ( $4.7 \pm 0.1$ ) nm. All other spectroscopic data were consistent with the literature values.<sup>157</sup>

**Br-An-BD.** To a solution of Br-An (500 mg, 1.75 mmol) in  $\text{CH}_2\text{Cl}_2$  (25 mL) a solution of pyrrole (6.1 mL, 87.5 mmol) was added dropwise at room temperature under Argon. TFA (30  $\mu\text{L}$ , 0.175 mmol) was added dropwise to the mixture. The mixture was stirred for 1 h. DDQ (400 mg, 1.75 mmol) was added and stirred for another 1 hr. The resulting mixture was extracted with brine

and Na<sub>2</sub>SO<sub>3</sub>. The organic layer was dried with Na<sub>2</sub>SO<sub>4</sub>. After removal of excess solvents in vacuo, the residue was purified by column chromatography on silica gel (Hexane:THF=8:2) to afford the dipyrin as a yellow solid (316 mg, 0.79 mmol) in 45% yield. <sup>1</sup>H NMR (CDCl<sub>3</sub>, δ): 8.61 (2H, dt, 3J = 9.0 Hz, 4J = 0.9 Hz), 7.93 (2H, dt, 3J = 8.8 Hz, 4J = 1.0 Hz), 7.71 (t, 3J = 1.3 Hz), 7.59 (2H, ddd, 3J = 9.0 and 6.5, 4J = 1.3 Hz), 7.41 (2H, ddd, 3J = 8.8 and 6.5, 4J = 1.0 Hz), 6.25 (2H, dd, 3J = 4.3 and 1.5 Hz), 6.02 (2H, dd, 3J = 4.3 and 1.3 Hz); MALDI-TOF (m/z): calcd for C<sub>23</sub>H<sub>15</sub>BrN<sub>2</sub>: 398.40; found; 399.120.

The dipyrin (300 mg, 0.75 mmol) was dissolved in CH<sub>2</sub>Cl<sub>2</sub> (18 mL) and stirred under Argon in the absence of light for 10 min. Triethylamine (1.0 mL, 7.5 mmol) was added into the remaining solid and stirred for another 10 min. BF<sub>3</sub>.Et<sub>2</sub>O was then added dropwise to the mixture. The resulting mixture was stirred for 1 hr. The mixture was then extracted with Na<sub>2</sub>CO<sub>3</sub> and brine. The organic layer was dried with Na<sub>2</sub>SO<sub>4</sub>. After removal of solvents in vacuo, the mixture was purified by column chromatography on silica gel (Hexanes/THF=9:1) to afford title compound as a red/green solid (237 mg, 0.53 mmol) in 70% yield (from the dipyrin). <sup>1</sup>H NMR (CDCl<sub>3</sub>, δ): 8.64 (2H, dt, 3J = 8.7 Hz, 4J = 1.0 Hz), 8.03 (2H, s), 7.84 (2H, dt, 3J = 8.8 Hz, 4J = 0.9 Hz), 7.64 (2H, ddd, 3J = 8.8 and 6.5 Hz, 4J = 1.3 Hz), 7.47 (2H, ddd, 3J = 8.8 and 6.5, 4J = 1.3 Hz), 6.40 (4H, m); MALDI-TOF (m/z): calcd for C<sub>23</sub>H<sub>14</sub>BBrF<sub>2</sub>N<sub>2</sub>: 446.04; found; 446.35.

**B-An-BD.** Br-An-BD (75 mg, 0.168 mmol), bis(pinacolato)diboron (130 mg, 0.503 mmol) and KOAc (49 mg, 0.503 mmol) were dissolved in DMF (6 mL). PdCl<sub>2</sub>(dppf)<sub>2</sub> (28 mg, 0.034 mmol, 20 %), used as a catalyst in this Miyaura coupling reaction, was dissolved separately in DMF (1 mL). The solution of the catalyst was added to the mixture of the reactants, and it was stirred vigorously at 80 °C for 1.5 hrs. The mixture was cooled down. The resulting mixture was passed through the silica pad and eluted with CH<sub>2</sub>Cl<sub>2</sub>. After removal of solvents in vacuo, the remaining solid was purified by column chromatography on silica gel (Hexanes/THF=8:2) to afford the title compound as a red/green solid after removing the solvent and drying the product in vacuum (37 mg, 0.075 mmol) in 35% yield. <sup>1</sup>H NMR (CDCl<sub>3</sub>, δ): 8.41 (2H, dt, 3J = 8.7 Hz, 4J = 1.1 Hz), 8.00

(2H, s), 7.81 (2H, dt, 3J = 8.8 Hz, 4J = 1.0 Hz), 7.51 (2H, ddd, 3J = 8.8 and 6.5 Hz, 4J = 1.3 Hz), 7.40 (2H, ddd, 3J = 8.8 and 6.5 Hz, 4J = 1.3 Hz), 6.40 (2H, dd, 3J = 4.1 and 1.4 Hz), 6.34 (2H, d, 3J = 4.3), 1.64 (12H, s); MALDI-TOF (m/z): calcd for C<sub>29</sub>H<sub>26</sub>B<sub>2</sub>F<sub>2</sub>N<sub>2</sub>O<sub>2</sub>: 494.21; found; 494.15.

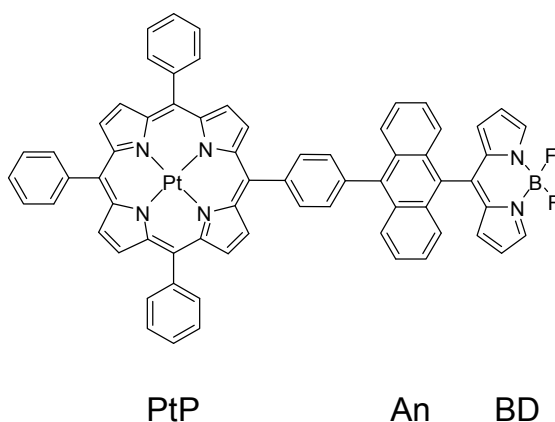
**PtP-An-BD.** A round-bottom flask was charged with PtP-Br (10 mg, 11.3  $\mu$ mol), 4 (6.7 mg, 13.5  $\mu$ mol), tBu<sub>3</sub>P•HBF<sub>4</sub>, (1.3 mg, 4.5  $\mu$ mol) and Cs<sub>2</sub>CO<sub>3</sub> (15 mg, 45.2  $\mu$ mol). The flask was capped with a rubber septum and filled with Argon. THF (3 mL) and H<sub>2</sub>O (20  $\mu$ L) were added *via* syringe through the septum. Pd<sub>2</sub>(dba)<sub>3</sub> (2.0 mg, 20 mol%) was separately dissolved in THF (0.4 mL), then added to the former mixture under Argon. The flask was sealed and the resulting reaction mixture was stirred vigorously at room temperature for 24 hrs. The reaction mixture was then filtered through a pad of Celite and eluted with CH<sub>2</sub>Cl<sub>2</sub>. After removal of solvents in vacuo, the remaining solid was purified by column chromatography on silica gel (Hexanes/THF=8:2) to afford the title compound as an orange solid after removing the solvent and drying the product in vacuum (4.6 mg, 3.9  $\mu$ mol) in 35% yield. <sup>1</sup>H NMR (CDCl<sub>3</sub>,  $\delta$ ): 9.04 (2H, d, 3J = 5.0 Hz), 8.91 (2H, d, 3J = 5.0 Hz), 8.81 (2H, d, 3J = 2.0 Hz), 8.45 (2H, dt, 3J = 8.3 Hz, 4J = 1.0 Hz), 8.19 (8H, m), 8.09 (2H, s), 7.99 (2H, dt, 3J = 8.8 Hz, 4J = 1.0 Hz) 7.89 (2H, d, 3J = 8.3 Hz), 7.78 (9H, m), 7.60 (2H, ddd, 3J = 8.8 and 6.5 Hz, 4J = 1.3 Hz), 7.54 (2H, ddd, 3J = 8.8 and 6.5 Hz, 4J = 1.3 Hz), 6.99 (2H, s), 6.60 (2H, dd, 3J = 4.0 and 1.3 Hz), 6.49 (2H, dd, 3J = 4.3 and 1.8 Hz); UV-Vis (CH<sub>2</sub>Cl<sub>2</sub>)  $\lambda_{\max}$  (log  $\epsilon$ ): 402 (5.6  $\pm$  0.1), 507 (5.0  $\pm$  0.1), 538 (4.0  $\pm$  0.1) nm; MALDI-TOF (m/z): calcd for C<sub>67</sub>H<sub>41</sub>BF<sub>2</sub>N<sub>6</sub>Pt: 1173.31; found; 1173.50.

### 5.3 Results and discussion

**5.3.1 Chromophores.** The chromophores suitable for the photophysical scheme depicted in Fig. 5.1B need to satisfy some energetic requirements as outlined in the Chapter 4.<sup>153</sup> The initially populated excited singlet state of the antenna (<sup>S1</sup>A) must have its energy higher than the energy of the triplet state of the core (<sup>T1</sup>C). The energy of the radical pair state RP, created as a result of the ET, must be higher than that of <sup>T1</sup>C to allow downhill radical recombination CR<sub>T</sub>. We also set

the requirement that  $^S1A$  need lie below the singlet state of the core ( $^S1C$ ) in order to prevent population of  $^S1C$  either directly or *via*  $^S1A \rightarrow ^S1C$  energy transfer(s), competing with ET. These requirements impose the limits for the entire energy cascade, which has to fit within the singlet-triplet gap (2J) of the phosphorescent core. The last requirement however is not crucial for a RP pathway just being operative as long as the rate of ET outcompetes that of  $^S1A \rightarrow ^S1C$  energy transfer(s). It is still important to completely prevent direct excitation of the core for desired applications. In the current study, we designed a molecular system so that the last requirement is not satisfied, testing whether we could observe a RP pathway leading to emissive triplet state by making ET process more favorable than energy transfer. Benniston et al. reported anthracenyl-BD (An-BD) dyad where exciplex-like emission was observed, indicating a possible production of the charge separated state.<sup>157</sup> We conjectured that An-BD can be incorporated in the energy cascade described in Fig. 5.1B by coupling with a suitable triplet core, ultimately leading to the formation of emissive triplet state of the core. For a phosphorescence core, we used PtP as it shows high phosphorescence quantum yield ( $QY_{\text{phos}} \sim 0.1$ ) and its modulability of electrochemical properties. The electrochemical potentials of PtP can be tuned by changing peripheral substituents in the *meso*-aryl rings while they do not affect spectroscopic features of PtP's significantly.<sup>86</sup> This feature gives the desired flexibility of tuning the level of the RP state without affecting the rest of the chromophoric system. It is also synthetically convenient as tetraarylporphyrins with various substitution patterns can be conveniently generated using well-established synthetic protocols.<sup>113, 118</sup> The triad (Chart 5.1) was successfully synthesized and characterized.

**Chart 5.1.** Studied triad PtP-An-BD.



**5.3.2 Steady-state spectroscopy.** The steady-state absorption and phosphorescence spectra of PtP-An-BD are shown in Fig. 5.2. The absorption spectra of the triad are nearly superpositions of the spectra of the individual chromophores, indicating small electronic interactions between PtP and An-BD in their ground and excited electronic states. The emission spectra of the parent An-BD in toluene and DMF are shown in Fig. 5.A1. Exciplex emission spectra could be fitted into the two Gaussian functions in toluene and three Gaussian functions in DMF. The emission spectra of PtP-An-BD are shown in Fig. 5.2C and 5.2D for toluene as well as in Fig. 5.2F and 5.2G for DMF. Assuming that the overall emission is a linear combination of the BD fluorescence, An-BD exciplex, and PtP phosphorescence, we could decompose the spectra into the sums of their components and estimate the corresponding quantum yields (Table 5.1) (see the Chapter 4 for details of decomposition and the Appendix to this chapter for details of analysis).

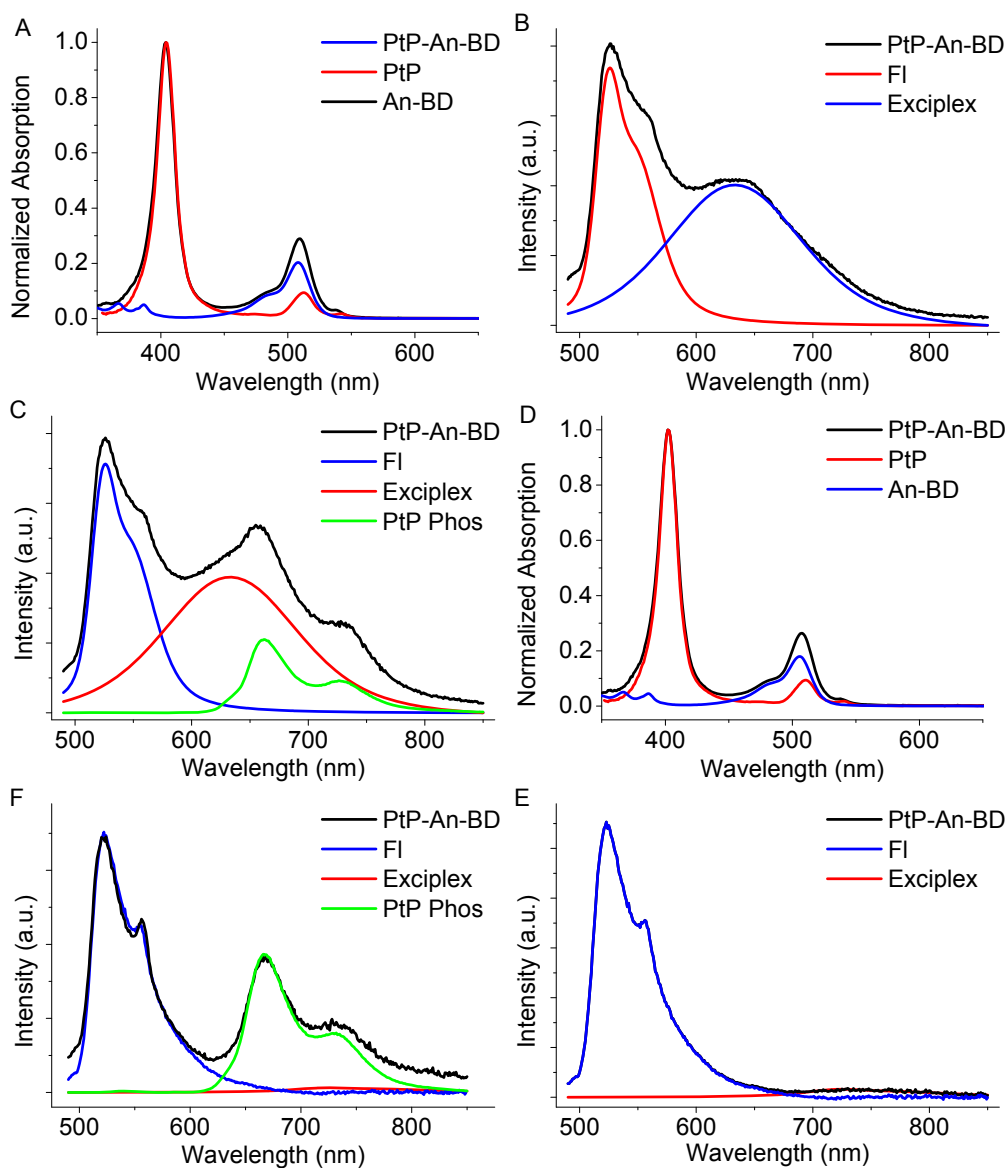


**Figure 5.2.** Absorption and emission spectra of PtP, An-BD, and the triad PtP-An-BD. (A) Normalized absorption spectra in toluene and in DMF (D). (B) Emission spectra of PtP-An-BD acquired in the presence of oxygen in toluene and in DMF (E) and the absence of oxygen in toluene (C) and in DMF (F). Excitation wavelength was 480 nm. The spectra of the components were obtained by linear decomposition.

Phosphorescence quantum yields of the triad were measured upon excitations with two different wavelengths at  $\lambda_{\text{ex}}=410$  nm (~99% of absorption is due to PtP) and at  $\lambda_{\text{ex}}=480$  nm (~80% of absorption is due to BD). Calculated quantum yields with two different wavelengths

yielded two different values. This indicates that phosphorescence occurs not only from the direct excitation of PtP (intramolecular ISC pathway) but also from the excitation of BD unit (RP pathway). We will demonstrate that the latter involves RPs below. We have determined the quantum yields of these two pathways (see the Appendix to this chapter for calculation). The quantum yield of the phosphorescence observed *via* the intramolecular ISC was small;  $\Phi_{\text{phos}} \sim 0.4 \times 10^{-2}$  in both toluene and DMF. They are  $\sim 20$  times lower than those of PtP;  $\Phi_{\text{phos}} \sim 0.10$  in toluene and  $\sim 0.07$  in DMF. The reduction in quantum yields in the triad stems from the efficient triplet energy transfer (TT) from  $^1\text{PtP}$  onto  $^1\text{BD}$  ( $\Delta G \sim -0.18$  eV). The energy transfer might occur first from  $^1\text{PtP}$  onto  $^1\text{An}$  as they are isoenergetic ( $\sim 1.85$  eV). However, since the spectroscopic signature of  $^1\text{An}$  was not observed, we reasoned that the anthracene triplet state merely acts as a bridge. We can safely rule out some other possible deactivation pathways such as the direct quenching of the porphyrin singlet Soret ( $S_2$ ) or Q ( $S_1$ ) states by either energy or electron transfer onto An or BD because both  $S_2 \rightarrow S_1$  internal conversion and  $S_1 \rightarrow T_1$  ISC in Pt porphyrins occur on the femtosecond time scale and the formation of the triplet state from the singlet excited state by intramolecular ISC is almost unity.<sup>125-126</sup> The evidence for TT from  $^1\text{PtP}$  onto  $^1\text{BD}$  was obtained by femtosecond and nanosecond pump-probe spectroscopy (see below). The quantum yield of phosphorescence *via* the RP pathway ( $\Phi_{\text{phos}}^{\text{RP}}$ ) was not so high either but still quantifiable in toluene ( $\Phi_{\text{phos}}^{\text{RP}} \sim 0.17 \times 10^{-2}$ ) but almost nonexistent in DMF ( $\Phi_{\text{phos}}^{\text{RP}} < 0.01 \times 10^{-2}$ ). If we assume that  $\Phi_{\text{phos}}$  is constant regardless of the formation pathways leading to the emissive state, then we can express the quantum yield of this RP pathway as  $\Phi_{\text{phos}}^{\text{RP}} = \Phi_{\text{phos}} \times \phi_{\text{RP}}$  where  $\phi_{\text{RP}}$  is the formation efficiency of the emissive triplet state. Using the determined values shown in Table 5.1, we obtained  $\phi_{\text{RP}} \sim 0.36 \pm 0.1$  in toluene. The quantum yields were similarly measured in other solvents of different polarity. The formation efficiency of the emissive triplet state generally decreases with increasing solvent polarity among the solvents examined (Table 5.A1).

**Table 5.1.** Quantum yields ( $\Phi \times 10^{-2}$ ) of emission at room temperature.

	Solvents	Fluorescence <sup>a,b</sup>	Exciplex <sup>a,b</sup>	Phosphorescence <sup>c</sup>	
				Intramolecular ISC	RP
An-BD	Toluene	$0.11 \pm 0.07^d$	$1.38 \pm 0.06$	-	-
	DMF	$0.05 \pm 0.05$	$0.06 \pm 0.01$	-	-
PtP	Toluene	-	-	$9.9 \pm 0.2$	-
	DMF	-	-	$7.2 \pm 0.5$	-
PtP-An-BD	Toluene	$0.8 \pm 0.2$	$0.8 \pm 0.1$	$0.47 \pm 0.09$	$0.17 \pm 0.02$
	DMF	$0.4 \pm 0.2$	$<0.01^e$	$0.77 \pm 0.2$	$<0.01^e$

<sup>a</sup> The measurements were performed in oxygenated solutions. <sup>b</sup>  $\lambda_{ex}=480$  nm <sup>c</sup> The measurements were performed in deoxygenated solutions. Emission quantum yields were determined relative to the fluorescence of Rhodamine 6G in EtOH ( $\Phi_f=0.94$ ).<sup>154</sup> <sup>d</sup> Benninston et al. reported rather higher value ( $3.1 \times 10^{-2}$ ).<sup>157</sup> <sup>e</sup> The intensities of the emission are too small for accurate determination of the quantum yields.

Another indication of the existence of the RP pathway originated from BD unit comes from the examination of the excitation spectra (Fig. 5.3). In both steady-state and time-resolved excitation spectra ( $\lambda_{em} = 660$  nm – phosphorescence from PtP) showed that excitation at BD leads to emission at this wavelength in toluene, but not in DMF. Convincingly, only emitting species at  $\mu$ s time scale is PtP triplet as the lifetime of exciplex emission is  $<3$  ns in toluene (Table 5.2). Therefore, a non-ordinary pathway exists in the triad, which originates in the antenna singlet state  $S^1$ BD and populates the emissive triplet states of PtP.

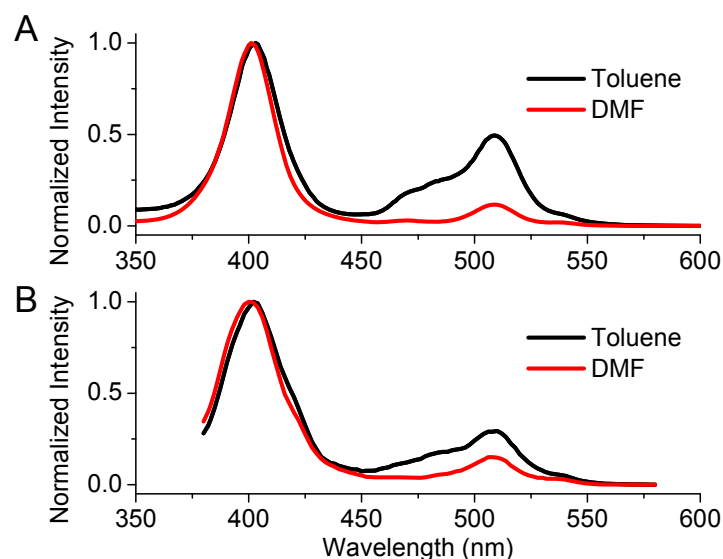


**Figure 5.3.** Excitation spectra of PtP-An-BD. (A) Normalized steady-state excitation spectra of PtP-An-BD ( $\lambda_{em}=660$  nm). (B) Normalized time-resolved excitation spectra of PtP-An-BD ( $\lambda_{em}=660$  nm, 25  $\mu$ s after excitation).

**5.3.3 Energy Levels.** The lowest energy state of a representative PtP, Pt tetraphenylporphyrin (PtTPP) is  $\lambda_{max}\sim 541$  nm, 2.29 eV. The energy of the PtP triplet state, based on its phosphorescence maximum ( $\lambda_{max}=670$  nm, 1.85 eV for PtTPP), is below that of  $S^1$ BD state ( $\lambda_{max} = 506$  nm, 2.45 eV). Redox potentials for PtTPP, anthracene, and BD were determined in DMF and they are +1.20V vs SCE (PtTPP<sup>+</sup>/PtTPP),<sup>86, 121</sup> 1.53V vs SCE (An<sup>+</sup>/An) and -0.70V vs SCE (BD<sup>-</sup>/BD), respectively. Redox potentials of An and BD are close to those reported in An-BD dyad in MeCN.<sup>157</sup> The redox potentials in the triad did not significantly differ from the individual molecules. The energies for the first and the second RPs in DMF are calculated as  $E_{RP1}(\text{PtP-An}^{+\bullet}\text{-BD}^{\bullet-})= 2.15$  eV and  $E_{RP2}(\text{PtP}^{+\bullet}\text{-An-BD}^{\bullet-}) = 1.87$  eV in accordance with the following equation (Rehm-Weller method):<sup>122</sup>

$$E_{RP} = E_{ox}(D) - E_{red}(A) - \frac{e^2}{r_{DA}\epsilon_S} + e^2 \left( \frac{1}{2r_D} + \frac{1}{2r_A} \right) \left( \frac{1}{\epsilon_S} - \frac{1}{\epsilon_{SP}} \right) \quad (\text{Eq. 5.1})$$

where  $E_{ox}(D)$  and  $E_{red}(A)$  are the oxidation and reduction potentials of the donor and acceptor in a high polarity solvent with a static dielectric constant  $\epsilon_{SP}$ , respectively,  $e$  is the charge of the electron,  $r_{DA}$  is the donor-acceptor distance,  $r_D$  and  $r_A$  are the ionic radii, and  $\epsilon_S$  is the static dielectric constant of a solvent with arbitrary polarity. The ionic radii  $r_D=4.8 \text{ \AA}$  and  $r_A=3.4 \text{ \AA}$  are used for the porphyrin cation radical<sup>158</sup> and BD anion radical. The calculated energies for both states are lower than  $S^1BD$  (~2.45 eV) and higher than the energy of  $T^1PtP$  (~1.85 eV) in DMF. The driving force for the respective electron transfer can be calculated by using the equation:

$$\Delta G_{ET} = E_{RP} - E_{00} \quad (\text{Eq. 5.2})$$

where  $\Delta E_{00}$  is the excitation energy of the initially populated state. The calculated driving forces are  $\Delta G_{ET1}=-0.33 \text{ eV}$  and  $\Delta G_{ET2}=-0.25 \text{ eV}$ . However the energy levels of radical pairs in toluene by the above equations give very high values:  $E_{RP1}(PtP-An^{+*}-BD^{-*})=2.63 \text{ eV}$  and  $E_{RP2}(PtP^{+*}-An-BD^{-*})=2.92 \text{ eV}$ . The driving forces are  $\Delta G_{ET1}=0.19 \text{ eV}$  and  $\Delta G_{ET2}=0.28 \text{ eV}$ , respectively. It is well known that Rehm-Weller method overestimates the degree of destabilization of a radical ion pair in low polarity solvents relative to those with high polarity.<sup>159</sup> As we observed exciplex emission in both An-BD and PtP-An-BD, it is reasonable for us to assume that the charge separations occurred to some degree even in toluene. Moreover, as we shall see below, the formation of cation radical of PtP is observed as well, indicating that the second RP is also formed. Trying to determine more reasonable values for the energies of RPs, we use the "spectroscopic method"<sup>60</sup> to estimate the energies of radical pair. The energy of the charge separated state can be estimated by the following equation if the potential surfaces describing the ground and charge separated states of the molecules are assumed similar:<sup>160</sup>

$$E_{RP} = \frac{E_a - E_e}{2} \quad (\text{Eq. 5.3})$$

where  $E_a$  and  $E_e$  are the charge transfer (CT) absorption and emission transitions which we can determine from the absorption maxima in the CT absorption and emission maxima in exciplex

emission. The peaks were not clearly observed in DMF. In the triad, we obtained  $E_a=520$  nm (2.38 eV) and  $E_e=622$  nm (1.99 eV) in toluene (Fig. 5.A2). Employment of Eq. 5.3 gave  $E_{RP1}=2.18$  eV. This value is slightly higher than  $E_{RP1}$  calculated for DMF ( $\sim 2.15$  eV). This is reasonable as destabilization of radical ions in a non-polar solvent is higher than in a polar solvent and we expect higher energy level of RPs in a non-polar solvent. We therefore set  $E_{RP1}=2.18$  eV as the energy of RP state in toluene. We obtained a similar free energy for exciplex energy level (2.17 eV) by fitting exciplex emission spectrum in toluene by using the developed method in the framework of semi-quantum Marcus theory of electron transfer,<sup>161-162</sup> which makes us believe that this value is at least reasonable for the energy level of RP considering charge separation within exciplex is  $\sim 0.97 \pm 0.1$  (see below for the calculation).

Given the energy level of the first RP [PtP-An<sup>δ+</sup>-BD<sup>δ-</sup>], or more precisely, PtP-An<sup>δ+</sup>-BD<sup>δ-</sup>, is assumed to be 2.18 eV in toluene, we can calculate the energy level of the second RP [PtP<sup>+</sup>-An-BD<sup>δ-</sup>] using the following equation,<sup>60</sup>

$$E_{RP2} = E_{RP1} - (E_{ox}(An) - E_{ox}(PtP)) + \frac{e^2}{\epsilon_S} \left( \frac{q^2}{r_{RP1}} - \frac{1}{r_{RP2}} \right) \quad (\text{Eq. 5.4})$$

where  $E_{ox}(An)$  and  $E_{ox}(PtP)$  are the oxidation potentials of anthracene and PtP, and  $r_{DA1}$  and  $r_{DA2}$  are the donor-acceptor distances for the first and the second RPs,  $q$  is the fractional degree of charge separation within An<sup>δ+</sup>-BD<sup>δ-</sup>. The distances  $r_{RP1}$  and  $r_{RP2}$  were estimated to be 4.8 and 15 Å respectively based on the optimized structure with density functional theory (DFT) using Becke's<sup>163</sup> three parameter hybrid functional with Lee, Yang, and Parr<sup>164</sup> correction functional (B3LYP) and the 6-31G basis set as implemented in Q-Chem (4.01).<sup>165</sup> We used Zn porphyrin instead of Pt porphyrin for the sake of computational costs, assuming that the replacement of metal ions do not change the molecular distance significantly. Based on the analysis of emission spectra in various solvents of different polarity, Benniston et al. determined the dipole moment ( $\mu_{EX}$ ) of the exciplex as  $22.5 \pm 2.2$  D.<sup>157</sup> The effective distance ( $r_{EX}$ ) across which the charge separation occurs within An<sup>δ+</sup>-BD<sup>δ-</sup> can be calculated as  $r_{EX}=\mu_{EX}/4.8=4.7 \pm 0.5$  Å if the full charge

transfer occurs ( $q=1$ ). Then, the fractional degree of charge separation can be calculated as  $q=r_{EX}/r_{RP1}=4.7/4.8=0.97 \pm 0.1$ . Using the redox potentials for anthracene and PtP reported above, we can obtain  $E_{RP2} = 2.56$  eV (with the lowest and highest limits being 2.33-2.63 eV). We assumed the difference between the oxidation potentials of anthracene and PtP are the same in toluene and DMF. The calculated results indicate the change in Coulomb energy, required to move a charge the additional distance, is higher than the differences in oxidation potentials between anthracene and PtP, resulting in  $E_{RP2} > E_{RP1}$  in toluene. Admittedly, the error associated with determination of radical pairs in toluene is rather big. Nevertheless, the important point here is that  $E_{RP1}$  and  $E_{RP2}$  in both toluene and DMF are higher than  ${}^T1PtP$  ( $\sim 1.85$  eV). The energies of all other possible RPs are much higher than  ${}^S1BD$  even in DMF; the calculated energies of  $[PtP^{\bullet-}An-BD^{+\bullet}]$  and  $[PtP^{\bullet-}An^{+\bullet}-BD]$  are  $\sim 2.9$  and  $3.0$  eV, respectively and we can safely exclude the involvement of these species in the photophysical pathways after excitation of  ${}^S1BD$  ( $\sim 2.45$  eV). Most importantly, the spectroscopic data do not show formations of these RPs.

**5.3.4 Evolution and decay of the radical pair states.** To elucidate the reasons of solvent dependence of the phosphorescence quantum yield in the triad, we used time-resolved spectroscopy techniques to identify the electron and energy pathways within the dyad and the triad in a polar solvent (DMF) and a non-polar solvent (toluene).

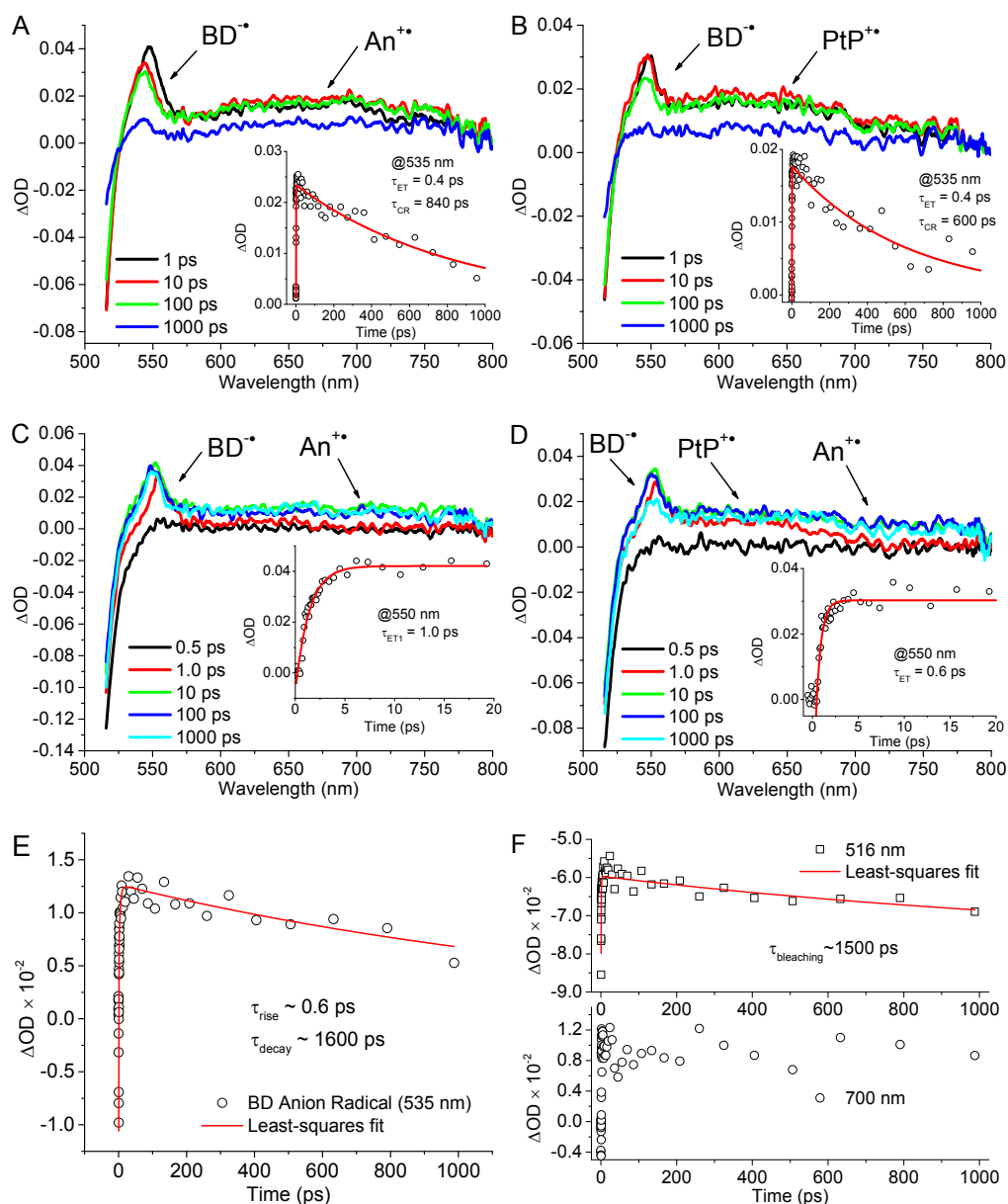


**Figure 5.4.** Early time evolution of An-BD and PtP-An-BD upon photo excitation at 490 nm. (A) FSTA spectra of An-BD in DMF, (B) PtP-An-BD in DMF, (C) An-BD in toluene, and (D) PtP-An-BD in toluene at selected times after excitation by a femtosecond laser pulse: FWHM=150 fs,  $\lambda_{max}$ =490 nm. The insets show the time evolutions at selected wavelengths. (E) Time evolutions of PtP-An-BD at 535 nm in toluene ( $\lambda_{ex} = 490$  nm). The lines show the single exponential fits. (F) Time evolutions of An-BD at 516 nm and 700 nm in toluene ( $\lambda_{ex} = 490$  nm).

First, we discuss the dyad and the triad in DMF. FSTA with photoexcitation at BD in the triad ( $\lambda_{ex} \sim 490$  nm, FWHM=150 fs, at this wavelength BD absorbance contributes > 80%) shows that photoinduced electron transfer quickly occurs from  $S^1$ BD (< 1ps), leading to the formation of the first RP [PtP-An $^{+\bullet}$ -BD $^{\bullet-}$ ] as a singlet state based on the spin selection rule. Similar fast charge separations were observed previously in BD based molecular dyads.<sup>166-167</sup> The RP formation is presumably preceded by the formation of exciplex state [PtP-An $^{\delta+}$ -BD $^{\delta-}$ ] and they might exist in equilibrium (Fig. 5.4A). The observed signature of BD anion radical well corresponds to the reported signature of BD anion radical.<sup>168</sup> The formation of the first RP is then followed by the second ET to produce the second RP [PtP $^{+\bullet}$ -An-BD $^{\bullet-}$ ], again as a singlet state. The spectrum at 10 ps is dominated by the signatures of BD $^{\bullet-}$  ( $\lambda_{max} \sim 545-550$  nm) and PtP $^{+\bullet}$  (broad absorption band around 600 nm<sup>121</sup>). Although a clear signature of anthracene cation radical (the reported highest absorption peak is at 720 nm<sup>169-171</sup> and broad and less intense absorption up to  $\sim 400$  nm<sup>169</sup>) was not observed, the rise time of PtP $^{+\bullet}$  ( $\tau_{ET2} = 1.5$  ps) is somewhat slower than that of BD $^{\bullet-}$  ( $\tau_{ET1} = 0.4$  ps), indicating that PtP $^{+\bullet}$  is produced after the formation of BD anion radical. It is in align with the observation that the exciplex emission was quenched in DMF indicating the existence of deactivating pathway of exciplex [PtP-An $^{\delta+}$ -BD $^{\delta-}$ ] and the associated RP [PtP-An $^{+\bullet}$ -BD $^{\bullet-}$ ], which turns out to be the second ET. The second RP decays within 1 ns to predominantly form the ground state ( $\tau_{CR} = 600$  ps). For the decay of BD anion radical, we probed the transient absorption kinetics at 535 nm, where BD anion radical predominantly contributes to the signal: namely the spectrum of  $T^1$ BD has zero absorption at this wavelength. Ground state bleaching (GSB) of BD recovers at slightly longer rate ( $\tau \sim 1000$  ps) (Fig. 5.A3A) while PtP cation radical peak as well as the peak in the redder region (700-720 nm –  $T^1$ PtP<sup>119</sup> and  $T^1$ BD<sup>172-173</sup> have absorption in this region if formed) decay at the similar rate as the BD anion radical ( $\tau \sim 600$  ps). This supports the formation of the triplet states is negligible, which is consistent with the result that a photon absorption by BD does not result in phosphorescence from PtP in DMF. The reason of the absence of triplet formation is discussed below. The rate of the first ET process in the triad

PtP-An-BD is similar to that found in the dyad An-BD ( $\tau_{ET1} = 0.4$  ps) where the RP recombines the ground state within 1 ns as well (Fig. 5.4B). In the dyad case, a clear signature of anion radical (broad absorption at 700-720nm) was observed whose assignment agrees with the reported absorption spectrum of anthracene cation radical. BD anion radical, anthracene cation radical, and BD GSB recovery decay at the rate of  $\sim 870$  ps (Fig. 5.A3B) which is similar to the lifetime of the exciplex ( $\tau \sim 850$  ps). No clear sign of the triplet formation is observed. It is worthwhile noting here that excitation of anthracene unit in the An-BD dyad ( $\lambda_{ex} = 385$  nm) results in ultrafast energy transfer from anthracene to BD ( $\tau \sim 0.5$  ps, see Fig. 5.A4). This supports the previous report<sup>157</sup> that no anthracene fluorescence was observed even at low temperature and efficient energy transfer occurs from anthracene onto BD. Note, the subsequent decay process are identical to those observed with  $\lambda_{ex} = 490$  nm (the same is true for the case in toluene).

Next, we look at electron and energy dynamics of the dyad and the triad in toluene. In the dyad, the rate of the formation of RP is slightly slower than in DMF, but still fast ( $\tau \sim 1.0$  ps, Fig. 5.4C). The clear difference was observed in the decay process. BD anion radical, probed at 535 nm, decays at longer time constant (Fig. 5.A5A,  $\tau \sim 3.0$  ns) than that in DMF ( $\tau \sim 840$  ps). The decay time is closely matched with the exciplex lifetime ( $\tau \sim 2.8$  ns). The red region (700-720 nm) does not show the sign of decay where the spectra of the anthracene radical cation and BD triplet state are overlapped. An interesting observation was made in the region of BD GSB: BD GSB peak does not show a sign of recovery. Rather it shows further bleaching (Fig. 5.A5B). This can be attributed to the fact that this region is overlapped with the anthracene cation radical absorption.<sup>169</sup> We can assign this decay to the formation of the BD triplet state. When the RP recombines onto the triplet state, we expect to have the same degree of BD GSB and the absorbance in these region further decreases because the anthracene radical cation disappears. On the other hand, when the RP recombines either onto the ground state or the triplet state of anthracene, we would expect to see the increase in this region, which is not the case. The rate of this further decay was determined as  $2.6 \times 10^9$  s<sup>-1</sup> ( $\tau \sim 380$  ps). The spectrum of NSTA at  $\sim 50$  ns is

dominated by  $T^1$ BD (Fig. 5.A6). These observations support that the radical pair recombines onto the triplet state of BD. While it is still possible that anthracene triplet state is also populated given  $T^1$ An $\rightarrow$  $T^1$ BD, no clear triplet-triplet absorption peaks of  $T^1$ An was observed.  $T^1$ An has characteristic triplet-triplet absorption peaks at 420-430 nm with  $\epsilon_T > 40000 \text{ M}^{-1}\text{cm}^{-1}$  and 520 nm<sup>174-175</sup> while  $T^1$ BD has the weak triplet-triplet absorption peak at  $\sim 700$  nm with  $\epsilon_T \sim 2000 \text{ M}^{-1}\text{cm}^{-1}$ .<sup>172, 176</sup> As the weak triplet-triplet absorption of  $T^1$ BD dominates the spectrum (Fig. 5.4C), we could conclude that  $T^1$ BD is preferentially produced by charge recombination. Even if  $T^1$ An is initially populated, triplet-triplet energy transfer from  $T^1$ An $\rightarrow$  $T^1$ BD quickly occurs to populate  $T^1$ BD like in the case of the triad's  $T^1$ PtP $\rightarrow$  $T^1$ BD (see below).

For the triad in toluene, the first RP presumably forms as  $^S[\text{PtP}^{+\bullet}\text{-An-BD}^{\bullet-}]$  within 1.0 ps (Fig. 5.4D). The spectrum at 1.0 ps time point mainly showed the absorption signatures of BD anion radical and PtP cation radical. This is followed by the appearance of An $^{+\bullet}$  at the time constant of  $< 1$  ps. Although the accurate determination of the second step is hampered due to the overlap of the spectra, the peak of PtP cation radical does not disappear and the spectrum at 10 ps time point showed the existence of all three radicals. These indicate that the two RPs  $[\text{PtP}^{+\bullet}\text{-An-BD}^{\bullet-}]$  and  $[\text{PtP-An}^{+\bullet}\text{-BD}^{\bullet-}]$  may coexist. The peak of BD anion radical decays at  $\sim 1.6$  ns. The observed decay rate of BD anion radical ( $k_{\text{obs}} \sim 1/1.6 \text{ ns}^{-1}$ ) is contributed by the decays of two RPs  $[\text{PtP}^{+\bullet}\text{-An-BD}^{\bullet-}]$  and  $[\text{PtP-An}^{+\bullet}\text{-BD}^{\bullet-}]$ . Interestingly, the observed decay rate is slower than the An-BD exciplex emission lifetime in the triad ( $k_{\text{exc}} \sim 1/0.61 \text{ ns}^{-1}$  – the emission decay is best fitted with double exponential curves with the shorter lifetime of 0.61 ns has 75% contribution and the longer lifetime of 1.81 ns has 25% contribution based on intensity). We assign the observed rate ( $k_{\text{obs}}$ ) as the lifetime of the RP  $[\text{PtP}^{+\bullet}\text{-An-BD}^{\bullet-}]$ , assuming that the RP  $[\text{PtP-An}^{+\bullet}\text{-BD}^{\bullet-}]$  decays at the same rate constant as the shorter component of the exciplex lifetime. The existence of longer component in exciplex lifetime might indicate that the two RPs exist in equilibrium. Contrary to BD anion peak, the redder region in the FSTA spectra (600-800 nm) does not show a sign of decay (Fig. 5.4F). This is a clear contrast from the case in DMF where we observed the decay in this

region (Fig. 5.A3A). Similar to the dyad in toluene, BD GSB region in the triad also showed further bleaching up to 1 ns which can be attributed to the formation of the triplet state at the rate constant of ~1.5 ns (we globally fitted the 515-525 nm region by fixing the first rise time at 0.6 ps which corresponds to the first ET process). This is close to the time constant of the observed decay of BD anion radical [PtP<sup>+</sup>\*-An-BD<sup>-</sup>\*]. These observations suggest that the decay of this RP leads to the formation of the triplet state. Presumably, <sup>T1</sup>PtP forms first and then triplet energy transfer occurs onto <sup>T1</sup>BD based on the results of phosphorescence quantum yields and FSTA results upon photo-excitation of PtP (see below).

**5.3.5 Triplet formation through radical pairs.** Combined spectroscopic studies above showed that triplet formations in both An-BD and PtP-An-BD highly depend on solvent polarity. In this section, we would like to clarify the mechanism leading to the triplet formation. First, we will examine the dyad An-BD. <sup>T1</sup>BD formation was observed in toluene at the rate of 380 ps, but not in DMF. BD triplet formation undoubtedly is RP origin as FSTA data shows. We can safely exclude the intramolecular ISC within BD that is hundreds ns to μs time scale<sup>177</sup> and outcompeted by picoseconds' ET processes in the studied dyad. Based on spectroscopic observation of RP signatures, we argue that the triplet formation proceeds through the RP state. Implication of "triplet charge transfer state" in local triplet formation was reviewed in the article by Verhoeven.<sup>178</sup> There are mainly two mechanisms to populate local triplet states from the singlet RP. One is *via* the spin-orbit induced intersystem crossing (SO-ISC) and the other is *via* RP-ISC. Among these, we conclude that the local triplet state formation occurs through SO-ISC which bypasses triplet RP formation and local triplet state forms directly from singlet RP: <sup>S</sup>[An<sup>+</sup>\*-BD<sup>-</sup>\*] → <sup>T1</sup>BD. SO-ISC is known to be highly orbital-dependent on the mutual orientation of the participating molecular orbitals of the electron donor-acceptor pairs and the resulting triplet state.<sup>179-180</sup> Okada et al, first proposed that an approximately perpendicular orientation of the donor and acceptor molecular orbitals enhanced the rate of SO-ISC.<sup>179</sup> This idea garners the experimental evidences over the past two decades. Notable electron donor/acceptor examples include zinc porphyrin/tetracyano-naphthoquinodimethane,<sup>181</sup> and phenothiazine/perylene-diimide systems<sup>130, 182</sup> all studied by

Wasielowski et al. and arene/10-methylacridinium system studied by van Willgen et al.<sup>183</sup> The latter system is particularly relevant to our study. Arene is attached to 9-position of 10-methylacridinium where the dihedral angle between the two aromatic planes is  $\sim 90^\circ$  for the electronic ground state structures. Calculations also show that energy minima occur at a dihedral angle close to  $\sim 90^\circ$  (the angle ranges from  $70-110^\circ$  depending on arene).<sup>183-184</sup> In our case, the dihedral angle found in An-BD is  $\sim 81.5^\circ$  (crystal structure) and  $85.5^\circ$  (DFT calculation).<sup>157</sup> Similar triplet formation of BODIPY by charge recombination and its solvent dependency was observed in quinone-BODIPY dyad although the exact mechanism was not clarified.<sup>166</sup>

The other mechanism involves the formation of triplet RP and recombines onto the local triplet state:  $S_1[\text{An}^{+\bullet}\text{-BD}^{\bullet-}] \rightarrow T_1[\text{An}^{+\bullet}\text{-BD}^{\bullet-}] \rightarrow T_1\text{BD}$ . Singlet-triplet interconversion within radical pair (RP-ISC) can proceed either by coherent mixing driven by Zeeman and hyperfine coupling (S- $T_0$ ) and/or by simple spin relaxation. In organic molecules the rate of hyperfine-induced mixing is typically in the range of  $10^8\text{-}10^9\text{ s}^{-1}$  ( $\sim 1\text{-}10\text{ ns}$ )<sup>7, 185</sup> when the singlet-triplet splitting or exchange integral ( $2J$ ) is on the order of the hyperfine interactions. In An-BD, exchange integral  $2J$  is expected to be larger than ordinary hyperfine coupling ( $\sim 0.001\text{ cm}^{-1}$ ) within such a short distance ( $4.8\text{ \AA}$ ) and this will effectively block RP-ISC in the absence of magnetic field.<sup>183</sup> While incoherent mixing by relaxation mechanism can still occur in the absence of magnet field,<sup>64, 186-188</sup> its rate is on the order of microseconds. Considering the lifetime of the RP ( $\tau \sim 2\text{ ns}$ ), the relaxation process is unlikely to make a major contribution in our system. Thus, we conclude that this pathway does not contribute significantly in our system. While the exact discrimination may require the use of time-resolved EPR spectroscopy, we think that the SO-ISC pathway is the dominant pathway in the dyad.

Similar arguments can be applied to the triad where radical pairs recombine onto the emissive triplet state  $T_1\text{PtP}$ . We reasoned that SO-ISC pathway is the dominant one in the triad as well. As the plane of porphyrin and that of BD are perpendicular, similar to An-BD, we think SO-ISC pathway is also favored for the triplet formation. Magnetic field effect on phosphorescence

from PtP in the triad was not observed in toluene at room temperature (up to 1T, data not shown), which partially supports the SO-ISC pathway.<sup>182, 189</sup> The hyperfine induced RP-ISC pathway might exist to some extent. Regardless of the exact pathways taken, we may say that the lifetime of the radical pair is critical for emissive triplet formation. A formation of any triplet states was not spectroscopically observed in DMF. Given that the energy of the second RP [PtP<sup>•+</sup>-An-BD<sup>•</sup>] is still higher than emissive triplet state <sup>T1</sup>PtP as well as dark triplet states <sup>T1</sup>An and <sup>T1</sup>BD, the reason for not observing triplet formation may be attributed to the short lifetime of RPs.

Our conclusion of involvement of RPs leading to the emissive triplet state in the triad can be further augmented by excluding other possible pathways. Energy transfer processes are much less likely. First, the direct singlet-triplet energy transfer <sup>S1</sup>BD→<sup>T1</sup>PtP is spin-forbidden. Secondly, spin-allowed singlet-singlet energy transfer from <sup>S1</sup>RhB<sup>+</sup> to populate <sup>S1</sup>PtP is down-hill and plausible ( $\Delta E_{00}(\text{S1BD})=2.44$  eV and  $\Delta E_{00}(\text{S1PtP})=2.29$  eV), yet we can rule out this pathway based on the following arguments. One mechanism of singlet energy transfer is through bond energy transfer including Dexter type energy transfer. This particular reaction type is highly unlikely to proceed because of the existence of anthracene unit between BD and PtP, whose singlet energy level ( $\Delta E_{00}(\text{S1An})=3.20$  eV) is much higher than that of <sup>S1</sup>BD, thus acting as an effective energy barrier. It is worth noting that an efficient and ultrafast energy transfer (<1 ps) from anthracene to BD through bond energy transfer has been reported in similar compounds collectively called “anthracene-BODIPY cassettes”.<sup>190</sup> Through-space ultrafast energy transfer is also observed in anthracene-BODIPY dyad where through-bond energy transfer is effectively blocked.<sup>191</sup> We also observed ultrafast energy transfer from <sup>S1</sup>An to <sup>S1</sup>BD in the dyad due to Dexter type energy transfer (see above). These results also suggest that energy transfer in the opposite direction (<sup>S1</sup>BD→<sup>S1</sup>PtP) overcoming the energy barrier of <sup>S1</sup>An is not likely to occur. The other mechanism of singlet energy transfer is through space based on dipole-dipole interaction (or Förster energy transfer).<sup>192-193</sup> This process can be ruled out by the structural considerations. Calculated Förster energy transfer rate is >10<sup>3</sup> times smaller than any other observed rate because of the dipole

orientation factor,  $\kappa^2$ , is close to zero in the triad (see the Appendix to this chapter for the details and the Appendix A.1 for the MATLAB calculation code). Although a pure dipole-dipole interaction may not be applicable in this short distance ( $r \sim 15 \text{ \AA}$ ), an example is known in anthracene-porphyrin based system in which dipole-dipole energy transfer is effectively quenched based on the geometry where the distance is  $< 10 \text{ \AA}$ .<sup>194</sup> Based on these considerations, we can confidently conclude that the SO-ISC pathway is the most probable and most consistent with available spectroscopic data.

**5.3.6 Intramolecular ISC and triplet-triplet energy transfer.** In this section, we examine the energy dynamics after population of triplet state of PtP. Direct excitation of PtP ( $\lambda_{\text{ex}}=415 \text{ nm}$ , at this wavelength PtP absorbance contributes  $> 99 \%$ ) in the triad leads to the population of  $^{\text{S1}}\text{PtP}$  and subsequent intramolecular ISC to produce  $^{\text{T1}}\text{PtP}$  within a picosecond, followed by the TT energy transfer onto  $^{\text{T1}}\text{BD}$  at 46 ps both in toluene and DMF (Fig. 5.5). It appears that the rate of TT at this short distance is insensitive to solvent polarity. The spectrum at 1 ns (the slowest by FSTA in our experiment) looks identical to those at  $\sim 100\text{-}300 \text{ ns}$  probed by NSTA ( $\lambda_{\text{ex}} = 532 \text{ nm}$ , Fig. 5.A7). This fast energy transfer effectively quenches PtP phosphorescence as reflected on the measured quantum yield of phosphorescence:  $\sim 20$  times less than those of the parent PtP. Interestingly, we still observe phosphorescence decay at  $\mu\text{s}$  time scale (Fig. 5.A8), which is explained by reversible TT energy transfer. The energy levels of the triplet states of the two molecules are  $^{\text{T1}}\text{PtP}=1.85 \text{ eV}$  and  $^{\text{T1}}\text{BD}= 1.68 \text{ eV}$ , the latter of which was determined by phosphorescence spectrum of An-BD in toluene at 77K (Fig. 5.A9). While the energy gap is large ( $\Delta G \sim 0.17 \text{ eV}$ ), relatively fast back energy transfer ( $< 1 \mu\text{s}$ , see the Appendix to this chapter for calculations) enables establishing energy pooling between  $^{\text{T1}}\text{PtP}$  and  $^{\text{T1}}\text{BD}$ . We thus conclude that the observed phosphorescence emission in the triad stems from the back energy transfer from  $^{\text{T1}}\text{BD}$ . The lifetimes of phosphorescence roughly correspond to the lifetime of  $^{\text{T1}}\text{BD}$  observed in NSTA (Fig. 5.A5), which is in the range of some reported values of  $^{\text{T1}}\text{BD}$  in similar compounds.<sup>173</sup>

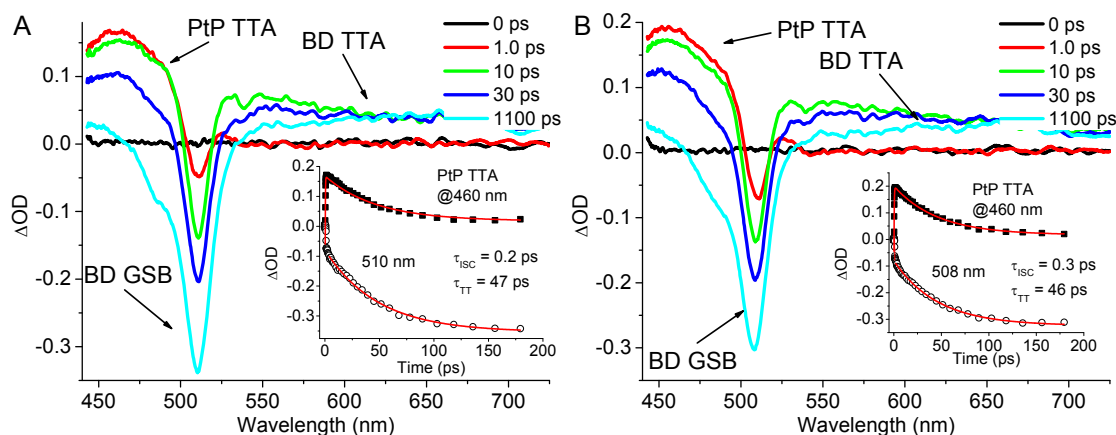


**Figure 5.5.** Time evolution of PtP-An-BD upon photo excitation at 415 nm. (A) FSTA spectra of PtP-An-BD in toluene and (B) in DMF at selected times after excitation by a femtosecond laser pulse: FWHM=150 fs,  $\lambda_{\text{max}}=415$  nm. The insets show the time evolutions at selected wavelengths. TTA stands for triplet-triplet absorption.

**5.3.7 Energy and electron transfer dynamics.** The complete diagrams describing the energy and electron transfer pathways in the studied triad PtP-An-BD in two different solvents are shown in Fig. 5.6 and those in the dyad An-BD are shown in Fig. 5.A10. The corresponding rate constants are summarized in Table 5.2. While most of the rate constants were available from the experimental data, dashed lines in the figures are the routes where the exact pathways are hard to determine. Namely,  $k_{\text{ET1}}$  in Fig. 5.6A may represent the rate constant of ET from  $S^1\text{BD}$  or from the RP  $^S[\text{PtP}^{+\bullet}\text{-An-BD}^{\bullet*}]$ , both of which leads to the formation of the RP  $^S[\text{PtP-An}^{+\bullet}\text{-BD}^{\bullet*}]$ . Nevertheless, we can conclude that the dominant pathway occurring in the triad upon excitation of BD in DMF is the following:  $\text{PtP-An-}S^1\text{BD} \rightarrow \text{PtP-An}^{\delta+}\text{-BD}^{\delta-}$  (exciplex)  $\rightarrow \text{PtP-An}^{+\bullet}\text{-BD}^{\bullet*}$  ( $^S\text{RP1}$ )  $\rightarrow \text{PtP}^{+\bullet}\text{-An-BD}^{\bullet*}$  ( $^S\text{RP2}$ )  $\rightarrow \text{PtP-An-BD}$  (ground state). On the other hand, the pathway occurring in toluene is the following:  $\text{PtP-An-}S^1\text{BD} \rightarrow \text{PtP-An}^{\delta+}\text{-BD}^{\delta-}$  (exciplex)  $\rightarrow \text{PtP-An}^{+\bullet}\text{-BD}^{\bullet*}$  ( $^S\text{RP1}$ )  $\rightarrow \text{PtP}^{+\bullet}\text{-An-BD}^{\bullet*}$  ( $^S\text{RP2}$ )  $\rightarrow {}^1\text{PtP-An-BD} \rightarrow \text{PtP-An-}^1\text{BD} \rightarrow \text{PtP-An-BD}$  (ground state).

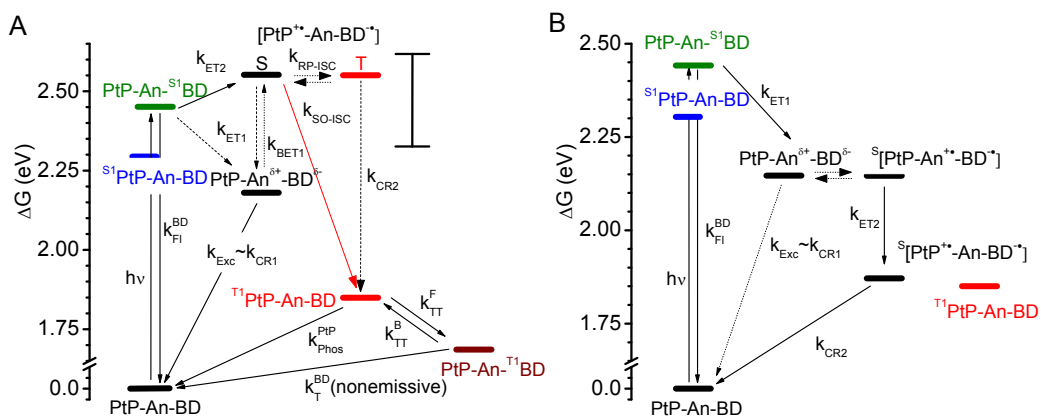


**Figure 5.6.** Pathways occurring in PtP-An-BD triad upon excitation of BD. (A) in toluene and (B) in DMF. The arrows indicate processes whose rate constants were estimated from the spectroscopic measurements. Dashed black line is the route we cannot completely exclude. Dotted lines indicate the routes for which the rate constants were not experimentally obtained.  $k_{TT}$  is the rate constant for the TT energy transfer. The big arrow next to the RP [PtP<sup>+</sup>-An-BD<sup>\*</sup>] state indicates the uncertainty of its energy level.

**Table 5.2.** Rate constants ( $s^{-1}$ ) associated with the pathway displayed in Fig. 5.6 and Fig. 5.A10.<sup>a</sup>

Solvent		$k_{ET1}$ $\times 10^{12}$	$k_{ET2}$ $\times 10^{12}$	$k_{Exc}$ $\times 10^9$	$k_{CR1}$ or $k_{CR2}$ $\times 10^9$	$k_{SO-ISC}$ $\times 10^9$	$K_{phos}$ $\times 10^4$	$k_{TT}^F$ $\times 10^{10}$	$k_{TT}^B$ <sup>b</sup> $\times 10^7$
PtP-An-BD	Toluene	-	$1.7 \pm 1.0$	$1.64 \pm 0.02^{c,d}$ $0.55 \pm 0.06^{c,d}$	-	$0.55-0.67^e$	$2.70 \pm 0.07$	$2.17 \pm 0.05$	$2.7 \pm 0.3$
	DMF	$2.5 \pm 0.2$	$0.7 \pm 0.3$	NA <sup>f</sup>	$1.7 \pm 0.3$	-	$2.08 \pm 0.04$	$2.17 \pm 0.05$	$2.7 \pm 0.3$
An-BD	Toluene	$1.0 \pm 0.2$	-	$0.36 \pm 0.02^d$	--	$2.6 \pm 0.2$	-	-	-
	DMF	$2.5 \pm 0.2$	-	$1.2 \pm 0.1^g$	$1.1 \pm 0.2$	-	-	-	-
PtP	Toluene	-	-	-	-	-	$1.59 \pm 0.02$	-	-
	DMF	-	-	-	-	-	$1.92 \pm 0.04$	-	-

<sup>a</sup> All the constants except for emissions and  $k_{TT}^B$  were estimated by FSTA. The rate constants of exciplex emission and phosphorescence emission were determined by TCSPC ( $\lambda_{ex} = 485$  nm) method and in-house phosphorometer ( $\lambda_{ex} = 510$  nm). <sup>b</sup> The rate of back triplet-triplet energy transfer was determined by the Eq. A3 (see the Appendix to this chapter). <sup>c</sup> Exciplex decay is best fitted with double exponential decay. Based on intensity, the shorter component contributes 75% and the slower one contributes 25%. <sup>d</sup> Probed at 625 nm. <sup>e</sup> The upper limit comes from FSTA data and the lower limit comes from the luminescence measurement. <sup>f</sup> Exciplex emission from PtP-An-BD is too weak to determine its lifetime confidently. <sup>g</sup> Probed at 725 nm.

## 5.4 Conclusions

We have demonstrated the incorporation of the RP in the photophysical pathway leading to phosphorescent triplet state in the newly synthesized PtP-An-BD triad. Photoexcitation of BD leads to the formation of the RP, PtP<sup>+</sup>-An-BD<sup>-</sup>, initially as a singlet. In a nonpolar solvent, the lifetime of this RP is long enough for the RP to recombine into emissive triplet state of PtP with ~20-40% efficiency, presumably through the spin-orbit intersystem crossing. On the other hand, in a polar solvent, this RP decays quickly by a singlet charge recombination, which prevents the formation of emissive triplet state. While the influence of RP's lifetime on charge recombination into dark triplet states are known, our demonstration on emissive triplet state adds further evidence to the possibility of controlling emissive excited triplet states through the RP's spin dynamics.

## 5.5 Appendix

### 5.5.1 Quantum yield calculations

The quantum yields of phosphorescence from PtP in the triad by the two different pathways were determined in the following way. Assuming that excitation of PtP and An-BD units take the different pathways leading to phosphorescence of PtP with the distinct quantum yields, the apparent quantum yields ( $\Phi_{ap}$ ) with one excitation wavelength can be represented as:

$$\Phi_{ap}(\lambda) = \alpha\Phi_{PtP}(\lambda) + \beta\Phi_{An-BD}(\lambda) \quad (\text{Eq. 5.A1})$$

where  $\alpha$  and  $\beta$  are linear coefficients, and  $\Phi_{PtP}(\lambda)$  and  $\Phi_{An-BD}(\lambda)$  are the individual quantum yields of the pathways from photon absorbance by PtP and An-BD, respectively. Measurements of apparent quantum yields with two different wavelengths that have two different ratios of PtP and An-BD absorbance allows us to determine  $\Phi_{PtP}$  and  $\Phi_{An-BD}$  by solving a system of linear equations.

**Table 5.A1.** Quantum yields ( $\Phi \times 10^{-2}$ ) of emission at room temperature. Uncertainties are  $\pm 10\%$ .

	PtP		PtP-An-BD		
	Dielectric Constant	Intramolecular ISC	Intramolecular ISC	RP	$\Phi_{RP}$
Benzene	2.28	10.0	0.84	0.21	0.25
Toluene	2.38	9.9	0.47	0.17	0.36
Dichlormethane	9.08	8.0	0.6	0.07	0.12
Benzonitrile	25.0	9.9	0.8	0.06	0.08
Dimethylformamide	38.3	7.2	0.77	<0.01	<0.01

### 5.5.2 Calculations of the rate of back triplet-triplet energy transfer

When the two states are in equilibrium whose energies are separated by the free energy difference  $\Delta G$ , then  $\Delta G$  can be calculated as:

$$\Delta G = -RT \ln(k_{TT}^F/k_{TT}^B) \quad (\text{Eq. 5.A2})$$

where  $\Delta G$  is the free energy difference between the two triplet states,  $R$  is the gas constant,  $T$  is the temperature, and  $k_{TT}^F$  and  $k_{TT}^B$  are the rate constants of forward and backward triplet energy transfer. The energy level of  $^T1\text{PtP}$  is 1.85 eV and that of  $^T1\text{BD}$  was determined to be  $\sim 1.68$  eV by phosphorescence measurements at 77K in toluene (Fig. 5.A9), which is fairly close to the values of similar boron dipyrromethene molecules ( $\sim 1.64$ - $1.69$  eV).<sup>110, 195</sup> Then,  $\Delta G$  between  $^T1\text{PtP}$  and  $^T1\text{BD}$  is  $\sim -0.17$  eV. The using the estimated  $k_{TT}^F$  by FSTA ( $k_{TT}^F \sim 2.17 \times 10^7 \text{ s}^{-1}$ ) and  $T = 295\text{K}$ , we obtained  $k_{TT}^B = 2.7 \pm 0.3 \times 10^7 \text{ s}^{-1}$ .

### 5.5.3 Estimations of the efficiency of Förster energy transfer

The rate of energy transfer for a donor and acceptor (BD and PtP in the current system, respectively) separated by a distance  $r$  based on dipole-dipole interaction is given by:

$$k_{FRET}(\lambda) = \frac{\Phi_D \kappa^2}{\tau_D r^6} \left( \frac{9000(\ln 10)}{128\pi^5 N n^4} \int_0^\infty F_D(\lambda) \varepsilon_A(\lambda) \lambda^4 d\lambda \right) \quad (\text{Eq. 5.A3})$$

where  $\Phi_D$  is the quantum yield of the donor in the absence of acceptor,  $n$  is the refractive index of the medium measurements are performed,  $N$  is the Avogadro's number,  $r$  is the distance between the dipole moments of donor and acceptor, and  $\tau_D$  is the emission lifetime of the donor in the absence of acceptor.  $F_D(\lambda)$  is the corrected fluorescence intensity of the donor in the wavelength range  $\lambda$  to  $\lambda + \Delta\lambda$  with the total intensity (area under the luminescence curve) normalized to unity.  $\varepsilon_A(\lambda)$  is the extinction coefficient of the acceptor at  $\lambda$ .  $\kappa^2$  is the orientation factor and is represented as:

$$\kappa^2 = (\cos\theta_T - 3\cos\theta_D \cos\theta_A)^2 \quad (\text{Eq. 5.A4})$$

where  $\theta_T$  is the angle between the emission transition dipole of the donor and the absorption transition dipole of the acceptor,  $\theta_D$  and  $\theta_A$  are the angles between these dipoles and the vector joining the donor and the acceptor.

In our system  $\theta_T$  and  $\theta_A$  are both close to  $90^\circ$  (Fig. 5.A11). The reported value of  $\theta_D$  is  $\sim 81.5^\circ$  determined by single-crystal by X-ray crystallography and  $\sim 85.5^\circ$  by DFT calculation. The structure optimization of the triad and the dyad was performed by geometry optimization with density functional theory (DFT) using Becke's<sup>163</sup> three parameter hybrid functional with Lee, Yang, and Parr<sup>164</sup> correction functional (B3LYP) and the 6-31GG basis set as implemented in Q-Chem (4.01).<sup>165</sup> The stationary point was confirmed by running frequency calculations. Instead of Pt metal ion in porphyrin, Zn complex (ZnP-An-BD) was used. Calculated  $\theta_D$  in the triad is close to the value obtained in the crystal structure.<sup>157</sup>

These translate into  $\kappa^2 \sim 0.028$ . By using  $r=15 \text{ \AA}$ ,  $Q_D=0.001^a$  and  $\tau_D=0.2 \text{ ns}$  (toluene) and  $\Phi_D=0.0005$  and  $\tau_D=0.03 \text{ ns}$  (DMF)<sup>b</sup>, the spectrum overlaps were calculated as  $J = 8.65 \times 10^{-14} \text{ M}^{-1} \text{ cm}^3$  (toluene) and  $7.01 \times 10^{-14} \text{ M}^{-1} \text{ cm}^3$  (DMF) and we obtained  $k_{\text{FRET}}(r) \sim 1.5 \times 10^7 \text{ s}^{-1}$  (toluene) and  $4.7 \times 10^8 \text{ s}^{-1}$  (DMF). One can calculate the efficiency of energy transfer as:

$$E = \frac{k_{\text{FRET}}(r)}{\frac{1}{\tau_D} + k_{\text{FRET}}(r)} \quad (\text{Eq. 5.A5})$$

We obtained  $E \sim 0.03$  (toluene) and  $0.01$  (DMF). The rates of energy transfer are  $10^3$ - $10^5$  times smaller compared to the observed rate constants of electron transfer ( $\sim 10^{12} \text{ s}^{-1}$ ). Therefore, we can safely rule out the possibility of singlet energy transfer from BD onto PtP by a dipole-dipole interaction.

<sup>a</sup> Benninston et al. reported rather higher value ( $\Phi_D = 3.1 \times 10^{-2}$ ). Even if we used this relatively high value of quantum yield, we obtained  $k_{\text{FRET}} = 4.35 \times 10^8 \text{ s}^{-1}$ . <sup>b</sup> The fluorescence lifetime of An-BD in DMF is too fast for TCSPC method ( $< 0.030 \text{ ns}$ ). We used the upper limit of  $0.03 \text{ ns}$ .

### 5.5.4 Additional Figures

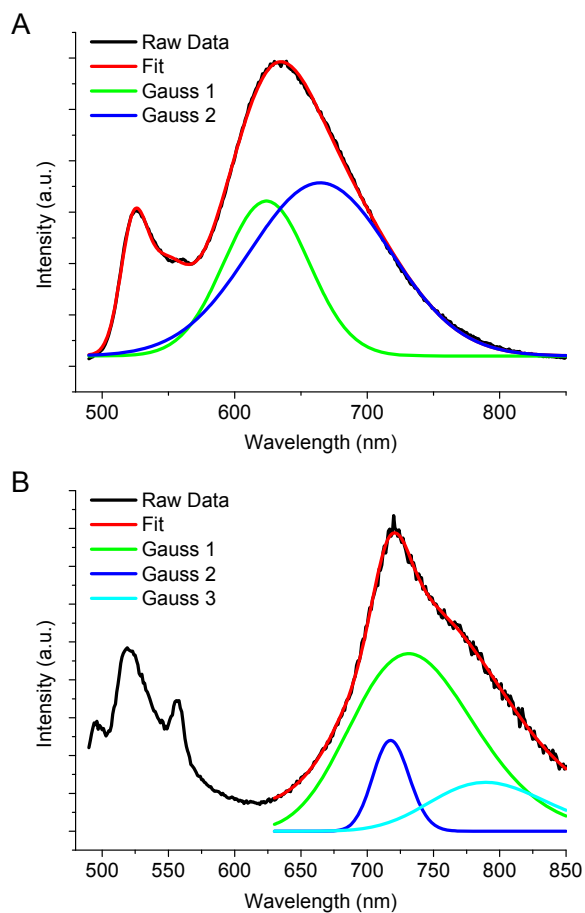


**Figure 5.A1.** Emission spectra of An-BD. (A) Emission spectra of An-BD in toluene ( $\lambda_{\text{ex}} = 480$  nm). (B) Emission spectra of An-BD in DMF ( $\lambda_{\text{ex}} = 480$  nm). The spectra can be decomposed into fluorescence from BD and exciplex emission. Exciplex emission can be fitted into two Gaussian functions in toluene and three Gaussian functions in DMF.

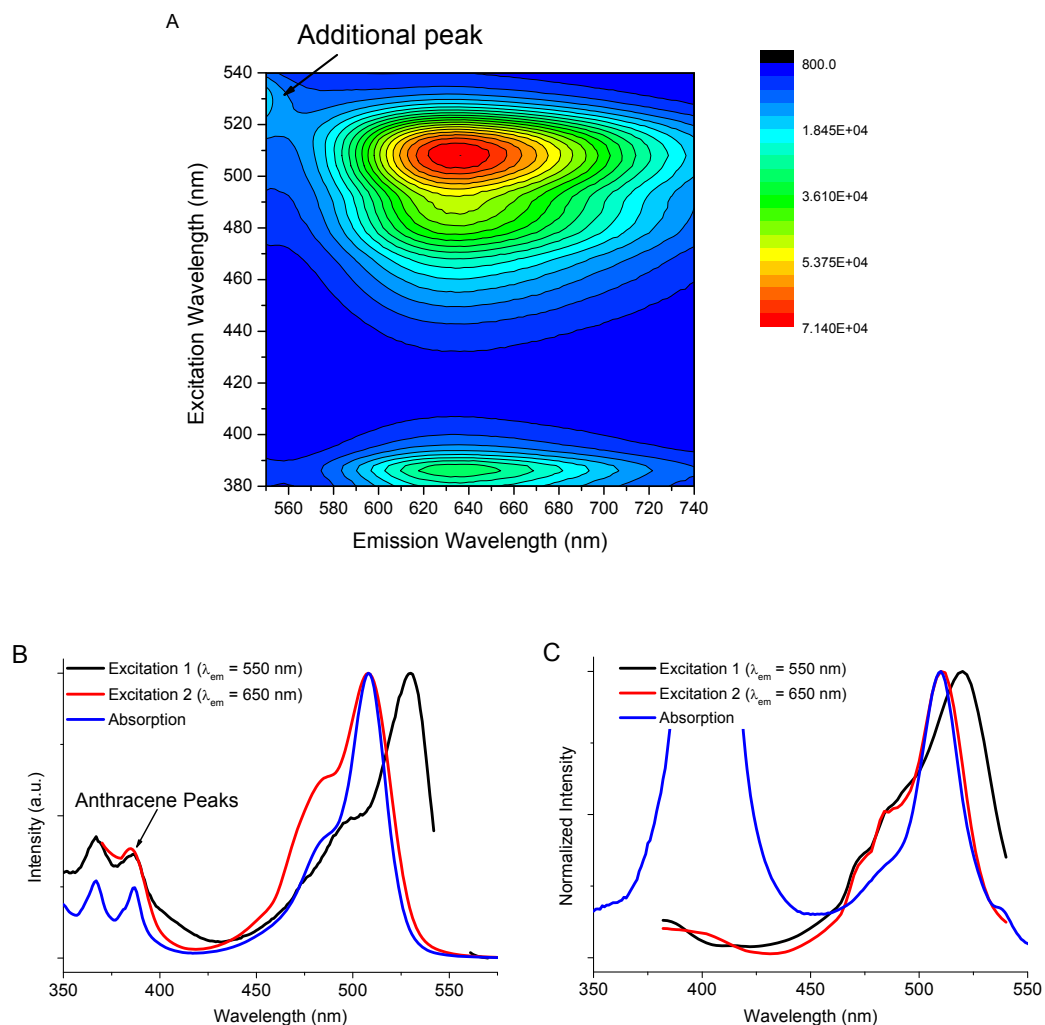


**Figure 5.A2.** Steady-state spectra of An-BD and PtP-An-BD in toluene. (A) Emission map of An-BD in toluene. Intensities are arbitrary and blue color is least intense and red color is most intense. (B) Comparison between the absorption spectrum and excitation spectra of An-BD in toluene. The peak in spectrum Excitation 1 is 530 nm ( $\lambda_{em} = 550$  nm). (C) Comparison between the absorption spectrum and excitation spectra of PtP-An-BD in oxygenated toluene. The peak in spectrum Excitation 1 is 520 nm ( $\lambda_{em} = 550$  nm).

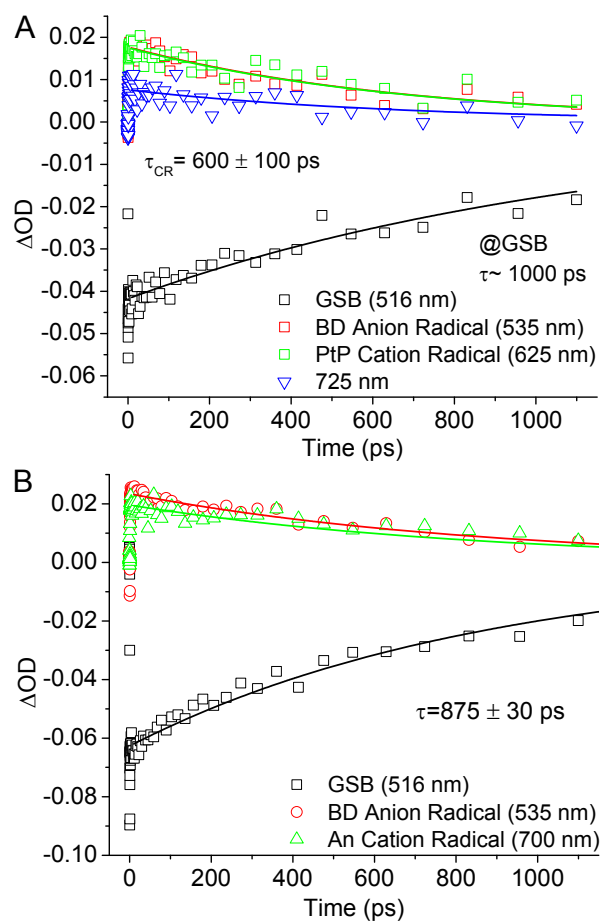


**Figure 5.A3.** Time evolution of PtP-An-BD and An-BD at selected wavelengths. (A) Time evolutions of PtP-An-BD and (B) An-BD ( $\lambda_{ex} = 490$  nm) in DMF. The lines show the single exponential fits.

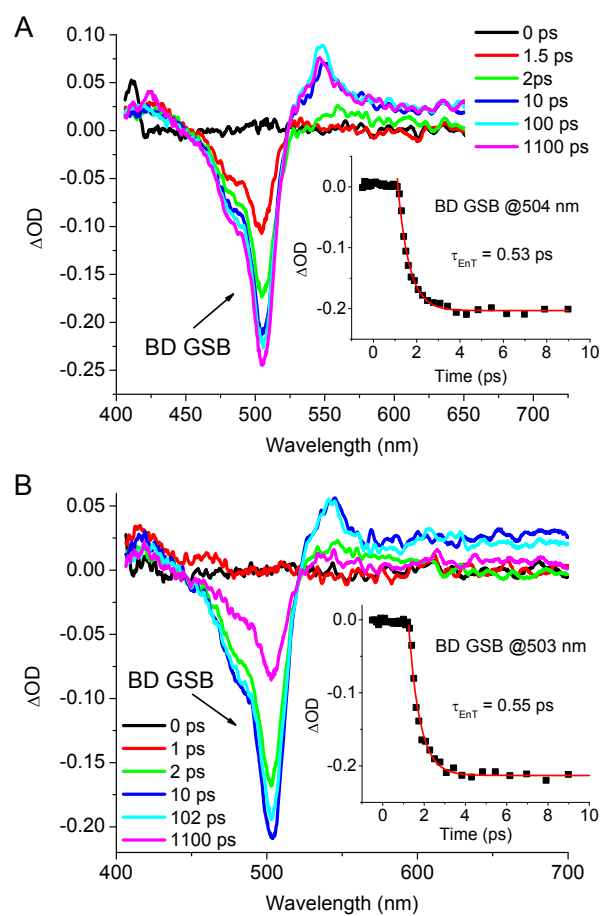


**Figure 5.A4.** FSTA spectra of An-BD at selected time points ( $\lambda_{ex} = 385$  nm) in Toluene (A) and DMF (B). The insets show the decay of BD ground state bleaching (GSB), which corresponds to the singlet energy transfer (EnT) from An to BD.

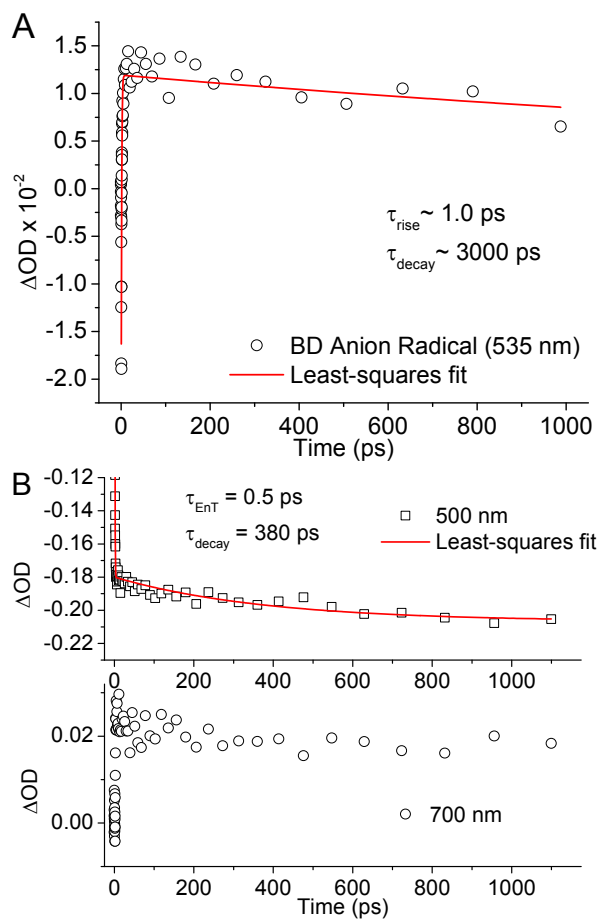


**Figure 5.A5.** Time evolution of An-BD in toluene. (A) The trace at 535 nm in toluene ( $\lambda_{\text{ex}} = 490 \text{ nm}$ ). The lines show the single exponential fits. (B) The traces at 500 nm (upper panel) and 700 nm (bottom panel) in toluene ( $\lambda_{\text{ex}} = 385 \text{ nm}$ ).  $\tau_{\text{EnT}}$  corresponds to the energy transfer from  $S^1\text{An}$  to  $S^1\text{BD}$ .

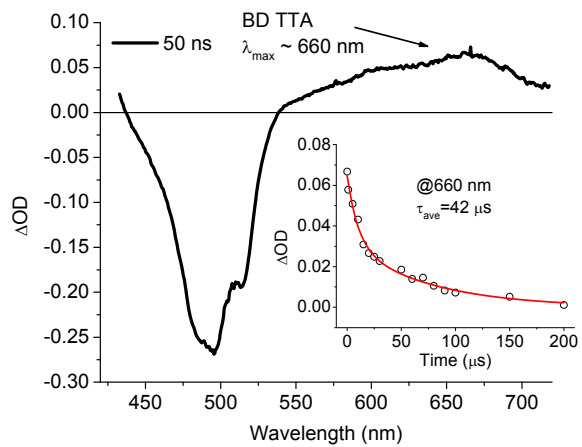


**Figure 5.A6.** NSTA spectra of An-BD at 50 ns time point ( $\lambda_{\text{ex}} = 532 \text{ nm}$ ) in toluene.

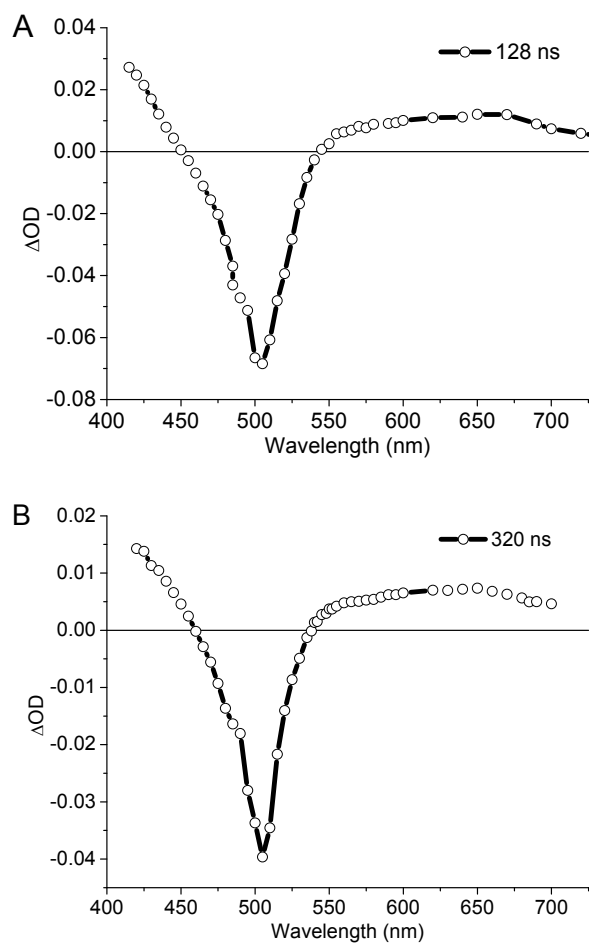


**Figure 5.A7.** NSTA spectra of PtP-An-BD. (A) in toluene at 128 ns after photo excitation ( $\lambda_{ex} = 532$  nm). (B) in DMF at 320 ns after photo excitation ( $\lambda_{ex} = 532$  nm).

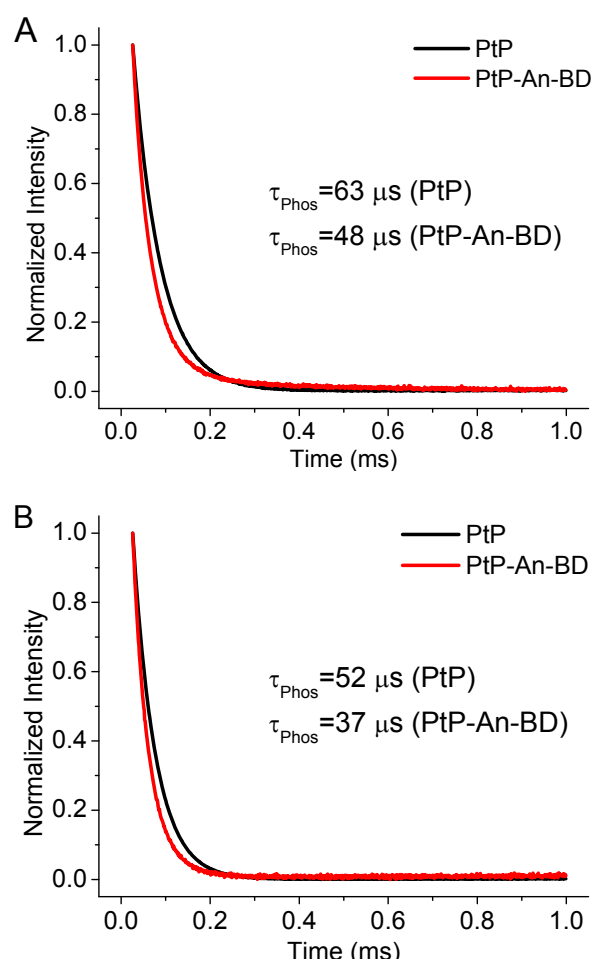


**Figure 5.A8.** Phosphorescence decay curves of PtP and PtP-An-BD. (A) in toluene and (B) in DMF.

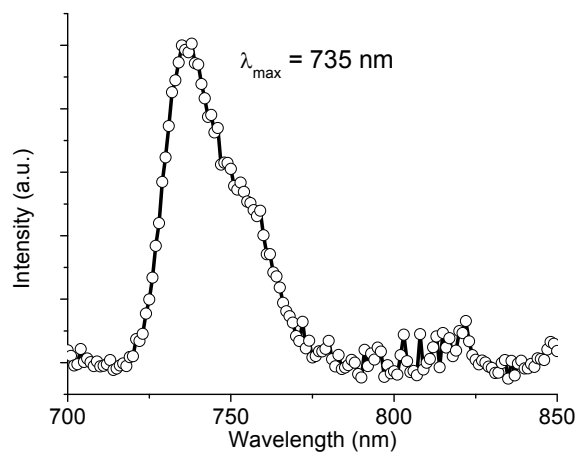


**Figure 5.A9.** Emission spectra of An-BD in toluene at 77K ( $\lambda_{\text{ex}} = 505 \text{ nm}$ ).

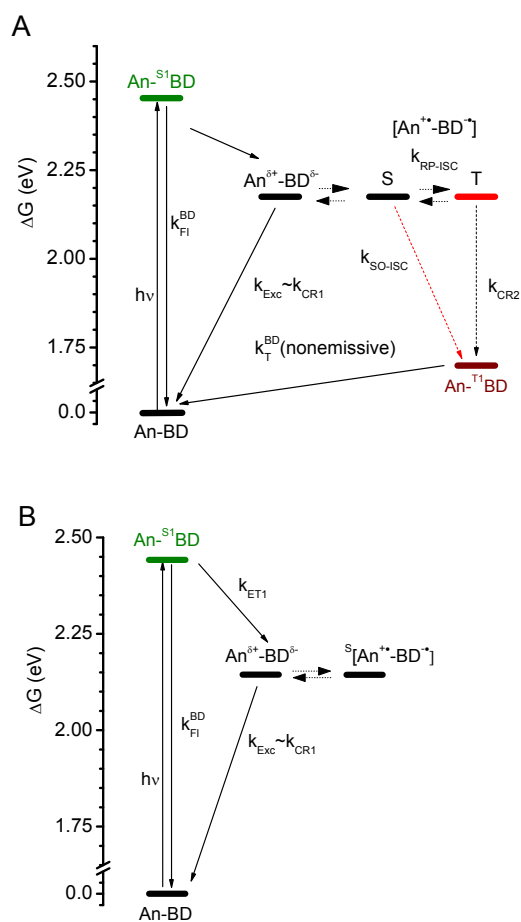


**Figure 5.A10.** Pathways occurring in PtP-An-BD triad upon excitation of BD unit in toluene (A) and in DMF (B). The arrows indicate processes whose rate constants were deduced from the spectroscopic measurements. Dashed red line is the favored route and dashed black line is the route we cannot completely exclude. Dotted lines indicate the routes for which the rate constants were not experimentally obtained.  $k_{TT}$  is the rate constant for the TT energy transfer.

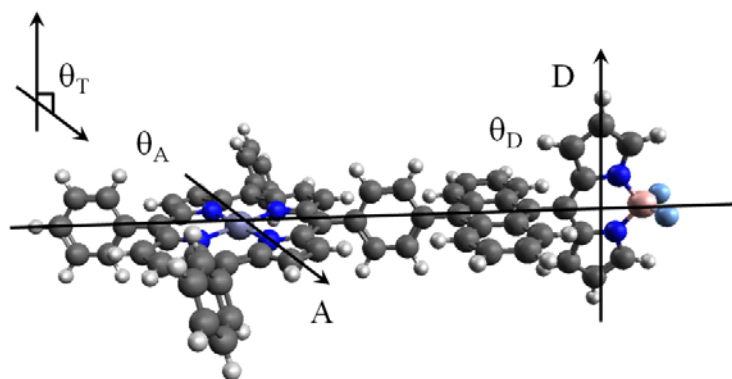


**Figure 5.A11.** Computed molecular structure of PtP-An-BD.

*Acknowledgements: Dr. Nikolai N. Tkachenko of Tampere University of Technology (experimental setup of femtosecond and nanosecond transient absorption spectroscopy, and discussion), Dr. Thomas Troxler (technical assistance for nanosecond transient absorption spectroscopy and fluorescence lifetime measurements).*

## CHAPTER 6 Modulation of Visible Room Temperature Phosphorescence by Weak Magnetic Fields

This work has been published: \* Modulation of Visible Room Temperature Phosphorescence by Weak Magnetic Fields. Mani, T.; Tanabe, M.; Yamauchi, S.; Tkachenko, N. V.; Vinogradov, S. A. *J. Phys. Chem. Lett.* **2012**, 3, 3115-3119.

### 6.1 Summary

Magnetic control over excited states of molecules presents interest for many applications. Here we show for the first time that visible room temperature phosphorescence in multichromophoric donor-acceptor systems can be modulated by weak magnetic fields (<1 Tesla) via Magnetic Field Effects (MFE) on the spin dynamics in photo-generated radical pairs (RP). The studied compounds comprise Pt porphyrin (PtP)-Rosamine B (RosB) dyads, which possess strong visible absorption bands and phosphoresce at room temperature. The observed MFE is unique in that it occurs upon direct excitation of the PtP in the dyads, whereby ultrafast quantitative formation of the local PtP triplet state precedes occurrence of radical intermediates. A model explaining the effect is proposed, which is based on reversible electron transfer between the local triplet state and a long-lived RP. External magnetic field modulates spin dynamics of the RP, affecting contribution of the singlet RP recombination channel and thereby influencing phosphorescence.

---

\* Adapted with permission. Copyright © 2012, American Chemical Society

## 6.2 Introduction

Magnetic Field Effects (MFE) on the spin dynamics in radical pairs (RP)<sup>7, 11</sup> underlie several important spectroscopic phenomena, e.g CIDNP,<sup>196-197</sup> and may play a key role in biological magnetoreception.<sup>60, 93</sup> In addition, MFE potentially offer a unique opportunity to impose magnetic control over excited electronic states of molecules, thus presenting interest for many areas of technology. For example, in biomedical arena the ability to magnetically modulate photosensitizer activity for photochemical generation of singlet oxygen could be a valuable asset for photodynamic therapy.<sup>59</sup> In optical imaging, magnetic control over probes' emissivity may serve to enhance spatial resolution.<sup>57-58</sup> The key to such applications are molecules with strong optical transitions in the visible/near infrared spectral regions and excited states responsive to magnetic fields. However, so far no such systems have been reported.

## 6.3 Experimental methods

**6.3.1 General information** All the experiments were performed in the University of Pennsylvania except for nanosecond transient absorption spectroscopy (NSTA) and femtosecond transient absorption spectroscopy (FSTA) measurements, which were performed in Tampere University of Technology, and TREPR experiments, which were performed in Tohoku University. All solvents and reagents were purchased from commercial sources and used as received. <sup>1</sup>H and <sup>13</sup>C NMR spectra were recorded on a Bruker DPX-400 spectrometer, operating at 400.1 or 100.6 MHz respectively. Mass-spectra were recorded on a MALDI-TOF Bruker Daltonics Microflex LRF, using  $\alpha$ -cyano-4-hydroxycinnamic acid (CCA) as a matrix, positive-ion mode. Samples were prepared by mixing 10  $\mu$ l of 1 mM solution of the compound in THF or MeOH with 100  $\mu$ l of matrix solution (10 mg/ml, 0.053 M) in THF. Approximately 1  $\mu$ l sample was then deposited on the probe tip, dried and analyzed.

**6.3.2 Optical measurements.** Optical glass cells and/or quartz fluorometric cells (1 cm optical path length) were used in all experiments. Samples were deoxygenated either by bubbling Ar or

applying four pump-freeze-thaw cycles under vacuum ( $10^{-3}$  mm Hg). All measurements were performed in anhydrous benzonitrile at 22 °C, unless otherwise noted. UV-vis absorption spectra were recorded on a Perkin-Elmer Lambda 35 UV-Vis spectrophotometer. Steady-state and time-resolved phosphorescence measurements were performed on a FS900 spectrofluorometer (Edinburgh Instruments, UK), equipped with R2658P PMT (Hamamatsu). Time-resolved phosphorescence measurements were performed using an in-house constructed time-domain phosphorometer. The detail of the instrument was described elsewhere.<sup>153</sup> The fluorescence quantum yields were measured against fluorescence of Rhodamine 6G in EtOH ( $\Phi_f=0.94$ ).<sup>111</sup>

**6.3.3 Electrochemical measurements.** The details of cyclic voltammetry experiments were described in the Chapter 4.

**6.3.4 Nanosecond Transient Absorption measurements.** The details of NSTA setups were described in Chapter 5.

**6.3.5 Femtosecond Transient Absorption measurements.** The details of FSTA setups were described in Chapter 5.

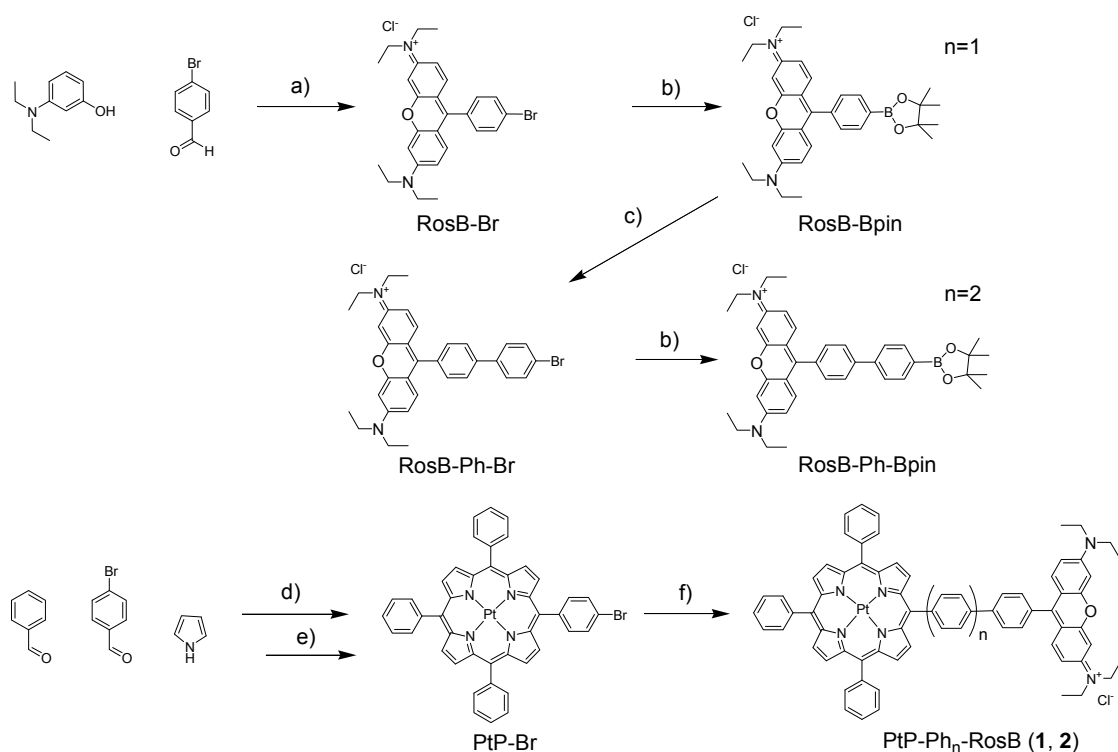
**6.3.6 Time-Resolved Electron Paramagnetic Resonance (TREPR) measurements.** The details of the TREPR setup have been described elsewhere.<sup>198</sup> Briefly, EPR signals were detected on a JEOL JES-FE2XGS EPR spectrometer. TREPR spectra were obtained over a defined time range as a function of the magnetic field. An optical parametric oscillator (Spectra Physics MOPO 710) was used for excitation in the range of 500–600 nm.

**6.3.7 Phosphorescence Magnetically Affected Reaction Yield (MARY) measurements.** The setup consists of an in-house constructed fiber optic time-domain phosphorometer (see above) coupled to either a magnet of an EPR instrument (EMX, Bruker) (50 mT-1 T) or a home-made solenoid coil (0-50 mT), which served as sources of controllable external magnetic field. Phosphorescence decays were measured upon excitation with a pulsed LED with repetition rate of 10 Hz, and the integrated intensity of phosphorescence was plotted as the magnetic field

strength was changed in time. Spectra were recorded upon photoexcitation of PtP at its Q-band transition ( $\lambda_{\text{ex}} \sim 510\text{nm}$ ). The block diagram of the setup is shown in Fig. 6.A1.

**6.3.8 Synthesis** The synthesis followed Scheme 6.1. RosB-Br was obtained by the method described previously.<sup>199</sup> RosB-B was obtained by Miyaura boronation, and further subjected to Suzuki-Miyaura coupling to yield (RosB-Ph-Br). The subsequent Miyaura boronation gave RosB-Ph-B. RosB-B and RosB-Ph-B were coupled with PtP-Br by Suzuki-Miyaura reaction to give compounds 1 and 2, respectively.

**Scheme 6.1** Synthesis of PtP-Ph<sub>n</sub>-RosB



a) i) 60%  $\text{H}_2\text{SO}_4$ ,  $160^\circ\text{C}$ ; ii) Chloroanil; b)  $\text{B}_2\text{pin}_2/\text{PdCl}_2(\text{dppf})/\text{DMF}$ ; c) 1-Br-4-I-Phenyl/ $\text{Pd}(\text{PPh}_3)_4/\text{KOAc}/\text{DMF}$ ; d) i)  $\text{BF}_3 \cdot \text{Et}_2\text{O}/\text{DCM}$ ; ii)  $\text{DDQ}/\text{DCM}$ ; e)  $\text{Pt}(\text{acac})_2/\text{Benzoic acid}$ ,  $128^\circ\text{C}$ ; f) RosB ( $n = 1$  and  $2$ )/ $\text{Pd}(\text{PPh}_3)_4/\text{KOAc}/\text{DMF}$ .

**RosB-Br.** 3-(diethylamino)phenol (500 mg, 3.0 mmol) and 4-bromobenzaldehyde (280 mg, 1.5 mmol) were dissolved in DCM (2 mL), and the solvent was removed in vacuum. The mixture was suspended in H<sub>2</sub>SO<sub>4</sub> (6 mL of 60%) and stirred at 160°C for 4 h. The reaction progress was monitored by UV-VIS. After cooling the mixture to room temperature, *p*-chloranil (1 eq, 370 mg, 1.5 mmol) was added in one portion, and the mixture was stirred for 10 min at room temperature. The dark brown solution was neutralized with 10 M NaOH (~10 mL) to bring pH to ~7. The resulting mixture was extracted with *i*PrOH solution in DCM (5%, 3x20 mL). The combined organic layers were washed with brine (3x60 mL), dried over anhydrous Na<sub>2</sub>SO<sub>4</sub>, and the solvents were removed in vacuum. The remaining solid was purified by column chromatography on silica gel (EtOH/CH<sub>2</sub>Cl<sub>2</sub>=1:19). The second band, bright pink in color, was identified as the title compound, which was isolated as a purple solid. Yield: 250 mg, 8.3 %. <sup>1</sup>H NMR (DMSO, δ): 7.9 (d, J = 8.3 Hz, 2H), 7.49 (d, J = 8.3 Hz, 2H), 7.25 (d, J = 8.3 Hz, 2H), 7.14 (m, 2H), 6.99 (d, J = 2.3 Hz, 2H), 3.66 (q, J = 6.9 Hz, 8H), 1.23-1.17 (m, 12H); MALDI-TOF (m/z): calcd for C<sub>27</sub>H<sub>30</sub>BrN<sub>2</sub>O<sup>+</sup>: 478.44; found; 479.12 [M+H<sup>+</sup>].

**RosB-B.** RosB-Br (60 mg, 0.125 mmol), bis(pinacolato)diboron (80 mg, 0.310 mmol) and KOAc (490 mg, 1.25 mmol) were dissolved in DMF (3 mL). PdCl<sub>2</sub>(dppf)<sub>2</sub> (10 mg, 0.012 mmol, 10 %), used as a catalyst in this Miyaura coupling reaction, was dissolved separately in DMF (1 mL). The solution of the catalyst was added to the mixture of the reactants, and it was stirred vigorously at 80°C for 4 hrs. The mixture was cooled down, CH<sub>2</sub>Cl<sub>2</sub> (10 mL) was added, and the resulting solution was washed with water (3x10 mL) in a separatory funnel. The organic phase was collected, dried over Na<sub>2</sub>SO<sub>4</sub>, and the solvent was evaporated to dryness. The remaining solid was purified by column chromatography on silica gel (THF/EtOH=3:2) to afford the target RosB-B as a purple solid after removal of the solvent and drying the product in vacuum. Yield: 60 mg, 98 %. <sup>1</sup>H NMR (CDCl<sub>3</sub>, δ): 8.05 (br s, 2H), 7.61-7.48 (m, 4H), 7.40 (m, 2H), 6.88 (br, 2H), 3.67 (br s, 8H), 1.41 (s, 12H), 1.27-1.24 (m, 12H); MALDI-TOF (m/z): calcd for C<sub>33</sub>H<sub>42</sub>BrN<sub>2</sub>O<sub>3</sub><sup>+</sup>: 525.51; found; 525.26.

**RosB-Ph-Br.** RosB-B (48 mg, 0.093 mmol), 1-bromo-4-iodo-benzene (32 mg, 0.110 mmol) and  $\text{Cs}_2\text{CO}_3$  (148 mg, 0.46 mmol) were dissolved in DMF (2 mL).  $\text{Pd}(\text{PPh}_3)_4$  (10 mg 0.008 mmol, 10 %), used as a catalyst in this Suzuki coupling reaction, was dissolved separately in DMF (1 mL). The catalyst solution was added to the mixture of the reactants, and the mixture was stirred vigorously at 80 °C for 12 hrs. The reaction mixture was cooled down,  $\text{CH}_2\text{Cl}_2$  (10 mL) was added, and the resulting solution was washed with water (3×10 mL). The organic phase was collected, dried over  $\text{Na}_2\text{SO}_4$ , and the solvent was evaporated to dryness. The remaining solid was purified by column chromatography on silica gel ( $\text{EtOH}/\text{CH}_2\text{Cl}_2=1:9$ ). The title compound was isolated as a purple solid (48 mg, 93%).  $^1\text{H}$  NMR ( $\text{CDCl}_3$ ,  $\delta$ ): 7.82 (d, J = 8.3 Hz, 2H), 7.66 (d, J = 8.5 Hz, 2H), 7.57 (d, J = 8.8 Hz, 2H), 7.450-7.43 (m, 4H), 6.98 (br, 4H), 3.68 (q, J = 6.9 Hz, 8H), 1.44 (m, 12H); MALDI-TOF (m/z): calcd for  $\text{C}_{33}\text{H}_{34}\text{BrN}_2\text{O}^+$ : 554.54; found; 555.51.

**RosB-Ph-B.** RosB-Ph-Br (21mg, 0.038 mmol), bis(pinacolato)diboron (24 mg, 0.096 mmol) and KOAc (150 mg, 0.38 mmol) were dissolved in DMF (3 mL).  $\text{PdCl}_2(\text{dppf})_2$  (6 mg, 0.007 mmol, 20 %), used as a catalyst in this Miyaura coupling reaction, was dissolved separately in DMF (1 mL). The solution of the catalyst was added to the mixture of the reactants, and the mixture was stirred vigorously at 80°C for 4 hrs. The mixture was cooled down,  $\text{CH}_2\text{Cl}_2$  (10 mL) was added, and the resulting solution was washed with water (3×10 mL) in a separatory funnel. The organic phase was collected, dried over  $\text{Na}_2\text{SO}_4$ , and the solvent was evaporated to dryness. The remaining solid was purified by column chromatography on silica gel ( $\text{THF}/\text{EtOH}=3:2$ ) to afford the target RosB-Ph-B as a purple solid after removal of the solvent and drying the product in vacuum. Yield: 8 mg, 35 %.  $^1\text{H}$  NMR (DMSO,  $\delta$ ): 7.97 (d, J = 7.8 Hz, 2H), 7.86 (m, 4H), 7.71 (d, J = 7.5 Hz, 2H), 7.62-7.55 (m, 4H), 6.94 (br, 4H), 3.67 (br s, 8H), 1.38 (s, 12H), 1.27-1.24 (m, 12H); MALDI-TOF (m/z): calcd for  $\text{C}_{39}\text{H}_{46}\text{BrN}_2\text{O}_3^+$ : 601.60; found; 601.69.

**Pt(II) 5-(4-bromophenyl)-10,15,20-triphenylporphyrin (PtP-Br).** 5-(4-bromophenyl)-10,15,20-triphenylporphyrin was synthesized in the same manner as described previously. Pt(II) insertion into the porphyrin was performed using the method of Anzenbacher et al.<sup>200</sup> 5-(4-bromophenyl)-

10,15,20-triphenylporphyrin (23 mg, 33  $\mu\text{mol}$ ) was dissolved in pre-heated benzoic acid melt (1.5 g) at 128°C. Pt(acetylacetonate)<sub>2</sub> (53 mg, 134  $\mu\text{mol}$ ) was added to the mixture. The reaction mixture was stirred at 128°C for 4 h. The reaction was monitored by UV-VIS spectroscopy. After the mixture was cooled to room temperature, MeOH (5 mL) was added. The residue collected by centrifugation and purified by column chromatography (silica gel, hexane:DCM=1:1). The title compound was isolated as a pale orange solid. Yield: 16 mg, 53 %. <sup>1</sup>H NMR (CDCl<sub>3</sub>,  $\delta$ ): 8.80-8.74 (m, 8H), 8.16 (m, 6H), 8.03 (m, 2H), 7.88 (m, 2H), 7.78-7.72 (m, 9H); MALDI-TOF (m/z): calcd for C<sub>44</sub>H<sub>27</sub>BrN<sub>4</sub>Pt: 886.69; found; 886.17.

**Dyad 1.** PtP-Br (8 mg, 9.0  $\mu\text{mol}$ ), RosB-B (5 mg, 9.5  $\mu\text{mol}$ ) and Cs<sub>2</sub>CO<sub>3</sub> (6 mg, 18.4  $\mu\text{mol}$ ) were dissolved in DMF (3 mL). The mixture was stirred under Ar for 15 min. Pd(PPh<sub>3</sub>)<sub>4</sub> (1.2 mg, 10 mol%) was dissolved separately in DMF (3 mL) and added to the mixture in one portion. The resulting mixture was stirred vigorously at 85 °C for 5 h under Ar. After cooling the mixture to room temperature, DMF was removed in vacuum. The residue was dissolved in DCM (10 mL) and washed with brine (3x10 mL). The organic layer was dried over anhydrous Na<sub>2</sub>SO<sub>4</sub>, and the solvent were removed in vacuum. The material compound was purified by chromatography (silica gel, EtOH:THF=1:9). The title compound was isolated as a pink solid. Yield: 8.1 mg, 75%. <sup>1</sup>H NMR (DMSO,  $\delta$ ): 8.76 (m, 8H), 8.23 (m, 2H), 8.17 (dd, J = 7.5, 1.8 Hz, 6H), 7.86-7.77 (m, 15H), 7.18 (m, 4H), 6.98 (m, 2H), 3.66-3.60 (br, 8H), 1.18 (t, 12H); MALDI-TOF (m/z): calcd for C<sub>71</sub>H<sub>57</sub>N<sub>6</sub>OPt<sup>+</sup>: 1205.33; found; 1205.2.

**Dyad 2.** PtP-Br (8.5 mg, 9.7  $\mu\text{mol}$ ), RosB-Ph-B (7.0 mg, 11.6  $\mu\text{mol}$ ) and Cs<sub>2</sub>CO<sub>3</sub> (13 mg, 39  $\mu\text{mol}$ ) were dissolved in DMF (3mL). The mixture was stirred under Ar for 15 min. Pd(PPh<sub>3</sub>)<sub>4</sub> (2.3 mg, 20 mol%) was dissolved separately in DMF (3 mL), and added to the mixture in one portion. The resulting mixture was stirred vigorously at 85 °C for 10 h under Ar. After cooling the mixture, DMF was removed in vacuum. The residue was dissolved in DCM (10 mL) and washed with brine (3x10 mL). The organic layer was dried over anhydrous Na<sub>2</sub>SO<sub>4</sub>, and the solvent was removed in vacuum. The material compound was purified by chromatography (silica gel, EtOH:THF=1:9).

The title compound was isolated as a pink solid. Yield: 3.0 mg, 25%.  $^1\text{H}$  NMR ( $\text{CDCl}_3$ ,  $\delta$ ): 8.77 (m, 8H), 8.29 (d, 2H), 8.19 (m, 6H), 8.08 (br s, 4H), 7.95 (m, 4H), 7.80-7.70 (m, 11H), 7.00 (m, 4H), 6.84 (m, 2H), 3.36 (br s, 8H), 1.26-1.25 (t, 12H); MALDI-TOF ( $m/z$ ): calcd for  $\text{C}_{77}\text{H}_{61}\text{N}_6\text{OPt}^+$ : 181.43; found; 1281.15.

## 6.4 Results and discussion

MFE on molecular luminescence are typically limited to UV-excitable materials with emission occurring from exciplex states.<sup>28</sup> Within the context of the radical pair mechanism,<sup>7, 11</sup> local excited triplet spin states (i.e. triplet states localized on individual chromophores), which are usually non-emissive, serve merely as non-radiative sinks for RP's. At the same time, there exist a number of molecules with strong optical transitions and bright emissive triplet states, e.g. porphyrin complexes of Pd(II) and Pt(II).<sup>120</sup> At ambient temperatures phosphorescence of these chromophores is not magnetically responsive due to the rapid population mixing between the three spin sublevels. However, by including a RP state into a pathway leading to the formation (or decay) of an emissive triplet state, magnetic influence on phosphorescence could be realized *via* modulation of the RP spin dynamics.

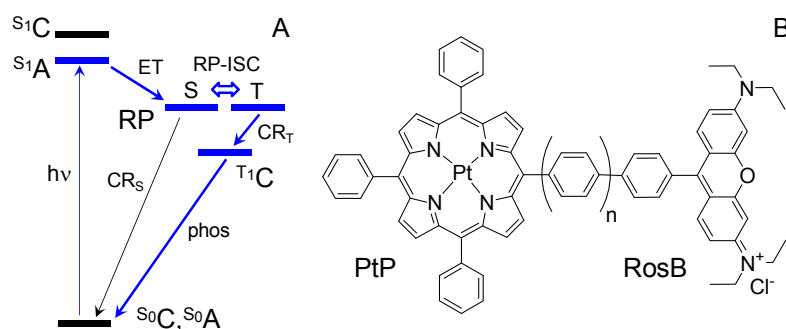


**Figure 6.1.** Energy diagram and structures of dyads  $\text{PtP-Ph}_n\text{-RosB}^+$  (**1-2**,  $n=1-2$ ). (A) Energy diagram depicting processes (blue lines) in antenna (A)-triplet core (C) dyads, leading to the formation of core-centered phosphorescent triplet state ( $^1\text{T}_1\text{C}$ ) *via* RP intermediates.  $\text{CR}_\text{T}$  and  $\text{CR}_\text{S}$  - triplet and singlet charge recombination pathways, respectively. (B) Structures of dyads studied in the present work.

Applications of molecular triplet states include, among others, imaging of oxygen<sup>41, 84</sup> and photodynamic therapy,<sup>72</sup> which would greatly benefit from magnetic control over the triplet yield. Our particular interest is in triplet imaging probes<sup>201-202</sup> and related donor-acceptor systems.<sup>82</sup> Recently we demonstrated that in dyads comprising triplet cores (C) and auxiliary antennae (A) chromophores, RP's can mediate formation of phosphorescent states by way of antenna excitation, photoinduced electron transfer (ET), radical pair intersystem crossing (RP-ISC) and subsequent triplet charge recombination (Fig. 6.1A).<sup>153</sup> We reasoned that magnetic modulation of RP-ISC in this pathway could in principle render magnetically responsive phosphorescent molecules. In the present report we disclose to the best of our knowledge the first example of magnetic modulation of visible room temperature phosphorescence. Remarkably, in this case RP's appear to intervene not in the formation, but decay of local phosphorescent states, populated prior to the electron transfer step.

The studied dyads comprise Pt(II) tetraarylporphyrin (PtP) and Rosamine B (RosB) (a derivative of Rhodamine B), connected by rigid oligophenylene linkers ( $\text{Ph}_n$ ) ( $\text{PtP-Ph}_n\text{-RosB}^+$ ,  $n=1-2$ , Fig. 6.1B). PtP serves as a phosphorescent emitter, while  $\text{RosB}^+$  plays the role of an auxiliary antenna. The singlet excited state of  $\text{RosB}^+$  ( $^{\text{S1}}\text{RosB}$ ,  $\lambda_{\text{max}}=565$  nm) resides below the  $\text{S}_1$  state of PtP ( $^{\text{S1}}\text{PtP}$ ,  $\lambda_{\text{max}}=540$  nm), but above its emissive  $\text{T}_1$  state ( $^{\text{T1}}\text{PtP}$ ,  $\lambda_{\text{max}}=670$  nm) (see Fig. 6.A2 for optical spectra). Based on spectro-electrochemical measurements (Table 6.A1), the RP ( $\text{PtP}^+\text{-RosB}^+$ ) lies between  $^{\text{S1}}\text{PtP}$  and  $^{\text{T1}}\text{PtP}$  states. The exact energy of the  $\text{RosB}^+$  triplet state ( $^{\text{T1}}\text{RosB}$ ) is not known, but closely related Rhodamine B ( $\text{RhB}^+$ ) has its triplet energy near 1.80-1.84 eV (674-689 nm).<sup>133-135</sup>

Direct excitation of PtP in **1** and **2** ( $\lambda_{\text{ex}}=540$  nm) leads to the quantitative formation of  $^{\text{T1}}\text{PtP}$  state, which phosphoresces with significantly lower quantum yield ( $\phi_{\text{ph}}=0.01$  and  $0.02$  for **1** and **2**, respectively) than does PtP alone ( $\phi_{\text{ph}}=0.13$ ), indicating presence of strong quenching pathways. Similar to the previously reported PtP- $\text{RhB}^+$  systems,<sup>153</sup> selective excitation of  $\text{RosB}^+$  in **1** and **2** ( $\lambda_{\text{ex}}=580$  nm) generates PtP phosphorescence *via* the ET pathway (Fig. 6.1A), as

opposed to local intrachromophoric processes. However, the overall emission quantum yield for this pathway is extremely low ( $\phi_{ph} < 10^{-4}$ ).

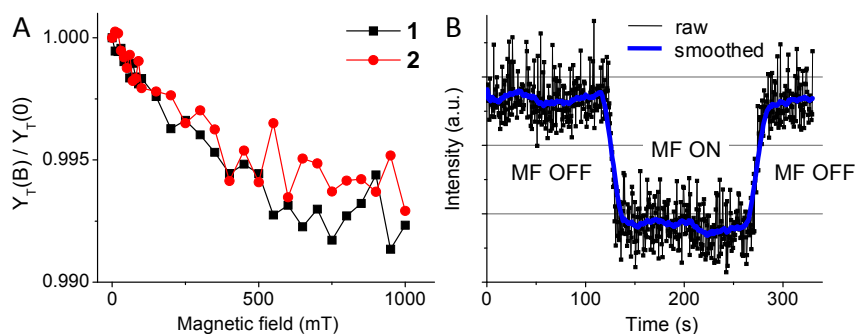


**Figure 6.2.** Magnetic field effects on phosphorescence emission from **1** and **2**. (A) MARY spectra of **1** and **2** at 22°C.  $Y_T(B)$  denotes integrated intensity of phosphorescence in the magnetic field of strength  $B$ . (B) Effect of magnetic field ( $B=200$  mT) on phosphorescence of **1**. (Blue line represents smoothed data to aid the eye.)

To examine the possibility of MFE on phosphorescence we constructed a MARY (Magnetically Affected Reaction Yield) setup by coupling a time-domain fiber optic phosphorometer with either a homemade solenoid coil or a magnet of an EPR spectrometer in order to conduct measurements in 0-50 mT and 50 mT-1 T magnetic fields, respectively. Upon selective excitation of  $\text{RosB}^+$  antenna, MARY measurements indeed indicated presence of a weak signal, but it was strongly obstructed by noise. However, to our surprise direct excitation of PtP into its  $Q_{01}$ -band ( $\lambda_{\text{abs}} \sim 510$  nm) led to a clear decrease in the phosphorescence emission upon increase in the magnetic field (Fig. 6.2A). Although  $^{\text{S}1}\text{RosB}^+$  state is also populated upon excitation at 510 nm, contribution of phosphorescence generated *via* this pathway can be disregarded due to its negligible quantum yield. Furthermore, shifting the excitation to the blue of the PtP absorption peak and thereby increasing the fraction of excited  $\text{RosB}^+$  did not result in any increase in the MARY signal. To exclude measurement artifacts (e.g. temperature-induced fluctuations), the effect was reproduced by switching the field on and off at a fixed  $B$ -value (Fig. 6.2B). Such abrupt changes in the field strength (e.g. from 0 to 200 mT) were accompanied by the fully reversible reduction and baseline recovery of the phosphorescence signal,

unambiguously confirming the magnetic origin of the phenomenon. Importantly, measurements at low fields (<500 Gauss) did not reveal any increase in the phosphorescence. The degree of the MFE was found to be somewhat weaker for **2** than for **1**.

Since in Pt(II) porphyrins  $S_1 \rightarrow T_1$  intersystem-crossing (ISC) occurs on the sub-picosecond time scale,<sup>125</sup> magnetically-sensitive radical intermediates, presumably responsible for the phosphorescence modulation, must arise already after the formation of  $T^1$ PtP. The most plausible pathway is the triplet ET from  $T^1$ PtP onto  $\text{RosB}^+$ . This ET is endergonic ( $\Delta G = +0.2$  eV) and therefore slow, but it still should be able to compete with intrinsically slow (tens of microseconds) triplet decay.

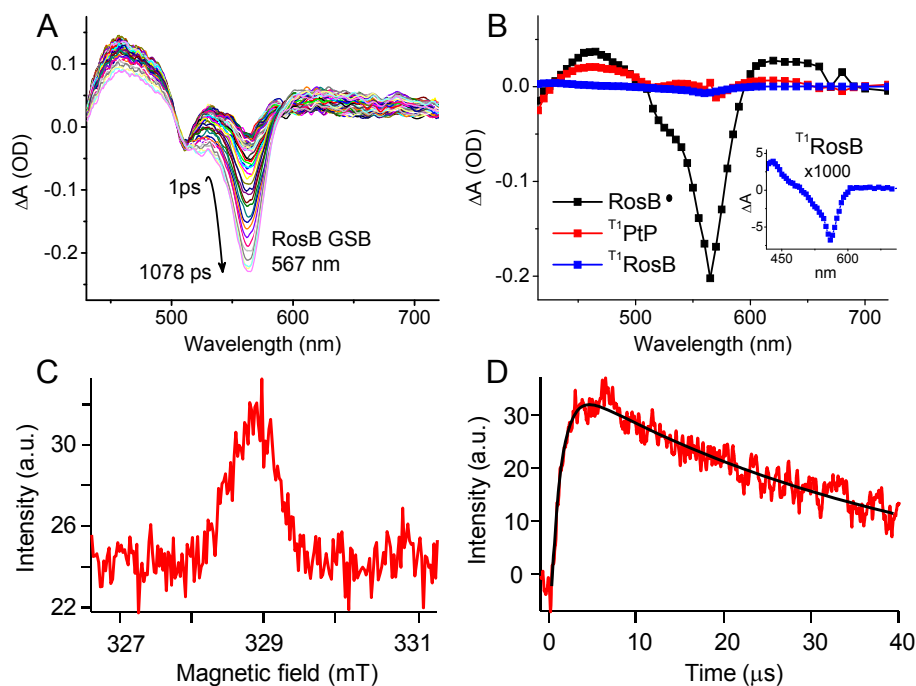


**Figure 6.3.** Spectral features of **1** probed by FSTA and TREPR. (A) FSTA spectra of **1** ( $\lambda_{\text{ex}}=405$  nm) (B) Decay-associated spectra of **1** obtained from global fitting of NSTA data ( $\lambda_{\text{ex}}=405$  nm). Inset shows magnified spectrum of  $T^1$ RosB. (C) TREPR spectrum of **1** in benzonitrile at 22 °C at 1.5-6.5  $\mu\text{s}$  after a laser pulse ( $\lambda_{\text{ex}}=510$  nm). (D) Time evolution of the EPR signal at 0.2 mW microwave power. The black line is the fit to the exponential rise-decay model (see the Appendix to this chapter for additional data).

Femtosecond and nanosecond transient absorption (FSTA and NSTA) measurements provided evidence in support of our hypothesis. According to FSTA, RosB<sup>+</sup> ground state bleaching begins after the population of <sup>T1</sup>PtP state (Fig. 6.3A, 6.A3A). (Excitation at 405 nm populates the Soret state of PtP, which undergoes internal conversion to the S<sub>1</sub> state, followed by ultrafast ISC.) Transient spectra recorded at 1 ns (the latest time point accessible by FSTA) and at 50 ns (the earliest time accessible by NSTA) show nearly identical features, indicating that all processes following <sup>T1</sup>PtP formation occur on a rather slow (microseconds) time scale.

Global fitting of the NSTA data revealed presence of three distinct intermediates (Fig. 6.3B, A3B), identified as <sup>T1</sup>PtP, <sup>T1</sup>RosB and RosB neutral radical (RosB•). The spectral signatures of the latter two species closely resemble those of similar xanthene dyes.<sup>127, 153, 203</sup> The decay constants for RosB• and <sup>T1</sup>RosB were found to be 6 and ~1000 μs, respectively, while the lifetime of <sup>T1</sup>PtP (τ~25 μs) agrees well with the phosphorescence data (Fig. 6.A2).

Time-resolved EPR (TREPR) measurements<sup>204-205</sup> also indicated presence of radical species. Upon pulsed excitation of compound **1** (λ<sub>ex</sub>=510 nm) we observed an absorptive peak with g=2.0022 and the line width of 0.7-0.8 mT (Fig. 6.3C, Fig. 6.A5). The peak's g value was found to be close to that of the Eosin Y radical (g=2.0025)<sup>206</sup> - a structural analog of RosB, but higher than that of PtP cation-radical (g=1.999).<sup>207</sup> Importantly, control experiments performed on RosB<sup>+</sup> and PtP solutions alone revealed no EPR signals. Both rise and decay phases of the signal g=2.0022 were found to be microwave power dependent (Table 6.A2), indicating that its kinetics is influenced by spin relaxation (Fig. 6.3D).<sup>208-209</sup>

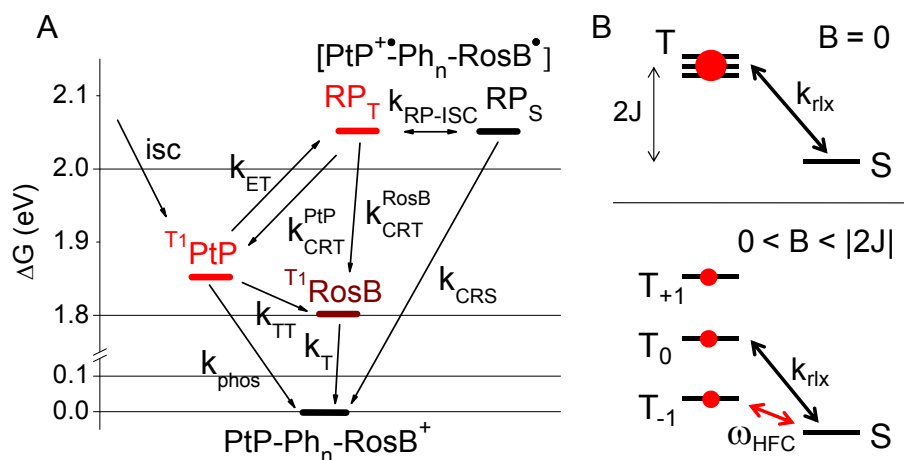


**Figure 6.4.** Energy diagram and a proposed mechanism of MFE on phosphorescence. (A) State energy diagram of dyads.  $\text{PtP-Ph}_n\text{-RosB}^+$  - ground state (GS);  $[\text{PtP}^{+\bullet}\text{-Ph}_n\text{-RosB}^{\bullet*}]$  - radical pair state (RP). (B) Diagram of RP-ISC in the absence and presence of magnetic field.

Both NSTA and TREPR data point towards existence of a long-lived (microsecond scale) radical intermediate(s), which is presumably a RP formed as a result of triplet ET originating in  $^{\text{T}1}\text{PtP}$  triplet state and not in  $^{\text{s}1}\text{RosB}^+$  (or  $^{\text{s}1}\text{PtP}$ ) singlet state. Indeed, the FSTA measurements clearly show that  $^{\text{T}1}\text{PtP}$  is populated immediately upon excitation. No  $\text{S}_1\text{-S}_n$  absorption features of  $\text{RosB}^+$  were observed by either FSTA nor NSTA. The TREPR measurements revealed that radical intermediates rise on the time scale of  $\sim 1 \mu\text{s}$ , while  $^{\text{s}1}\text{RosB}^+$  state is much shorter lived ( $\tau \sim 3 \text{ ns}$ ). Therefore, we reasoned that the RP is first created in the triplet state.

A proposed diagram of the processes occurring in the dyads upon population of  $^{\text{T}1}\text{PtP}$  is shown in Fig. 6.4A. (For rate constants and quantum yields see Table 6.A3.) Once formed by way of triplet ET, the RP may either recombine back to the local  $^{\text{T}1}\text{PtP}$  state ( $k_{\text{CRT}}$ ) or decay non-radiatively *via* singlet charge recombination ( $k_{\text{CRS}}$ ). In addition, RP may lose spin coherence during its long lifetime and recombine as two uncorrelated radicals, or it may decay to the local  $^{\text{T}1}\text{RosB}$  triplet state directly ( $k_{\text{CRT}}^{\text{RosB}}$ ) or *via*  $^{\text{T}1}\text{PtP} \rightarrow ^{\text{T}1}\text{RosB}$  triplet-triplet energy transfer ( $k_{\text{TT}}$ ).

Notably, unlike in PtP-RhB<sup>+</sup> systems,<sup>153</sup> we could not observe lengthening of the PtP triplet decay, which would be expected for <sup>T1</sup>PtP ↔ <sup>T1</sup>RosB thermal equilibrium.

In the context of the proposed scheme, the essence of the observed MFE on the phosphorescence is the magnetic modulation of the intersystem crossing in the RP (RP-ISC). In the absence of the field (Fig. 6.4B), spin-lattice relaxation<sup>64</sup> is thought to be the dominant process coupling the RP triplet and singlet states.<sup>210</sup> Spin relaxation rates in RPs ( $k_{\text{rlx}}$ ) are typically on the order of  $10^5$ - $10^6$  s<sup>-1</sup>,<sup>64, 189</sup> which is comparable to the observed RP decay kinetics and consistent with the fact the TREPR signals exhibit microwave power dependence.

In the presence of external magnetic field, Zeeman splitting moves T<sub>1</sub> sublevel closer to the singlet state (Fig. 6.4B), facilitating their mixing *via* hyperfine coupling (HFC) interactions.<sup>7</sup> HFC-mediated mixing corresponds to rates of  $\sim 10^8$  s<sup>-1</sup> ( $\omega_{\text{HFC}}$ ) at resonance,<sup>185</sup> i.e. 2-3 orders of magnitude faster than the spin relaxation. Therefore, at fields approaching the resonance, HFC acts to increase the fraction of singlet character in the RP, facilitating the subsequent singlet charge recombination. S-T mixing by the  $\Delta g$  mechanism<sup>7</sup> may also play a role, since the  $g$ -factor of PtP<sup>+</sup> is different from that of RosB<sup>\*</sup> by 0.003, which corresponds  $\omega \sim 10^8$  s<sup>-1</sup> at 1 T.

It is important to emphasize that the singlet and triplet states of the RP are coupled even in the absence of the field. Consequently, the <sup>T1</sup>PtP state is able to decay *via* the ET-spin relaxation-singlet charge recombination pathway, as well as other pathways (i.e. CR<sub>T</sub> with formation of non-emissive <sup>T1</sup>RosB, TT pathway, spin dephasing and incoherent radical recombination) with the net effect of decreasing the quantum yield of phosphorescence. As a result, the fraction of the channel potentially susceptible to magnetic influence in the whole RP deactivation process is small, and the observed MFE on phosphorescence is only ~1% (Fig. 6.2A).

The phosphorescence did not show tendency to intensify upon increase in the field strength up to 1 T. Assuming that S-T<sub>1</sub> mixing is predominantly due to the HFC interaction, this

suggests that the singlet-triplet energy gap ( $2J$ ) in the RP's is rather high, which is not uncommon for RP's with short interchromophoric distances ( $r_{DA}$ ),<sup>182, 189, 211</sup> including triplet ET systems incorporating metalloporphyrins.<sup>212</sup> Based on modeling, in **1** and **2** edge-to-edge  $r_{DA}$  distances are 10 and 14.1 Å, respectively.

Kinetic simulations using the proposed model successfully reproduced the observed MFE, i.e. a ~1% decrease in the triplet yield when the rate of RP-ISC changed from  $k_{RP-ISC}=10^5 \text{ s}^{-1}$  (spin relaxation in the absence of magnetic field) to  $k_{RP-ISC}=10^8 \text{ s}^{-1}$  (HFC and/or  $\Delta g$  mediated coupling in the presence of the field). RP-ISC was approximated by an equilibrium with the forward and reverse rate constants set to the reciprocal of the oscillation frequency ( $k_{RP-ISC}=1/\omega$ ), taking into account slow RP decay rate relative to  $1/\omega$ .<sup>213</sup> The model shows that the MFE could be larger (see the Appendix to this chapter) if there would be lesser fraction of the RP decaying *via* alternative pathways (e.g. spin relaxation). Therefore, future molecular designs should attempt to reduce these pathways.

The proposed model bears similar features with the mechanism of MFE on the fluorescence of exciplexes,<sup>28</sup> except that in our case RP exists in equilibrium not with an exciplex, but with a local phosphorescent triplet state. Recent studies of ET processes originating in triplet states shed light on the electron spin polarization in the corresponding RPs.<sup>214-215</sup> For example, pertinent to our case, slow ET step suggests that the net absorption signal in the RP should reflect population of the triplet sublevels in  $^1\text{PtP}$ .<sup>216-217</sup> In the future, it will be interesting to examine this correlation.

## 6.5 Conclusions

In conclusion, we have demonstrated feasibility of magnetic modulation of phosphorescence at room temperature by influencing spin dynamics in radical pairs, formed as a result of photoinduced electron transfer. The developed model of the effect suggests approaches

to maximization of the MFE and sets the stage for rational design of optical probes with magnetically controlled emissivity.

## 6.6 Appendix

### 6.6.1 The setup of MARY spectroscopy

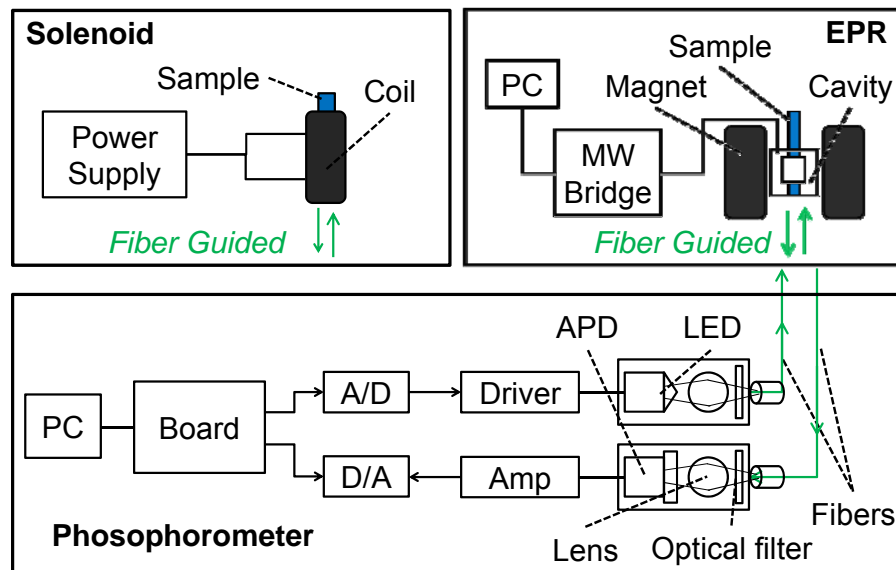


**Figure 6.A1.** Diagram of the setup for phosphorescence MARY spectroscopy.

## 6.6.2 Optical spectroscopy data

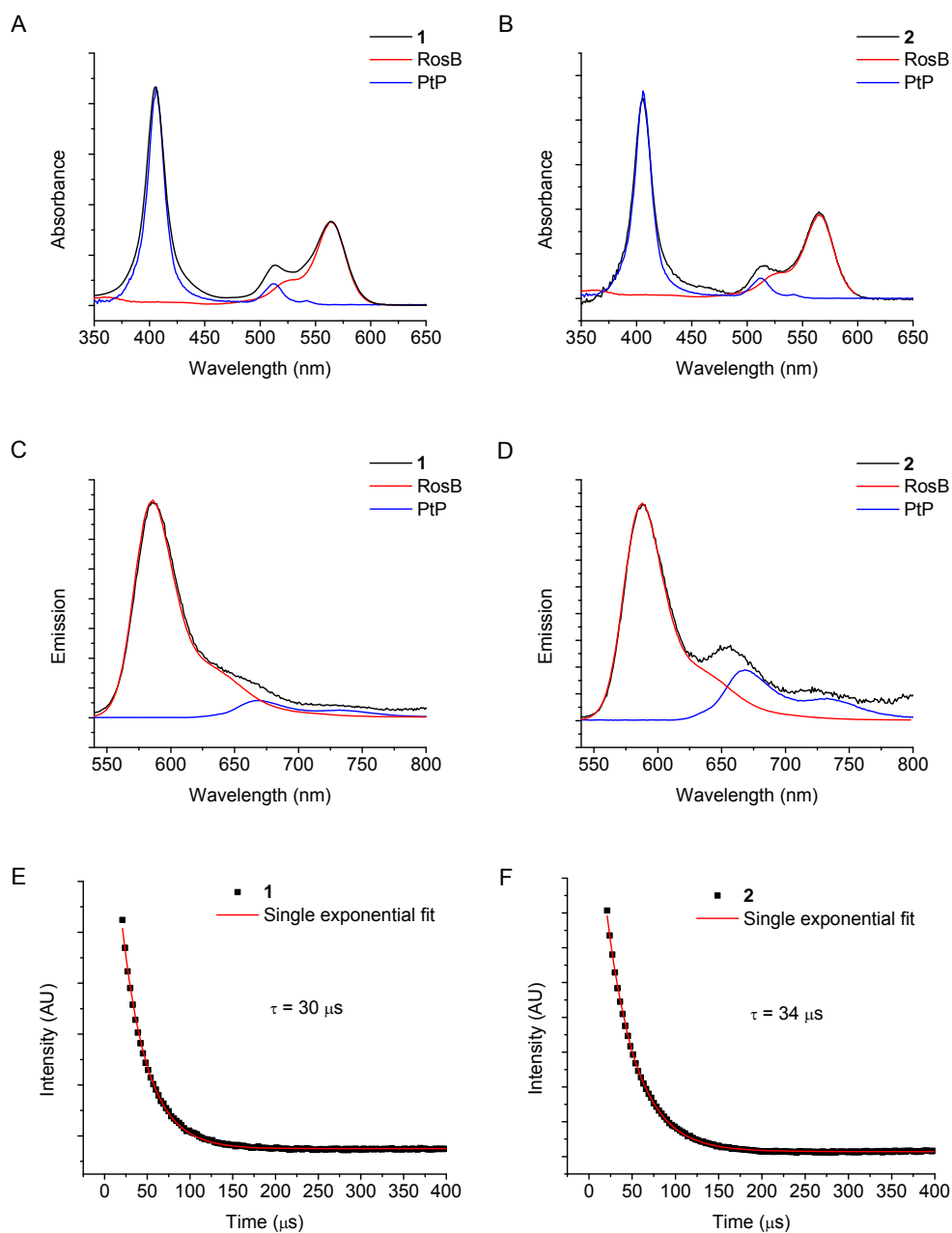


**Figure 6.A2.** Some spectral features of **1** and **2**. Steady state absorption spectra: **1** (A) and **2** (B). Spectra of individual components were obtained by linear decomposition. Steady state emission spectra ( $\lambda_{\text{ex}}=430$  nm): **1** (C) and **2** (D). Phosphorescence decays in deoxygenated solutions: **1** (E) and **2** (F).

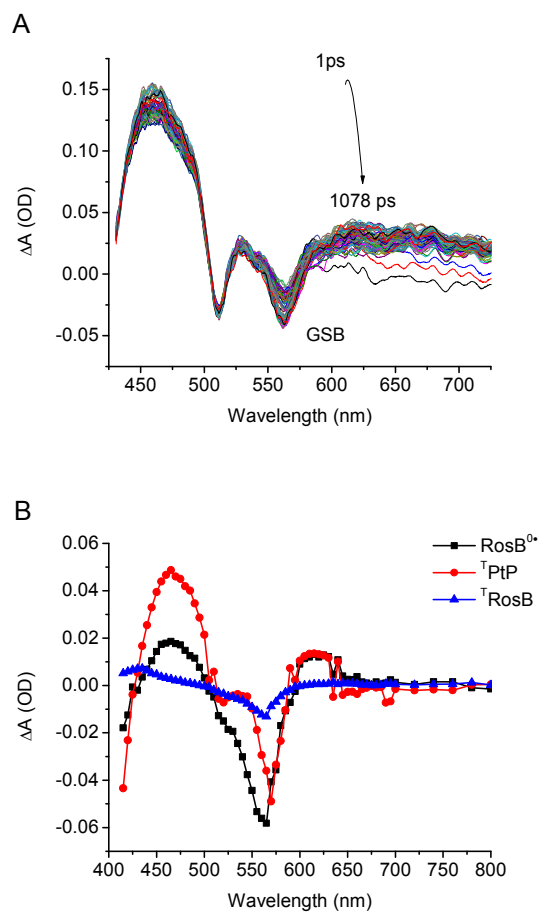
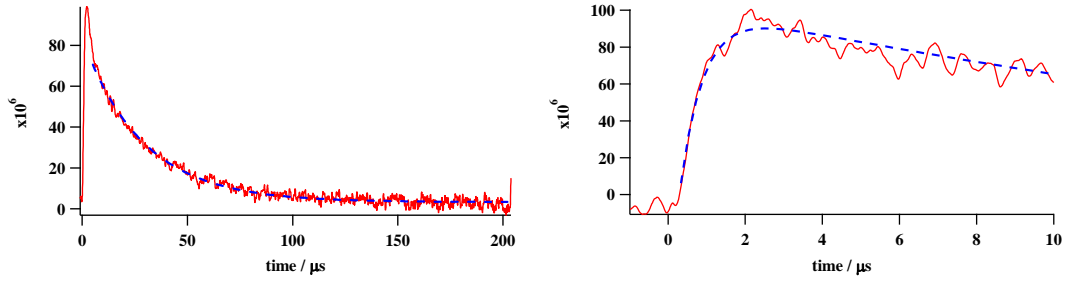


**Figure 6.A3.** Time evolution of **2** upon photo excitation at 405 nm. (A) FSTA spectra of **2** ( $\lambda_{ex}=405$  nm). (B) Decay associated spectra of **2** obtained from global fitting of NSTA data ( $\lambda_{ex}=405$ nm).

### 6.6.3 TREPR data

(Top) 3 mW ( $\tau_{\text{rise}}=600$  ns,  $\tau_{\text{decay}}=28.8$   $\mu\text{s}$ )



(Bottom) 0.2 mW ( $\tau_{\text{rise}} = 1.21$   $\mu\text{s}$ ,  $\tau_{\text{decay}} = 40.8$   $\mu\text{s}$ )

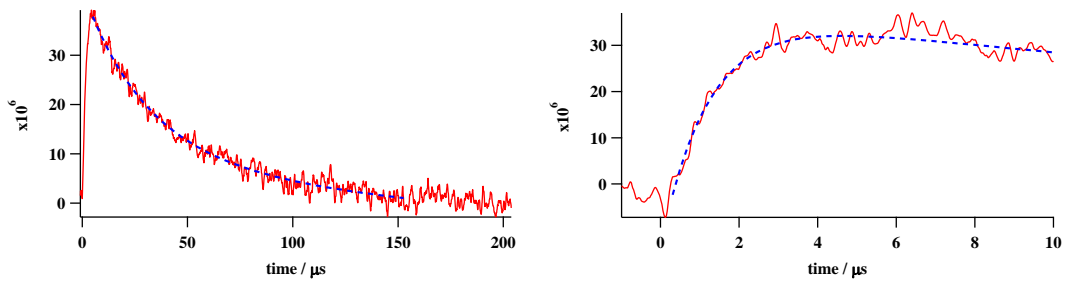
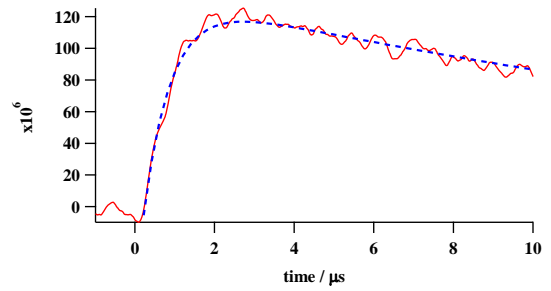
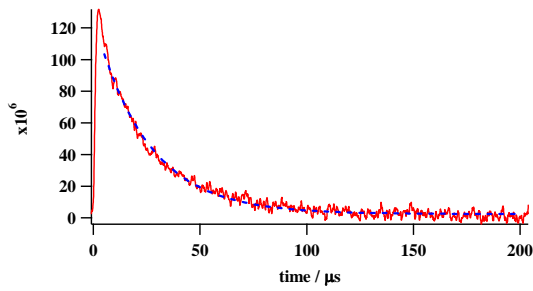


**Figure 6.A4.** TREPR signal evolution for 1. Top - microwave power 3 mW. Bottom - microwave power 0.2 mW.

(Top) 3 mW ( $\tau_{\text{rise}} = 690 \text{ ns}$ ,  $\tau_{\text{decay}} = 25.0 \text{ } \mu\text{s}$ )



(Bottom) 0.2 mW ( $\tau_{\text{rise}} = 1.18 \text{ } \mu\text{s}$ ,  $\tau_{\text{decay}} = 36.2 \text{ } \mu\text{s}$ )

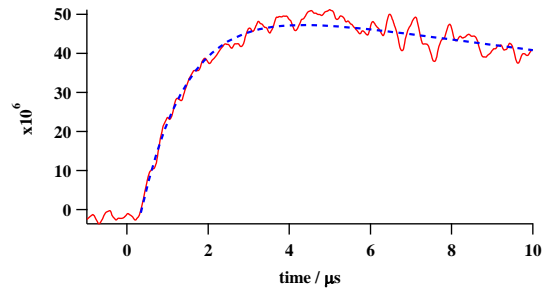
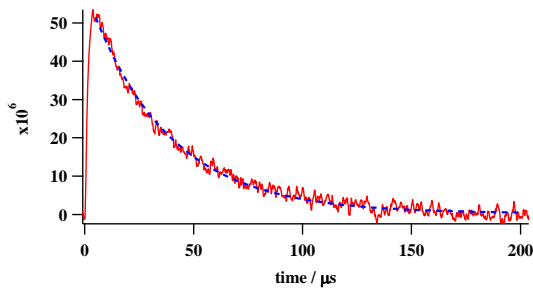


**Figure 6.A5.** TREPR signal evolution for **2**. Top - microwave power 3 mW. Bottom - microwave power 0.2 mW.

## 6.6.4 Data tables

**Table 6.A1.** Redox potentials (vs SCE).

Compound	$E_{\text{ox}}$	$E_{\text{red}}$
PtP	$1.20 \pm 0.05$	--
RosB-Br	$1.33 \pm 0.05$	$-0.85 \pm 0.05$
<b>1</b>	$1.17 \pm 0.05$	$-0.88 \pm 0.05$
<b>2</b>	$1.16 \pm 0.05$	$-0.88 \pm 0.05$

**Table 6.A2.** Time constants of rise and decay phases of TREPR signals (in  $\mu\text{s}$ ).

Compound	3 mW		0.2 mW	
	Rise	Decay	Rise	Decay
<b>1</b>	0.60	28.8	1.21	40.8
<b>2</b>	0.69	25	1.18	36.2

**Table 6.A3.** Photophysical rate constants and emission quantum yields.<sup>a</sup>

Compound	$\Phi_{\text{phos}}$ ( $\lambda_{\text{ex}} = 510\text{nm}$ )	$k_{\text{phos}} (\text{s}^{-1})$	$k_{\text{ET}} (\text{s}^{-1})$	$k_{\text{T}} (\text{s}^{-1})$	$\Phi_{\text{fl}}$	$k_{\text{fl}} (\text{s}^{-1})$
<b>1</b>	0.01	$3.33 \times 10^4$	$<1.00 \times 10^6$	$7.7 \times 10^2$	0.07	$1.67 \times 10^9$
<b>2</b>	0.02	$2.94 \times 10^4$	$\sim 1.00 \times 10^6$	$7.4 \times 10^2$	0.25	$0.57 \times 10^9$
PtP	0.13	$1.88 \times 10^4$	--	--	--	--
RosB-Br	--	--	--	--	0.30	$0.33 \times 10^9$

<sup>a</sup>All measurements were performed in deoxygenated anhydrous benzonitrile solutions at room temperature.

### 6.6.5 Kinetic simulations

All the simulations were performed using MATLAB R2009a (MathWorks, MA).

Definition of states:

|1> = PtP triplet state

|2> = RP triplet state

|3> = RP singlet state

|4> = RosB triplet state

|5> = Ground state (GS)

After formation of the PtP triplet state, the evolution of the states can be described by a system of linear differential equations:

$$\begin{pmatrix} \frac{\partial |1\rangle}{\partial t} \\ \frac{\partial |2\rangle}{\partial t} \\ \frac{\partial |3\rangle}{\partial t} \\ \frac{\partial |4\rangle}{\partial t} \\ \frac{\partial |5\rangle}{\partial t} \end{pmatrix} = \begin{pmatrix} -k_{phos} - k_{ET} - k_{FTT} & k_{BET} & 0 & k_{BTT} & 0 \\ k_{ET} & k_{BET} - k_{ISC} - k_{CRT} & k_{BISC} & k_{CST} & 0 \\ 0 & k_{ISC} & -k_{BISC} & 0 & 0 \\ k_{FTT} & k_{CRT} & 0 & -k_T - k_{CST} - k_{BTT} & 0 \\ k_{phos} & 0 & k_{CRS} & k_T & 0 \end{pmatrix} \begin{pmatrix} |1\rangle \\ |2\rangle \\ |3\rangle \\ |4\rangle \\ |5\rangle \end{pmatrix}.$$

The decay constants ( $s^{-1}$ ) are defined as follows:

$k_{phos} = 1.8 \times 10^4$ ; % PtP phosphorescence

$k_{ET} = 10^6$ ; % Primary ET from triplet PtP to triplet RP

$k_{BET} = 10^7$ ; % Back electron transfer from triplet RP to triplet PtP

$k_{ISC} = k_{no-rlx}$  or  $k_{rlx}$  or  $k_{HFC}$ ; % Forward RP-ISC

$k_{\text{BISC}}=k_{\text{no-rlx}}$  or  $k_{\text{rlx}}$  or  $k_{\text{HFC}}$ ; % Backward RP-ISC

$k_{\text{FTT}}=10^4$ ; % Forward triplet energy transfer (TT) from PtP to RosB

$k_{\text{BTT}}=0$ ; % Backward TT from RosB to PtP

$k_{\text{CRT}}=1.7 \times 10^5$ ; % Triplet charge recombination from triplet RP to triplet RosB

$k_{\text{CST}}=10$ ; % Triplet ET from triplet RosB to triplet RP

$k_{\text{CRS}}=2.5 \times 10^4$ ; % Singlet charge recombination from singlet RP to ground state

$k_{\text{T}}=10^3$ ; % Triplet RosB decay to ground state

The initial condition (at time 0) were set to be: (1; 0; 0; 0; 0). Simulations span the period from  $t=0$  to  $t=1$  ms with the time step of 10 ns.

Triplet RP and singlet RP are considered to be in "equilibrium":  $k_{\text{ISC}}=k_{\text{BISC}}$ .

The MFE is defined as follows:  $\text{MFE}(\%)=100 \times (1 - Y_{\text{T}}(\text{MF ON})/Y_{\text{T}}(\text{MF OFF}))$ , where  $Y_{\text{T}}$  is the population of PtP triplet state.

In simulations all constants were fixed, but  $k_{\text{ISC}}=k_{\text{BISC}}$  were varied.

#### Case 1:

MF OFF:  $\text{RP}_{\text{S}}$  and  $\text{RP}_{\text{T}}$  are coupled *via* spin relaxation:  $k_{\text{ISC}}=k_{\text{BISC}}=k_{\text{rlx}}=10^5 \text{ s}^{-1}$ .

MF ON:  $\text{RP}_{\text{S}}$  and  $\text{RP}_{\text{T}}$  are coupled *via* HFC:  $k_{\text{ISC}}=k_{\text{BISC}}=k_{\text{HFC}}=10^8 \text{ s}^{-1}$ .

MFE=1.3%

#### Case 2:

MF OFF:  $\text{RP}_{\text{S}}$  and  $\text{RP}_{\text{T}}$  are not coupled:  $k_{\text{ISC}}=k_{\text{BISC}}=k_{\text{no-rlx}}=0 \text{ s}^{-1}$ .

MF ON:  $\text{RP}_{\text{S}}$  and  $\text{RP}_{\text{T}}$  are coupled *via* HFC:  $k_{\text{ISC}}=k_{\text{BISC}}=k_{\text{HFC}}=10^8 \text{ s}^{-1}$ .

MFE = 6.5 %

*Acknowledgements: Dr. Mana Tanabe and Dr. Seigo Yamauchi of Tohoku University (data collection of time-resolved electron paramagnetic spectroscopy), Dr. Nikolai N. Tkachenko of Tampere University of Technology (experimental setup of femtosecond and nanosecond transient absorption spectroscopy), Dr. Thomas Troxler (technical assistance for nanosecond transient absorption spectroscopy and fluorescence lifetime measurements), and Dr. Robin M. Hochstrasser (discussion).*

## CHAPTER 7 Introduction to The Magnetic Field Effects on Triplet-Triplet Exciton Pair

In this chapter, we outline the theory behind the magnetic field effects (MFE) on triplet-triplet exciton (TT) pair.

### 7.1 Johnson-Merrifield theory

Johnson et al.<sup>218</sup> discovered that the intensity of delayed fluorescence originating from triplet-triplet annihilation in anthracene crystals is affected by external magnetic field at ambient temperatures. This delayed fluorescence can be generated according to the following scheme:



where  $S_0$ ,  $S_1$ , and  $T_1$  are the electronic ground state, the first singlet and triplet excited states of the molecule, respectively;  $k_1$ ,  $k_{-1}$  and  $k_S$  represent the rate constants of each reaction.

Magnetically affected processes are those involving pairs of two triplet excitons. Equations 7.3-7.5 show that TT pairs can interact, transferring electronic energy onto products through processes involving change in spin multiplicity. These equations can be combined into a single equation:

$$T_1 + T_1 \rightleftharpoons (TT) \rightarrow S_1 + S_0 \quad (\text{Eq. 7.7})$$

The reverse of this process is called singlet fission.

In the Johnson-Merrifield theory, the spin Hamiltonian of the TT pair is written as a superposition of the individual triplet spin Hamiltonians, while neglecting any exchange interaction.

$$H_{T(i)} = D_i(S_{z,i}^2 - 1/3S_i^2) + E(S_{x,i}^2 - S_{y,i}^2) + g\mu_B B_0 S_i \quad (\text{Eq. 7.8})$$

where the first two terms correspond to ZFS (Zero-Field Splitting), where D and E are the ZFS parameters, and the last term is the electronic Zeeman Hamiltonian, where g is the g-factor for the triplet exciton, which is considered to be isotropic and identical to each other (g=2).  $\mu_B$  is the Bohr magneton, and  $B_0$  is the external magnetic field.  $S_i$  denotes spin operators for triplet excitons. One of the most important properties of this expression lies in the fact that it is invariant under interchange of the two excitons, assuming equal ZFS tensors, i.e. identical excitons. Therefore, the eigenstates of  $H_{T(i)}$  can be classified into those which are even and odd under the interchange operation.

In the low-field limit, these eigenstates can be expressed in terms of the ZFS wave functions of individual excitons:

$$\begin{aligned} |S\rangle &= 3^{-1/2}(|xx\rangle + |yy\rangle + |zz\rangle) \\ |T_x\rangle &= 2^{-1/2}(|yz\rangle - |zy\rangle) \\ |T_y\rangle &= 2^{-1/2}(|zx\rangle - |xz\rangle) \\ |T_z\rangle &= 2^{-1/2}(|xy\rangle - |yx\rangle) \\ |Q_a\rangle &= 2^{-1/2}(|xx\rangle - |yy\rangle) \\ |Q_b\rangle &= 6^{-1/2}(|xx\rangle + |yy\rangle - 2|zz\rangle) \\ |Q_x\rangle &= 2^{-1/2}(|yz\rangle + |zy\rangle) \\ |Q_y\rangle &= 2^{-1/2}(|zx\rangle + |xz\rangle) \\ |Q_z\rangle &= 2^{-1/2}(|xy\rangle + |yx\rangle) \end{aligned} \quad (\text{Eq. 7.9})$$

The singlet and quintet states are even under interchange of the two triplet excitons, while the triplet states are odd. This is general, regardless of the strength of the field. Thus, the Hamiltonian can mix the quintet and singlet states, while the triplet states cannot mix with either singlet or quintet states. It should be noted that spin relaxation still can cause decay between odd and even states, and that is explicitly treated in the Atkins-Evans theory (Chapter 7.2). However, relaxation can be considered negligible for the case of anthracene crystals, for which the Johnson-Merrifield theory was initially developed.

In the high-field limit (i.e. the Zeeman interaction is much larger than ZFS), the spin states of the pair can be expressed in terms of the high-field eigenstates of individual triplets, i.e. the pure spin states:

$$\begin{aligned}
|S\rangle &= 3^{-1/2}(|00\rangle - |+-\rangle - |-+\rangle) \\
|T_{+1}\rangle &= 2^{-1/2}(|+0\rangle - |0+\rangle) \\
|T_0\rangle &= 2^{-1/2}(|+-\rangle - |-+\rangle) \\
|T_{-1}\rangle &= 2^{-1/2}(|-0\rangle - |0-\rangle) \\
|Q_{+2}\rangle &= |++\rangle \\
|Q_{+1}\rangle &= 2^{-1/2}(|+0\rangle + |0+\rangle) \\
|Q_0\rangle &= 6^{-1/2}(2|00\rangle + |+-\rangle + |-+\rangle) \\
|Q_{-1}\rangle &= 2^{-1/2}(|-0\rangle + |0-\rangle) \\
|Q_{-2}\rangle &= |--\rangle
\end{aligned}
\tag{Eq. 7.10}$$

In the presence of degeneracy, the linear combinations of the degenerate pair states are to be used. In the case of degeneracy resulting from the interchange symmetry (e.g.  $|+-\rangle$  and  $|-+\rangle$ ), even and odd combinations are used (e.g.  $2^{-1/2}(|+-\rangle + |-+\rangle)$  and  $2^{-1/2}(|+-\rangle - |-+\rangle)$ ). This means that the odd combination is a pure triplet.

Based on kinetics arguments, it can be shown that the reaction probability  $\gamma_{TT}$  for triplet-triplet annihilation leading to the formation of singlet state can be expressed in the following manner:

$$\gamma_{TT} = \frac{1}{9} k_1 \sum_i \frac{k_S |S_i|^2}{k_{-1} + k_S |S_i|^2} \quad (\text{Eq. 7.11})$$

where the singlet amplitudes  $|S_i|^2$  are constrained by the rule:  $\sum_i |S_i|^2 = 1$ . The value  $\gamma_{TT}$  depends on the manner in which the singlet character is distributed over the mixable pair states. If N pair states have equal singlet character, we can rewrite the Eq. 7.11 as:

$$\gamma_{TT} = \frac{1}{9} k_1 \frac{k_S}{k_{-1} + k_S / N} \quad (\text{Eq. 7.12})$$

where  $\gamma_{TT}$  is a monotonically increasing function of N. In the absence of magnetic field, from the Eq. 7.9, three pair states have singlet character (i.e.  $|xx\rangle$ ,  $|yy\rangle$ ,  $|zz\rangle$ ). In the high-field limit, from the Eq. 7.10, one can see that only two states can possess singlet character, namely,  $|00\rangle$  and  $2^{-1/2}(|+-\rangle + |-+\rangle)$ . This shows that  $\gamma_{TT}$  is smaller in the high-field limit than in the low field. At certain magnetic field orientations, the above two states can be degenerate, and  $\gamma_{TT}$  is lower. At intermediate fields, where the magnetic field is comparable to ZFS, the singlet character can be distributed over all of the even pair states, and  $\gamma_{TT}$  is larger than at zero field. This is a resonance effect, which depends on the orientation of triplet excitons in the magnetic field.

The essence of the Johnson-Merrifield theory is that the magnetic field dependence of triplet-triplet annihilation comes from the ZFS interaction and its influence on the level-crossing of the pair eigenstates. The ZFS interactions mix the singlet and quintet states of a TT pair and a level crossing resonance can be induced in a crystal by varying the orientation of the crystal with respect to the laboratory field direction. In general, the Johnson-Merrifield theory is successful in quantitatively describing both the anisotropy and magnetic field dependence of the delayed

fluorescence resulting from triplet-triplet annihilation in molecular crystals because one can assume that the energy separation of the pair eigenstates is larger than the kinetic width due to the relatively large ZFS in molecular crystals.

## 7.2 Atkins-Evans theory

The Johnson-Merrifield theory does not take into account the interference between the effect of ZFS and molecular tumbling. In solutions, where the molecular constituents of the TT pair can undergo rapid rotational tumbling, the ZFS is averaged out. Thus magnetic field can exhibit its influence only by inducing spin relaxation between the eigenstates of the spin Hamiltonian. Atkins and Evans incorporated dynamical properties of liquids to extend the Johnson-Merrifield theory.

The magnetic field dependence arises because of the Zeeman energy difference between the singlet, triplet, and quintet states within a TT pair, which are degenerate in the absence of magnetic field and if no spin-exchange interaction is present ( $J=0$ ). The dependence on rotational parameters arises from the relaxation behavior of the triplets. The rotational modulation of the ZFS interactions relaxes the quintet phasing of the component spins into the phasing appropriate to the singlet. The dependence on translational parameters enters through the diffusion controlled re-encounter probability of the triplets.

In this theory, the reaction proceeds spin-selectively in the first encounter, producing some overpopulation of quintet and triplet spin states of the TT pair. The spin evolution of the pairs is calculated on the basis of independent spin relaxation in the separated triplets with quantitative use of the Redfield formalism of relaxation. The following result is obtained for the time dependence of singlet character of a TT pair after a random encounter at  $t=0$ , when the singlet probability was zero, and then the probability of triplet-triplet annihilation integrating over time can be expressed as:

$$P_{TT}(B) = \lambda_T [1 - \lambda_T + \lambda_T f_{TT}(B)] \quad (\text{Eq. 7.13})$$

$$\phi_{TT} = \frac{\lambda_{TT}}{1 - \lambda_{TT}} \quad (\text{Eq. 7.14})$$

Here,  $f_{TT}(B)$  is expressed as:

$$f_{TT}(B) = \frac{1}{9} \{8 - [F(6R_{1100}) + F(2W_{1T}) + 2F(-2R_{1-1-1}) + 2F(2W_{2T}) + 2F(2R_{1010} - 2R_{100-1})]\} \quad (\text{Eq. 7.15})$$

with the following parameters

$$F(s) = \frac{\sinh[(s\tau_a)^{1/2}] \exp[-(s\tau_a)^{1/2}]}{(s\tau_a)^{1/2}} \quad (\text{Eq. 7.16})$$

$$\tau_a = 9\tau_r \quad (\text{Eq. 7.17})$$

$$W_{1T} = R_{1100} + 2R_{1-1-1} \quad (\text{Eq. 7.18})$$

$$W_{2T} = -R_{1010} - R_{100-1} \quad (\text{Eq. 7.19})$$

$\tau_a$  is the translational correlation time and is connected to  $\tau_r$ , the rotational correlation time, by the Stokes-Einstein relation.  $W_{1T}$  and  $W_{2T}$  are the reciprocal of the longitude relaxation (or spin-lattice relaxation) time and the reciprocal of the transverse relaxation (or spin-spin relaxation) time, respectively.  $R$  is the Redfield relaxation matrix and given by:

$$R_{1100} = \frac{2}{15} k(B) \quad (\text{Eq. 7.20})$$

$$R_{1-1-1} = \frac{4}{15} k(2B) \quad (\text{Eq. 7.21})$$

$$R_{1010} = -\frac{1}{5} [k(0) + k(B) + \frac{2}{3} k(2B)] \quad (\text{Eq. 7.22})$$

$$R1 - 11 - 1 = \frac{2}{5}[k(B) + 2k(2B)] \quad (\text{Eq. 7.23})$$

where

$$k(B) = \frac{(D^2 + 3E^2)\tau_r}{1 + (g\mu_B B \hbar^{-1} \tau_r)} \quad (\text{Eq. 7.24})$$

The application of the external magnetic field diminishes the ZFS-induced transition probabilities through relaxations, which decreases the population of singlet state within a TT pair, resulting in the reduction of the delayed fluorescence.

### 7.3 Summary

We overviewed the Johnson-Merrifield theory and the Atkins-Evans theory. A major difference between the two theories is the origin of the magnetic field dependence. In the Johnson-Merrifield theory, the MFE comes from the competition between ZFS within the individual triplets and the interaction with the applied field (Zeeman splitting). On the other hand, in the Atkins-Evans theory the MFE originates in the magnetic field dependence of spin relaxation. We employed the Atkins-Evans theory to the molecular system in solutions in Chapter 8.

## CHAPTER 8 Magnetic Field Effects on Triplet-Triplet Annihilation in Solutions: Modulation of Visible/NIR Luminescence

In this chapter, we discuss the molecular system in which we observed magnetic modulation of molecular emissivity in solutions sensitized *via* triplet-triplet annihilation. This work has been published: \* Magnetic Field Effects on Triplet-Triplet Annihilation in Solutions: Modulation of Visible/NIR Luminescence. Mani, T.; Vinogradov, S.A.; *J. Phys. Chem. Lett.* **2013**, *4*, 2799-2804.

### 8.1 Summary

Photon upconversion based on sensitized triplet-triplet annihilation (TTA) presents interest for such areas as photovoltaics and imaging. Usually energy upconversion is observed as  $\rho$ -type delayed fluorescence from molecules whose triplet states are produced *via* energy transfer from a suitable triplet donor, followed by TTA. Magnetic field effects (MFE) on delayed fluorescence in molecular crystals are well known; however, there exist only a few examples of MFE on TTA in solutions, and all of them are limited to UV-emitting materials. Here we present MFE on TTA-mediated visible emission, sensitized by far-red absorbing metalloporphyrins in solutions at room temperature. In addition to visible delayed fluorescence from annihilator, we also observed near-infrared emission from the sensitizer, occurring as a result of triplet-triplet energy transfer back from annihilator, termed "delayed phosphorescence". This emission also exhibits MFE, but opposite in sign to the annihilator fluorescence.

---

\* Adapted with permission. Copyright © 2013, American Chemical Society

## 8.2 Introduction

Magnetic field effects (MFE)<sup>7</sup> present an attractive opportunity to impose control over excited electronic states of molecules, drawing attention from many areas of technology. For example, in optical imaging magnetic control over probes' emissivity may serve to enhance spatial resolution,<sup>57, 219</sup> while in the medical arena the ability to magnetically modulate sensitized generation of singlet oxygen could be a valuable asset for photodynamic therapy.<sup>59</sup> The key to such applications are molecules with strong optical transitions in the visible/NIR spectral region and excited states responsive to magnetic fields.

Three kinds of MFE on molecular luminescence are known. The first involves emission from exciplex states existing in equilibrium with radical pairs (RP) formed upon photoinduced electron transfer (PET).<sup>27-28</sup> External magnetic field modulates spin interconversion within a RP, affecting the charge recombination channel coupled to the formation of emissive exciplexes. In some cases fluorescence from the parent local singlet state may also be modulated.<sup>28</sup> Another kind, reported recently, is the MFE on phosphorescence, whereby a RP is included into a pathway leading to the formation (or decay) of an emissive local triplet state.<sup>220</sup> The third kind is the MFE on triplet-triplet annihilation (TTA) and subsequent *p*-type delayed fluorescence.<sup>218, 221</sup> This effect has been observed in molecular crystals and studied extensively by Merrifield and co-workers,<sup>218, 222-223</sup> and soon thereafter reported for photosensitized TTA in solutions.<sup>30-31</sup> Several related studies, including MFE's on quenching of delayed fluorescence by oxygen<sup>224-225</sup> and electro-generated luminescence<sup>226-227</sup> have also been published.

During the past decade significant progress has been made in the TTA field,<sup>73, 228-229</sup> and many efficient photosensitized upconversion systems have been developed, including ones with absorption in the red and near infrared (NIR) spectral regions.<sup>230-234</sup> In one such system, MFE on TTA in polymeric membranes has been observed,<sup>235</sup> and more recently a study of MFE on fluorescence dynamics in closely related singlet fission systems has been published.<sup>236</sup> Here we report MFE's in solution-based TTA systems where the role of photosensitizers is played by

strongly red-absorbing  $\pi$ -extended metalloporphyrins. Such systems may present interest for bio-imaging applications,<sup>237</sup> where multiphoton excitation by low-power NIR sources is especially attractive because of low risk of photodamage and reduced scattering. In addition to the well-known MFE on delayed fluorescence we also report a new effect, which is manifested by magnetic modulation of the emission originated from the sensitizer, termed "delayed phosphorescence". The two MFE's were found to exhibit opposite signs.

The process leading to photo-sensitization of delayed fluorescence involves in its initial step triplet-triplet energy transfer (TTET) from donor-sensitizer to acceptor-annihilator (Fig. 8.1). Sensitizers are usually chosen to be molecules efficiently forming long-lived triplet states *via* fast intersystem crossing (ISC). In this regard, Pt and Pd porphyrins are especially attractive, as they are characterized by very strong spin-orbit coupling and form triplet states with nearly unity efficiency.<sup>120, 125</sup> The corresponding upconversion gaps, reported for porphyrin-based TTA systems, reach up to  $\sim 0.8$  eV.<sup>73</sup>

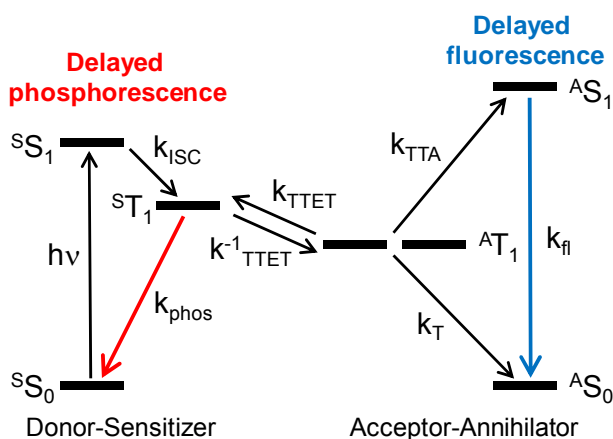


**Figure 8.1.** Energy diagram associated with sensitized triplet-triplet annihilation.

In a well-designed TTA system the triplet state of the sensitizer ( $^3T_1$ ) should be efficiently quenched by the annihilator *via* TTET. Therefore, little or no phosphorescence from the donor (provided the donor triplet state is phosphorescent) should be observed. However, if the triplet

state of the acceptor  $^A T_1$  is energetically close to  $^S T_1$ , and its own decay is slower than that of the donor phosphorescence,  $k_T \ll k_{\text{phos}}$ , the equilibrium between the two states may be established, leading to the appearance of "delayed phosphorescence". This kind of emission is usually not mentioned in the TTA literature, however in our systems it has been detected and found to be magnetically sensitive.

The theory of MFE on TTA was originally developed by Merrifield<sup>222, 238</sup> and Suna<sup>239</sup> for triplet excitons in molecular crystals, and later extended by Atkins and Evans<sup>240</sup> to include the dependence of TTA on rotational and translational parameters of freely moving triplet molecules in solution. Recently, extension of the theory has been applied to systems undergoing singlet exciton fission.<sup>236</sup> The rate of the TTA *via* the singlet channel - the one that leads to the appearance of delayed fluorescence, - depends on the distribution of singlet character over the nine spin states of the interacting triplet-triplet (TT) pair, i.e. singlet, triplets and quintets. Based on kinetic arguments, more uniform distribution leads to a higher recombination rate and *vice versa* (singlet dilution principle).<sup>222</sup> For a pair of equivalent triplets, i.e. the case most relevant to photon upconversion *via* TTA, symmetry considerations dictate that only six out of nine spin states of the TT pair (singlet and quintets) can possess singlet character regardless of the field strength.<sup>238</sup> The triplet states of the pair are able to enter only the triplet recombination channel, and that is field-independent. The singlet character distribution changes from zero-field, when the spin is quantized along the axes of the ZFS (zero-field splitting) tensor in each triplet molecule, to the high field limit, when the states of the pair are derived from the pure spin states of the triplet components, split by the Zeeman interaction. In low field, the singlet character is distributed more uniformly over the pair states, leading to a higher rate of recombination and hence higher yield of delayed fluorescence. In the high field limit, the singlet becomes "concentrated" on just two pair states, and the yield of fluorescence decreases. Importantly, fewer annihilator triplets ( $^A T_1$ ) entering the singlet recombination channel mean higher population of the sensitizer triplets ( $^S T_1$ ) *via* the triplet-triplet energy transfer equilibrium (Fig. 8.1). Thus, one should expect an increase in the yield of delayed phosphorescence with application of the field.

### 8.3 Experimental methods

**8.3.1 General information** Perylene and N,N'-dimethylformamide (DMF) were purchased from Signal-Aldrich Inc. and used as received. PtTBP and PdTBP were synthesized and purified as described previously.<sup>44, 241</sup>

**8.3.2 Optical measurements.** Optical glass or quartz fluorometric cells (1 cm path length) were used in all experiments. Samples were deoxygenated either by Ar bubbling or applying four freeze-pump-thaw cycles under vacuum ( $10^{-3}$  mm Hg). All measurements were performed in anhydrous DMF at 22°C, unless otherwise noted. UV-vis absorption spectra were recorded on a Perkin-Elmer Lambda 35 UV-Vis spectrophotometer. Steady-state and time-resolved phosphorescence measurements were performed on a FS900 spectrofluorometer (Edinburgh Instruments, UK), equipped with R2658P PMT (Hamamatsu). Time-resolved phosphorescence measurements were performed using an in-house constructed time-domain phosphorometer (detector rise time  $\sim 1 \mu\text{s}$ ).

**8.3.3 Magnetically Affected Reaction Yield (MARY) spectroscopy.** Our custom-built setup consists of a fiber-optic phosphorometer and a tunable magnet (see the Chapter 6 for details). MARY spectra (integrated luminescence intensity vs field strength; in the case of delayed phosphorescence, the slow portion of the biphasic decay was integrated) were recorded upon excitation of metalloporphyrins (sensitizers) at their Q-band maxima ( $\lambda_{\text{ex}} \sim 635 \text{ nm}$ ). Appropriate band-pass filters were used to selectively measure delayed fluorescence ( $< 550 \text{ nm}$ ) and phosphorescence ( $> 730 \text{ nm}$ ).

### 8.4 Results and discussions

In this work we used Pd and Pt tetrabenzoporphyrins (MTBP) as triplet donors (sensitizers) and perylene as a triplet acceptor (annihilator) (Fig. 8.2A). TTA systems based on MTBP's and other  $\pi$ -extended porphyrins have been studied in the past.<sup>230-233</sup> It has been

confirmed that in all such systems fluorescence signal has second order, i.e. it occurs upon absorption of two photons (*p*-type delayed fluorescence).<sup>231</sup> Using the oxidative aromatization method,<sup>241-243</sup> MTBP's can be conveniently synthesized having various substituents in the macrocycle, thus ensuring compatibility with a large selection of solvents. In the present work experiments were performed in *N,N'*-dimethylformamide (DMF).

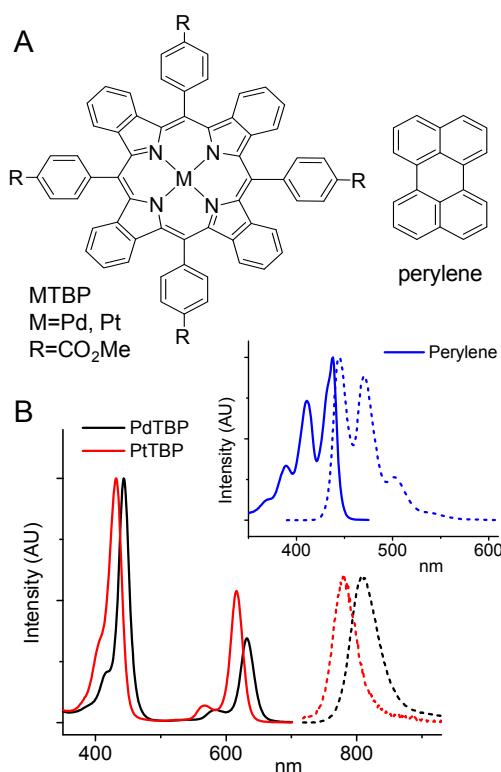


**Figure 8.2.** Structures and steady-state electronic properties of the molecules used in this work. (A) Molecular structures of the sensitizers (PtTBP and PdTBP) and the acceptor (perylene). (B) Absorption (solid line) and emission (dashed line) spectra of the chromophores.

The absorption and emission spectra of the components are shown in Fig. 8.2B. The energy levels of the first excited triplet states of Pd and PtTBP's ( $^3T_1$ ) are 1.55<sup>244</sup> and 1.61 eV,<sup>245</sup> respectively, while that of perylene ( $^3T_1$ ) is 1.53 eV.<sup>246</sup> The charge separated states, which potentially could form as a result of photoinduced electron transfer (PET), are significantly higher in energy than the triplet states. Therefore, PET could not be a significant pathway in these

systems. Pd and PtTBP are known to be brightly phosphorescent at ambient temperatures, and their triplet states are efficiently quenched by molecular oxygen, underpinning their applications in oxygen sensing.<sup>244, 247-248</sup> Accordingly, all experiments were conducted in rigorously deoxygenated solutions.

In the absence of perylene and oxygen, phosphorescence of Pd and PtTBP (~5  $\mu\text{M}$ ) decays mono-exponentially with lifetimes of ~200  $\mu\text{s}$  and 30  $\mu\text{s}$  and quantum yields of 0.03 and 0.12, respectively (measured against fluorescence of Rhodamine 6G in EtOH,  $\phi_{\text{fl}}=0.94$ ).<sup>111</sup> In mixtures with perylene, excitation of MTBP's at the Q-bands ( $S_0$ - $S_1$ ) results in phosphorescence from MTBP's along with delayed fluorescence from perylene (Fig. 8.3A). The decays of the phosphorescence were pronouncedly biphasic (Fig. 8.3B), and the decay time of the faster ("prompt") component matched the rise time of the perylene delayed fluorescence. As expected, increase in the perylene concentration caused decrease in the lifetime of the "prompt" phosphorescence in agreement with enhanced bimolecular quenching (Fig. 8.3C).

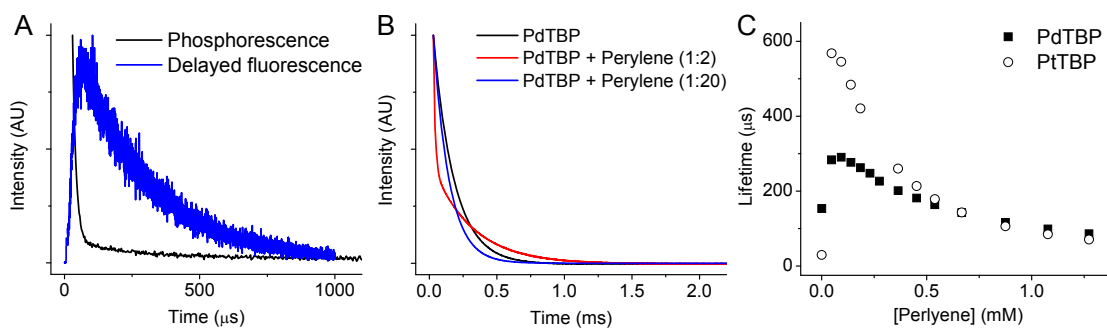


**Figure 8.3.** Some spectral features of PdTBP and PtTBP in the presence and absence of perylene. (A) Decays of phosphorescence of PdTBP and delayed fluorescence of perylene ( $\lambda_{\text{em}}=470$  nm). (B) Phosphorescence decays of PdTBP alone and in mixture with perylene (molar ratio shown in parenthesis). (C) Dependencies of the longer decay phase of phosphorescence (i.e. delayed phosphorescence) of PdTBP and PtTBP in concentration of perylene.

The slower component of the phosphorescence decay is a manifestation of the delayed phosphorescence, occurring as a result of TTET-mediated equilibrium between the sensitizer and acceptor triplet states,  $^S\text{T}_1$  and  $^A\text{T}_1$  (Fig. 8.1). Indeed, the time constants of the slower decays for both PtTBP and PdTBP (290  $\mu\text{s}$  and 540  $\mu\text{s}$ , respectively; perylene concentration 100  $\mu\text{M}$ ) were longer than the corresponding decays in the absence of perylene. The TTET equilibrium is facilitated by the proximity of the triplet energy levels of MTBP's and perylene as well as by the long lifetime of the perylene triplet state ( $\tau \sim 5000 \mu\text{s}$ ).<sup>233, 249</sup> Intramolecular delayed phosphorescence *via* TTET in porphyrin-based systems has been observed previously,<sup>110</sup> however, in the present case the reaction is bi-molecular in nature. Accordingly, the decay rate of the delayed phosphorescence, as well as of the delayed fluorescence, increased with an increase in the concentration of perylene, which led to a higher rate of depletion (self-quenching *via* annihilation) of the perylene triplet population (Fig. 8.3C).

Magnetically Affected Reaction Yield (MARY) spectroscopy was further employed to study MFE on the TTA in MTBP/perylene systems. In both cases (PdTBP/perylene and PtTBP/perylene), switching of the magnetic field "ON" caused pronounced decrease in the delayed fluorescence (Fig. 8.4A, B=1T) accompanied by an increase in the delayed phosphorescence. Both signals were fully recoverable to the baseline level upon switching the field "OFF" (Fig. 8.4B). The reversibility confirms that the observed changes are truly effected by the magnetic field and not artifacts of the measurement. The dependencies of the fluorescence and phosphorescence on the field are opposite to each other: the fluorescence decreases with an increase in the field and the phosphorescence increases (Fig. 8.4C). The MFE's in Fig. 8.4C are quantified as the percent change in the emission intensity with application of the field:  $\text{MFE}(\%) = 100 \times [Y(B) - Y(0)] / Y(0)$ , where  $Y(B)$  and  $Y(0)$  are the integrated emission intensities in the presence and absence of the magnetic field, respectively. The positive MFE on the phosphorescence *via* TTA contrasts the negative MFE in the systems where the phosphorescence is modulated *via* pathway including radical pairs.<sup>220</sup>

Due to the instrument limitations we could not examine the early time course of the delayed fluorescence signal with good accuracy. However, we conjecture that this curve may exhibit its own dependence on the magnetic field. Such an MFE may occur if spin polarization is present in the donor triplet state, it gets transferred from the donor to acceptor *via* TTET, and intermolecular TTA takes place prior to spin relaxation within the acceptor triplet population.<sup>250-252</sup> To this end, it is known that triplet states of Pt (and Pd) porphyrins, born by  $S_1 \rightarrow T_1$  ISC, are strongly spin-polarized.<sup>253-254</sup> At sufficiently high concentrations of perylene (~1 mM), the rise time of the fluorescence is much shorter than  $10^{-6}$  s, indicating that the collisional TTET followed by the TTA likely occurs faster than spin relaxation, which has time scale of  $10^{-7}$ - $10^{-6}$  s.<sup>205, 255</sup> Therefore, the slope of the rise is expected to exhibit magnetic field dependence.

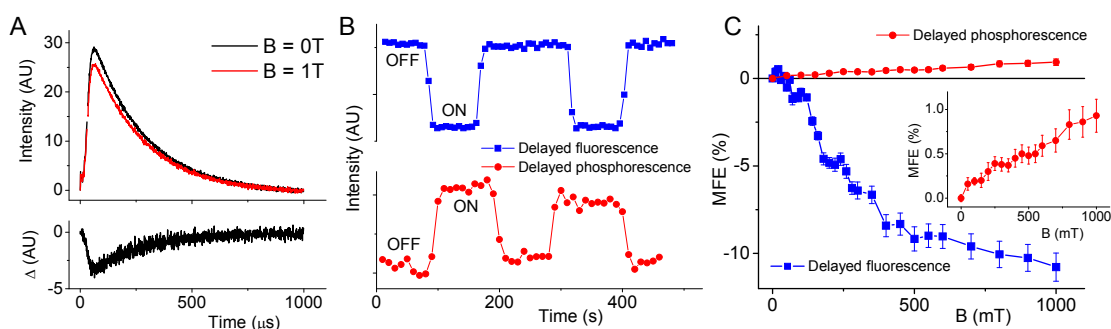


**Figure 8.4.** Magnetic field effects on luminescence in PdTBP/perylene system. (A) Time courses of delayed fluorescence of perylene in PdTBP/perylene system ( $[PdTBP] \sim 5 \mu M$ ,  $[perylene] \sim 100 \mu M$ ) in the absence and presence of magnetic field ( $B=1T$ ) – upper graph; time course of the difference between the two signals – lower graph. (B) Changes in perylene delayed fluorescence and PdTBP delayed phosphorescence with application of magnetic field ( $B=1T$ ). (C) MARY curves for delayed fluorescence and delayed phosphorescence (inset) in PdTBP/perylene mixtures. Delayed fluorescence:  $[PdTBP] \sim 5 \mu M$ ,  $[perylene] \sim 100 \mu M$ . Delayed phosphorescence:  $[PdTBP] \sim 5 \mu M$ ,  $[perylene] \sim 1$  mM.

Following Murai et al.,<sup>256</sup> we can employ the analytical model of Atkins and Evans<sup>240</sup> to quantitatively account for our observations. Assuming that the only magnetically sensitive parameter in TTA systems is rate constant  $k_{TTA}$  (Fig. 8.1), the following expression holds true:<sup>240</sup>

$$\frac{k_{TTA}(B)}{k_{TTA}(0)} = \frac{P_{TTA}(B)}{P_{TTA}(0)} = \frac{1 + \varphi_{TTA} f_{TTA}(B)}{1 + \varphi_{TTA} f_{TTA}(0)}, \quad (\text{Eq. 8.1})$$

where:

$$\varphi_{TTA} = \frac{\lambda_T}{1 - \lambda_T}, \quad (\text{Eq. 8.2})$$

$P_{TTA}(B)$  is the probability of the TTA,  $f_{TTA}(B)$  is the field-dependent parameter related to the singlet character distribution in the TT pair, and  $\lambda_T$  is the reaction probability for the singlet recombination channel that accounts for delayed fluorescence. Parameters  $P_{TTA}(B)$  and  $f_{TTA}(B)$  (see Appendix to this chapter and in refs. [240, 256] for details) are specific to the molecules forming the TT pairs (i.e. perylene), i.e. ZFS constants (D and E) of the triplet state and the rotational correlation time ( $\tau_r$ ). These values could be found in the literature.<sup>257-259</sup>

The integrated intensity of the delayed fluorescence ( $Y_F$ ), which is a direct observable in our experiments, is proportional to the product of the square of the concentration of the annihilator triplet state ( $[^A T_1]^2$ ) and the second order rate constant ( $k_{TTA}$ ). On the other hand, the intensity of the delayed phosphorescence ( $Y_P$ ) is proportional the product of the annihilator triplet concentration ( $[^A T_1]$ ), the sensitizer ground state ( $[^S S_0]$ ) and the field-independent constant ( $k_{TTET}^1$ ). Thus, we can write:

$$\frac{Y_F(B)}{Y_F(0)} = \frac{k_{TTA}(B)[^A T_1]_B^2}{k_{TTA}(0)[^A T_1]_0^2} \quad \frac{Y_P(B)}{Y_P(0)} = \frac{[^A T_1]_B [^S S_0]_B}{[^A T_1]_0 [^S S_0]_0} \approx \frac{[^A T_1]_B}{[^A T_1]_0} \quad (\text{Eq. 8.3})$$

where  $[^A T_1]_B$ ,  $[^S S_0]_B$ ,  $[^A T_1]_0$  and  $[^S S_0]_0$  indicate concentrations of the corresponding species under steady-state conditions (i.e. constant rate of excitation) in the presence and absence of the field, respectively. In deriving expressions (Eq. 8.3) we assumed that the relative change in the concentration of  $^S S_0$  with application of the field is negligible, which should be the case at low light intensities. Combining expressions (Eq. 8.3) and substituting into (Eq. 8.1) we obtain the

relationship between the theoretical MFE on the TTA rate constants<sup>240</sup> and the experimental observables:

$$\frac{Y_F(B)}{Y_F(0)} \times \left( \frac{Y_P(0)}{Y_P(B)} \right)^2 = \frac{1 + \phi_{TTA} f_{TTA}(B)}{1 + \phi_{TTA} f_{TTA}(0)} \quad (\text{Eq. 8.4})$$

Fitting the MARY data with Eq. 8.4 (Fig. 8.5) leads to a value of  $\lambda_T \sim 0.7$ , which is higher than used in previous calculations,<sup>256</sup> but still lies within the acceptable range ( $< 1$ ).

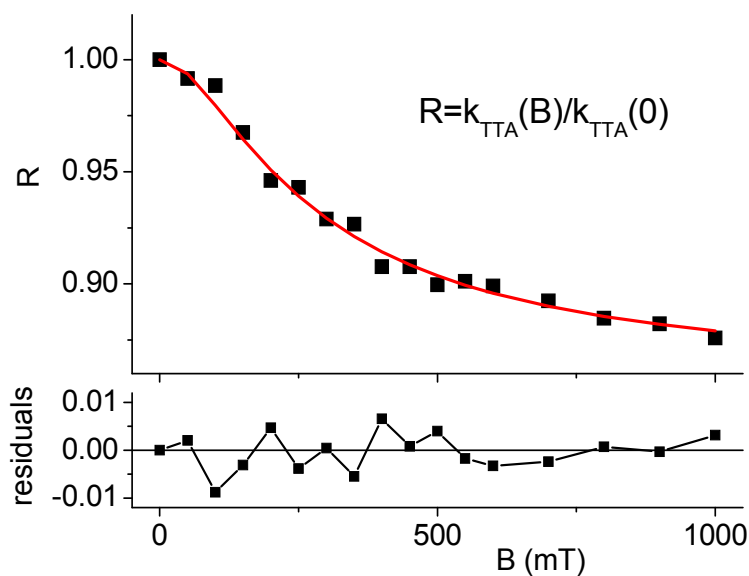


**Figure 8.5.** Ratio of rate constants ( $k_{TTA}$ ) as a function of magnetic field. The solid line shows the fit to Eq. 8.4. Experimental conditions: [PdTBP] $\sim 5 \mu\text{M}$ , [perylene] $\sim 1 \text{mM}$ .

The MFE values at  $B=1\text{T}$  (the highest accessible field in our setup) are summarized in Table 8.1 for the studied chromophore combinations.

**Table 8.1.** MFE on delayed emission in systems containing MTBP's as donors and perylene as acceptor.

Donor	Acceptor	MFE (%) <sup>a</sup>	
		Delayed fluorescence <sup>b</sup>	Delayed phosphorescence <sup>c</sup>
PtTBP	perylene	-9.5 ± 0.2	1.2 ± 0.2
PdTBP		-10.8 ± 0.8	0.9 ± 0.2

<sup>a</sup> MFE(%)=100×[Y(B)-Y(0)]/Y(0), where Y(B) and Y(0) are the integrated intensities at B=1T and in zero-field, respectively; <sup>b</sup>[Donor]=~5 μM, [Acceptor]=~100 μM; <sup>c</sup>[Donor]=~5 μM [Acceptor]=~1 mM.

The MFE on the delayed fluorescence is negative relative to the field increase and has the absolute value of ~10%, regardless of the sensitizer-porphyrin. For the systems studied, the rise and decay phases of the signal are determined by constants  $k_{TTET}$  and  $k_T$ , while TTET is the rate-limiting step in the overall upconversion process, i.e.  $k_{TTA} \gg k_{TTET}$ . The magnetic modulation of the fluorescence intensity is due to the modulation of  $k_{TTA}$ , which is partially compensated by the changes in concentration of  $^1T_1$ . The MFE on the delayed phosphorescence is positive and has smaller magnitude (1-2%). This effect is solely due to the modulation of the  $^1T_1$  pool, as it is affected by the modulation of the TTA channel. The decay time of the delayed phosphorescence signal is effectively increased at higher magnetic fields and, as expected, it is about two times longer than the decay time of the delayed fluorescence.

It is interesting to note that according to the recently performed studies,<sup>236</sup> for ensembles of TT pairs with statistical mutual orientation of chromophores, such as in solution-based systems, increase in the field up to 100-200 Gauss is predicted to distribute singlet character almost uniformly over all nine pair spin eigenstates (compared to the three states in zero-field), and hence the average rate of TTA should increase. Our MARY curves, however, do not exhibit such a low-field feature (increase in the delayed fluorescence), suggesting that parallel orientations, for

which the original theoretical treatment was elaborated, are somehow preferentially formed and/or longer-lived.

## 8.5 Conclusions

In conclusion, we have demonstrated magnetic modulation of delayed fluorescence and delayed phosphorescence in solution-based TTA systems comprising perylene as annihilator and red-absorbing  $\pi$ -extended porphyrins as triplet sensitizers. The MFE on the delayed phosphorescence is due to the equilibrium of the porphyrin and perylene triplet state pools mediated by triplet-triplet energy transfer. The latter phenomenon bears some similarity with magnetic modulation of "prompt" fluorescence in systems where triplet excitons are produced upon singlet fission, and the equilibrium between the singlet and triplet populations is established already at early stages of the singlet decay.<sup>236</sup> The described results may present interest for development of new imaging and sensing approaches that combine optical and magnetic modalities. Further studies employing other combinations of sensitizer/annihilator pairs and methods for studying MFE in time-resolved fashion are underway.

## 8.6 Appendix

### 8.6.1 Analytical expressions for dependence of delayed fluorescence and phosphorescence on magnetic field

In our analysis we used expressions derived by Atkins and Evans<sup>240</sup> and later applied in similar analysis by Murai et al.<sup>256</sup>

Assuming that the magnetic field dependence of the fluorescence intensity,  $Y_F(B)$ , is only due to the MFE on the probability of triplet-triplet annihilation  $P_{TTA}(B)$ , we express  $Y(B)_F/Y_F(0)$  by the following equation:

$$\frac{Y_F(B)}{Y_F(0)} = \frac{P_{TTA}(B)}{P_{TTA}(0)} = \frac{1 + \phi_{TTA} f_{TTA}(B)}{1 + \phi_{TTA} f_{TTA}(0)}, \quad (\text{Eq. 8.A1})$$

where:

$$P_{TTA}(B) = \lambda_T [1 - \lambda_T + \lambda_T f_{TTA}(B)] \quad (\text{Eq. 8.A2})$$

$$\phi_{TTA} = \frac{\lambda_T}{1 - \lambda_T} \quad (\text{Eq. 8.A3})$$

The parameters  $f_{TTA}(B)$  are expressed as described in the Chapter 7. In these expressions (Eq. 7.15-7.24),  $\tau_a$  is the translational correlation time, which is related to the rotational correlation time,  $\tau_r$ , via the Stokes-Einstein equation. The average rotational correlation time of perylene in DMF (viscosity 0.92 cP) is estimated as ~22 ps. This value is based on the two literature sources. One estimates the average rotational correlation time of perylene as  $\tau_r=21.6$  ps in cyclohexane (viscosity 0.98 cP).<sup>259</sup> Another gives values  $\tau_r=21\pm3$  ps in *n*-decane (viscosity 0.92 cP) and  $\tau_r=28\pm3$  ps in *n*-dodecane (viscosity 1.35 cP).<sup>257</sup> These authors determined that  $\tau_r$  is nearly linearly dependent on viscosity.<sup>257</sup> D and E are the zero-field splitting (ZFS) constants of the excited triplet state of perylene, whose values could be found in the literature:<sup>258</sup>  $D\sim 0.008$  cm<sup>-1</sup>,  $E\sim -0.0008$  cm<sup>-1</sup>.

## CHAPTER 9 Concluding Remarks

This work was driven by an interest to gain control over molecular emissivity using external forces or fields other than optical field. Such capabilities of modulating the emissivity of molecules may create new imaging modalities with potentially higher sensitivity, selectivity and resolution. We have explored the possibility of magnetic modulation of molecular emissivity at ambient temperatures in solutions by incorporating magnetically susceptible intermediates in photophysical pathways leading to emissive triplet states. We have concentrated here on a few of magnetically susceptible intermediates, namely radical pairs (RPs) and triplet-triplet exciton pairs. In the case of RPs, we focused on phosphorescent emitters. Magnetic control of RP recombination products and triplet-triplet annihilation are not new phenomena, but molecular systems containing triplet emitters were not explored previously and MFE on emissive states at room temperature in solutions in general have not been extensively explored.

We have shown that emissive triplet states can be populated by indirect ways, i.e. not only *via* intramolecular intersystem crossing. In a PtP-RhB<sup>+</sup> system, photoinduced electron transfer upon selective photoexcitation of Rhodamine B leads to a creation of radical pair initially as a singlet state, followed by radical pair intersystem crossing (RP-ISC) and triplet charge recombination onto emissive PtP triplet state. In another molecular system comprising PtP, anthracene, and boron dipyrromethene (BD), we have shown that photoexcitation of BD leads to a RP of PtP cation radical and BD anion radical, which undergoes direct spin-orbit intersystem crossing (SO-ISC) to populate PtP triplet state. In the latter series, the mutual orientation of the participating molecular orbitals of the electron donor-acceptor favors SO-ISC over RP-ISC.

In both cases, clear MFE on phosphorescence from PtP were not observed at fields up to 1 Tesla at ambient temperature. In the first series, the lack of MFE can be attributed to: 1) too short lifetime of RPs (<1 ns); and 2) molecular flexibility, which results in an ensemble of effective

exchange interactions within the RP, giving smaller MFE. In the latter series, the absence of MFE is simply because SO-ISC, which plays the role of the dominant pathway populating the emissive triplet state, is not magnetically sensitive.

In a different series of molecular systems comprising PtP and Rosamine B, we have demonstrated that room-temperature phosphorescence can be indeed modulated by external magnetic fields. Here photo-excitation of PtP results in the formation of emissive triplet state *via* intramolecular intersystem crossing, which is followed by ET to produce a RP initially as a triplet state, and then it undergoes RP-ISC to singlet RP. A model explaining the effect is developed, which is based on reversible ET between the local triplet state of PtP and a long-lived RP. External magnetic field modulates spin dynamics of the RP, affecting contribution of the singlet RP recombination channel and thereby influencing phosphorescence. In contrast to PtP-RhB<sup>+</sup> case, the lifetime of the RP is long enough ( $\mu\text{s}$  time scale) for MFE on phosphorescence to be observed.

We have shown that delayed fluorescence and delayed phosphorescence can be magnetically modulated in solution-based triplet-triplet annihilation systems comprising perylene as annihilator and red-absorbing  $\pi$ -extend porphyrins as triplet sensitizers. MFE through upconverted triplet-triplet annihilation in solutions are not limited to molecular combinations presented here and can be observed in many other systems as long as emissive states are involved. MFE through triplet-triplet annihilation might possess some immediate applicability in imaging if one can make molecular systems biocompatible.

Finally, a few comments are made on the challenges in constructing more usable *magneto-optical* probes for biomedical applications. We have demonstrated plausibility of rational design of *magneto-optical* probes based on triplet emitters. The difficulty in designing appropriate RP-based molecular systems comes from the requirements imposed by applications. For intended biologically related applications, as already stated, molecules need to have visible-NIR range photon absorption and emission, which limits energy window available for all the involved

states. We can define the energy window as the energy difference between the energies of excitation and of emissive state: the energy window is  $\sim 0.7$  eV when a molecule is excited with 500 nm light and an emissive state lies at 700 nm. In the PtP-RhB<sup>+</sup> system discussed in Chapter 4, the window is only  $\sim 0.3$  eV. Within such a small energy window it becomes difficult to regulate electron and energy flow in a controllable fashion. This limitation may be alleviated by using two-photon excitation. From the synthetic viewpoint, it would be advantageous if we could obtain relevant properties *a priori* such as the rates of electron transfer and the magnitude of inter-radical exchange coupling within RPs through the studies of individual molecules and diffusion-based systems either experimentally or computationally before synthesizing new molecular systems.

In conclusion, we have demonstrated that emissive triplet states can be modulated by external magnetic fields at room temperature in solutions through radical pair and triplet-triplet annihilation mechanisms. These demonstrations are two new additions to MFEs on molecular emissivity and will contribute to our knowledge of spin chemistry. Studies of molecular systems with emissive units including triplet emitters help to build structure-function relationships that are essential to the developments of effective *magneto-optical* probes.

## APPENDIX

### A.1 Matlab (MathWorks, MA) code for Förster-type energy transfer

This MATLAB code is used to calculate the estimated rates of energy transfer by dipole-dipole mechanism in the Chapter 4. The code will calculate the parameters such as distance  $R_0$ , transfer efficiency, the rate of energy transfer for Förster-type energy transfer between donor and acceptor molecules. It requires a files of the fluorescence spectrum of the donor (2 columns; the first with the wavelength range in nm, the second with the intensity of the fluorescence) and a file containing the absorption spectrum of the acceptor (2 columns, the first with the wavelength in nm, the second with the absorption of the acceptor in extinction coefficients,  $M^{-1}cm^{-1}$ ). The following data are also needed; refractive index of the solvent used, the quantum yield of the donor, and the angles  $\phi_T$ ,  $\theta_D$ , and  $\theta_A$  for calculations of Kappa squared or  $K^2$ . When the angles are not known or orientational averaging is assumed, use 2/3 for  $K^2$ . In order to calculate the transfer efficiency,  $E$ , and the rate of energy transfer,  $k_{FRET}$ , the distance between the donor and acceptor and the rate of donor's fluorescence (or rate of deactivating pathway of the donor excited state) in the absence of an acceptor are required. Here we assumed that FRET is the only additional deactivating passage in a given molecular system.

$q=0.001$ ; % The quantum yield (QY) of the donor, here QY is 0.001 or 0.1%

$\theta_D = \pi/2$ ;

$\theta_A = \pi/4$ ;

$\phi_T = \pi/2 * 0.815 / 0.90$ ;

$K^2 = (\cos(\phi_T) - 3 * \cos(\theta_D) * \cos(\theta_A))^2$ ; % Enter in the value K (2/3 for orientational averaging)

$n=1.496$ ; %refractive index

```

R = 15; % Distance between the donor and the acceptor (A - angstrom)

kfl = 1/(2.0*10^-9); %rate of fluorescence decay

f=load('XXXX.dat'); % Load the luminescence spectrum (the file name is XXXX.dat)

a=load('YYYY.dat'); % Load the absorption spectrum (the file name is YYYY.dat)

ra = a(:,2); %absorbance

aa = ra/norm(ra); %normalized absorbance

% Interpolate the absorption spectrum at the set of fluorescence x values.

a1=[f(:,1) interp1(a(:,1),a(:,2),f(:,1))];

f1=[(1e7)*f(:,1).^-1 f(:,2)]; % Convert nm to wavenumbers cm-1 (for luminescence)

a2=[(1e7)*a1(:,1).^-1 a1(:,2)]; % Convert nm to wavenumbers cm-1 (for absorption)

A=sum(diff(f1(:,1)).*f1(2:end,2)); % Calculate area of fluorescence curve

f2=[f1(:,1) f1(:,2)/abs(A)]; % Unit normalize the fluorescence.

% Calculate the overlap function O.

O=[f2(:,1) (a2(:,2).*f2(:,2))./(f2(:,1).^4)];

% Calculate the overlap integral J (unit in M-1cm-1nm4)

J=sum(abs(diff(f2(:,1))).*O(2:end,2));

% Calculate Ro (A - angstrom)

Ro=((8.8e-25)*(K2*q/(n^4))*abs(J))^(1/6)*10^8;

% Calculate transfer efficiency (%)

```

$$E = 1/(1+(R/R_0)^6)*100;$$

% Calculate the rate of energy transfer (s<sup>-1</sup>)

$$k_{\text{FRET}} = k_{\text{fl}}*(R_0/R)^6;$$

% Calculate the quantum yield of fluorescence in the presence of FRET.

$$Q_{\text{flFRET}} = q*k_{\text{fl}}/(k_{\text{fl}}+k_{\text{FRET}});$$

## BIBLIOGRAPHY

1. Jablonski, A. Efficiency of Anti-Stokes Fluorescence in Dyes. *Nature* **1933**, 131, 839.
2. McGlynn, S. P.; Azumi, T.; Kinoshita, M. *Molecular Spectroscopy of THE TRIPLET STATE*. Prentice-Hall, Inc.: Englewood Cliffs, N.J., 1969.
3. Turro, N. J.; Ramamurthy, V.; Scaiano, J. C. *Modern Molecular Photochemistry of Organic Molecules*. University Science Books: Sausalito, California, 2010.
4. Kasha, M. Characterization of Electronic Transitions in Complex Molecules. *Discuss. Faraday Soc.* **1950**, 14-19.
5. Lewis, G. N.; Lipkin, D.; Magel, T. T. Reversible Photochemical Processes in Rigid Media. A Study of the Phosphorescent State. *J. Am. Chem. Soc.* **1941**, 63, 3005-3018.
6. Porter, G.; Windsor, M. W. Studies of the Triplet State in Fluid Solvents. *Discuss. Faraday Soc.* **1954**, 178-186.
7. Steiner, U. E.; Ulrich, T. Magnetic-Field Effects in Chemical-Kinetics and Related Phenomena. *Chem. Rev.* **1989**, 89, 51-147.
8. Atkins, P. W. Role of Electron Exchange in Cidep. *Chem. Phys. Lett.* **1979**, 66, 403-405.
9. Syage, J. A. A Vector Model for CIDEP - the Role of the Exchange Interaction. *Chem. Phys. Lett.* **1982**, 91, 378-382.
10. Monchick, L.; Adrian, F. J. Theory of Chemically-Induced Electron Polarization (Cidep) - Vector Model and an Asymptotic Solution. *J. Chem. Phys.* **1978**, 68, 4376-4383.
11. Hayashi, H. *Introduction to Dynamic Spin Chemistry*. World Scientific: Singapore, 2004; Vol. 8.
12. May, V.; Kühn, O. *Charge and Energy Transfer Dynamics in Molecular Systems*. Third, Revised and Enlarged ed.; Wiley-VCH: Weinheim, 2011.
13. Atkins, P. W.; Stannard, P. R. Magnetic Quenching of Fluorescence. *Chem. Phys. Lett.* **1977**, 47, 113-114.

14. Kuttner, H. G.; Selzle, H. L.; Schlag, E. W. Radiationless Processes and Isotope Effect in Glyoxal in Presence of a Weak Magnetic-Field at Low-Pressures. *Chem. Phys.* **1978**, *28*, 1-9.
15. Marcus, R. A.; Sutin, N. Electron Transfers in Chemistry and Biology. *Biochim. Biophys. Acta* **1985**, *811*, 265-322.
16. Jortner, J. Temperature-Dependent Activation-Energy for Electron-Transfer between Biological Molecules. *J. Chem. Phys.* **1976**, *64*, 4860-4867.
17. Marcus, R. A. On the Theory of Oxidation-Reduction Reactions Involving Electron Transfer .1. *J. Chem. Phys.* **1956**, *24*, 966-978.
18. Marcus, R. A. Theory of Oxidation-Reduction Reactions Involving Electron Transfer .4. A Statistical-Mechanical Basis for Treating Contributions from Solvent, Ligands, and Inert Salt. *Discuss. Faraday Soc.* **1960**, 21-31.
19. Closs, G. L.; Miller, J. R. Intramolecular Long-Distance Electron-Transfer in Organic-Molecules. *Science* **1988**, *240*, 440-447.
20. Closs, G. L.; Calcaterra, L. T.; Green, N. J.; Penfield, K. W.; Miller, J. R. Distance, Stereoelectronic Effects, and the Marcus Inverted Region in Intramolecular Electron-Transfer in Organic Radical-Anions. *J. Phys. Chem.* **1986**, *90*, 3673-3683.
21. Anderson, P. W. New Approach to the Theory of Superexchange Interactions. *Phys. Rev.* **1959**, *115*, 2-13.
22. Anderson, P. W. Antiferromagnetism - Theory of Superexchange Interaction. *Phys. Rev.* **1950**, *79*, 350-356.
23. Davis, W. B.; Wasielewski, M. R.; Ratner, M. A.; Mujica, V.; Nitzan, A. Electron transfer rates in bridged molecular systems: A phenomenological approach to relaxation. *J. Phys. Chem. A* **1997**, *101*, 6158-6164.
24. Davis, W. B.; Svec, W. A.; Ratner, M. A.; Wasielewski, M. R. Molecular-wire behaviour in p-phenylenevinylene oligomers. *Nature* **1998**, *396*, 60-63.
25. Gray, H. B.; Winkler, J. R. Long-range electron transfer. *P. Natl. Acad. Sci. USA* **2005**, *102*, 3534-3539.

26. Skourtis, S. S.; Waldeck, D. H.; Beratan, D. N. Fluctuations in Biological and Bioinspired Electron-Transfer Reactions. *Annu. Rev. Phys. Chem.* **2010**, *61*, 461-485.
27. Schulten, K.; Staerk, H.; Weller, A.; Werner, H. J.; Nickel, B. Magnetic Field Dependence of Geminate Recombination of Radical Ion Pairs in Polar Solvents. *Z. Phys. Chem.* **1976**, *101*, 371-390.
28. Kattnig, D. R.; Rosspeintner, A.; Grampp, G. Magnetic field effects on exciplex-forming systems: the effect on the locally excited fluorophore and its dependence on free energy. *Phys. Chem. Chem. Phys.* **2011**, *13*, 3446-3460.
29. Kattnig, D. R.; Rosspeintner, A.; Grampp, G. Fully reversible interconversion between locally excited fluorophore, exciplex, and radical ion pair demonstrated by a new magnetic field effect. *Angew. Chem. Int. Edit.* **2008**, *47*, 960-962.
30. Faulkner, L. R.; Bard, A. J. Magnetic Field Effects on Anthracene Triplet-Triplet Annihilation in Fluid Solutions. *J. Am. Chem. Soc.* **1969**, *91*, 6495-6497.
31. Wyrsh, D.; Labhart, H. Magnetic field effects on P-type delayed fluorescence of 1,2-benzanthracene in solution. *Chem. Phys. Lett.* **1971**, *8*, 217-219.
32. Boas, D. A.; Brooks, D. H.; Miller, E. L.; DiMarzio, C. A.; Kilmer, M.; Gaudette, R. J.; Zhang, Q. Imaging the body with diffuse optical tomography. *IEEE Signal Process. Mag.* **2001**, *18*, 57-75.
33. Ntziachristos, V.; Hielscher, A. H.; Yodh, A. G.; Chance, B. Diffuse optical tomography of highly heterogeneous media. *IEEE Trans. Med. Imag.* **2001**, *20*, 470-478.
34. Arridge, S. R. Optical tomography in medical imaging. *Inverse Probl.* **1999**, *15*, R41-R93.
35. Ntziachristos, V.; Bremer, C.; Weissleder, R. Fluorescence imaging with near-infrared light: new technological advances that enable in vivo molecular imaging. *Eur. Radiol.* **2003**, *13*, 195-208.
36. Montet, X.; Figueiredo, J. L.; Alencar, H.; Ntziachristos, V.; Mahmood, U.; Weissleder, R. Tomographic fluorescence imaging of tumor vascular volume in mice. *Radiology* **2007**, *242*, 751-758.

37. Ishimaru, A. *Wave propagation and scattering in random media*. Academic Press: New York, 1978.
38. Pogue, B. W.; Geimer, S.; McBride, T. O.; Jiang, S. D.; Osterberg, U. L.; Paulsen, K. D. Three-dimensional simulation of near-infrared diffusion in tissue: boundary condition and geometry analysis for finite-element image reconstruction. *Appl. Opt.* **2001**, *40*, 588-600.
39. Wang, L. V. Multiscale photoacoustic microscopy and computed tomography. *Nature Photon.* **2009**, *3*, 503-509.
40. Razansky, D.; Distel, M.; Vinegoni, C.; Ma, R.; Perrimon, N.; Koster, R. W.; Ntziachristos, V. Multispectral opto-acoustic tomography of deep-seated fluorescent proteins in vivo. *Nature Photon.* **2009**, *3*, 412-417.
41. Apreleva, S. V.; Wilson, D. F.; Vinogradov, S. A. Tomographic imaging of oxygen by phosphorescence lifetime. *Appl. Opt.* **2006**, *45*, 8547-8559.
42. Soloviev, V. Y.; Wilson, D. F.; Vinogradov, S. A. Phosphorescence lifetime imaging in turbid media: the inverse problem and experimental image reconstruction. *Appl. Opt.* **2004**, *43*, 564-574.
43. Shives, E.; Xu, Y.; Jiang, H. Fluorescence lifetime tomography of turbid media based on an oxygen-sensitive dye. *Opt. Express* **2002**, *10*, 1557-1562.
44. Lebedev, A. Y.; Cheprakov, A. V.; Sakadzic, S.; Boas, D. A.; Wilson, D. F.; Vinogradov, S. A. Dendritic phosphorescent probes for oxygen imaging in biological systems. *ACS Appl. Mater. Interfaces* **2009**, *1*, 1292-1304.
45. Kalyanasundaram, K. *Photochemistry of Polypyridine and Porphyrin Complexes*. Academic Press: London, 1992.
46. Roundhill, D. M. *Photochemistry and Photophysics of Metal Complexes*. Plenum Press: New York, 1994.
47. DeRosa, M. C.; Mosher, P. J.; Yap, G. P. A.; Focsaneanu, K. S.; Crutchley, R. J.; Evans, C. E. B. Synthesis, characterization, and evaluation of Ir(ppy)<sub>2</sub>(vpy)Cl as a polymer-bound oxygen sensor. *Inorg. Chem.* **2003**, *42*, 4864-4872.

48. Kavitha, J.; Chang, S. Y.; Chi, Y.; Yu, J. K.; Hu, Y. H.; Chou, P. T.; Peng, S. M.; Lee, G. H.; Tao, Y. T.; Chien, C. H.; Carty, A. J. In search of high-performance platinum(II) phosphorescent materials for the fabrication of red electroluminescent devices. *Adv. Func. Mat.* **2005**, *15*, 223-229.
49. Borisov, S. M.; Klimant, I. Efficient metallation in diphenylether - A convenient route to luminescent platinum(II) complexes. *Dyes and Pigments* **2009**, *83*, 312-316.
50. Tseng, Y. H.; Bhattacharya, D.; Lin, S. M.; Thanasekaran, P.; Wu, J. Y.; Lee, L. W.; Sathiyendiran, M.; Ho, M. L.; Chung, M. W.; Hsu, K. C.; Chou, P. T.; Lu, K. L. Highly Emissive Cyclometalated Rhenium Metallacycles: Structure-Luminescence Relationship. *Inorg. Chem.* **2010**, *49*, 6805-6807.
51. Hell, S. W. Far-field optical nanoscopy. *Science* **2007**, *316*, 1153-1158.
52. Dedecker, P.; Flors, C.; Hotta, J. I.; Uji-I, H.; Hofkens, J. 3D nanoscopy: Bringing biological nanostructures into sharp focus. *Angew. Chem. Int. Edit.* **2007**, *46*, 8330-8332.
53. Betzig, E.; Patterson, G. H.; Sougrat, R.; Lindwasser, O. W.; Olenych, S.; Bonifacino, J. S.; Davidson, M. W.; Lippincott-Schwartz, J.; Hess, H. F. Imaging intracellular fluorescent proteins at nanometer resolution. *Science* **2006**, *313*, 1642-1645.
54. Rust, M. J.; Bates, M.; Zhuang, X. W. Sub-diffraction-limit imaging by stochastic optical reconstruction microscopy (STORM). *Nat. Methods* **2006**, *3*, 793-795.
55. Moneron, G.; Hell, S. W. Two-photon excitation STED microscopy. *Opt. Express* **2009**, *17*, 14567-14573.
56. Hell, S. W. Toward fluorescence nanoscopy. *Nat. Biotechnol.* **2003**, *21*, 1347-1355.
57. Yang, N.; Cohen, A. E. Optical imaging through scattering media via magnetically modulated fluorescence. *Opt. Express* **2010**, *18*, 25461-25467.
58. Lee, H.; Yang, N.; Cohen, A. E. Mapping Nanomagnetic Fields Using a Radical Pair Reaction. *Nano Lett.* **2011**, *11*, 5367-5372.
59. Mermut, O.; Diamond, K. R.; Cormier, J. F.; Gallant, P.; Ho, N.; Leclair, S.; Marois, J. S.; Noiseux, I.; Morin, J. F.; Patterson, M. S.; Vernon, M. L. The use of magnetic field effects on

photosensitizer luminescence as a novel probe for optical monitoring of oxygen in photodynamic therapy. *Phys. Med. Biol.* **2009**, *54*, 1-16.

60. Schulten, K.; Swenberg, C. E.; Weller, A. BIOMAGNETIC SENSORY MECHANISM BASED ON MAGNETIC-FIELD MODULATED COHERENT ELECTRON-SPIN MOTION. *Z. Phys. Chem.* **1978**, *111*, 1-5.

61. Schulten, K.; Wolynes, P. G. Semi-Classical Description of Electron-Spin Motion in Radicals Including Effect of Electron Hopping. *J. Chem. Phys.* **1978**, *68*, 3292-3297.

62. Rodgers, C. T.; Hore, P. J. Chemical magnetoreception in birds: the radical pair mechanism. *P. Natl. Acad. Sci. USA* **2009**, *106*, 353-60.

63. Gilch, P.; Pollinger-Dammer, F.; Musewald, C.; Michel-Beyerle, M. E.; Steiner, U. E. Magnetic field effect on picosecond electron transfer. *Science* **1998**, *281*, 982-984.

64. Hayashi, H.; Nagakura, S. Theoretical Study of Relaxation Mechanism in Magnetic Field Effects on Chemical-Reactions. *Bull. Chem. Soc. Jpn.* **1984**, *57*, 322-328.

65. Leung, M.; Elsayed, M. A. Spin Selectivity in Low-Temperature Solid-State Photochemistry. *J. Am. Chem. Soc.* **1975**, *97*, 669-670.

66. Kaneto, K.; Yoshino, K.; Inuishi, Y. Effects of a Magnetic-Field on Triplet-Triplet Annihilation in a Pt-Phthalocyanine Single-Crystal at 4.2 K. *Chem. Phys. Lett.* **1976**, *40*, 505-507.

67. Vankan, J. M. J.; Veeman, W. S. Magnetic-Field Effects on 1,4-Dibromonaphthalene Phosphorescence Emission. *Chem. Phys. Lett.* **1983**, *94*, 133-136.

68. de Winter, A.; Boxer, S. G. Energetics of primary charge separation in bacterial photosynthetic reaction center mutants: Triplet decay in large magnetic fields. *J. Phys. Chem. A* **2003**, *107*, 3341-3350.

69. Takiff, L.; Boxer, S. G. Phosphorescence from the Primary Electron-Donor in Rhodobacter-Sphaeroides and Rhodospseudomonas-Viridis Reaction Centers. *Biochim. Biophys. Acta* **1988**, *932*, 325-334.

70. Chidsey, C. E. D.; Takiff, L.; Goldstein, R. A.; Boxer, S. G. Effect of Magnetic-Fields on the Triplet-State Lifetime in Photosynthetic Reaction Centers - Evidence for Thermal Repopulation of the Initial Radical Pair. *P. Natl. Acad. Sci. USA* **1985**, *82*, 6850-6854.
71. Zhu, T. C.; Finlay, J. C. The role of photodynamic therapy (PDT) physics. *Med. Phys.* **2008**, *35*, 3127-3136.
72. Celli, J. P.; Spring, B. Q.; Rizvi, I.; Evans, C. L.; Samkoe, K. S.; Verma, S.; Pogue, B. W.; Hasan, T. Imaging and photodynamic therapy: mechanisms, monitoring and optimization. *Chem. Rev.* **2010**, *110*, 2795-2838.
73. Singh-Rachford, T. N.; Castellano, F. N. Photon upconversion based on sensitized triplet-triplet annihilation. *Coordin. Chem. Rev.* **2010**, *254*, 2560-2573.
74. Ceroni, P. Energy Up-Conversion by Low-Power Excitation: New Applications of an Old Concept. *Chem. Eur. J.* **2011**, *17*, 9560-9564.
75. Sasabe, H.; Kido, J. Multifunctional Materials in High-Performance OLEDs: Challenges for Solid-State Lighting. *Chem. Mat.* **2011**, *23*, 621-630.
76. Graham, K. R.; Yang, Y. X.; Sommer, J. R.; Shelton, A. H.; Schanze, K. S.; Xue, J. G.; Reynolds, J. R. Extended Conjugation Platinum(II) Porphyrins for use in Near-Infrared Emitting Organic Light Emitting Diodes. *Chem. Mat.* **2011**, *23*, 5305-5312.
77. Wilson, D. F. Quantifying the role of oxygen pressure in tissue function. *Am. J. Physiol. Heart C.* **2008**, *294*, H11-H13.
78. Vinogradov, S. A.; Wilson, D. F. Porphyrin-dendrimers as biological oxygen sensors. In *Designing Dendrimers*, Capagna, S.; Ceroni, P., Eds. Wiley: New York, 2010.
79. Rumsey, W. L.; Vanderkooi, J. M.; Wilson, D. F. Imaging of phosphorescence: A novel method for measuring the distribution of oxygen in perfused tissue. *Science* **1988**, *241*, 1649-1651.
80. Apreleva, S. V.; Wilson, D. E.; Vinogradov, S. A. Feasibility of diffuse optical imaging with long-lived luminescent probes. *Opt. Lett.* **2006**, *31*, 1082-1084.

81. Briñas, R. P.; Troxler, T.; Hochstrasser, R. M.; Vinogradov, S. A. Phosphorescent Oxygen Sensor with Dendritic Protection and Two-Photon Absorbing Antenna. *J. Am. Chem. Soc.* **2005**, *127*, 11851-11862.
82. Finikova, O. S.; Troxler, T.; Senes, A.; DeGrado, W. F.; Hochstrasser, R. M.; Vinogradov, S. A. Energy and electron transfer in enhanced two-photon-absorbing systems with triplet cores. *J. Phys. Chem. A* **2007**, *111*, 6977-6990.
83. Finikova, O. S.; Lebedev, A. Y.; Aprelev, A.; Troxler, T.; Gao, F.; Garnacho, C.; Muro, S.; Hochstrasser, R. M.; Vinogradov, S. A. Oxygen microscopy by two-photon-excited phosphorescence. *ChemPhysChem* **2008**, *9*, 1673-1679.
84. Sakadzic, S.; Roussakis, E.; Yaseen, M. A.; Mandeville, E. T.; Srinivasan, V. J.; Arai, K.; Ruvinskaya, S.; Devor, A.; Lo, E. H.; Vinogradov, S. A.; Boas, D. A. Two-photon high-resolution measurement of partial pressure of oxygen in cerebral vasculature and tissue. *Nat. Methods* **2010**, *7*, 755-U125.
85. Lecoq, J.; Parpaleix, A.; Roussakis, E.; Ducros, M.; Houssen, Y. G.; Vinogradov, S. A.; Charpak, S. Simultaneous two-photon imaging of oxygen and blood flow in deep cerebral vessels. *Nat. Med.* **2011**, *17*, 893-U262.
86. Finikova, O. S.; Chen, P.; Ou, Z. P.; Kadish, K. M.; Vinogradov, S. A. Dynamic quenching of porphyrin triplet states by two-photon absorbing dyes: Towards two-photon-enhanced oxygen nanosensors. *J. Photoch. Photobio. A* **2008**, *198*, 75-84.
87. Brocklehurst, B. Magnetic fields and radical reactions: recent developments and their role in nature. *Chem. Soc. Rev.* **2002**, *31*, 301-11.
88. Rodgers, C. T. Magnetic field effects in chemical systems. *Pure. Appl. Chem.* **2009**, *81*, 19-43.
89. Wasielewski, M. R. Energy, charge, and spin transport in molecules and self-assembled nanostructures inspired by photosynthesis. *J. Org. Chem.* **2006**, *71*, 5051-5066.
90. Schulten, K.; Weller, A. Exploring Fast Electron-Transfer Processes by Magnetic-Fields. *Biophys. J.* **1978**, *24*, 295-305.

91. Ritz, T.; Adem, S.; Schulten, K. A model for photoreceptor-based magnetoreception in birds. *Biophys. J.* **2000**, *78*, 707-718.
92. Kodis, G.; Liddell, P. A.; Moore, A. L.; Moore, T. A.; Gust, D. Synthesis and photochemistry of a carotene-porphyrin-fullerene model photosynthetic reaction center. *J. Phys. Org. Chem.* **2004**, *17*, 724-734.
93. Maeda, K.; Henbest, K. B.; Cintolesi, F.; Kuprov, I.; Rodgers, C. T.; Liddell, P. A.; Gust, D.; Timmel, C. R.; Hore, P. J. Chemical compass model of avian magnetoreception. *Nature* **2008**, *453*, 387-U38.
94. Ward, H. R. Chemically Induced Dynamic Nuclear Polarization (Cidnp) .1. Phenomenon, Examples, and Applications. *Acc. Chem. Res.* **1972**, *5*, 18-24.
95. Lawler, R. G. Chemically Induced Dynamic Nuclear Polarization (Cidnp) .2. Radical-Pair Model. *Acc. Chem. Res.* **1972**, *5*, 25-33.
96. Grissom, C. B. Magnetic-Field Effects in Biology - a Survey of Possible Mechanisms with Emphasis on Radical-Pair Recombination. *Chem. Rev.* **1995**, *95*, 3-24.
97. Timmel, C. R.; Henbest, K. B. A study of spin chemistry in weak magnetic fields. *Philos. Transact. A Math. Phys. Eng. Sci.* **2004**, *362*, 2573-89.
98. Carbonera, D. Optically detected magnetic resonance (ODMR) of photoexcited triplet states. *Photosynth. Res.* **2009**, *102*, 403-414.
99. Werner, H. J.; Schulten, K.; Weller, A. Electron-Transfer and Spin Exchange Contributing to Magnetic-Field Dependence of Primary Photo-Chemical Reaction of Bacterial Photosynthesis. *Biochim. Biophys. Acta* **1978**, *502*, 255-268.
100. Levanon, H.; Norris, J. R. Photoexcited Triplet-State and Photosynthesis. *Chem. Rev.* **1978**, *78*, 185-198.
101. Schulten, K. Magnetic-Field Effects in Chemistry and Biology. *Festkor. Adv. Solid St.* **1982**, *22*, 61-83.
102. Schulten, K.; Weller, A. MAGNETIC-FIELDS IN CHEMISTRY AND PHYSICS. *Umschau* **1984**, *84*, 779-782.

103. Wiederrecht, G. P.; Svec, W. A.; Wasielewski, M. R.; Galili, T.; Levanon, H. Novel mechanism for triplet state formation in short distance covalently linked radical ion pairs. *J. Am. Chem. Soc.* **2000**, *122*, 9715-9722.
104. Durr, H.; Bossmann, S. Ruthenium polypyridine complexes. On the route to biomimetic assemblies as models for the photosynthetic reaction center. *Acc. Chem. Res.* **2001**, *34*, 905-917.
105. Montes, V. A.; Pérez-Bolívar, C.; Agarwal, N.; Shinar, J.; Anzenbacher, P. Molecular-Wire Behavior of OLED Materials: Exciton Dynamics in Multichromophoric Alq3-Oligofluorene-Pt(II)porphyrin Triads. *J. Am. Chem. Soc.* **2006**, *128*, 12436-12438.
106. Montes, V. A.; Pérez-Bolívar, C.; Estrada, L. A.; Shinar, J.; Anzenbacher, P. Ultrafast Dynamics of Triplet Excitons in Alq3-Bridge-Pt(II)porphyrin Electroluminescent Materials. *J. Am. Chem. Soc.* **2007**, *129*, 12598-12599.
107. Tyson, D. S.; Castellano, F. N. Intramolecular Singlet and Triplet Energy Transfer in a Ruthenium(II) Diimine Complex Containing Multiple Pyrenyl Chromophores. *J. Phys. Chem. A* **1999**, *103*, 10955-10960.
108. Harriman, A.; Hissler, M.; Khatyr, A.; Ziessel, R. A ruthenium(II) tris(2,2[prime or minute]-bipyridine) derivative possessing a triplet lifetime of 42 [small micro]s. *Chem. Commun.* **1999**, 735-736.
109. Ford, W. E.; Rodgers, M. A. J. Reversible triplet-triplet energy transfer within a covalently linked bichromophoric molecule. *J. Phys. Chem.* **1992**, *96*, 2917-2920.
110. Whited, M. T.; Djurovich, P. I.; Roberts, S. T.; Durrell, A. C.; Schlenker, C. W.; Bradforth, S. E.; Thompson, M. E. Singlet and Triplet Excitation Management in a Bichromophoric Near-Infrared-Phosphorescent BODIPY-Benzoporphyrin Platinum Complex. *J. Am. Chem. Soc.* **2011**, *133*, 88-96.
111. Kubin, R. F.; Fletcher, A. N. Fluorescence quantum yields of some rhodamine dyes. *J. Lumin.* **1982**, *27*, 455-462.

112. Vinogradov, S. A.; Wilson, D. F. Recursive maximum entropy algorithm and its application to the luminescence lifetime distribution recovery. *Appl. Spectrosc.* **2000**, *54*, 849-855.
113. Lindsey, J. S.; Schreiman, I. C.; Hsu, H. C.; Kearney, P. C.; Marguerettaz, A. M. Rothmund and Adler-Longo Reactions Revisited - Synthesis of Tetraphenylporphyrins under Equilibrium Conditions. *J. Org. Chem.* **1987**, *52*, 827-836.
114. Nguyen, T.; Francis, M. B. Practical synthetic route to functionalized rhodamine dyes. *Org. Lett.* **2003**, *5*, 3245-8.
115. Araki, N.; Obata, M.; Ichimura, A.; Mikata, Y.; Yano, S. Unprecedented pendant group exchange of a porphyrinato platinum(II) in benzonitrile. *Chem. Lett.* **2004**, *33*, 450-451.
116. Wennerström, O.; Ericsson, H.; Raston, I.; Svensson, S.; Pimlott, W. meso-tetra(meso-tetraphenylporphyrinyl)porphyrin, a macrocycle with five covalently linked porphyrin units. *Tetrahedron Lett.* **1989**, *30*, 1129-1132.
117. Holmes, A. E.; Das, D.; Canary, J. W. Chelation-enhanced circular dichroism of tripodal bisporphyrin ligands. *J. Am. Chem. Soc.* **2007**, *129*, 1506-+.
118. Senge, M. O. Nucleophilic substitution as a tool for the synthesis of unsymmetrical porphyrins. *Acc. Chem. Res.* **2005**, *38*, 733-743.
119. Kim, D.; Holten, D.; Gouterman, M.; Buchler, J. W. Comparative photophysics of platinum(II) and platinum(IV) porphyrins. *J. Am. Chem. Soc.* **1984**, *106*, 4015-4017.
120. Eastwood, D.; Gouterman, M. Porphyrins. XVIII. Luminescence of (Co), (Ni), Pd, Pt Complexes. *J. Mol. Spectrosc.* **1970**, *35*, 359-375.
121. Ou, Z. P.; Chen, P.; Kadish, K. M. First electrogeneration of a platinum(IV) porphyrin: elucidation of the Pt(II)/(IV) and Pt(IV)/(II) oxidation-reduction processes in nonaqueous media. *Dalton Trans.* **2010**, *39*, 11272-11276.
122. Rehm, D.; Weller, A. Kinetics of Fluorescence Quenching by Electron and H-Atom Transfer. *Israel J. Chem.* **1970**, *8*, 259-&.
123. Wenger, O. S. Photoinduced electron and energy transfer in phenylene oligomers. *Chem. Soc. Rev.* **2011**, *40*, 3538-3550.

124. Miyaura, N.; Suzuki, A. Palladium-Catalyzed Cross-Coupling Reactions of Organoboron Compounds. *Chem. Rev.* **1995**, *95*, 2457-2483.
125. Kobayashi, T.; Straub, K. D.; Rentzepis, P. M. Energy Relaxation Mechanism in Ni(II), Pd(II), Pt(II) and Zn(II) Porphyrins. *Photochem. Photobiol.* **1979**, *29*, 925-931.
126. Ponterini, G.; Serpone, N.; Bergkamp, M. A.; Netzel, T. L. Comparison of radiationless decay processes in osmium and platinum porphyrins. *J. Am. Chem. Soc.* **1983**, *105*, 4639-4645.
127. Korobov, V. E.; Shubin, V. V.; Chibisov, A. K. Triplet-State of Rhodamine Dyes and Its Role in Production of Intermediates. *Chem. Phys. Lett.* **1977**, *45*, 498-501.
128. Saik, V. O.; Goun, A. A.; Fayer, M. D. Photoinduced electron transfer and geminate recombination for photoexcited acceptors in a pure donor solvent. *J. Chem. Phys.* **2004**, *120*, 9601-9611.
129. Okada, T.; Mataga, N.; Sakata, Y.; Misumi, S. Ultrafast Intersystem Crossing of Intramolecular Heteroexcimers. *J. Photochem.* **1981**, *17*, 130-131.
130. Dance, Z. E.; Mi, Q.; McCamant, D. W.; Ahrens, M. J.; Ratner, M. A.; Wasielewski, M. R. Time-resolved EPR studies of photogenerated radical ion pairs separated by p-phenylene oligomers and of triplet states resulting from charge recombination. *J. Phys. Chem. B* **2006**, *110*, 25163-73.
131. Livesey, A. K.; Brochon, J. C. Analyzing the distribution of decay constants in pulse-fluorimetry using maximum entropy method. *Biophys. J.* **1987**, *52*, 693-706.
132. Pevenage, D.; Van der Auweraer, M.; De Schryver, F. C. Intramolecular photo-induced electron transfer between pyrene and a xanthene dye. *Chem. Phys. Lett.* **2000**, *319*, 512-520.
133. Korobov, V. E.; Chibisov, A. K. Primary Photoprocesses in Dye Molecules. *Usp. Khim.* **1983**, *52*, 43-71.
134. Kunavin, N. I.; Nurmukhametov, R. N.; Khachaturova, G. T. Phosphorescence and orbital nature of triplet state of xanthene dyes. *Journal of Applied Spectroscopy* **1977**, *26*, 735-739.
135. Chambers, R. W.; Kearns, D. R. Effect of Dimer Formation on Triplet States of Organic Dyes. *J. Phys. Chem.* **1968**, *72*, 4718-4720.

136. Morales, A. F.; Accorsi, G.; Armaroli, N.; Barigelletti, F.; Pope, S. J. A.; Ward, M. D. Interplay of light antenna and excitation "energy reservoir" effects in a bichromophoric system based on ruthenium-polypyridine and pyrene units linked by a long and flexible poly(ethylene glycol) chain. *Inorg. Chem.* **2002**, *41*, 6711-6719.
137. Lavie-Cambot, A.; Lincheneau, C.; Cantuel, M.; Leydet, Y.; McClenaghan, N. D. Reversible electronic energy transfer: a means to govern excited-state properties of supramolecular systems. *Chem. Soc. Rev.* **2010**, *39*, 506-515.
138. Chambers, R. W.; Kearns, D. R. Triplet States of Some Common Photosensitizing Dyes. *Photochem. Photobiol.* **1969**, *10*, 215-219.
139. Closs, G. L.; Piotrowiak, P.; Macinnis, J. M.; Fleming, G. R. Determination of Long-Distance Intramolecular Triplet Energy-Transfer Rates - a Quantitative Comparison with Electron-Transfer. *J. Am. Chem. Soc.* **1988**, *110*, 2652-2653.
140. Closs, G. L.; Johnson, M. D.; Miller, J. R.; Piotrowiak, P. A Connection between Intramolecular Long-Range Electron, Hole, and Triplet Energy Transfers. *J. Am. Chem. Soc.* **1989**, *111*, 3751-3753.
141. Welter, S.; Salluce, N.; Belser, P.; Groeneveld, M.; De Cola, L. Photoinduced electronic energy transfer in modular, conjugated, dinuclear Ru(II)/Os(II) complexes. *Coordin. Chem. Rev.* **2005**, *249*, 1360-1371.
142. Helms, A.; Heiler, D.; McLendon, G. Electron transfer in bis-porphyrin donor-acceptor compounds with polyphenylene spacers shows a weak distance dependence. *J. Am. Chem. Soc.* **1992**, *114*, 6227-6238.
143. Wenger, O. S.; Leigh, B. S.; Villahermosa, R. M.; Gray, H. B.; Winkler, J. R. Electron Tunneling Through Organic Molecules in Frozen Glasses. *Science* **2005**, *307*, 99-102.
144. Andreasson, J.; Kajanus, J.; Martensson, J.; Albinsson, B. Triplet energy transfer in porphyrin dimers: Comparison between pi- and sigma-chromophore bridged systems. *J. Am. Chem. Soc.* **2000**, *122*, 9844-9845.

145. Vura-Weis, J.; Abdelwahed, S. H.; Shukla, R.; Rathore, R.; Ratner, M. A.; Wasielewski, M. R. Crossover from single-step tunneling to multistep hopping for molecular triplet energy transfer. *Science* **2010**, *328*, 1547-50.
146. Barigelletti, F.; Flamigni, L.; Guardigli, M.; Juris, A.; Beley, M.; ChodorowskiKimmes, S.; Collin, J. P.; Sauvage, J. P. Energy transfer in rigid Ru(II)/Os(II) dinuclear complexes with biscyclometalating bridging ligands containing a variable number of phenylene units. *Inorg. Chem.* **1996**, *35*, 136-142.
147. Wenger, O. S. How Donor-Bridge-Acceptor Energetics Influence Electron Tunneling Dynamics and Their Distance Dependences. *Acc. Chem. Res.* **2011**, *44*, 25-35.
148. Albinsson, B.; Eng, M. P.; Pettersson, K.; Winters, M. U. Electron and energy transfer in donor-acceptor systems with conjugated molecular bridges. *Phys. Chem. Chem. Phys.* **2007**, *9*, 5847-5864.
149. Eng, M. P.; Albinsson, B. The dependence of the electronic coupling on energy gap and bridge conformation Towards prediction of the distance dependence of electron transfer reactions. *Chem. Phys.* **2009**, *357*, 132-139.
150. Meerholz, K.; Heinze, J. Electrochemical solution and solid-state investigations on conjugated oligomers and polymers of the alpha-thiophene and the p-phenylene series. *Electrochim. Acta* **1996**, *41*, 1839-1854.
151. Berlman, I. B. *Handbook of fluorescence spectra of aromatic molecules*. 2nd ed.; Academic Press: New York, 1971.
152. Murov, S. L.; Carmichael, I.; Hug, G. L. *Handbook of photochemistry*. 2nd ed.; M. Dekker: New York, 1993.
153. Mani, T.; Niedzwiedzki, D. M.; Vinogradov, S. A. Generation of Phosphorescent Triplet States via Photoinduced Electron Transfer: Energy and Electron Transfer Dynamics in Pt Porphyrin-Rhodamine B Dyads. *J. Phys. Chem. A* **2012**, *116*, 3598-3610.
154. Fischer, M.; Georges, J. Fluorescence quantum yield of rhodamine 6G in ethanol as a function of concentration using thermal lens spectrometry. *Chem. Phys. Lett.* **1996**, *260*, 115-118.

155. Vellis, P. D.; Mikroyannidis, J. A.; Bagnis, D.; Valentini, L.; Kenny, J. M. New Anthracene-Containing Phenylene- or Thienylene-Vinylene Copolymers: Synthesis, Characterization, Photophysics, and Photovoltaics. *J. Appl. Polym. Sci.* **2009**, *113*, 1173-1181.
156. Hayashi, Y.; Yamaguchi, S.; Cha, W. Y.; Kim, D.; Shinokubo, H. Synthesis of Directly Connected BODIPY Oligomers through Suzuki-Miyaura Coupling. *Org. Lett.* **2011**, *13*, 2992-2995.
157. Benniston, A. C.; Harriman, A.; Whittle, V. L.; Zelzer, M.; Harrington, R. W.; Clegg, W. Exciplex-like emission from a closely-spaced, orthogonally-sited anthracenyl-boron dipyrromethene (Bodipy) molecular dyad. *Photochem. Photobiol. Sci.* **2010**, *9*, 1009-1017.
158. Schuster, D. I.; Cheng, P.; Jarowski, P. D.; Guldi, D. M.; Luo, C. P.; Echegoyen, L.; Pyo, S.; Holzwarth, A. R.; Braslavsky, S. E.; Williams, R. M.; Klihm, G. Design, synthesis, and photophysical studies of a porphyrin-fullerene dyad with parachute topology; Charge recombination in the Marcus inverted region. *J. Am. Chem. Soc.* **2004**, *126*, 7257-7270.
159. Warman, J. M.; Smit, K. J.; Jonker, S. A.; Verhoeven, J. W.; Oevering, H.; Kroon, J.; Paddonrow, M. N.; Oliver, A. M. Intramolecular Charge Separation and Recombination in Nonpolar Environments Via Long-Distance Electron-Transfer through Saturated-Hydrocarbon Barriers. *Chem. Phys.* **1993**, *170*, 359-380.
160. Gould, I. R.; Noukakis, D.; Gomezjahn, L.; Young, R. H.; Goodman, J. L.; Farid, S. Radiative and Nonradiative Electron-Transfer in Contact Radical-Ion Pairs. *Chem. Phys.* **1993**, *176*, 439-456.
161. Vehmanen, V.; Tkachenko, N. V.; Imahori, H.; Fukuzumi, S.; Lemmetyinen, H. Charge-transfer emission of compact porphyrin-fullerene dyad analyzed by Marcus theory of electron-transfer. *Spectrochim. Acta A* **2001**, *57*, 2229-2244.
162. Imahori, H.; Tkachenko, N. V.; Vehmanen, V.; Tamaki, K.; Lemmetyinen, H.; Sakata, Y.; Fukuzumi, S. An extremely small reorganization energy of electron transfer in porphyrin-fullerene dyad. *J. Phys. Chem. A* **2001**, *105*, 1750-1756.

163. Becke, A. D. A New Mixing of Hartree-Fock and Local Density-Functional Theories. *J. Chem. Phys.* **1993**, *98*, 1372-1377.
164. Lee, C. T.; Yang, W. T.; Parr, R. G. Development of the Colle-Salvetti Correlation-Energy Formula into a Functional of the Electron-Density. *Phys. Rev. B.* **1988**, *37*, 785-789.
165. Krylov, A. I.; Gill, P. M. W. Q-Chem: an engine for innovation. *Wiley Interdisciplinary Reviews: Computational Molecular Science* **2013**, *3*, 317-326.
166. Benniston, A. C.; Copley, G.; Lemmetyinen, H.; Tkachenko, N. V. Exciplex Formation and Excited State Deactivation of Difluoroborondipyrromethene (Bodipy) Dyads. *ChemPhysChem* **2010**, *11*, 1685-1692.
167. Benniston, A. C.; Clift, S.; Hagon, J.; Lemmetyinen, H.; Tkachenko, N. V.; Clegg, W.; Harrington, R. W. Effect on Charge Transfer and Charge Recombination by Insertion of a Naphthalene-Based Bridge in Molecular Dyads Based on Borondipyrromethene (Bodipy). *ChemPhysChem* **2012**, *13*, 3672-3681.
168. Richards, V. J.; Gower, A. L.; Smith, J. E. H. B.; Davies, E. S.; Lahaye, D.; Slater, A. G.; Lewis, W.; Blake, A. J.; Champness, N. R.; Kays, D. L. Synthesis and characterisation of BODIPY radical anions. *Chem. Commun.* **2012**, *48*, 1751-1753.
169. Masnovi, J. M.; Kochi, J. K.; Hilinski, E. F.; Rentzepis, P. M. Reactive Ion-Pairs from the Charge-Transfer Excitation of Electron-Donor Acceptor Complexes. *J. Am. Chem. Soc.* **1986**, *108*, 1126-1135.
170. Fukuzumi, S.; Nakanishi, I.; Tanaka, K. Multielectron oxidation of anthracenes with a one-electron oxidant via water-accelerated electron-transfer disproportionation of the radical cations as the rate-determining step. *J. Phys. Chem. A* **1999**, *103*, 11212-11220.
171. Naqvi, K. R.; Melo, T. B. Reduction of tetranitromethane by electronically excited aromatics in acetonitrile: Spectra and molar absorption coefficients of radical cations of anthracene, phenanthrene and pyrene. *Chem. Phys. Lett.* **2006**, *428*, 83-87.
172. Pavlopoulos, T. G.; Boyer, J. H. Pyrromethene-BF<sub>2</sub> laser dyes. *Proc. SPIE* **1994**, 231-239.

173. Huang, L.; Yu, X. R.; Wu, W. H.; Zhao, J. Z. Styryl Bodipy-C-60 Dyads as Efficient Heavy-Atom-Free Organic Triplet Photosensitizers. *Org. Lett.* **2012**, *14*, 2594-2597.
174. Slifkin, M. A.; Alchalabi, A. O. High-Resolution Study of Triplet-Triplet Transitions of Some Aromatic-Hydrocarbons. *Spectrochim. Acta A* **1977**, *33*, 1091-1097.
175. Compton, R. H.; Grattan, K. T. V.; Morrow, T. Extinction Coefficients and Quantum Yields for Triplet-Triplet Absorption Using Laser Flash-Photolysis. *J. Photochem.* **1980**, *14*, 61-66.
176. Pavlopoulos, T. G.; Boyer, J. H.; Shah, M.; Thangaraj, K.; Soong, M. L. Laser Action from 2,6,8-Position Trisubstituted 1,3,5,7-Tetramethylpyrromethene-Bf<sub>2</sub> Complexes .1. *Appl. Opt.* **1990**, *29*, 3885-3886.
177. Ziessel, R.; Allen, B. D.; Rewinska, D. B.; Harriman, A. Selective Triplet-State Formation during Charge Recombination in a Fullerene/Bodipy Molecular Dyad (Bodipy = Borondipyrromethene). *Chem. Eur. J.* **2009**, *15*, 7382-7393.
178. Verhoeven, J. W. On the role of spin correlation in the formation, decay, and detection of long-lived, intramolecular charge-transfer states. *J. Photoch. Photobio. C* **2006**, *7*, 40-60.
179. Okada, T.; Karaki, I.; Matsuzawa, E.; Mataga, N.; Sakata, Y.; Misumi, S. Ultrafast Intersystem Crossing in Some Intramolecular Heteroexcimers. *J. Phys. Chem.* **1981**, *85*, 3957-3960.
180. Lim, B. T.; Okajima, S.; Chandra, A. K.; Lim, E. C. Radiationless Transitions in Electron Donor-Acceptor Complexes - Selection-Rules for S<sub>1</sub>-T Intersystem Crossing and Efficiency of S<sub>1</sub>-S<sub>0</sub> Internal-Conversion. *Chem. Phys. Lett.* **1981**, *79*, 22-27.
181. Wasielewski, M. R.; Johnson, D. G.; Svec, W. A.; Kersey, K. M.; Minsek, D. W. Achieving High Quantum Yield Charge Separation in Porphyrin-Containing Donor-Acceptor Molecules at 10-K. *J. Am. Chem. Soc.* **1988**, *110*, 7219-7221.
182. Miura, T.; Carmieli, R.; Wasielewski, M. R. Time-Resolved EPR Studies of Charge Recombination and Triplet-State Formation within Donor-Bridge-Acceptor Molecules Having Wire-Like Oligofluorene Bridges. *J. Phys. Chem. A* **2010**, *114*, 5769-5778.

183. vanWilligen, H.; Jones, G.; Farahat, M. S. Time-resolved EPR study of photoexcited triplet-state formation in electron-donor-substituted acridinium ions. *J. Phys. Chem.* **1996**, *100*, 3312-3316.
184. Jones, G.; Farahat, M. S.; Greenfield, S. R.; Gosztola, D. J.; Wasielewski, M. R. Ultrafast Photoinduced Charge-Shift Reactions in Electron Donor-Acceptor 9-Arylacridinium Ions. *Chem. Phys. Lett.* **1994**, *229*, 40-46.
185. Kaptein, R. Chemically Induced Dynamic Nuclear Polarization .8. Spin Dynamics and Diffusion of Radical Pairs. *J. Am. Chem. Soc.* **1972**, *94*, 6251-6262.
186. Miura, T.; Maeda, K.; Arai, T. The spin mixing process of a radical pair in low magnetic field observed by transient absorption detected nanosecond pulsed magnetic field effect. *J. Phys. Chem. A* **2006**, *110*, 4151-4156.
187. Miura, T.; Murai, H. Real-time observation of the spin-state mixing process of a micellized radical pair in weak magnetic fields by nanosecond fast field switching. *J. Phys. Chem. A* **2008**, *112*, 2526-2532.
188. Maeda, K.; Miura, T.; Arai, T. A practical simulation and a novel insight to the magnetic field effect on a radical pair in a micelle. *Mol. Phys.* **2006**, *104*, 1779-1788.
189. Miura, T.; Scott, A. M.; Wasielewski, M. R. Electron Spin Dynamics as a Controlling Factor for Spin-Selective Charge Recombination in Donor-Bridge-Acceptor Molecules. *J. Phys. Chem. C* **2010**, *114*, 20370-20379.
190. Wan, C. W.; Burghart, A.; Chen, J.; Bergstrom, F.; Johansson, L. B. A.; Wolford, M. F.; Kim, T. G.; Topp, M. R.; Hochstrasser, R. M.; Burgess, K. Anthracene-BODIPY cassettes: Syntheses and energy transfer. *Chem. Eur. J.* **2003**, *9*, 4430-4441.
191. Bai, D.; Benniston, A. C.; Hagon, J.; Lemmetyinen, H.; Tkachenko, N. V.; Clegg, W.; Harrington, R. W. Exploring Forster electronic energy transfer in a decoupled anthracenyl-based borondipyrromethene (bodipy) dyad. *Phys. Chem. Chem. Phys.* **2012**, *14*, 4447-4456.
192. Förster, T. Zwischenmolekulare Energiewanderung und Fluoreszenz. *Ann. Phys. (Berlin)* **1948**, *437*, 55-75.

193. Förster, T. Transfer Mechanisms of Electronic Excitation Energy. *Radiat. Res. Suppl.* **1960**, *2*, 326-339.
194. Giribabu, L.; Kumar, A. A.; Neeraja, V.; Maiya, B. G. Orientation dependence of energy transfer in an anthracene-porphyrin donor-acceptor system. *Angew. Chem. Int. Edit.* **2001**, *40*, 3621-3624.
195. Rachford, A. A.; Ziesel, R.; Bura, T.; Retailleau, P.; Castellano, F. N. Boron Dipyrromethene (Bodipy) Phosphorescence Revealed in [Ir(ppy)(2)(bpy-C C-Bodipy)](+). *Inorg. Chem.* **2010**, *49*, 3730-3736.
196. Closs, G. L.; Closs, L. E. Induced Dynamic Nuclear Spin Polarization in Reactions of Photochemically and Thermally Generated Triplet Diphenylmethylenes. *J. Am. Chem. Soc.* **1969**, *91*, 4549-4550.
197. Kaptein, R.; Oosterhoff, J. L. Chemically induced dynamic nuclear polarization II - (Relation with anomalous ESR spectra). *Chem. Phys. Lett.* **1969**, *4*, 195-197.
198. Yamauchi, S. Recent developments in studies of electronic excited states by means of electron paramagnetic resonance spectroscopy. *Bull. Chem. Soc. Jpn.* **2004**, *77*, 1255-1268.
199. Jiao, G. S.; Castro, J. C.; Thoresen, L. H.; Burgess, K. Microwave-assisted syntheses of regioisomerically pure bromorhodamine derivatives. *Org. Lett.* **2003**, *5*, 3675-3677.
200. Montes, V. A.; Perez-Bolivar, C.; Agarwal, N.; Shinar, J.; Anzenbacher, P. Molecular-wire behavior of OLED materials: Exciton dynamics in multichromophoric Alq(3)-oligofluorene-Pt(II) porphyrin triads. *J. Am. Chem. Soc.* **2006**, *128*, 12436-12438.
201. Brinas, R. P.; Troxler, T.; Hochstrasser, R. M.; Vinogradov, S. A. Phosphorescent oxygen sensor with dendritic protection and two-photon absorbing antenna. *J. Am. Chem. Soc.* **2005**, *127*, 11851-11862.
202. Vinogradov, S. A.; Wilson, D. F. Porphyrin-dendrimers as biological oxygen sensors. In *Designing Dendrimers*, Capagna, S.; Ceroni, P.; Puntoriero, F., Eds. Wiley: New York, 2012.

203. Beaumont, P. C.; Johnson, D. G.; Parsons, P. J. Excited state and free radical properties of rhodamine dyes in aqueous solution: A laser flash photolysis and pulse radiolysis study. *J. Photoch. Photobiol. A* **1997**, *107*, 175-183.
204. Forbes, M. D. E. Time-resolved (CW) electron paramagnetic resonance spectroscopy: An overview of the technique and its use in organic photochemistry. *Photochem. Photobiol.* **1997**, *65*, 73-81.
205. Hirota, N.; Yamauchi, S. Short-lived excited triplet states studied by time-resolved EPR spectroscopy. *J. Photoch. Photobiol. C* **2003**, *4*, 109-124.
206. Katsuki, A.; Terokubota, S.; Ikegami, Y. Cidep Study on the Photosensitized Reactions of P-Benzoquinone and Hydroquinone by Eosin-Y. *Chem. Phys. Lett.* **1993**, *209*, 258-262.
207. Chen, P.; Finikova, O. S.; Ou, Z. P.; Vinogradov, S. A.; Kadish, K. M. Electrochemistry of Platinum(II) Porphyrins: Effect of Substituents and pi-Extension on Redox Potentials and Site of Electron Transfer. *Inorganic Chemistry* **2012**, *51*, 6200-6210.
208. Weissman, S. I. Recent Developments in Electron-Paramagnetic Resonance - Transient Methods. *Annu. Rev. Phys. Chem.* **1982**, *33*, 301-318.
209. Hirota, N.; Yamauchi, S.; Terazima, M. Time-Resolved Electron-Paramagnetic-Res Investigation of Very Short-Lived Triplet-States of Azaaromatics. *Rev. Chem. Intermed.* **1987**, *8*, 189-205.
210. Scott, A. M.; Miura, T.; Ricks, A. B.; Dance, Z. E. X.; Giacobbe, E. M.; Colvin, M. T.; Wasielewski, M. R. Spin-Selective Charge Transport Pathways through p-Oligophenylene-Linked Donor-Bridge-Acceptor Molecules. *J. Am. Chem. Soc.* **2009**, *131*, 17655-17666.
211. Weiss, E. A.; Ahrens, M. J.; Sinks, L. E.; Gusev, A. V.; Ratner, M. A.; Wasielewski, M. R. Making a molecular wire: Charge and spin transport through para-phenylene oligomers. *J. Am. Chem. Soc.* **2004**, *126*, 5577-5584.
212. Schlupmann, J.; Lenzian, F.; Plato, M.; Mobius, K. Light-Induced Triplet Electron-Transfer in Cyclohexene-Bridged Porphyrin Quinones Detected by Time-Resolved Electron-Paramagnetic-Resonance Spectroscopy. *J. Chem. Soc. Faraday. T.* **1993**, *89*, 2853-2862.

213. Murakami, M.; Maeda, K.; Arai, T. Dynamics of intramolecular electron transfer reaction of FAD studied by magnetic field effects on transient absorption spectra. *J. Phys. Chem. A* **2005**, *109*, 5793-5800.
214. Kobori, Y.; Fuki, M.; Murai, H. Electron Spin Polarization Transfer to the Charge-Separated State from Locally Excited Triplet Configuration. Theory and Its Application to Characterization of Geometry and Electronic Coupling in the Electron Donor-Acceptor System. *J. Phys. Chem. B* **2010**, *114*, 14621-14630.
215. Kobori, Y.; Fuki, M. Protein-Ligand Structure and Electronic Coupling of Photoinduced Charge-Separated State: 9,10-Anthraquinone-1-sulfonate Bound to Human Serum Albumin. *J. Am. Chem. Soc.* **2011**, *133*, 16770-16773.
216. Vandijk, N.; Noort, M.; Voelker, S.; Canters, G. W.; Vanderwaals, J. H. Zeeman Experiments on the 3eu Reversible 1a1g Transition of Platinum Porphin in a Normal-Alkane Single-Crystal at 4.2-K. *Chem. Phys. Lett.* **1980**, *71*, 415-423.
217. Vanderpoel, W. A. J. A.; Nuijs, A. M.; Vanderwaals, J. H. Electron-Spin-Resonance in the 4-E-U State of Copper Porphine and the 3-E-U State of Platinum Porphine in Normal-Octane and Normal-Decane Crystals. *J. Phys. Chem.* **1986**, *90*, 1537-1540.
218. Johnson, R. C.; Merrifield, R. E.; Avakian, P.; Flippen, R. B. Effects of Magnetic Fields on Mutual Annihilation of Triplet Excitations in Molecular Crystals. *Phys. Rev. Lett.* **1967**, *19*, 285.
219. Le Sage, D.; Arai, K.; Glenn, D. R.; DeVience, S. J.; Pham, L. M.; Rahn-Lee, L.; Lukin, M. D.; Yacoby, A.; Komeili, A.; Walsworth, R. L. Optical magnetic imaging of living cells. *Nature* **2013**, *496*, 486-489.
220. Mani, T.; Tanabe, M.; Yamauchi, S.; Tkachenko, N. V.; Vinogradov, S. A. Modulation of Visible Room Temperature Phosphorescence by Weak Magnetic Fields. *J. Phys. Chem. Lett.* **2012**, *3*, 3115-3119.
221. Johnson, R. C.; Merrifield, R. E. Effects of Magnetic Fields on Mutual Annihilation of Triplet Excitons in Anthracene Crystals. *Phys. Rev. B* **1970**, *1*, 896-902.

222. Merrifield, R. E. Theory of magnetic field effects on mutual annihilation of triplet excitons. *J. Chem. Phys.* **1968**, *48*, 4318.
223. Groff, R. P.; Merrifield, R. E.; Avakian, P. Singlet and triplet channels for triplet-exciton fusion in anthracene crystals. *Chem. Phys. Lett.* **1970**, *5*, 168-170.
224. Geacintov, N. E.; Swenberg, C. E. Possible Effects of Magnetic-Fields on Quenching of Triplet Excited-States of Polynuclear Hydrocarbons by Oxygen. *J. Chem. Phys.* **1972**, *57*, 378.
225. Tachikawa, H.; Bard, A. J. Magnetic-Field Effects on Oxygen Quenching of Delayed Fluorescence of Anthracene and Pyrene in Fluid Solution. *J. Am. Chem. Soc.* **1973**, *95*, 1672-1673.
226. Tachikawa, H.; Bard, A. J. Electrogenerated Chemiluminescence. Effect of a Magnetic Field on Delayed Fluorescence and Ecl of Several Systems Involving Excimers or Exciplexes. *Chem. Phys. Lett.* **1974**, *26*, 568-573.
227. Santhana, K. S. V. Magnetic Field Effect on Electrochemiluminescence of Carbazole. *Can. J. Chem.* **1971**, *49*, 3577-3578.
228. Simon, Y. C.; Weder, C. Low-power photon upconversion through triplet-triplet annihilation in polymers. *J. Mater. Chem.* **2012**, *22*, 20817-20830.
229. Zhao, J. Z.; Ji, S. M.; Guo, H. M. Triplet-triplet annihilation based upconversion: from triplet sensitizers and triplet acceptors to upconversion quantum yields. *Rsc Adv.* **2011**, *1*, 937-950.
230. Balushev, S.; Yakutkin, V.; Miteva, T.; Avlasevich, Y.; Chernov, S.; Aleshchenkov, S.; Nelles, G.; Cheprakov, A.; Yasuda, A.; Mullen, K.; Wegner, G. Blue-green up-conversion: Noncoherent excitation by NIR light. *Angew. Chem. Int. Edit.* **2007**, *46*, 7693-7696.
231. Balushev, S.; Yakutkin, V.; Miteva, T.; Wegner, G.; Roberts, T.; Nelles, G.; Yasuda, A.; Chernov, S.; Aleshchenkov, S.; Cheprakov, A. A general approach for non-coherently excited annihilation up-conversion: transforming the solar-spectrum. *New. J. Phys.* **2008**, *10*, 013007.

232. Balushev, S.; Yakutkin, V.; Wegner, G.; Miteva, T.; Nelles, G.; Yasuda, A.; Chernov, S.; Aleshchenkov, S.; Cheprakov, A. Upconversion with ultrabroad excitation band: Simultaneous use of two sensitizers. *Appl. Phys. Lett.* **2007**, *90*, 181103.
233. Singh-Rachford, T. N.; Castellano, F. N. Triplet Sensitized Red-to-Blue Photon Upconversion. *J. Phys. Chem. Lett.* **2010**, *1*, 195-200.
234. Singh-Rachford, T. N.; Nayak, A.; Muro-Small, M. L.; Goeb, S.; Therien, M. J.; Castellano, F. N. Supermolecular-Chromophore-Sensitized Near-Infrared-to-Visible Photon Upconversion. *J. Am. Chem. Soc.* **2010**, *132*, 14203-14211.
235. Mezyk, J.; Tubino, R.; Monguzzi, A.; Mech, A.; Meinardi, F. Effect of an External Magnetic Field on the Up-Conversion Photoluminescence of Organic Films: The Role of Disorder in Triplet-Triplet Annihilation. *Phys. Rev. Lett.* **2009**, *102*, 087404.
236. Piland, G. B.; Burdett, J. J.; Kurunthu, D.; Bardeen, C. J. Magnetic Field Effects on Singlet Fission and Fluorescence Decay Dynamics in Amorphous Rubrene. *J. Phys. Chem. C* **2013**, *117*, 1224-1236.
237. Wohnhaas, C.; Turshatov, A.; Mailander, V.; Lorenz, S.; Balushev, S.; Miteva, T.; Landfester, K. Annihilation Upconversion in Cells by Embedding the Dye System in Polymeric Nanocapsules. *Macromol. Biosci.* **2011**, *11*, 772-778.
238. Johnson, R. C.; Merrifield, R. E. Effects of Magnetic Fields on Mutual Annihilation of Triplet Excitons in Anthracene Crystals. *Phys. Rev. B.* **1970**, *1*, 896-902.
239. Suna, A. Kinematics of Exciton-Exciton Annihilation in Molecular Crystals. *Phys. Rev. B.* **1970**, *1*, 1716-1739.
240. Atkins, P. W.; Evans, G. T. Magnetic-Field Effects on Chemiluminescent Fluid Solutions. *Mol. Phys.* **1975**, *29*, 921-935.
241. Finikova, O. S.; Cheprakov, A. V.; Beletskaya, I. P.; Carroll, P. J.; Vinogradov, S. A. Novel versatile synthesis of substituted tetrabenzoporphyrins. *J. Org. Chem.* **2004**, *69*, 522-535.

242. Finikova, O. S.; Cheprakov, A. V.; Vinogradov, S. A. Synthesis and luminescence of soluble meso-unsubstituted tetrabenzo- and tetranaphtho[2,3]porphyrins. *J. Org. Chem.* **2005**, *70*, 9562-9572.
243. Cheprakov, A. V.; Filatov, M. A. The dihydroisoindole approach to linearly annelated pi-extended porphyrins. *J. Porphyr. Phthalocya.* **2009**, *13*, 291-303.
244. Vinogradov, S. A.; Wilson, D. F. Metallotetrabenzoporphyrins - New Phosphorescent Probes for Oxygen Measurements. *J. Chem. Soc. Perk T. 2* **1995**, 103-111.
245. Aartsma, T. J.; Gouterman, M.; Jochum, C.; Kwiram, A. L.; Pepich, B. V.; Williams, L. D. Porphyrins .43. Triplet Sublevel Emission of Platinum Tetrabenzoporphyrin by Spectro-Thermal Principal Component Decomposition. *J. Am. Chem. Soc.* **1982**, *104*, 6278-6283.
246. Clarke, R. H.; Hochstrasser, R. M. Location and Assignment of Lowest Triplet State of Perylene. *J. Mol. Spectrosc.* **1969**, *32*, 309-319.
247. Esipova, T. V.; Karagodov, A.; Miller, J.; Wilson, D. F.; Busch, T. M.; Vinogradov, S. A. Two New "Protected" Oxyphors for Biological Oximetry: Properties and Application in Tumor Imaging. *Anal. Chem.* **2011**, *83*, 8756-8765.
248. Borisov, S. M.; Larndorfer, C.; Klimant, I. Triplet-Triplet Annihilation-Based Anti-Stokes Oxygen Sensing Materials with a Very Broad Dynamic Range. *Adv. Func. Mat.* **2012**, *22*, 4360-4368.
249. Parker, C. A.; Joyce, T. A. Formation Efficiency and Energy of Perylene Triplet. *Chem. Commun.* **1966**, 108-109.
250. Imamura, T.; Onitsuka, O.; Murai, H.; Obi, K. Conservation of Spin Polarization during Triplet Triplet Energy-Transfer in Low-Temperature Matrices. *J. Phys. Chem.* **1984**, *88*, 4028-4031.
251. Elsayed, M. A.; Tinti, D. S.; Yee, E. M. Conservation of Spin Direction and Production of Spin Alignment in Triplet-Triplet Energy Transfer. *J. Chem. Phys.* **1969**, *51*, 5721.
252. Clarke, R. H. Magnetic resonance studies of optical spin polarization in triplet state anthracene. *Chem. Phys. Lett.* **1970**, *6*, 413-416.

253. Vandijk, N.; Noort, M.; Voelker, S.; Canters, G. W.; Van der Waals, J. H. Zeeman Experiments on the 3eu Reversible 1a1g Transition of Platinum Porphin in an Normal-Alkane Single-Crystal at 4.2-K. *Chem. Phys. Lett.* **1980**, *71*, 415-423.
254. Vanderpoel, W. A. J. A.; Nuijs, A. M.; Van der Waals, J. H. Electron-Spin-Resonance in the 4-E-U State of Copper Porphine and the 3-E-U State of Platinum Porphine in Normal-Octane and Normal-Decane Crystals. *J. Phys. Chem.* **1986**, *90*, 1537-1540.
255. Steren, C. A.; Vanwilligen, H.; Dinse, K. P. Spin Dynamics of C-60 Triplets. *J. Phys. Chem.* **1994**, *98*, 7464-7469.
256. Iwasaki, Y.; Maeda, K.; Murai, H. Time-domain observation of external magnetic field effects on the delayed fluorescence of N,N,N',N'-tetramethyl-1,4-phenylenediamine in alcoholic solution. *J. Phys. Chem. A* **2001**, *105*, 2961-2966.
257. Jiang, Y.; Blanchard, G. J. Rotational Diffusion Dynamics of Perylene in N-Alkanes - Observation of a Solvent Length-Dependent Change of Boundary-Condition. *J. Phys. Chem.* **1994**, *98*, 6436-6440.
258. Lifshitz, E.; Kaplan, A.; Ehrenfreund, E.; Meissner, D. Optically detected magnetic resonance as a tool to study the morphology of perylene-derivative thin film. *Chem. Phys. Lett.* **1999**, *300*, 626-632.
259. Jas, G. S.; Larson, E. J.; Johnson, C. K.; Kuczera, K. Microscopic details of rotational diffusion of perylene in organic solvents: Molecular dynamics simulation and experiment vs Debye-Stokes-Einstein theory. *J. Phys. Chem. A* **2000**, *104*, 9841-9852.